Petrogenesis of the early Archean komatiites from the Gorumahishani greenstone belt, Singhbhum Craton, India

Thesis submitted for the Degree of Doctor of Philosophy (Science) in Geology of Jadavpur University

2023

Ratul Banerjee

CEFIPRA Senior Research Fellow

PhD INDEX No: 167/18/Geol. Sc./26

PhD Registration No: SOGEO1116718

Department of Geological Sciences

Jadavpur University

Kolkata- 700032

India

যাদবপুর বিশ্ববিদ্যালয়
কলকাতা - ৭০০০৩২, ভারত

JADAVPUR UNIVERSITY
KOLKATA-700 032, INDIA

FACULTY OF SCIENCE : DEPARTMENT OF GEOLOGICAL SCIENCES

CERTIFICATE FROM THE SUPERVISOR

This is to certify that the thesis entitled **'Petrogenesis of the early Archean komatiites from the Gorumahishani greenstone belt, Singhbhum Craton, India'** submitted by **Ratul Banerjee** who got his name registered on **12.09.2018 (PhD Index No: 167/18/Geol. Sc./26** and **PhD Registration No: SOGEO1116718)** for the award of PhD (Science) degree of Jadavpur University, is absolutely based upon his own work under the supervision of **Professor Sisir Kanti Mondal** and that neither this thesis nor any part of it has been submitted for either any degree/ diploma or any other academic award anywhere before.

Sisir Kanti Mondal

14.09.2023

Dr Sisir Kanti Mondal, Supervisor
Professor of Geology
Department of Geological Sciences
Jadavpur University, India
e-Mail: sisir.mondal@jadavpuruniversity.in

Sisir Kanti Mondal
Professor of Geology
Jadavpur University

Dedicated to all the people who

have helped me to learn something new

in my research work as well as in my life

Contents

Acknowledgements

I would like to express my sincere gratitude to my supervisor Professor Sisir K. Mondal for his constant encouragement to pursue this degree. His guidance in every aspect of my research is very helpful in improving the quality of my work. I have received international exposure from my supervisor to communicate science and present my research work in front of the eminent scientists of the world. His tenacity and perseverance in research always motivate me to come out of my comfort zone.

I am thankful to the Indo-French Centre for the Promotion of Advanced Research (IFCPAR/CEFIPRA) and the Department of Science and Technology (DST) for the research fellowship that has provided financial support during my Ph.D. tenure. I also wish to thank Jadavpur University for giving me the research opportunity.

I would like to acknowledge Dr. Laurie Reisberg (CNRS-CRPG, France), Professor Jung-Woo Park (Seoul National University, South Korea), and Dr. Xiaoyu Zhou (CNRS-CRPG, France) for their extended support in the analytical works through the CEFIPRA collaborative project 6007-1 with my supervisor. My research advisory committee members Professor Dipak C. Pal and Professor Susanta K. Samanta are acknowledged for their insightful comments which helped me to improve my understanding. I am also thankful to the past and present scholars from our laboratory for helping me to develop my research work.

Last, but not least, I would like to thank my mother Mrs. Ratna Banerjee, my father Mr. Shyamal Banerjee, and all other family members for their constant support and encouragement through thick and thin. I would not be able to complete my thesis without their unselfish cooperation.

Abstract

In the Archean Gorumahishani greenstone belt of the Singhbhum Craton, a ~3.5 Ga komatiitic suite of rocks is present at the lower part of the volcano-sedimentary sequence. Primary silicate minerals from the komatiitic suite of rocks are altered to serpentine, tremolite, chlorite, hornblende, and epidote, indicating a greenschist to amphibolite facies metamorphism. The metamorphosed chromites show three types of zoning and are classified as type-I, II, and III with differences in major (MgO, Al_2O_3), trace (Zn, Co, Mn, Ti, V), and platinum-group elements (Os, Ir, Ru, Rh) concentrations from the central core to inner ferritchromit to outer chrome magnetite rims. The modal abundances of minerals are reflected in the bulk-rock major and trace elements of the komatiitic rocks that show a decrease in Ni and MgO together with an increase in CaO, Al_2O_3, $FeO_{(T)}$, Sc, Sr, and V from lower to upper part of the sequence. Bulk-rock Pd/Ru and Pd/Ir show a negative relation with MgO and Cr due to the crystallization of chromite that removes Ru and Ir from the magma while Pd and Pt are concentrated in the fractionated komatiitic magma. Compositionally, the komatiites are Ti-depleted in the northern part (Maharajgunj-Chukapahar) and Al-depleted in the middle (Tua-Dungri) and southern parts (Kapili) of the greenstone belt. Two-stage melting of a rising mantle plume produced the Al-depleted komatiite melt at the garnet peridotite stability field, and Ti-depleted komatiite melt at the spinel peridotite stability field. The komatiitic magma erupted in an intracontinental rift setting and interacted with the mafic-dominated proto-crust. The komatiitic magma supplied the necessary heat to melt the proto-crust at different depths and in different degrees and generated the parental magma of the contemporary (~3.6 - 3.3 Ga) tonalite-trondhjemite-granodiorite-granite suite of rocks.

Chapter 1

Introduction

1. Introduction

The early lithosphere of the Earth formed the outer stagnant lid and was separated from the vigorously convecting Hadean mantle by a thermal boundary layer (Harrison et al. 2008; Debaille et al. 2013). This stagnant-lid tectonics that had shaped the early Earth's surface was gradually transformed into active plate tectonics and added more crustal materials to produce a thicker crust (e.g. O'Neill et al. 2007; Nebel et al. 2018). There are several hypotheses to explain the Earth's crustal thickening processes: (i) melting of the existing crust by high heat flow and dripping of the melted rock back into the mantle that might have added water to the mantle and thus produced a high degree of melts to add with the existing crustal material (Smithies et al. 2003; Johnson et al. 2014), (ii) new melts generated from the existing crust by the impact of meteorites (Hansen 2015), and (iii) high heat flow at the base of the existing crust melts parts of it to produce more buoyant and less dense melts forming some crustal pockets (Smithies et al. 2003). These proto-crusts were rarely preserved and functioned as a basement or source of the parental magmas for the early Archean tonalite-trondhjemite-granodiorite-granite rocks. The preserved Archean crustal components are generally small in size, highly fragmented, and complex. Archean rocks with an age >2.5 Ga are outcropped in most of the continents and range in size from < 0.1 to 2.6 X 10^6 km^2 (Condie 1976). Although the Archean rock exposures occupy a small part of the total continental crust, these are widely distributed because much of the Archean crust is buried by the Proterozoic platform sediments or present as lower crustal material (Bleeker 2002). A complete understanding of the evolution of an ancient craton is challenging because the older

crusts of small dimensions are extensively altered, deformed, and in many places poorly preserved (e.g. Bleeker 2002, 2003).

The Archean supracrustal rocks are mostly represented by the granite-greenstone terrains of any ancient cratons. The greenstone assemblages include ultramafic-mafic volcanic and intercalated sedimentary rocks and are distributed in linear or arcuate-shaped belts (e.g. DeWit and Ashwal 1995). The greenstone belts are surrounded by vast granite to granodioritic and gneissic rocks which comprise ~75% of the granite-greenstone association (e.g. Condie 1967, 1981). The komatiitic suite of rocks is present at the lower part of the greenstone sequence which is intercalated with quartzite, chert, felsic tuffs, carbonate-rich schists, and conglomerates (e.g. Barnes 2006). The felsic volcanics and banded iron formation are present at the upper part of this sequence. The rocks of the greenstone belts are commonly metamorphosed under greenschist and/or amphibolite facies and are extensively deformed (e.g. Barnes 2000). The abundance of komatiitic rocks is relatively low in the early Archean greenstone belts of ˜3.6 - 3.3 Ga e.g. Barberton and Schapenburg (South Africa), Coonterunah (Western Australia), Gorumahishani-Badampahar-Tomka-Daitari, and Sargur (India). The abundance of komatiites is higher in the Mesoarchean to late Archean greenstone belts of ~3.2 - 2.7 Ga e.g. Weltevreden (South Africa), Regal-Ruth well, Forrestania, and Kambalda (Western Australia), Belingwe (Zimbabwe), Kostomuksha (Russia and East Europe), Alexo and Pyke Hill (Canada) (e.g. Condie 1981). High mantle temperature and production of high heat flows by plume-induced magmatic underplating are considered for the development of wide-spread rift systems in the early Archean (~3.6 - 3.3 Ga) through which extensive ultramafic-mafic magmatism occurred (e.g. Bleeker 2002; Johnson

et al. 2019). The inter-continental rift basins were slowly transformed into ocean basins (e.g. Kröner and Layer 1992; Bleeker 2002) which was responsible for a gradual shift of geodynamics of the Earth to initiate subduction processes from Mesoarchean that resulted in the assembly of supercontinents by accretion (e.g. Friend and Nutman 2019) and a secular cooling of the Earth's mantle (e.g. Keller and Schoene 2012). The geochemical composition of the early Archean to Late Archean tonalite-trondhjemite-granodiorite rocks also helps in understanding the secular change of mantle temperatures and geodynamic processes in the Precambrian. It has been noted that there was an increase in MgO along with Ni, Cr, Sr, and (Na_2O + CaO) from early to late Archean tonalite-trondhjemite-granodiorite rocks (e.g. Smithies 2000). The higher concentrations of these elements indicate a subduction-driven origin of tonalite-trondhjemite-granodiorites during the late Archean due to the interaction of the ascending parental felsic magma with the overlying mantle wedge (e.g. Johnson et al. 2019). On the other hand, most of the low- and high-HREE tonalite-trondhjemite-granodiorites with low-MgO indicate an origin from different crustal depths during the early Archean (e.g. Martin and Moyen 2002).

The komatiitic suite of rocks within the greenstone belts exhibits a range of textures and volcanic structures. The ultramafic lava sequence was differentiated into komatiitic dunite (cumulate zone) at the bottom part that grades into spinifex-textured komatiitic peridotite (spinifex zone) to komatiitic basalt at the top (e.g. Arndt and Nisbet 1982). The presence of pillow basalts, columnar joints, and chilled margins at the top of the komatiitic basalt indicate rapid cooling of the komatiitic lava flow (e.g. Viljoen and Viljoen 1969; Nesbitt 1971; Arndt et al. 1977; Donaldson 1982). The komatiitic magmas commonly have >18 wt.% MgO, <1 wt.% (Na_2O + K_2O),

and <52 wt.% SiO_2. The komatiites are classified into three major types based on their chemical composition (e.g. Arndt et al. 2008): (i) Al-depleted Barberton-type komatiite that has sub-chondritic Al_2O_3/TiO_2 (< 15) and depleted with heavy rare earth elements (HREE), (ii) Al-undepleted Munro-type komatiite having Al_2O_3/TiO_2 ratios (~22) close to primitive mantle composition and flat HREE patterns, and (iii) Ti-depleted komatiite with Al_2O_3 content similar to Al-undepleted komatiites but low TiO_2 content resulting an Al_2O_3/TiO_2 ratio >25 and flat to depleted HREE pattern. Al-depleted komatiites show HREE depletion due to the retention of majorite garnet at the source which sequesters Al and HREE compared to Ti and middle REE (MREE; e.g. Nesbitt and Sun 1979; Nesbitt et al. 1982; Sossi et al. 2016). Garnet is increasingly stable at high pressure (≥ 6 to 13 GPa; Herzberg 1995) at the garnet-peridotite stability field (Ringwood and Major 1971; Zhang and Herzberg 1994). Therefore, the Al-depleted komatiites are thought to have originated from > 200 km depth with ~25% - 30% partial melting without exhausting garnet from the mantle source (e.g. Arndt 2003). Conversely, Al-undepleted and Ti-depleted komatiites with unfractionated or less fractionated Gd_N/Yb_N ratios, are thought to have formed by larger degrees of partial melting (up to ~50%) of a depleted mantle source at a shallower depth (e.g. Arndt 2003). Retention of garnet in the depleted mantle source after extraction of the Al-depleted komatiitic melt gives rise high Gd_N/Yb_N ratio in the Al-undepleted and Ti-depleted komatiites as Yb is highly compatible and Gd is incompatible with garnet (e.g. Walter 1998; Robin-Popieul et al. 2012). An alternative theory on the origin of komatiitic magma suggests a hydrous melting of the mantle wedge within a supra-subduction setting (e.g. Allègre 1982; Grove et al. 1999; Parman et al. 2001, 2004). However, this model can not explain the difference

in the geochemical character of the three types of komatiites as commonly encountered in different greenstone belts (e.g. Arndt et al. 2008).

The komatiitic rocks represent a unique window to understand the dynamics of the Archean mantle, however, interpretation based on these rocks becomes challenging due to the modification of the original rocks during metamorphism and deformation. Chromite is a common accessory phase in the komatiitic dunite and peridotites from the cumulate and spinifex zones in the greenstone belt (e.g. Barnes 1998, 2000; Banerjee et al. 2023). Chromite appears late in the crystallization sequence after olivine and as a consequence shows relatively higher modal abundance in the spinifex zone than in the lower cumulate zone (e.g. Barnes 1998). The Cr/(Cr+Al) ratio, Ti, Al, and V of chromites are used as petrogenetic indicators in massive chromitites (e.g. Irvine 1967; Roeder 1994; Stowe 1997; Mondal et al. 2006; Mukherjee et al. 2010) and volcanic rocks (Kamenetsky et al. 2001; Canil 2002; Nicklas et al. 2016). However, in komatiitic rocks, chromites as well as the primary silicate phases are often strongly affected by hydrothermal alteration and metamorphism (e.g. Barnes 1998, 2000). Such processes have led to textural variability and chemical modification of chromite in many ultramafic-mafic rocks from widely varying geological settings (Evans and Frost 1975; Kimball 1990; Burkhard 1993; Proenza et al. 2004; González Jiménez et al. 2009, 2014; Mukherjee et al. 2015; Colás et al. 2019, 2020; Staddon et al. 2021; Datta and Mondal 2021; Bussolesi et al. 2022) although studies of komatiitic chromites are relatively scarce (e.g. Zhou and Kerrich 1992; Barnes 1998, 2000; Barnes and Brand 1999; Locmelis et al. 2011, 2013; Pagé et al. 2012; Godel et al. 2013; Haugaard et al. 2021; Staude et al. 2022; Barnes et al. 2023). Major and minor element studies of komatiitic chromites

(Barnes 1998, 2000) showed that at low metamorphic grades, the core compositions may retain their primary magmatic character and can be used to understand the magmatic crystallization environment. Diverse opinions exist concerning the formation of the characteristic optical and chemical zoning of ferritchromit and chrome magnetite rims in chromites, e.g. (a) such rims may result from a subsolidus elemental exchange with silicate minerals during prograde metamorphism (Evans and Frost 1975; Wylie et al. 1987; Burkhard 1993; Barnes 2000; González Jiménez et al. 2009; Merlini et al. 2009; Locmelis et al. 2011; Staddon et al. 2021), (b) in ophiolitic chromitites these features may reflect retrograde metamorphism during cooling from the eclogite facies (Proenza et al. 2008; Gervilla et al. 2012; Colás et al. 2014, 2017; Hernández-González et al. 2020; Lenaz et al. 2021). The trace element data obtained from LA-ICPMS studies of chromites have been particularly useful in developing a more precise understanding of how these zoned rims formed (e.g. Pagé and Barnes 2009; Mukherjee et al. 2015; Colás et al. 2017; Yu et al. 2019). Such *in situ* techniques have also been used to study trace and platinum-group element (PGE) partitioning between chromites and co-existing high-Mg silicate melt from a variety of geological settings (Locmelis et al. 2011; Pagé et al. 2012; Kamenetsky et al. 2015; Pagé and Barnes 2016; Arguin et al. 2016; Park et al. 2012, 2017; Barnes et al. 2021).

Two types of major ore deposits are associated with the komatiitic suite of rocks. Among these, the most common type is the primary magmatic sulfide deposits which are economically important for their high Ni concentration (~10% of the world's total Ni production) alongside minor Cu and PGEs (e.g. Alexo deposit, Canada; Kambalda deposit, Western Australia; Vaara deposit, Finland; Barnes et al.

1993; Elias 2006; Arndt 2008; Fiorentini et al. 2010; Konnunaho et al. 2013, 2016). The second type is the laterite-hosted deposit present at the top of the dunite-peridotitic rocks and is economically important for its high Ni and Co content (e.g. Yilgarn Craton, Western Australia; Elias 2006; Arndt 2008). Barnes (2006) classified the style of komatiite-hosted magmatic Ni-Cu-(PGE) sulfide mineralization into five types. Type-I sulfide deposits are high-grade massive or net textured ore found at the komatiitic flow's basal contact (e.g. Alexo deposit, Canada; Kambalda and Black Swan deposits, Western Australia). Type-II variety is low-grade disseminated sulfide ores compared to the type-I variety and is found in interstitial spaces of the thick dunite bodies at the lower part of the komatiitic litho-unit (e.g. Mt. Keith deposit, Western Australia). Type-III deposits are stratiform PGE-rich layers in fractionated flows. Type-IV and V varieties are disseminated sulfide ores and are also mobilized by metamorphism and alteration (e.g. Proterozoic deposits of the Thompson belt, Canada; Lesher and Barnes 2009). The composition of sulfide ores in terms of the metal content (e.g. Ni-Cu-Co-PGEs) is dependent on the composition of the ultramafic-mafic magmas from which they were crystallized (Lesher and Keays 2002; Arndt 2008). Komatiitic magmas were formed by high degrees of partial melting of the mantle peridotite at different depths and consumed high modal% of olivine as well as sulfide and platinum-group minerals (e.g. Arndt 2008; Waterton et al. 2021). After reaching sulfide supersaturation, the komatiitic magma segregates immiscible sulfide liquid with a high concentration of platinum-group elements (e.g. Lesher and Keays 2002; Arndt 2008; Fiorentini et al. 2010; Gole and Barnes 2020). Type-I sulfides have crystallized early in the crystallization sequence before olivine and they have a higher concentration of Ni, Co, Os, Ir, and Ru than the type-II varieties which are

mostly present in the dunite-peridotite rock unit (Lesher and Keays 2002; Arndt 2008; Barnes and Fiorentini 2012). On the contrary, the concentration of Cu, Au, Pt, and Pd are high in the late crystallizing disseminated sulfides (mostly type-IV and V) compared to the type-I and type-II varieties (Barnes et al. 1985; Lesher and Keays 2002; Arndt 2008).

Together with major and trace elements, the platinum-group elements (PGEs) geochemistry of the komatiites can be used as a tracer of the Earth's mantle through time (e.g. Puchtel and Humayun 2000; Maier et al. 2009; Puchtel et al. 2009, 2020; Fiorentini et al. 2011; Mukherjee et al. 2012; Waterton et al. 2021). The PGE geochemistry of komatiites also helps to understand the sulfide saturation history of the magmas and the chemical character of mantle source (e.g. Lesher et al. 2001; Fiorentini et al. 2010; Konnunaho et al. 2016). The increasing PGE concentration from early to late Archean komatiites is explained by Maier et al. (2009) based on the mixing of late accreted materials into the mantle sources and the gradual increase in PGEs in komatiites. Researchers suggested alternative theories such as (i) formation of PGE-enriched and PGE-depleted silicate mantle domains by fractionation of the primitive magma-ocean (e.g. Puchtel et al. 2009, 2014), (ii) mixing of PGE-depleted mantles and PGE-enriched late accreted planetesimals at different domains of the Earth's Primitive Mantle (e.g. Puchtel et al. 2018, 2020), and (iii) exchange of PGEs across the outer core-lower mantle boundary (e.g. Brandon et al. 1998; Humayun 2011; Puchtel et al. 2020). Waterton et al. (2021) proposed that the komatiitic melts originated from a significantly PGE-depleted mantle source compared to the Primitive Upper Mantle composition (PUM; Becker et al. 2006). This model suggests that the komatiite PGE concentrations strictly depend on the

interplay of various factors like temperature, pressure, mantle fO_2 condition during partial melting, the difference in sulfur content of the mantle source and their prior depletion, and the concentration of PGEs in the source mantle itself (Waterton et al. 2021).

In India, significant occurrences of the komatiitic suite of rocks are found in three Archean greenstone belts of the Singhbhum Craton, eastern India. These Archean greenstone belts are known as the Noamundi-Jamda-Koira in the western part, Tomka-Daitari in the southern part, and Gorumahishani-Badampahar in the eastern part. Previous research on the Singhbhum komatiitic suite of rocks mainly focused on the whole-rock major and trace element geochemistry and geochronological studies of rocks from limited field exposures without much mineralogical and petrological information (e.g. Yadav et al. 2015; Chaudhuri et al. 2015, 2017; Ghosh et al. 2019; Bacchar et al. 2021; Jodder et al. 2021; Adhikari et al. 2021a). Based on the limited number of samples the previous studies discussed the genesis of the Singhbhum komatiites and reported the early Archean ages for the volcanic suites. The age of the komatiites from the northern Gorumahishani greenstone belt is so far very poorly constrained. In addition, most of the previous geochronological and geochemical studies on the Singhbhum komatiites lack detailed mineralogical and petrological background. In addition, there is no previous PGE geochemical study of the Singhbhum komatiitic suite of rocks. Detailed mineral-chemical studies based on major, trace, and platinum-group elements of the accessory chromites and disseminated sulfides in the Singhbhum komatiitic rocks are also lacking.

In this research for my PhD thesis, I have conducted a systematic mineralogical-petrological and geochemical study of the komatiitic suite of rocks from the Gorumahishani greenstone belt. A total 68 numbers of samples in 3 sections from the ~120 km long greenstone belt were collected in three field seasons. *In situ,* major, minor, trace, and platinum-group element concentrations of the komatiitic chromites were determined. In combination with petrographic information, these data have been used to classify the chromites in different compositional types. The chromites with textural and compositional zoning are quite common in these komatiitic rocks. The characteristic trace and PGE concentration patterns in the compositionally modified chromites, and the differences between chromite cores and rims, are explained in terms of magmatic versus subsolidus processes. This study is the first to discuss post-magmatic modification of PGE distribution in komatiitic chromites and to correlate the patterns with the degree of metamorphism of the rocks. Furthermore, I have calculated trace element (Sc, Ti, V, Mn, Zn, Co, Ni, Ga) and PGE (Os, Ir, Ru, Rh) chromite-komatiite melt apparent partition coefficients using mass balance models based on the data of less altered chromite cores. These data are compared with other experimental and natural partitioning values worldwide to better discriminate between magmatic and subsolidus processes. The primary goal of this particular study is to look at the PGEs and other trace elements hosted by the chromite itself but not at platinum-group mineral microinclusions. The petrographic study and *in situ,* major element chemistry of primary and secondary sulfide minerals are used to understand the origin of Ni-Cu-sulfide minerals that are present in the Gorumahishani komatiitic suite of rocks.

The whole-rock major, trace, and platinum-group element geochemical study of the Gorumahishani komatiitic suite of rocks are also conducted to understand the mantle source character, magma differentiation processes that involve crustal-contamination, fractional crystallization, and sulfide saturation history of the magma. Based on the whole-rock major and trace element data I have modeled the processes of mantle melting to generate the komatiitic melts parental to the Singhbhum komatiitic rocks. Whole-rock Sm-Nd isotopic study of the representative samples from the komatiitic suite of rocks has been conducted to obtain the crystallization age of the komatiites. This age is correlated with the tonalite-trondhjemite-granodioritic-granite suite of rocks (TTG) in the Singhbhum Craton and with other Archean komatiites around the world. Based on this research, a geodynamic model is proposed for the evolution of the early Archean to Mesoarchean Singhbhum Craton within the Indian Shield.

Chapter 2

Geological background

2. Geological background

2.1. Regional Geology

The Indian shield is composed of five cratonic blocks: (i) Dharwar Craton at the southern part, (ii) Baster Craton at the south-eastern part, (iii) Bundelkhand and (iv) Aravalli Cratons at the northern part, and (v) Sighbhum Craton at the eastern part (**Fig. 1a**). Among these, the Singhbhum Craton occupies an area of 50,000 km^2 in Orissa, Bihar, and Jharkhand states in eastern India (Saha 1994; Mukhopadhyay 2001; Mukhopadhyay and Matin 2020). The Singhbhum Craton bears a continuous record of Earth's evolutionary history from the Early Archean to Late Archean with traces of the Hadean crust (e.g. Chaudhuri et al. 2018). In the northern part, the Singhbhum Craton is bounded by the Singhbhum Mobile Belt primarily composed of the Singhbhum Group of rocks, the 200 km long Singhbhum Shear Zone (SSZ), and the east-west trending Dalma volcano-sedimentary belt (**Fig. 1a**). To the south, the Singhbhum Craton is bounded by the Eastern Ghat Mobile Belt with a tectonic contact marked by the Sukinda Shear Zone. The northwest-southwest part of the Singhbhum Craton is occupied by the high-grade metamorphic Satpura belt and the Bastar Craton. The alluvium of the Bengal basin occupies the eastern part of the Craton.

The Early Archean records of the Singhbhum Craton are represented by the four major geological units: (a) the Older Metamorphic Tonalite Gneiss (OMTG), (b) the Older Metamorphic Group (OMG), (c) the Iron Ore Group (IOG), and (d) the older phases of the Singhbhum Granite Batholithic Complex (SGBC - phase I and phase II; Dey et al. 2019; **Fig. 1a, b**). The supracrustal rocks of the Iron Ore Group are distributed in three greenstone belts: (i) Noamundi-Jamda-Koira, Tomka-Daitari, and

Gorumahisani-Badampahar (e.g. Mondal 2009; **Fig. 1a, b**). From the Mesoarchean to Early Paleoproterozoic, the craton was stabilized through several pulses of high-K felsic intrusions namely Mayurbhanj-Nilgiri-Bonai granitic intrusions and the younger phase of the SGBC (phase III) and plutonic ultramafic-mafic complexes of the Sukinda-Nuasahi-Mayurbhanj Complexes (Augé et al. 2003; Chakraborti et al. 2019; Mondal et al. 2019, 2021), and volcano-sedimentary rocks of the Dhanjori-Simlipal-Malangtoli-Jagannathpur-Ongarbira-Dalma belts (Mazumder and Sarkar 2004; Misra 2006; Acharyya et al. 2010b**;** Adhikari et al. 2021b; **Fig. 1a, b**). The Craton was intruded by a series of mafic dykes swarms from the late Archean to Proterozoic (Kumar et al. 2017; Srivastava et al. 2019; Dey and Mondal 2022) along with widespread deposition of sediments (e.g. Olierook et al. 2019). The detailed petrological background of each stratigraphic unit from the Singhbhum Craton and their geochronological information is discussed in **Table 1**.

Bhattacharjee et al. (2021) reported detrital zircons of 4.02 - 4.03 Ga from the sandstone unit of the Simlipal Complex (**Fig. 1a**). Sreenivas et al. (2019) reported early Archean (3.6 - 3.4 Ga) detrital zircons from the Mahagiri quartzite unit unconformably overlain the Singhbhum granite around the Tomka-Daitari greenstone belt (**Fig. 1a**). Chaudhuri et al. (2018) reported Hadean xenocrystic and detrital zircons (4.24 - 4.03 Ga) from the gneissic rocks of the OMTG. Olierook et al. (2019) reported a ~3.6 Ga age of detrital zircons from the metasedimentary rocks of the Proterozoic Chandil Formation located within the North Singhbhum Mobile Belt (**Fig. 1a**). Miller et al. (2018) reported detrital zircon of ~3.6 Ga from the modern river sediments of the Baitarani River at 50 km ESE of Keonjhar, Odisha.

Geochronological information suggests similar ages of 3.6 Ga - 3.3 Ga for the rocks of the Older Metamorphic Group, Older Metamorphic Tonalite Gneiss, and the Iron Ore Group (Sharma et al. 1994; Olierook et al. 2019; Adhikari et al. 2021a). The rocks of the Older Metamorphic Group are present as enclaves within the Singhbhum granite batholithic complex (**Fig. 1a, b**). The rocks of the Older Metamorphic Group were metamorphosed under amphibolite facies and represented by biotite-muscovite-sillimanite-garnet schist, quartz-magnetite schist, calc-silicate rocks and amphibolites (Saha 1994). Goswami et al. (1995) reported the 3.6 Ga depositional age of the Older Metamorphic Group sediments by the $^{207}Pb/^{206}Pb$ method from a single zircon grain in quartzite. $^{207}Pb/^{206}Pb$ ion probe spot age from zircon grains of the Older Metamorphic Group meta-sediments indicate age clusters at ca. 3.6, 3.4, and 3.2 Ga (Mishra et al. 1999). The 3.4 Ga and 3.2 Ga age clusters represent metamorphic modification events as suggested by a Pb-loss event at ca. 3.4 Ga that resulted in nonlinearity in the U-Pb concordia diagram (Mishra et al. 1999). Sharma et al. (1994) obtained a whole rock Sm-Nd isochron age of 3.3 Ga from amphibolites of the Older Metamorphic Group which is thought to be their crystallization age.

Older Metamorphic Tonalite Gneissic rocks are greenschist to amphibolite facies metamorphosed biotite-hornblende tonalite, trondhjemite, and granodiorite gneisses (Saha 1994; Nelson et al. 2014). Basu et al. (1981) obtained a bulk-rock Sm-Nd age of ~3.9 Ga for the granitic and tonalitic gneisses of the OMTG. Moorbath et al. (1986) obtained a Pb-Pb isochron age of ~3.4 Ga for the same suite of rocks. Ghosh et al. (1996) reported Pb-Pb isochron ages of ~3.7 Ga and ~ 3.4 Ga for the OMTG rocks. The Rb-Sr age of ~3.12 Ga for the OMTG by Sarkar et al. (1979) is consistent

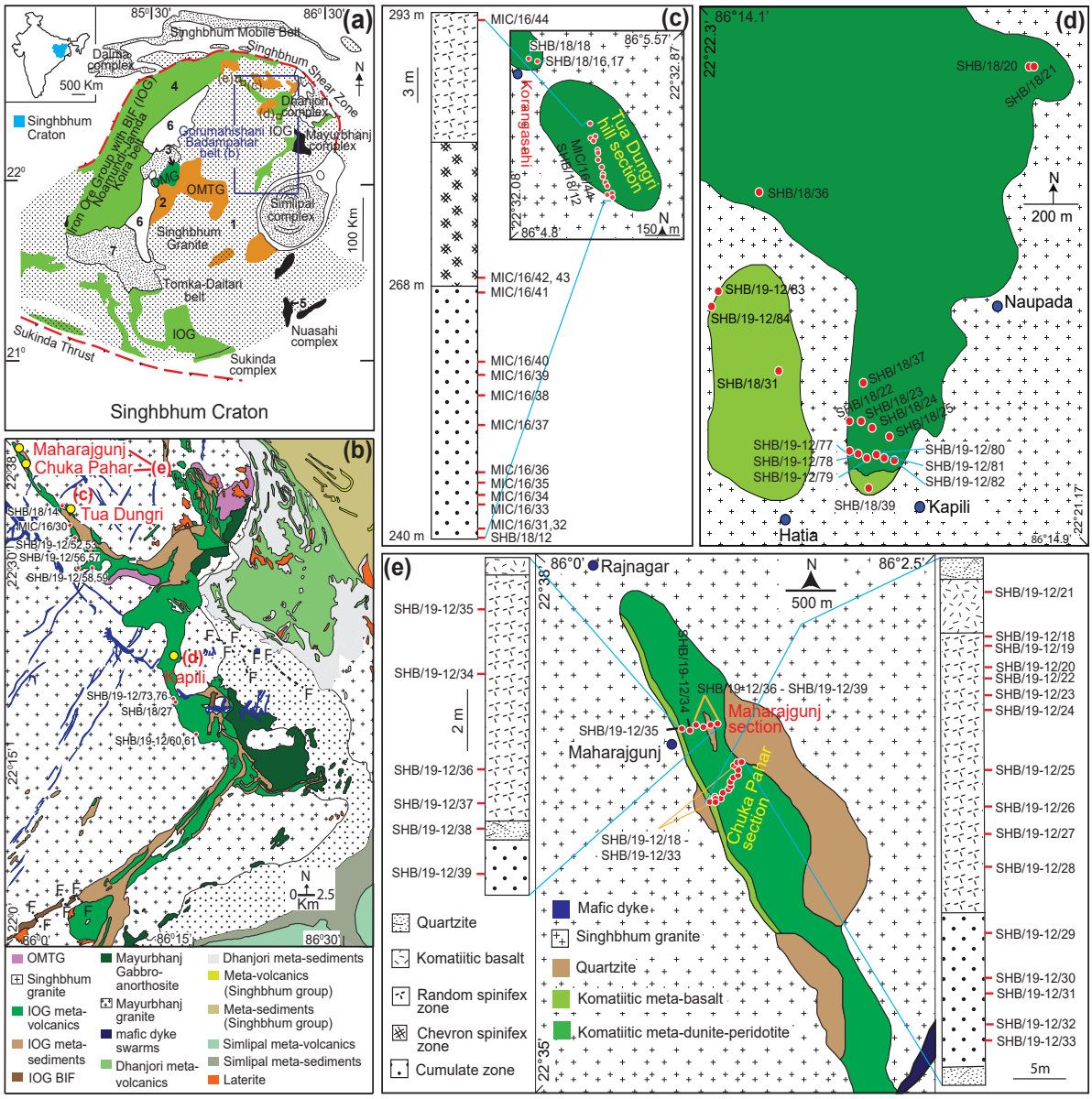

Fig. 1 a Generalized geology of the Singhbhum Craton, India (after Saha 1994; Mondal et al. 2006) with the locations of komatiitic meta-basalt samples. The Inset map of India shows the location of the Singhbhum Craton. 1- Singhbhum Granite Batholithic Complex, 2- OMTG Tonalite-Granodiorite, 3- OMG Supracrustals, 4- Iron Ore Group greenstone sequences with BIF, 5- Ultramafic-mafic rocks with chromite-PGE deposits, 6- Late Archean-Proterozoic sedimentary sequence, 7- Late Archean volcanic sequence. **b** Geological map of the Gorumahishani-Badampahar greenstone belt (modified from www.gsi.gov.in) showing the locations of Maharajgunj-Chuka Pahar (Section A), Tua Dungri (Section B), and Kapili (Section C) komatiite hillocks. **c** Lithological column of Tua Dungri komatiite hill. The map in the right top corner shows the sample locations. **d** Geology of the Kapili area showing the sample locations. **e** Lithological column of the komatiitic suite of rocks from Maharajgunj and Chuka Pahar sections. The map in the middle shows the sample locations.

with ^{40}Ar-^{39}Ar ages of ~ 3.2 Ga from biotite by Baksi et al. (1987). Acharyya et al. (2010a) dated primary magmatic zircons from the Older Metamorphic Tonalite Gneiss by LA-ICP-MS $^{207}Pb/^{206}Pb$ and the U-Pb methods that yielded ages of ~3.45 Ga and ~3.53 Ga. Upadhyay et al. (2014) reported ~3.45-3.44 Ga ages for the tonalites and trondhjemites and ~3.35 - 3.32 Ga ages for the granites from the OMTG by $^{207}Pb/^{206}Pb$ analysis of magmatic zircons.

The rocks of the Singhbhum granite batholithic complex (SGBC) occupy one-third of the craton (**Fig. 1a, b**). Saha (1972, 1994) proposed three major phases of the emplacement of these granitic suites of rocks (phases I, II, and III). The phase I and phase II suite of rocks are known as the Singhbhum granite type A (SBG-A) and the phase-III rocks are known as the Singhbhum granite type B (SBG-B) (Saha 1994). The phase I rocks are granodiorites-trondhjemites, and the phase II and phase III rocks are granodiorites grading to adamellitic granites. Detailed geochronological data contradicts the emplacement of three phases of the granitic suite of rocks as there are overlapping ages for different phases (Mishra et al. 1999; Tait et al. 2011; Upadhyay et al. 2014; Dey et al. 2017; Chakraborti et al. 2019). Upadhyay et al. (2014) determined the crystallization age of ~3.35 Ga from magmatic zircons in the phase I granites by the LA-ICP-MS U-Pb method. Chaudhuri et al. (2018) reported ~3.4 - 3.27 concordant age of the phase-I granites by SHRIMP analysis of magmatic zircons. The phase-II granites show a Pb-Pb whole rock isochron age of ~3.44 - 3.3 Ga (Moorbath and Taylor 1988; Ghosh et al. 1996). The crystallization ages of phase II granites and trondhjemites from magmatic zircons revealed a range between 3.4 and 3.31 Ga (Misra 1999; Upadhyay et al. 2014; Dey et al. 2017; Pandey et al. 2019). The phase III granites have a whole-rock Pb-Pb isochron age of 3.1 Ga (Ghosh et al. 1996).

Magmatic zircons in granite and trondhjemite of phase III granitic rocks revealed ages of ~3.45 - 3.31 Ga (Upadhyay et al. 2014; Dey et al. 2017; Pandey et al. 2019).

Major metamorphic events of the OMTG and the Singhbhum granitic suite of rocks are synchronous with the later magmatic pulses. For example, the ~3.16 - 3.11 Ga metamorphic resetting of the OMTG is linked to younger felsic plutonic emplacements of the Mayurbhanj-Nilgiri-Bonai granitic complexes (~3.1 Ga; Mishra et al. 1999). The Mayurbhanj granitic suite of rocks are present at the south-eastern margin of the Singhbhum Craton and consist of granophyric biotite-hornblende-alkali feldspar granite and ferrohastingsite-biotite granite (**Fig. 1a, b;** Saha 1994; Nelson 2014). Based on the geochemical study researchers (e.g. Mishra 1999; Misra et al. 2002) considered the Mayurbhanj granite as an A-type anorogenic granite. Bonai granites occur in the southwestern part of the Singhbhum Craton (**Fig. 1a**). The Noamundi-Jamda-Koira greenstone belt separates the Bonai granitic complex from the Singhbhum granites (**Fig. 1a**). These are mainly porphyritic to equigranular trondhjemite-granodiorite, with minor granite having an emplacement age of ~3.1 Ga (magmatic zircon ages; Sengupta et al. 1991, 1993; Chakraborti et al. 2019). The Nilgiri granitic complex occupies the southeastern part of the Singhbhum Craton and is surrounded by the older phases of the Singhbhum granites and ultramafic-mafic intrusive rocks. The rock type varies from tonalite-trondhjemite-granodiorite to granite which are geochemically similar to the Mayurbhanj and the Bonai granites (Sengupta et al. 1991, 1993).

The Iron Ore Group (IOG) consists of supracrustal volcano-sedimentary successions which are metamorphosed under greenschist to amphibolite facies (Chaudhuri et al. 2017). The supracrustal rocks occur in three principal greenstone

belts namely, Noamundi-Jamda-Koira at the western part, Gorumahishani-Badampahar at the eastern part, and Tomka-Daitari at the southern part (**Fig. 1a, b**). The lower part of the greenstone sequence is a komatiitic suite of rocks ranging from meta-dunite (cumulates), and meta-peridotite (spinifex textured) to meta-basalt. The metavolcanic rocks are intercalated with meta-sediments of quartzite, chert, felsic tuffs, carbonate-rich schists, conglomerate, and banded iron formation. The upper part of the greenstone sequence is occupied by acid to intermediate volcanic rocks, cherts, and banded iron formation (Sahu and Mukherjee 2001; Mukhopadhyay et al. 2008). In places, supracrustal rocks of the greenstone belts are underlain by the quartz-conglomerate horizon (e.g. Ghosh et al. 2019). The banded iron formations are mineralogically different from the Noamundi-Jamda-Koira and the Gorumahishani-Badampahar greenstone belts showing more magnetite-rich character in the later (Acharya 1984; Chakraborty and Majumder 1986). Detrital zircon grains from the base of the dacitic lava in the Tomka-Daitari greenstone belt revealed an age of ~3.5 Ga (Mukhopadhyay et al. 2008). Adhikari et al. (2021a) obtained Sm-Nd isochron age of ~3.6 Ga from komatiite, komatiitic basalt, and tholeiitic basalt of the Tomka-Daitari greenstone belt and ~3.5 Ga for the dacite of the same volcanic sequence. Basu et al. (2008) reported an ion-probe U-Pb zircon (detrital) age of ~3.4 Ga from tuffaceous rocks below the banded iron formation of the Noamundi-Jamda-Koira greenstone belt. Jodder et al. (2021) obtained ~3.5 Ga U-Pb LA-ICP-MS age for magmatic zircons from the upper felsic volcaniclastic rocks of the Gorumahishani greenstone belt. Bachhar et al. (2021) reported a $^{207}Pb/^{206}Pb$ zircon age of ~3.3 Ga from the komatiites of the spinifex-texture zone at the Badampahar belt, however, this age does not represent the crystallization age of the

komatiitic suite of rocks as these zircons are possibly xenocryst grains. Adhikari et al. (2021a) reported a Sm-Nd isochron age of ~3.3 Ga from the north-eastern part of the Gorumahishani greenstone belt based on bulk-rock komatiite, komatiitic basalt, tholeiitic basalt, and basaltic andesite suite of rocks.

The ultramafic-mafic plutonic bodies of the Nuasahi-Sukinda complexes and the Mayurbhanj mafic complex are closely associated with the supracrustal rocks of the IOG greenstone belts and are located along the southern and eastern margin of the Singhbhum Craton (Mondal et al. 2006, 2019; Khatun et al. 2014; Bhattacharjee and Mondal 2021). The sill-like layered ultramafic-mafic bodies of the Nuasahi and Sukinda areas have chromitite-bearing dunite and orthopyroxenite in the lower ultramafic unit and magnetitite-bearing gabbroic rocks in the upper mafic unit (Mondal and Zhou, 2010; Prichard et al. 2018). A tectonic breccia zone is present in the Nuasahi complex that marks the upper contact of the ultramafic unit with the gabbro unit (Mondal et al. 2001). Augé et al. (2003) reported a U-Pb detrital zircon age of ~3.1 Ga from the gabbroic matrix of the breccia zone. Augé et al. (2003) also reported a bulk-rock Sm-Nd age of ~3.2 Ga from the eight samples of the Nuasahi gabbro. Besides this, Mondal et al. (2006) have suggested that the Sukinda massifs are contemporaneous with the Nuasahi massifs and possibly formed between ~3.3 - 3.1 Ga. The Mayurbhanj mafic complex is located in the southeastern part of the Gorumahishani greenstone belt (**Fig. 1a, b**) and is mainly composed of gabbro-noritic and anorthositic rocks with magnetitite ore bodies (e.g. Bhattacharjee and Mondal 2021). The gabbro-noritic rocks are present at the lower part of the mafic complex which is followed by gabbro-anorthosite rocks at the upper part. Mondal et al. (2021)

reported an Sm-Nd whole-rock age of ~3.02 Ga for the upper gabbro-anorthositic rocks of the plutonic complex.

Ultramafic-mafic volcanic and sedimentary rocks of the late Archean to early Proterozoic greenstone belts encircle the older rocks of the Singhbhum Craton and are represented by the Simlipal, Dalma, Dhanjori, Jagannathpur, and Malangtoli belts (Mondal 2009; Acharyya et al. 2010b; Misra and Johnson 2005; Mondal et al. 2019). The younger greenstone belts overly the early Archean tonalite-trondhjemite-granodiorite and granitic rocks (Saha 1994). The Jagannathpur (or Dungoaposi)-Malangtoli-Ongarbira belt is present at the western part of the Singhbhum Craton around the early Archean Noamundi-Jamda-Koira greenstone belt (**Fig. 1a**). The volcanic rocks within the younger greenstone belts are intercalated with quartzite and phyllite with the occasional presence of a conglomerate bed at the base (Singh et al. 2016; Singh et al. 2017). The Jagannathpur-Malangtoli belt has picritic rock at the lower part that grades into tholeiitic basalt, basaltic andesite, and andesite towards the top (Saha 1994; Blackburn and Srivastava 1994; Bose 2009; Singh et al. 2016; Singh et al. 2017; Adhikari et al. 2021b). Pillow basalts and amygdular basalt with highly deformed character are also reported from the top part of the Jagannathpur-Malangtoli belt (Saha 1994, Adhikari et al. 2021b). Adhikari et al. (2021b) reported a whole-rock Sm-Nd isochron age of ~2.8 Ga for the Jagannathpur basaltic rocks and ~2.7 Ga for felsic amygdules present within the basaltic rocks. Adhikari et al. (2022) also reported a whole-rock Sm-Nd isochron age of ~3.1 Ga for the basaltic rocks from the Ongarbira area. Kolhan sediments represent the top part of the Jagannathpur-Malangtoli-Ongarbira belt and are present from Chaibasa in the north to Noamundi in the south (**Fig. 1a**). The three main formations of the Kolhan

group are the basal sandstone unit followed by a limestone unit and the shale unit at the top with thin manganese oxide layers interbedded with shale (Saha 1994; Mukhopadhyay and Matin 2020). There is no reliable radiometric age dating from the Kolhan sediments, however, based on a lithostratigraphic study Mukhopadhyay et al. (2006) suggested a terminal Mesoproterozoic age.

The Dhanjori belt is situated at the northeastern boundary of the Singhbhum Craton and is abutted against the Mesoproterozoic North Singhbhum Mobile Belt (**Fig. 1a, b**). The upper part of the Dhanjori belt is composed of volcanics and volcaniclastic rocks with intercalated quartzites and phyllites and the lower part consists of pebbly phyllite and conglomerate along with an ultramafic-mafic suite of rocks (Gupta 1985; Mazumder and Sarkar 2004; Mazumder and Arima 2009; De et al. 2015). The basal quartz-pebble conglomerate unit of the Dhanjori belt has gold and uranium mineralization and is known as Phuljhari Formation (Acharyya et al. 2010b). The Dhanjori belt is overlain by mica-schist-quartzite rocks of the Chaibasa Formation (Bose et al. 1997; Mazumder and Sarkar 2004; Mazumder 2005). Two sets of Sm-Nd isochron ages of ~2.07 Ga (Roy and Bhattacharya 2012) and 2.79 Ga (Misra and Johnson 2005) are reported from the mafic volcanic rocks of the Dhanjori belt. Mishra and Johnson (2005) obtained a five-point isochron age of ~2.8 Ga from the whole-rock Pb-Pb isotope analysis of the mafic volcanics from the Dhanjori belt. Sunilkumar et al. (1996) obtained ~3.1 Ga U-Th-Pb age of detrital zircons from the basal conglomerate unit of the Dhanjori belt. Detrital zircon from the same basal conglomerate unit of the Dhanjori belt provided an upper intercept age of ~ 3.33 Ga (Acharyya et al. 2010b).

The Simlipal volcano-sedimentary belt is located in the southeastern part of the Singhbhum Craton and overlies the Singhbhum and Mayurbhanj granites (**Fig. 1a**; Saha 1994; Mukhopadhyay and Matin 2020). The volcano-sedimentary succession begins with a quartz pebble conglomerate unit which unconformably overlain by intercalated mafic volcanics, quartz-rich sandstone, and tuffs (Saha 1994; Bhattacharjee et al. 2021). An 800 m thick differentiated sill, known as the Amjori sill, occupies the central part of the Simlipal belt (Iyenger et al. 1981; Roy and Bhattacharya 2012). The basal part of the sill consists of dunite which grades into peridotite, gabbro, and quartz diorite towards the top (Saha 1994). Bhattacharjee et al. (2021) reported a U-Pb age of ~3.08 Ga for detrital zircons from the sandstone unit and considered this as the maximum depositional age for the sedimentary rocks from the Simlipal belt. Bhattacharjee et al. (2021) also mentioned that the provenance of the detrital zircons of ~3.1 Ga was the Mayurbhanj granite unconformably underlying the Simlipal sandstone.

The Dalma volcano-sedimentary greenstone belt is located in the northern part of the Singhbhum Craton and occupies the central zone of the Singhbhum Mobile Belt (Fig. 1a; Saha 1994; Chatterjee et al. 2018). The Dalma belt is flanked by the meta-sedimentary rocks of the Dhalbhum Formation and Chaibasa Formation in the northern and southern parts (collectively known as the Singhbhum Group of rocks; Saha 1994; Alvi et al. 2019). The volcanic rocks are more ultramafic in the lower part and tholeiitic in the upper part and are separated by a horizon of pyroclastic rocks (Saha 1994). Alvi et al. (2019) reported ultramafic-mafic plutonic enclaves within the Dalma belt which are meta-gabbro to meta-dolerite, meta-peridotite, fragments of mafic metavolcanic rocks, and non-fragmental mafic

metavolcanic rocks. Singh et al. (2001) reported acid agglomeratic rocks that are present along the northern flank of the Dalma belt. Mishra and Johnson (2005) obtained an eight-point Rb-Sr isochron age of ~2.4 Ga for the whole-rock Dalma volcanics. Bhattacharya et al. (2015) obtained a SHRIMP U-Pb zircon igneous crystallization age of ~1.6 Ga from a felsic volcanic rock unit at the base of the Dalma volcanic sequence.

Younger siliciclastic rocks (mainly quartzite) are exposed along the western and southern boundaries of the Singhbhum granite pluton and separate the Singhbhum granite from the Noamundi-Jamda-Koira, Tomka-Daitari, and Jagannathpur-Malangtoli-Ongarbira greenstone belts (**Fig. 1a**; Ghosh et al. 2015; Mukhopadhyay and Matin 2020). The Keonjhar quartzite (Ghosh et al. 2016) is a thick rock unit that is exposed between Joda and Keonjhargarh area and separates the Noamundi-Jamda-Koira and Jagannathpur-Malangtoli-Ongarbira greenstone belts from the Singhbhum granite. Similar quartzites are present in the west of Keonjhargarh up to Sukinda and are known as Mahagiri quartzite (Mukhopadhyay et al. 2012, 2014). Mahagiri quartzite separates the Tomka-Daitari greenstone belt from the Singhbhum granite (**Fig. 1a**). Quartzites are also present along the southern boundary of the Singhbhum Craton which separates the Pallahara gneiss from the Singhbhum granite and is known as the Tikra quartzite (Mahalik 1994). Recent studies on the quartzites have indicated that these siliciclastic rocks are broadly time-equivalents with the younger greenstone belts from the Singhbhum Craton (e.g. Mukhopadhyay et al. 2007; Bandyopadhyay et al. 2010; Mazumder et al. 2012).

Numerous dykes transgress the granite-greenstone terrains in the Singhbhum Craton (**Fig. 1b**). The dykes are noritic to doleritic in composition (Shankar et al. 2014;

Kumar et al. 2017; Srivastava et al. 2019; Dey and Mondal, 2021). Based on trends, seven major dyke swarms are reported (e.g. Srivastava et al. 2019): (i) Keshargaria swarm of NE-SW trend, (ii) Ghatgaon swarm of NNE-SSW to NE-SW trend, (iii) Kaptipada swarm of NE-SW to ENE-WSW trend, (iv) Pipilia swarm of WNW-ESE trend, (v) Keonjhar swarm of E-W to ENE-WSW trend, (vi) Bhagamunda swarm of NW-SE to NNW-SSE trend, and (vii) Barigaon swarm of N-S to NNE-SSW trend. Four dyke swarms are dated by the U-Pb baddeleyite (ZrO_2) method and are petrologically well-studied. The ~2.8 Ga NNE-SSW to NE-SW trending Keshargaria dyke swarm (Kumar et al. 2017) is noritic to doleritic in composition. The ~2.75 - 2.76 Ga NE-SW trending Ghatgaon dyke swarm (Kumar et al. 2017) shows a similar mineralogical character to the Keshargaria dyke swarm except for a lower degree of hydrothermal alteration. The ~2.26 Ga NE-SW trending Kaptipada dyke swarm is doleritic in composition (Srivastava et al. 2019). The ~1.77 Ga WNW-ESE trending Pipilia dyke swarm is basaltic in composition (Shankar et al. 2014; Dey and Mondal 2021). Dey and Mondal (2021) described the occurrence and discussed the origin of the sulfide and oxide minerals from this dyke swarm. The Dyke Swarms were feeders of the overlying extrusive sequences from the Archean to Proterozoic (Srivastava et al. 2019; Mazumder and Chaudhuri 2019; Adhikari et al. 2021b). A whole-rock Sm-Nd isochron age of ~2.8 Ga is reported for the Jagannathpur basaltic rocks and their petrogenetic relation is established with the ~2.8 Ga NE-SW to NNE-SSW trending Keshargaria dyke swarm and the ~2.75 - 2.76 Ga NNE-SSW trending Ghatgaon dyke swarm (Adhikari et al. 2021b). The felsic volcanic rocks of ~1.6 Ga in the Dalma belt (SHRIMP U-Pb; Bhattacharya et al. 2015) are correlated with the ~1.77 Ga WNW-ESE trending Pipilia dyke swarm (Mazumder and Chaudhuri 2019; Srivastava et al. 2019).

Table 1 Chrono-stratigraphy of the Singhbhum Craton

Stratigraphy	Lithological units	Age	Reference	Remarks
Kolhan group (KG)	Kolhan sediments	1531 Ma	Saha, 1994	Whole rock Rb-Sr age from Kolhan shale
Newer dolerite dyke swarms	Pipilia dyke swarm (WNW-ESE)	1765 ± 0.9 Ma	Shankar et al. 2014	TIMS $^{207}Pb/^{206}Pb$ baddeleyite weighted mean age
	Kaptipada dyke swarm (NE-SW)	2256 ± 6 Ma	Srivastava et al. 2019	TIMS U-Pb upper intercept age from baddeleyite
	Ghatgaon dyke swarm (NE-SW)	2752 ± 0.9 Ma	Kumar et al. 2017	TIMS $^{207}Pb/^{206}Pb$ baddeleyite weighted mean age
	Keshargaria dyke swarm (NNE-SSW to NE-SW)	2800 ± 0.7 Ma	Kumar et al. 2017	TIMS $^{207}Pb/^{206}Pb$ baddeleyite weighted mean age
		2613 ± 177 Ma	Roy et al. 2004	Whole rock Rb-Sr isochron age
Late Archean-Proterozoic volcano-sedimentary sequences	Dalma volcano-sedimentary sequences	2396 ± 110 Ma	Misra and Johnson, 2005	Whole rock Pb-Pb isochron age
	Dhanjori volcano-sedimentary sequences	2787 ± 270 Ma	Misra and Johnson, 2005	Whole rock Sm-Nd isochron age
		2794 ± 210 Ma	Misra and Johnson, 2005	Whole rock Pb-Pb isochron age
	Jagannathpur-Malangtoli volcano-sedimentary sequences	2799 ± 67 Ma	Adhikari et al. 2021b	Whole rock Sm-Nd isochron age
		2682 ± 28 Ma	Adhikari et al. 2021b	Whole rock Rb-Sr isochron age
		2250 ± 81	Misra and	Whole rock Pb-Pb

		Ma	Johnson, 2005	isochron age
Archean granite-greenstone terrain	Tamperkola granite	2809 ± 12 Ma	Bandyopadhyay et al. 2001	Ion-microprobe $^{207}Pb/^{206}Pb$ zircon crystallization age
	Mayurbhanj granite	3079.4 ± 6.8 Ma	Chakraborti et al. 2019	LA-ICPMS U-Pb zircon crystallization age
		3080 ± 8 Ma	Mishra et al. 1999	Ion-microprobe $^{207}Pb/^{206}Pb$ zircon crystallization age
	Mayurbhanj gabbro-anorthosite complex	3022 ± 180 Ma	Mondal et al. 2021	Whole rock Sm-Nd isochron age
	Nuasahi ultramafic-mafic complex	3123 ± 7 Ma	Augé et al. 2003	SHRIMP U-Pb detrital zircon age
		3205 ± 280 Ma	Augé et al. 2003	Whole rock Sm-Nd isochron age
	Bonai granite	3115 ± 10 Ma	Chakraborti et al. 2019	LA-ICPMS U-Pb zircon crystallization age
	Singhbhum granite type-B (SBG-B) (phase-III)	3308 ± 31 Ma	Dey et al. 2017	LA-ICPMS U-Pb zircon crystallization age
		3351 ± 8 Ma	Pandey et al. 2019	LA-ICPMS U-Pb zircon crystallization age
		3377 ± 11 Ma	Chaudhuri et al. 2018	SHRIMP $^{207}Pb/^{206}Pb$ zircon crystallization age
		3445 ± 4 Ma	Upadhyay et al. 2014	LA-ICPMS U-Pb zircon crystallization age
	Noamundi-	3285 ± 7	Nelson et al.	SHRIMP U-Pb

	Jamda-Koira greenstone belt	Ma	2014	zircon crystallization age from granodiorite
		3392 ± 21 Ma	Basu et al. 2008	Ion-microprobe U-Pb detrital zircon age from tuffaceous rocks
	Gorumahishani-Badampahar greenstone belt	3250 to 3100 Ma	Ghosh et al. 2019	LA-ICPMS U-Pb detrital zircon age from basal clastic rocks
		3313 ± 10 Ma	Adhikari et al. 2021a	Whole rock Sm-Nd isochron age from komatiitic suite of rocks
		3510 ± 3 Ma	Jodder et al. 2021	LA-ICPMS U-Pb zircon crystallization age from upper felsic volcanic unit
		3508 ± 190 Ma	This study	Whole rock Sm-Nd errorchron age from komatiitic suite of rocks
	Tomka-Daitari greenstone belt	3506 ± 2 Ma	Mukhopadhyay et al. 2008	SHRIMP U-Pb zircon crystallization age from granodiorite
		3507 ± 180 Ma	Adhikari et al. 2021a	Sm-Nd isochron age from dacite lava
		3573 ± 63 Ma	Adhikari et al. 2021a	Sm-Nd isochron age from komatiite suite of rocks
	Singhbhum granite type-A (SBG-A) (phase-II)	3311 ± 57 Ma	Dey et al. 2017	LA-ICPMS U-Pb zircon crystallization age

		3326 ± 5 Ma	Nelson et al. 2014	SHRIMP U-Pb zircon crystallization age from monzogranite
		3328 ± 7 Ma	Mishra et al. 1999	Ion-microprobe $^{207}Pb/^{206}Pb$ zircon crystallization age
		3390 ± 9 Ma	Pandey et al. 2019	LA-ICPMS U-Pb zircon crystallization age
		3336 ± 4 Ma	Upadhyay et al. 2014	LA-ICPMS U-Pb zircon crystallization age
	Singhbhum granite type-A (SBG-A) (phase-I)	3442 ± 26 Ma	Ghosh et al. 1996	Whole rock Pb-Pb isochron age
		3350 ± 20 Ma	Upadhyay et al. 2014	LA-ICPMS U-Pb zircon crystallization age
		3397 ± 9 Ma	Chaudhuri et al. 2018	SHRIMP $^{207}Pb/^{206}Pb$ zircon crystallization age
	Older metamorphic tonalite gneiss (OMTG)	3113 ± 85 Ma	Sarkar et al. 1979	Whole rock Rb-Sr isochron age
		3135 ± 85 Ma	Sarkar et al. 1979	Whole rock Rb-Sr isochron age
		3331 ± 9 Ma	Pandey et al. 2019	LA-ICPMS U-Pb zircon crystallization age
		3363 ± 12 Ma	Nelson et al. 2014	SHRIMP U-Pb zircon crystallization age
		3378 ± 98 Ma	Moorbath et al. 1986	Whole rock Pb-Pb isochron age

		3400 Ma	Mishra et al. 1999	Ion-microprobe $^{207}Pb/^{206}Pb$ zircon crystallization age
		3405 ± 53 Ma	Ghosh et al. 1996	Whole rock Pb-Pb isochron age
		3437 ± 23 Ma	Upadhyay et al. 2014	LA-ICPMS U-Pb zircon crystallization age
		3437 ± 23 Ma	Acharyya et al. 2010	LA-ICPMS U-Pb zircon crystallization age
		3471 ± 24 Ma	Dey et al. 2017	LA-ICPMS U-Pb zircon crystallization age
	Older metamorphic group (OMG): sediments and volcanics	3775 ± 24 Ma	Basu et al. 1981	Whole rock Sm-Nd isochron age
		3305 ± 60 Ma	Sharma et al. 1994	whole rock Sm-Nd isochron age from OMG amphibolite
		3317 ± 8 Ma	Upadhyay et al. 2014	LA-ICPMS U-Pb metamorphic age from rutile
		3504 ± 30 Ma	Mishra et al. 1999	Ion-microprobe $^{207}Pb/^{206}Pb$ detrital zircon age from ortho-quartzite
		3551 ± 13 Ma	Goswami et al. 1995	Ion-microprobe $^{207}Pb/^{206}Pb$ detrital zircon age from quartzite and quartz mica-schist
Evidence of unpreserved primitive crust from detrital		3628 ± 38 Ma	Goswami et al. 1995	Ion-microprobe $^{207}Pb/^{206}Pb$ detrital zircon age from OMG metasediments

zircon age		4015 ± 9 Ma	Miller et al. 2018	LA-ICPMS $^{207}Pb/^{206}Pb$ detrital zircon age of a single crystal from modern sediment of Baitarani river
		4017 ± 15 Ma - 4026 ± 24 Ma	Bhattacharjee et al. 2021	LA-ICPMS U-Pb detrital zircon age from the lower sandstone unit of Simlipal volcano-sedimentary sequence
		4031 ± 5 Ma - 4239 ± 4 Ma	Chaudhuri et al. 2018	SHRIMP U-Pb xenocrystic zircon age from OMTG of the Champua area

The Singhbhum Shear Zone (SSZ) is a fold-thrust belt known as the Singhbhum U-Cu belt because of its largest U resources in India, and huge Cu sulfide deposits that are present almost all along the belt (**Fig. 1a**; Banerji 1981; Pal et al. 2009, 2011; Pal and Rhede 2013; Chowdhury et al. 2020). The ~200 km long arcuate-shaped belt is a tectonic contact between the Proterozoic North Singhbhum Mobile Belt to the north and the Achaean Singhbhum Craton to the south. The major rock types of the Singhbhum Shear Zone are sericite schist, chlorite schist, biotite schist, kyanite-sericite schist, meta conglomerate, quartzite, tourmalinite, and granite (Pal et al. 2022). A six-point whole rock Rb-Sr isochron age of ~1.05 Ga (Sengupta et al. 1994) is reported from the granitic rocks. The Singhbhum Shear Zone is the loci of a deep-seated fault between the northern supracrustal province and the southern Archean Craton. The southward thrusting of the North Singhbhum Mobile Belt onto the Archean Singhbhum Craton during the Mesoproterozoic resulted in continuous deformation and metamorphism of the rocks (Banerji 1969, 1981). The shear zone transgressed the rocks of the Gorumahishani greenstone belt at its northern extension, the Dhanjori belt, and the Singhbhum Group of rocks and suffered two different phases of metamorphism (e.g. Banerjee et al. 2023). The prograde metamorphism (M1) culminated in epidote-amphibolite transition facies with peak metamorphic temperature ~480 ± 40°C and pressure ~6.4 ± 0.4 kbar (e.g. Bandyopadhyay 2003, Sengupta et al. 2005), and hydration of the prograde assemblages manifest the retrograde metamorphism (Srivastava and Pradhan 1995).

2.2. Geology of the Gorumahishani-Badampahar greenstone belt

The arcuate-shaped Gorumahishani-Badampahar greenstone belt at the eastern part of the Singhbhum Craton is extended from the Kudada area (South of Singhbhum Shear Zone) to the north up to the Nauna and Budhipat area (west of Badampahar village) to the south-west (**Fig. 1a, b**; Bhattacharya et al. 2007; Banerjee et al. 2023). The Gorumahishani-Badampahar greenstone belt is largely surrounded by the granite-gneissic rocks of the Singhbhum granite batholithic complex and the rocks of the OMTG and OMG. The rocks of the Singhbhum granite phase III show an intrusive relationship with the greenstone belt rocks near the Gorumahisani and Badampahar areas (Sengupta 1990; Nelson et al. 2014). Nelson et al. (2014) and Dey et al. (2017) obtained ~3.4 Ga - 3.3 Ga age for the granites at the western part of the Gorumahisani area by U-Pb zircon age dating. The Mayurbhanj granite of ~3.1 Ga intruded the Gorumahishani greenstone belt at the south-eastern part (**Fig. 1b**; Mishra et al. 1999). The lower sequence of the Gorumahishani-Badampahar greenstone belt is dominated by komatiitic dunite, komatiitic peridotite, komatiitic basalt, pillow basalt, banded iron formation (BIF), and interbedded sedimentary rocks, whereas, the upper sequence is dominated by clastic sedimentary rocks (e.g. Bhattacharya et al. 2007; Chaudhuri et al. 2015; Mukhopadhyay et al. 2008, 2012; Ghosh et al. 2019; Bachhar et al. 2021; Jodder et al. 2021; Banerjee et al. 2022). The ultramafic-mafic volcanic sequence begins with meta-dunite cumulate rocks which grade into spinifex textured meta-peridotite to komatiitic meta-basalt to pillowed and massive tholeiitic meta-basalt. The whole supracrustal assemblage is metamorphosed from greenschist-amphibolite transition to amphibolite facies. A texturally and compositionally immature sandstone-conglomerate association is quite common between the upper and lower sequences of the greenstone belt

(Mazumder et al. 2019, 2022). The sandstones are poorly sorted and matrix-supported and the conglomerates have clasts of quartz, chert, fuchsite quartzite, jasper, and BIFs. The clasts are angular to rounded and very poorly sorted (Mazumder et al. 2022). The upper sequence unconformably overlies the conglomerate unit with a major abundance of clastic sediments like carbonaceous phyllite, chert-arenite, quartzite, and pelitic rocks, with a low abundance of mafic to felsic volcanics (Sengupta et al. 1997; Jodder et al. 2021; Mazumder et al. 2022). The sedimentary rocks are more abundant in the northernmost part of the greenstone belt with minor exposures of ultramafic rocks (Jena and Behera 2000). Ultramafic-mafic rocks from the Kudada area (Talsa and Ukam Pahar, south of Tatanagar) at the northern part of the greenstone belt are mainly talc-carbonate schist and serpentinite (Sinha et al. 2019; Banerjee et al. 2023). Patches of talc-carbonate schists are exposed in the open pits at the base of the Talsa Pahar, west of Kudada. The serpentinized peridotite is present on the northwest slope of Ukam Pahar, associated with hematite-quartzite rocks, and lies at the northern outskirt of the Singhbhum granite pluton. The ultramafic-mafic body of the Kudada is surrounded by tuffaceous phyllitic rocks that are closely associated with feldspathic schist (or soda granite) in the northern part.

Mazumder et al. (2022) studied the sedimentary rock associations and their primary sedimentary structures from the Gorumahishani-Badampahar greenstone belt. The carbonaceous sandstone-shale facies are most dominant in the lower stratigraphic sequence, and the fine-grained sandstones are characterized by parallel lamination and cross-lamination. The sandstones also bear mud drapes and evidence of current reversal (Mazumder et al. 2022). Banded Iron Formation at the top of the

ultramafic-mafic unit from the lower stratigraphic sequence also shows the presence of straight crested ripples with locally bifurcated crest lines. The dominant sedimentary facies association in the upper stratigraphic sequence is represented by texturally immature sandstone-conglomerate facies (Mazumder et al. 2022). Sandstones are very poorly sorted and are classified based on the presence of sedimentary structures like parallel laminated sandstone, trough cross-bedded sandstone, and tabular cross-bedded sandstone.

The ultramafic-mafic volcanic rock samples of this research are collected from the three major sections of the ~120 km long Gorumahishani greenstone belt: Maharajgunj-Chuka Pahar in the North, Tua Dungri in the middle, and Kapili in the South (**Fig. 1a, b**). The northern part of the greenstone belt near the Maharajgunj-Chuka Pahar and Tua Dungri area is up to ˜1 km wide, whereas the southern part of the belt from the Kapili area is up to ˜5 km wide. Komatiitic meta-dunite and meta-peridotite rocks are dominant in the northern part of the greenstone belt and present as small hillocks whereas the southern part is dominated by thick continuous spinifex-textured komatiitic meta-peridotite with komatiitic meta-basalt at the top (**Fig. 2a-e**). The average thickness of komatiitic meta-dunite-peridotite rocks at the lower cumulate zone from the Maharajgunj-Chuka Pahar area is ~10 m, from the Tua Dungri area is ~27 m, and from the Kapili area is ~5 m. The average thickness of the spinifex-textured meta-peridotite rocks (spinifex zone) from the Maharajgunj-Chuka Pahar area is ~40 m, from the Tua Dungri area is ~27 m, and from the Kapili area is ~200 m. The average thickness of the komatiitic meta-basalt rocks from the Maharajgunj-Chuka Pahar area is ~5 m, from the Tua Dungri area is ~5 m, and from the Kapili area is ~250 m. Meta-sedimentary rock units like quartzite and chert are

interbedded with the komatiitic meta-basalt at the top of the komatiitic suite of rocks from the three study areas. Multi-phase deformation event is quite distinct from the interbedded meta-sedimentary units with open-type folds (**Fig. 2f**). Schistosity planes are also developed in the meta-sedimentary rocks and those planes are defined by sericite and muscovite minerals. Sedimentary structures like ripple lamination with straight and bifurcated crest lines and graded bedding are dominant in the meta-sedimentary rocks of the Gorumahishani greenstone belt. All rock units throughout this belt are dipping towards the east with a dip that varies between 28° and 30°.

Chapter 3

Petrography

3. Petrography

Komatiitic rocks are collected from the three main cross sections of the ˜120 km long Gorumahishani greenstone belt at the eastern part of the Singhbhum Craton (**Fig. 1b**). At the northernmost part, samples are collected from the Chuka Pahar-Maharajgunj sector (Section A) (**Fig. 1e**). The Tua Dungri sector is the Section B which is located ˜10 Km south-east of the section-A (**Fig. 1c**). At the southern part of the Gorumahishani greenstone belt, samples are collected from the Kapili sector (Section C, ˜25 Km south-east of section-B) (**Fig. 1d**). A complete sequence of the komatiitic suite of rocks are present in each of the three sections (**Figs. 2a-f, 3a-p**). In the komatiite sequence, meta-dunite and meta-peridotite are present at the lower cumulate zone that grades into platy, chevron, and random spinifex textured meta-peridotite zone. The komatiitic meta-basalt occurs at the upper part of the volcanic sequence and intercalated with the meta-sediments.

3.1. Komatiitic meta-dunite and meta-peridotite from the Cumulate Zone

Serpentinized dunite occurs at the lowermost part of the cumulate zone and shows adcumulate texture. The dunite merges with cumulate peridotites showing mesocumulate to orthocumulate texture (**Figs. 2a; 3a, b**). In hand specimens, these rocks show a fine-grained melanocratic character with high specific gravity. The rocks have an overall greenish tinge because of serpentinization. Shapes of euhedral to subhedral olivine and a few pyroxene grains are identified in hand specimens as well as grains of feebly magnetic chromite or chrome magnetite. Under transmitted light microscope, the modal abundances of mineral phases in cumulate meta-dunite and meta-peridotites from the Maharajgunj-Chuka Pahar sector include, in

Fig. 2 Field photographs: **a** Meta-dunite from Tua Dungri (lower cumulate zone), **b** Chevron spinifex textured metaperidotite from Kapili (spinifex zone), **c** Platy spinifex textured meta-peridotite from Tua Dungri (spinifex zone), **d** Random spinifex textured meta-peridotite from Kapili (spinifex zone), **e** Schistose meta-basalt from Tiring, and **f** Quartzite band interlayered with schists from Kapili.

decreasing order, serpentine, tremolite, carbonate, and chlorite (**Fig. 4**). In the Tua Dungri sector, modal abundances of minerals include, in decreasing order, serpentine, carbonates, tremolite, chlorite, and talc (**Fig. 4**). In the Kapili sector, the decreasing order of mineral abundances changes to serpentine, tremolite, chlorite, hornblende, and carbonate (**Fig. 4**). Serpentine mostly exhibits mesh and interlocking textures (**Fig. 3b**). Single micrometre-sized olivine cores are also observed in samples from the Kapili area (**Fig. 3a**). Interstitial spaces of serpentine minerals (pseudomorphic after olivine) are occupied by chlorite, tremolite, hornblende, and carbonate minerals. Under reflected light, zoned chromites and chrome magnetites are identified in the meta-peridotites. Fine, anhedral magnetite grains are identified in the chlorite veins (**Fig. 3h-l**). Sulfide minerals include pentlandite, cobalt-rich violarite, millerite, chalcopyrite, and bornite and are present in the disseminated form within the meta-dunite and meta-peridotites at a low modal abundance (<1 modal%) (**Fig. 3m-p**; **Fig. 4**). Under reflected light, bornite form a thin rim surrounding the chalcopyrite mineral grains and cobalt-rich violarite partially replace the pentlandite mineral grains as irregular patches (**Fig. 3m-o**).

3.2. Komatiitic meta- peridotite from the Spinifex Zone

The metamorphosed komatiitic peridotites from the spinifex zone show platy, random, and chevron spinifex textures (**Figs. 2b-d; 3d, e**). The rocks are greenish and often develop weak schistosity planes. The spinifexes (~0.5-40 cm in length, and ~2-5 mm in width) are marked by deep cavities on the weathered surface of the rocks. Microscopic study reveals that in spinifex textured meta-peridotites of the Maharajgunj-Chuka Pahar and Tua Dungri sections, the modal abundance of

serpentine is lower while modes of tremolite and chlorite are higher compared to the cumulate zone. Tremolite, chlorite, hornblende, and serpentine are the major minerals in the meta-peridotites of the spinifex zone from the Kapili area. The modal abundance of serpentine in the spinifex zone of the Kapili area is also lower compared to the cumulate zone (**Fig. 4**). The primary minerals in spinifexes are replaced by tremolite (after clinopyroxene) in the Kapili area and a lesser extent by serpentine (after olivine) in the Tua Dungri area (**Fig. 3d, e**). Zones of various shapes in between the crisscrossing spinifexes from the greenstone belt are occupied by fine-grained chlorite, tremolite, carbonate, and magnetite minerals. Under the reflected light, zoned chromites and chrome magnetites are identified in the meta-peridotites of the spinifex zone (**Fig. 3h-j**). The modal abundance of these zoned chromites is higher compared to the cumulate zone (**Fig. 4**). Sulfide minerals in the spinifex zone are pentlandite, cobalt-rich violarite, and millerite and show a higher modal abundance but similar petrographic character to the sulfides in the lower cumulate zone (**Fig. 3m-p**). The overall modal proportion of sulfides is low (<1modal %) in the spinifex textured komatiitic peridotite rocks from the three areas. However, their abundance is relatively higher in the Tua Dungri area than in the Maharajgunj-Chuka Pahar and Kapili areas (**Fig. 4**). Under reflected light, the patchy appearance of cobalt-rich violarite minerals is also observed which partially replace the pentlandite mineral grains (**Fig. 3o**).

3.3. Komatiitic meta-basalts from the Upper Zone

The komatiitic basalts are altered to meta-basalts and show schistose character (**Fig. 2e**). The rocks have moderate specific gravity with an overall greenish appearance. In

places, meta-basalts are interlayered with quartzites and chert indicating the top part of the komatiitic litho package (**Fig. 2f**) (e.g. Arndt et al. 2008). The quartzite layer shows an open fold structure with a fold axis trending: 165°-345° and plunging towards the southwest. Schistosity planes are defined by the presence of platy mineral phases which are very difficult to identify in the naked eye because of their fine-grained texture. The strike of the schistosity planes of the meta-basalt unit is 155°-335° with a dip amount of 70° towards 252°. The meta-basaltic rocks have a high modal abundance of tremolite, actinolite, hornblende, and chlorite with mineral modes differing from place to place (**Fig. 3f, g**). Epidote occurs replacing plagioclase (**Fig. 3f, g**). The meta-basalts have higher modal abundances of tremolite, chlorite, and actinolite in the Tua Dungri and Chuka Pahar sections, whereas hornblende is more abundant in the Kapili section (**Fig. 4**). The schistosity planes are mainly defined by chlorite, tremolite, or hornblende, and their modal abundance increases with increasing schistosity. Oxide minerals in the meta-basalt are represented by variable modes of fine-grained, anhedral magnetite and minor ilmenite (**Fig. 3l**). Only a few samples (SHB/18/27, SHB/19-12/73) from the komatiitic basalt of the Kapili section have sulfide minerals (chalcopyrite, pentlandite) while section A and B samples are barren.

3.4. Textural types of chromite

Chromite is present ubiquitously throughout the cumulate and spinifex zones of the komatiite sequences. Spinifex zones have a higher modal abundance of chromites than the cumulate zones. Most of the chromite grains are small to medium sizes with euhedral to anhedral morphology. Microscopic study and BSE imaging

Table 2 Classification of komatiitic chromites from the Gorumahishani greenstone belt

Types of chromite	Study area	Host rock	Grain size	Textural and mineralogical character
Type-I	Tua Dungri	Serpentinized peridotite	~400 - 530 µm × ~350 - 390 µm	Subhedral grain; non-porous low reflectance core and high reflectance ferritchromit to chrome-magnetite rim with a sharp contact in between.
Type-II	Southern part of Kapili	Spinifex textured serpentinized peridotite	~550 - 620 µm × ~480 - 510 µm	Subhedral grain; low reflectance non-porous core with high reflectance thin ferritchromit rim, and wider, less porous chrome-magnetite rim. Diffused contact in between cores and rims.
Type-III	Northern part of Kapili	Spinifex textured serpentinized peridotite	~255 - 268 µm × ~125 - 160 µm	Subhedral to anhedral grain; low and high reflectance inner rims with extensively porous outer chrome-magnetite envelope. Diffused contact in between cores and rims.
Type-IV	Maharajgunj	Serpentinized peridotite	~30 - 50 µm × ~70 - 100 µm	Anhedral grain; small fractured ferritchromit with almost homogeneous character. Occasionally, thin high reflectance magnetite rims are observed along the fracture planes.
Type-V	Maharajgunj, Chuka Pahar, Tua Dungri, Kapili	Serpentinized peridotite, spinifex textured serpentinized peridotite, komatiitic basalt	~40 - 60 µm × ~25 - 50 µm	Subhedral to euhedral grain. Optically and compositionally homogenous chrome-magnetite and magnetite with non-porous character.

(Backscattered Electron image) show that a few chromite grains have compositional rims with different textures and variable reflectances (**Table 2**; **Fig. 3h-j**). These are zoned chromite grains and typically have a pristine chromite core with a ferritchromit inner rim and chrome-magnetite to magnetite outer rim (**Fig. 3h, i**). Multiple inner rims of different reflectance and composition between chromite core and outer chrome-magnetite rim are also observed (**Fig. 3j**). In some grains along the outermost margin of zoned chromites, irregular patches of ilmenite are present (**Fig. 3i, j**). The chromite grains are classified into five broad types based on petrography and mineral chemistry. Many of the chromite grains may not cut through the center of the grains and the original zoning pattern may not be visible.

Type-I chromites (**Fig. 3h**) are present in the serpentinized peridotite from the Tua Dungri area. Type-II and type-III chromites are present in the spinifex textured serpentinized peridotite from the Kapili area. These type-I, type-II, and type-III chromite grains are optically and texturally inhomogeneous (**Fig. 3i, j**). In contrast, type-IV chromites in the serpentinized peridotite from the Maharajgunj area and type-V chromites in the komatiitic sequences from all locations are homogeneous (**Fig. 3k, l**). Type-I chromites (400 - 530 µm × 350 - 390 µm) are euhedral and have a non-porous core and ferritchromit to chrome magnetite rim with a sharp contact in between (**Fig. 3h**). Type-II chromites (550 - 620 µm × 480 - 510 µm) have a wider, less porous chrome magnetite rim, thin non-porous ferritchromit rim, with a darker non-porous core (**Fig. 3i**). Type-III chromites are subhedral (255 - 268 µm × 125 - 160 µm) and show lighter and darker inner rims with extensive porous outer chrome magnetite envelopes and small non-porous cores (**Fig. 3j**). Both type-II and type-III grains have diffused contacts in between their

core and rim. Type-IV chromites are small fractured ferritchromit grains (< 50 µm) with almost homogenized character except for highly irregular thin higher reflectance magnetite bands along the fracture planes (**Fig. 3k**). Type-V oxide grains are optically and compositionally homogeneous chrome magnetite and magnetite grains (40 - 60 µm × 25 - 50 µm) that are non-porous and subhedral to euhedral (**Fig. 3l**). Among the five types, type-V chromites have the highest modal abundance in komatiitic rocks while the lowest modal abundance is displayed by the type-IV grains. If compared between the zoned chromites, type-II grains have a higher modal abundance than type-I and type-III varieties.

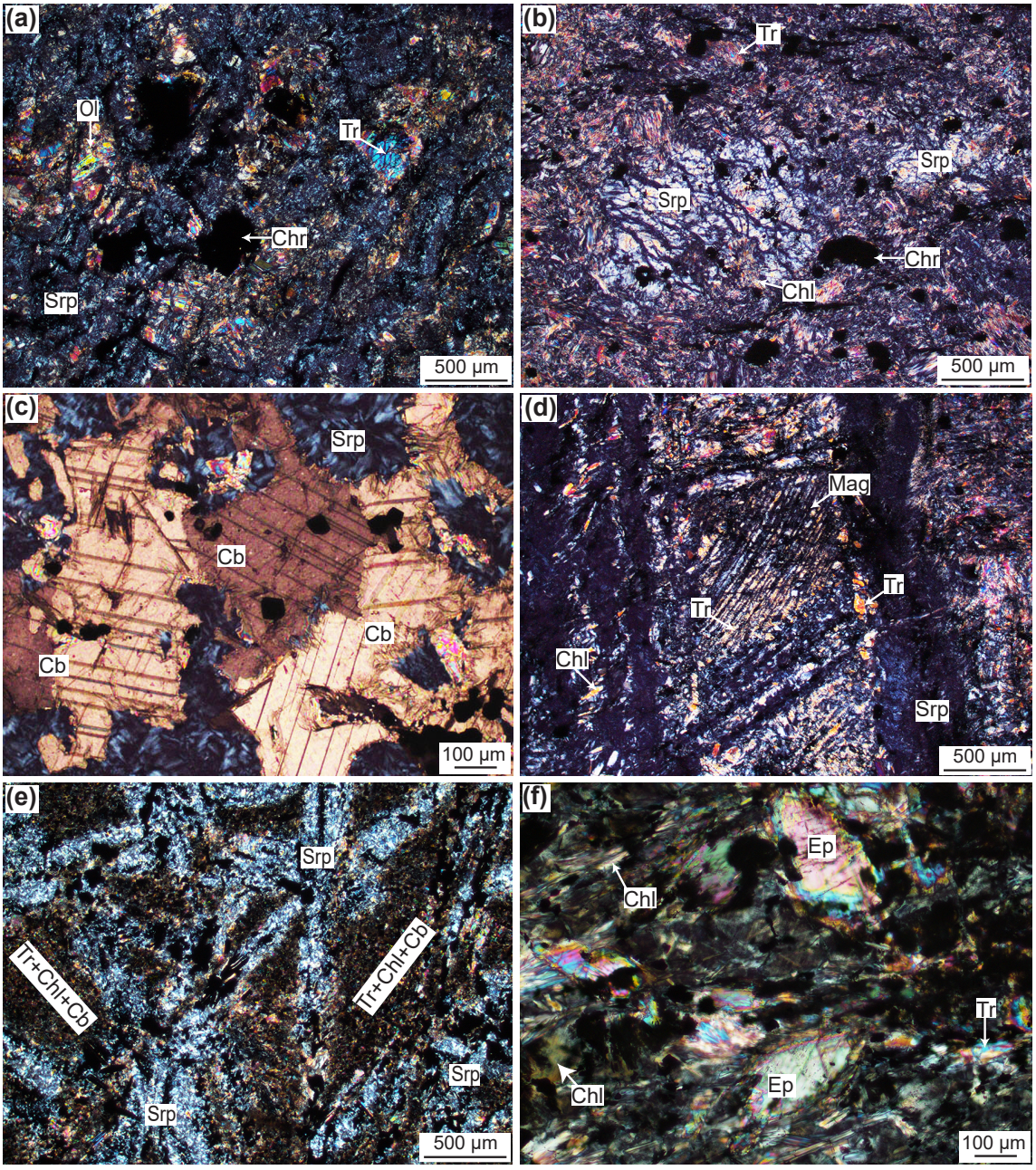

Fig. 3 Photomicrographs of komatiitic rocks in transmitted light, reflected light and BSE images: **a** Small olivine (ol) core is surrounded by serpentine (srp) and associated with accessory chromite (chr); **b** Serpentine shows pseudomorphic texture (after olivine) with accessory chromite. Chlorite (Chl) and tremolite (Tr) form the interstitial assemblage; **c** Carbonate (Cb) minerals in the meta-peridotite; **d** Spinifex texture is represented by tremolite after pyroxene grains. Magnetite is present in between tremolite grains; **e** Spinifex texture is represented by serpentine after olivine grains. An assemblage of chlorite+tremolite+carbonate is present in between serpentine spinifexes; **f-g** Meta-basalt contains epidote (Ep) after plagioclase along with chlorite, tremolite, and hornblende (after clinopyroxene); **h-j** Type-I, type- II, and type-III zoned chromites with chromite (Chr) core and ferritchromit (Fcmt) to chrome magnetite rims; **k** Fractured type-IV ferritchromit grain; **l** Type-V homogeneous chrome magnetite grain; **m** Chalcopyrite (Ccp) mineral is present between chromite grains; **n** Primary chalcopyrite (Ccp) is rimmed by low-temperature secondary bornite (Bn); **o** Primary Pentlandite (Pn) and violarite (Viol) is replaced by low tem-perature secondary millerite (Mlr). Magnetite (Mag) is presently associated with the sulfide mineral assemblages; **p** Primary pentlandite (Pn) associated with barite (Brt). Mineral names abbreviations are from Whitney and Evans (2010).

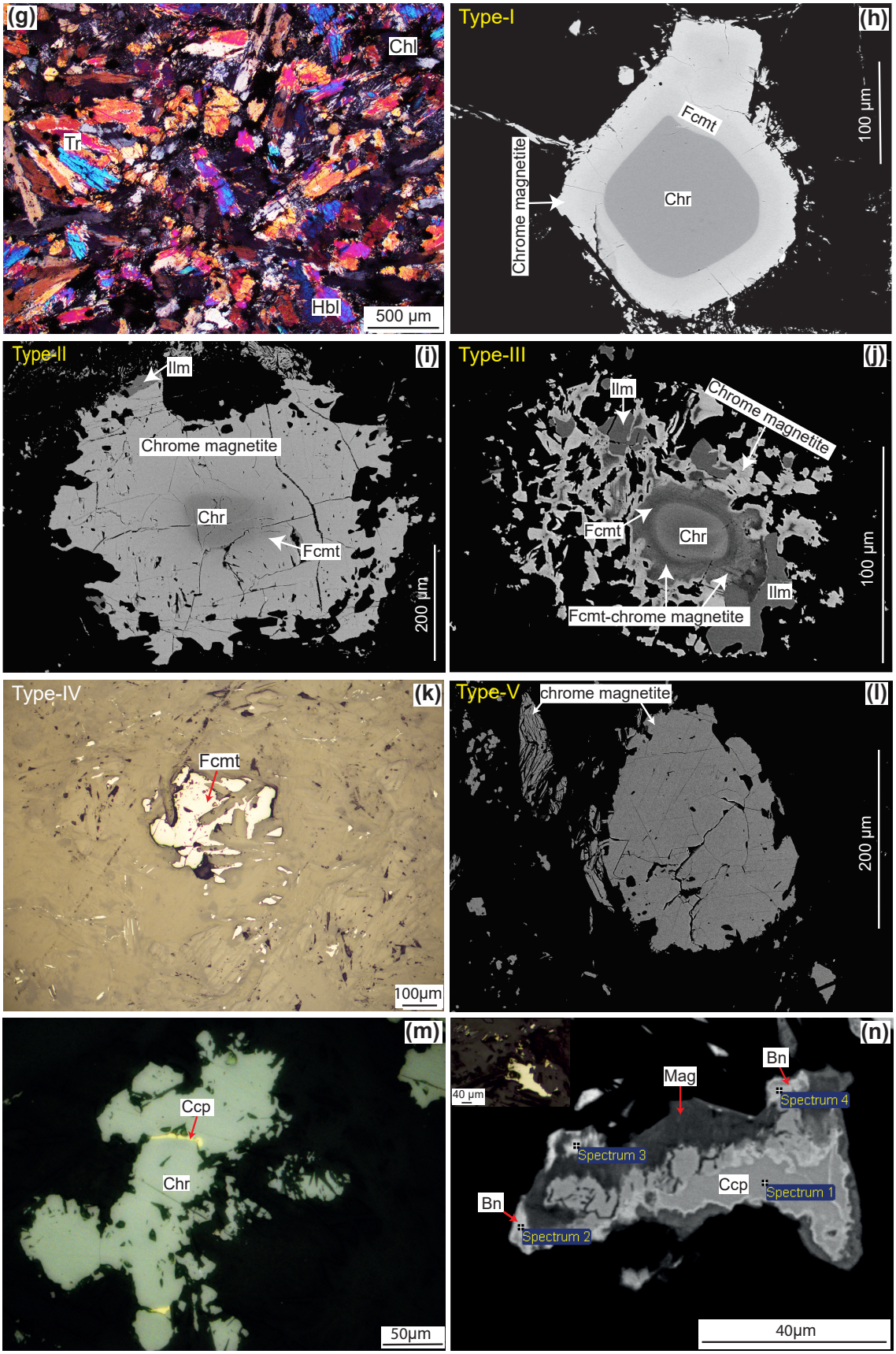

Fig. 3 Continued.

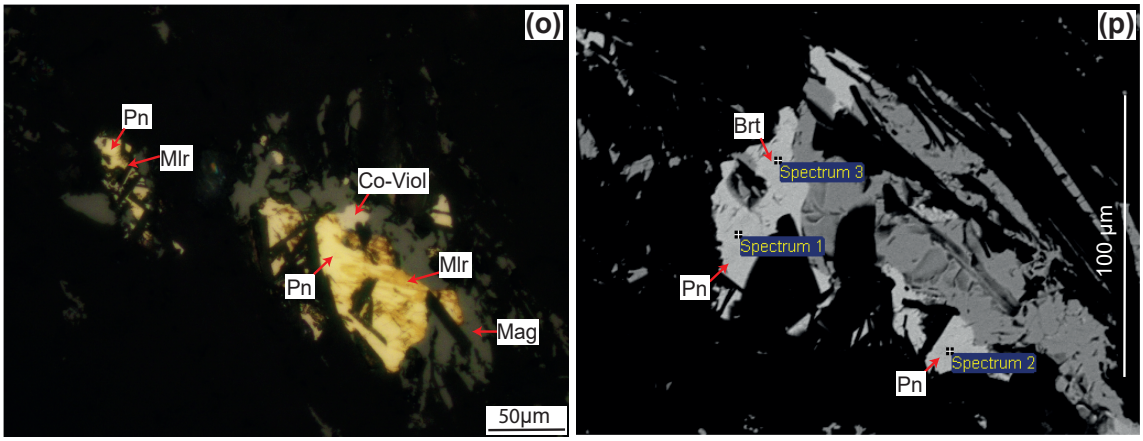

Fig. 3 Continued.

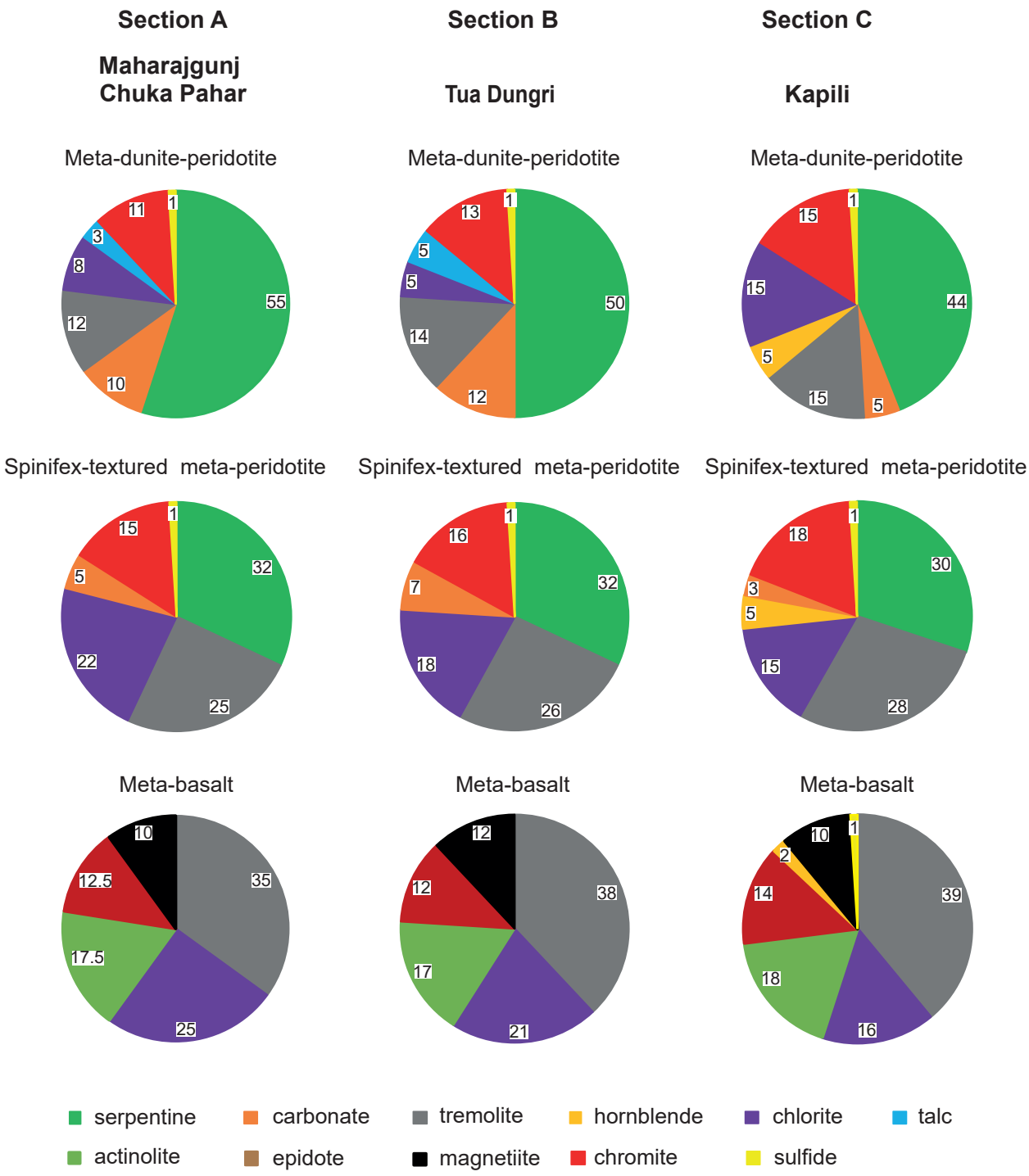

Fig. 4 Comparison of modal abundances (in vol.%) of mineral phases from the komatiitic suite of rocks between Maharajgunj-Chuka Pahar, Tua Dungri, and Kapili areas.

Chapter 4

Analytical methods

4. Analytical methods

4.1. Mineral chemical analysis

4.1.1. Major elements

Back-scattered electron (BSE) imaging and microanalysis of the mineral phases (oxides, sulfides, and silicates) are carried out using a CAMECA SXFive EPMA instrument at DST-SERB National Facility, Department of Geology, Banaras Hindu University (India). Another set of samples is analyzed by 4-WDX CAMECA SX-100 EPMA at the Department of Geology and Geophysics, Indian Institute of Technology, Kharagpur (India) for oxide and sulfide minerals. The CAMECA SXFive EPMA is operated by SXFive Software at a voltage of 15 kV and beam current of 10 nA whereas the 4-WDX CAMECA SX-100 EPMA is controlled by a beam current of 15 nA and acceleration voltage of 20 kV. Natural mineral standards fluorite, apatite, albite, halite, periclase, peridote, corundum, wollastonite, orthoclase, rutile, chromite, rhodonite, celestite, barite, hematite, crocoite, pyrite, and synthetic Ag_2Te, InAs, InSb, Ni, Co, Cu, Zn metal supplied by CAMECA-AMETEK are used for routine calibration and quantification during analysis. Routine calibration, acquisition, quantification, and data processing are carried out using SxSAB version 6.1 and SX-Results software of CAMECA. ZAF matrix corrections are performed by the CAMECA-supplied PAPSIL software. The compositions of chromite and silicate are recalculated to cation proportions using the Fe^{3+} calculation scheme of Droop (1987). The Major elements data of silicate minerals for all analyzed points are tabulated in **Table 3**. The major and minor elements data of oxide minerals for all analyzed points are tabulated in **Appendix 1** and the data ranges are in **Table 4**.

Sulfide minerals are also analyzed using a Scanning Electron Microscope (SEM), JSM 6490 series at the Department of Geology and Geophysics, Indian Institute of Technology, Kharagpur, and the DST-SERB National Facility, Department of Geology, Banaras Hindu University. The complete set of data on the sulfide minerals from the Scanning Electron Microscope is tabulated in **Table 5**.

4.1.2. Trace elements and Platinum-Group element (PGE)

Trace element and PGE contents in chromite, ferritchromit, and chrome-magnetite are also measured by an LA-ICP-MS system for selected elements (Sc, Ti, V, Mn, Co, Ni, Cu, Zn, Ga, Os, Ir, Ru, Rh, Pt, Pd) consisting of a New Wave 193 nm ArF excimer laser and an Agilent 7800 quadrupole ICP-MS at Korea Institute of Ocean Sciences and Technologies, South Korea. The ablation conditions are a 10 Hz repetition rate, an 80-100 μm beam size, and ~ 5 J/cm^2 energy density. The NIST 610 glass is used as a primary standard and Al contents measured by a microprobe is an internal standard element for calculating trace elements. The sulfide reference material UQAC-FeS-1 is used as a primary standard and Fe contents as an internal standard element for platinum-group elements (PGE). The data reduction is conducted by Iolite software (Paton et al. 2011). The isobaric interference by metal oxides (MO+) and metal argides (MAr+) are checked by analyses of pure Cu metal (C-430, Fisher Scientific Company) and PGE-free synthetic Ni-sulphide. The expected isobaric interferences are ~1 ppb Ru per 1000 ppm Ni and ~7 ppb Rh per 1000 ppm Cu in Cr-spinels, which result in negligible isobaric interferences of $^{61}Ni^{40}Ar$ + and $^{63}Cu^{40}Ar$ + on ^{101}Ru and ^{103}Rh (<2 %) for most samples. Any micro inclusions, identified as spikes in time-resolved spectra data, are excluded when calculating the concentrations.

Multiple analyses (n = 7) of Cr-spinels from Kamchatka picrite (Ty24) are performed using the UQAC-FeS-1 reference material to externally monitor the quality of the PGE data. Our results are consistent with the values reported by Park et al. (2017) within 1 standard deviation. The complete set of analyses for chromite trace elements and platinum-group elements are tabulated in **Table 6** and **Table 7** respectively.

4.2. Bulk-rock analysis

For bulk-rock analysis, samples are cleaned, crushed, and pulverized to a 200-mesh size in the Department of Geological Sciences, at Jadavpur University, India. The crushing and pulverization work is carried out by single bowl RO milling systems (Model MBM 07, Insmart systems) using agate (99.9% SiO_2, 7.0 Mohs hardness, and 2.65 g/cc density) balls. At 600 rpm, 100 g of the sample is crushed by the machine. bulk-rock major and trace element and the Loss On Ignition (LOI) analysis of 68 samples are performed from Intertek Genalysis, Perth, Western Australia (e.g. Bourdeau et al. 2021; Datta et al. 2021). Platinum-group elements analysis alongside Sulfur (S) for 42 samples is conducted from Intertek Genalysis, Perth, Western Australia (e.g. Prichard et al. 2018; Datta et al. 2021). Sm-Nd isotopic study for 22 komatiite samples is performed at the CNRS-CRPG, Nancy, France (e.g. Maltese et al. 2022).

4.2.1. Major elements

Approximately 0.7g sample is catch-weighed into a platinum crucible and then mixed with a pre-weighed amount of flux which is comprised of a mixture of lithium

tetraborate and lithium metaborate. An oxidant is added and the sample is fused to produce a homogeneous melt which is cast into a platinum mold to produce a fusion disk. The fusion disk is analyzed on a Panalytical Axios sequential wavelength-dispersive X-ray fluorescence spectrometer. Here, calibration is affected by standard glass beads of known composition. Corrections are made for the catch weights, instrumental drift, line overlaps, and inter-element enhancement/absorption matrix effects. Standard OREAS 24b is used as reference material for this case.

LOI is analyzed using a TGA or Thermo Gravimetric Analyzer. First, the inert crucible is weighed by the instrument and then ˜1 g of the sample is added to the crucible. The crucible and sample are weighed again by the instrument. The exact mass of the sample taken is determined by the difference. The sample is then heated to constant mass at 105°C and weighed. The mass lost as a fraction of the mass taken is moisture. The sample is then heated to constant mass at 1000°C and weighed. The mass lost as a fraction of the dry mass is the loss on ignition or LOI.

The complete set of data for bulk-rock major elements is presented in **Table 8**.

4.2.2. Trace elements

The pulped samples are catch-weighed at 0.20 ± 0.02 g into a Teflon tube. The tube is placed in a rack and the digesting acids are added sequentially. The rack is then placed on a “hot block” which provides even heat to decompose the sample to ensure maximum dissolution. The perchloric ($HClO_4$) acid is evaporated and the residue is leached by boiling in HCl. The solution is transferred to a polystyrene tube where it is volumed and mixed. A further dilution of the digest solution is required before reading on the Agilent 7900 ICP-MS with collision cell technology because

calibration is affected using solution standards of known concentration. Standard OREAS 45h is used for trace element analysis.

The complete set of data for bulk-rock trace elements alongside major elements is presented in **Table 8**.

4.2.3. Platinum-Group element (PGE)

In Intertek Genalysis the pulped samples are catch-weighed at 25 g, then mixed with a flux and fired in a furnace. When fired, the mixed sample forms a nickel sulfide matte and an immiscible slag which separates owing to density differences. The precious metals are collected in the nickel sulfide matte (button). The button is separated from the slag, weighed, and pulverized. A portion of the pulverized button is catch-weighed and dissolved in boiling HCl. The addition of various reagents to the boiling HCl solution and careful observation of the dissolution process ensures that the platinum group elements and gold are quantitatively recovered by filtration as insoluble residues. These residues are dissolved in aqua regia. Then the solution is diluted and read on an ICP-MS with collision cell technology to remove polyatomic interferences. Internal standards are used to correct for drift and plasma fluctuations. The results are corrected for the various catch weights and button weights by the LIMS system. Standard OREAS 13b is used for PGE+Au analysis.

The complete set of data for bulk-rock platinum-group elements is presented in **Table 9.**

4.2.4. Sulfur (S)

Sulfur (S) analysis is performed in an Eltra CS800 Sulphur Analyzer. The pulped sample is weighed out and placed in a ceramic crucible. An accelerant is added to act as a flux and improve the fluidity and oxidation of the carbon and sulfur. Heating is accomplished in a high-frequency induction furnace as this provides both speed and accuracy. Any sulfur in the sample is converted to gaseous oxides. These gases absorb infrared radiation at specific wavelengths which are proportional to the concentration of the S in the sample. Any water in the sample is removed by passing the gases through magnesium perchlorate as water interferes with the analysis. Calibration is affected by the standard of known S concentration. Standard OREAS 600b is used here as reference material.

The complete set of data for bulk-rock S alongside platinum-group elements is presented in **Table 9.**

4.2.5. Sm-Nd isotopic analysis

Bulk rock Sm-Nd isotopic analysis is performed at the CNRS-CRPG, Nancy, France. Before digestion, a mixed $^{147}Sm/^{150}Nd$ isotopic tracer is added to each powdered sample and each analytical blank to allow Sm and Nd concentrations to be determined by isotope dilution. The mass of samples is varied between ~30 and 100 mg depending on the Nd concentration previously determined by ICPMS. The bulk powders are dissolved by adding 1.5 mL of concentrated HF and 1.5 mL of concentrated HNO_3 and heating for 3 days at 120°C. After that, the samples are dried down and heated again for 2 days after the addition of 3 ml 6N HCl. To verify the digestion efficiency, duplicates of four samples with high Zr contents are dissolved in PTFE/TFM BOLA bombs, and in these cases, 1 ml each of concentrated HF and HNO3

is added and samples are heated for 8 days at 150°C in an oven, followed by drying and reheating in 5ml 6N HCl. Nd and Sm are separated using procedures adapted from Pin and Zalduegui (1997) including two chromatographic column steps, the first using Eichrom TRU Spec resin to extract the REE from the matrix and the second using Eichrom LN Spec to isolate Nd and Sm. The resulting solutions are analyzed using the Thermo-Scientific Neptune MC-ICPMS instrument at the CRPG laboratory. Instrumental mass fractionation is corrected using an exponential law and assuming $^{146}Nd/^{144}Nd = 0.7219$. Liquid standard JNdi (Tanaka et al. 2000) is analyzed after every third sample, yielding a mean value for $^{143}Nd/^{144}Nd$ of 0.512097 ± 0.000010 (2σ, n=16). As this value is slightly lower than the nominal value of 0.512115 proposed by Tanaka et al. (2000) for this standard, a correction of +0.000018 is included in each value to facilitate comparison with literature data. Two total chemistry blanks are analyzed with the samples yielded 23 and 38 pg for Nd, and 28 and 36 pg for Sm. These values are negligible relative to the quantities of Nd (>120 ng) and Sm (>40 ng) measured in the samples. The measured isotopic ratios were then corrected offline for iteratively corrects for fractionation, isobaric interferences, and the spike contribution.

The complete set of data for bulk-rock Sm-Nd isotopes is tabulated in **Table 10.**

Chapter 5

Results

5. Results

5.1. Major elements mineral chemistry

5.1.1. Silicates and carbonates

Mineral chemical data of serpentine, chlorite, carbonate, amphibole, clinopyroxene, and olivine from the komatiitic meta-dunite and meta-peridotites of the Gorumahishani greenstone belt are presented in **Figure 5a-d** and are tabulated in **Table 3**. Serpentine shows a wide range of SiO_2 = 43.05 - 50.54 wt.% and MgO = 32.93 - 40.19 wt.% with low Al_2O_3 = 0.18 - 1.09 wt.% **(Fig. 5a**). Amphiboles are mainly tremolite (SiO_2 = 54.67 - 59.09 wt.%, MgO = 22.23 - 23.73 wt.%, CaO = 12.01 - 13.41 wt.%, Al_2O_3 = 0.26 - 3.09 wt.%, FeO = 1.52 - 3.97 wt.%) from the Maharajgunj and Kapili areas whereas low modal abundances of magnesiohornblende (SiO_2 = 52.77 - 53.76 wt.%, MgO = 19.94 - 23.09 wt.%, CaO = 8.31 - 11.79 wt.%, Al_2O_3 = 3.18 - 5.62 wt.%, FeO = 1.29 - 9.62 wt.%) and actinolite (SiO_2 = 53.91 - 57.04 wt.%, MgO = 20.04 - 23.82 wt.%, CaO = 6.5 - 12.33 wt.%, Al_2O_3 = 0.42 - 3.88 wt.%, FeO = 6.14 - 7.99 wt.%) are also found in the southern Kapili area (**Fig. 5b**). Chlorites are Mg-rich (Mg# = 0.93 - 0.96) with variable Al_2O_3 = 11.37 - 17.73 wt.%. In the Si vs. $Fe_{total}/(Fe^{2+}+Mg^{2+})$ plot, chlorites are identified as corundophilite and sheridanite (**Fig. 5d**). Chlorite grains surrounding the type-II and type-III chromite grains in the Kapili area have higher Cr_2O_3 = 0.74 - 0.98 wt.% than the other grains (Cr_2O_3 = 0.21 - 0.69 wt.%). The carbonate minerals are mainly dolomite in the Tua Dungri komatiitic rocks (MgO = 21.46 - 22.01 wt.%, CaO = 33.31 - 33.42 wt.%) and calcite (MgO = 3.3 - 3.52 wt.% CaO = 55.2 - 55.35 wt.%) in the Chuka Pahar (**Fig. 5c**). The forsterite content of one tiny olivine found in the Kapili dunite-peridotite is 88 with SiO_2 = 40.62 wt.% while the clinopyroxenes are augite (MgO = 0.22 - 3.53 wt.%, FeO = 1.79 -

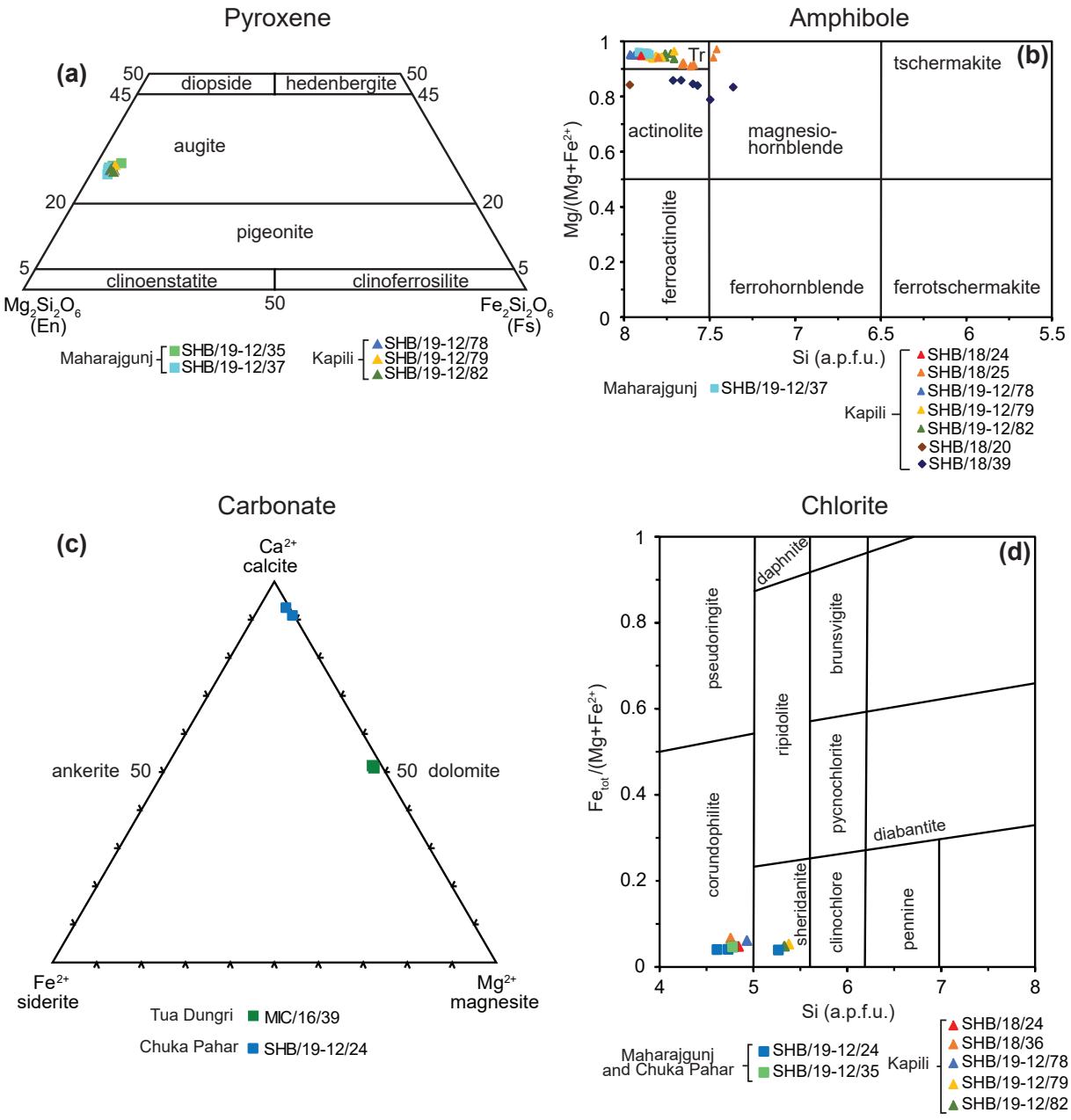

Fig. 5 Classification of **a** pyroxene (after Morimoto 1988), **b** amphibole (after Leake et al. 1997), **c** carbonate, and **d** chlorite (after Hey 1954) minerals from the komatiitic rocks of the Gorumahishani greenstone belt.

Table 3 EPMA major and minor elements composition (wt.%) of silicate minerals from the Gorumahishani greenstone belt

Sample number	SHB/19-12/82	SHB/19-12/78	SHB/19-12/78	SHB/19-12/78	SHB/19-12/79	SHB/19-12/79	SHB/19-12/82	SHB/19-12/82	SHB/19-12/35	SHB/19-12/35	SHB/19-12/35	SHB/19-12/37	SHB/19-12/37
Location	Kapili	Kapili	Kapili	Kapili	Kapili	Kapili	Kapili	Kapili	Maharaj-gunj	Maharaj-gunj	Maharaj-gunj	Maharaj-gunj	Maharaj-gunj
EPMA point	84 / 1 .	160 / 1 .	174 / 1 .	183 / 1 .	54 / 1 .	56 / 1 .	128 / 1 .	129 / 1 .	141 / 1 .	150 / 1 .	151 / 1 .	199 / 1 .	200 / 1 .
Mineral	Olivine	Clinopy-roxene	Clinopy-roxene	Clinopy-roxene	Clinopy-roxene	Clinopy-roxene	Clinopy-roxene	Clinopy-roxene	Clinopy-roxene	Clinopy-roxene	Clinopy-roxene	Clinopy-roxene	Clinopy-roxene
Na_2O	0.03	0.14	0.38	0.32	0.60	0.44	0.73	0.23	0.61	0.27	0.17	0.19	0.25
K_2O	0.00	0.02	0.03	0.00	0.03	0.01	0.02	0.04	0.08	0.02	0.01	0.03	0.01
CaO	0.01	13.32	12.69	12.86	12.87	13.54	12.86	13.26	13.61	13.42	13.47	13.01	13.14
Al_2O_3	0.00	0.22	0.89	0.56	1.64	0.89	1.66	0.48	3.53	1.71	1.16	1.21	2.25
MnO	0.13	0.08	0.15	0.00	0.18	0.01	0.08	0.02	0.05	0.00	0.01	0.11	0.00
TiO_2	0.00	0.02	0.06	0.04	0.13	0.08	0.10	0.02	0.04	0.00	0.05	0.08	0.09
Cr_2O_3	0.00	0.06	0.14	0.00	0.29	0.10	0.34	0.00	0.31	0.00	0.01	0.15	0.23
MgO	47.98	23.33	23.21	23.12	23.17	23.03	23.65	23.61	22.06	22.85	23.56	23.61	22.76
SiO_2	40.62	58.52	57.98	58.02	56.97	57.22	57.32	58.40	55.28	57.73	58.52	57.59	57.16
Fe_2O_3	0.00	0.00	0.00	0.00	0.00	0.00	0.00	0.00	0.00	0.00	0.00	0.00	0.00
FeO	11.73	2.31	2.20	2.71	2.60	2.44	2.81	2.14	2.85	2.02	1.79	1.90	2.06
V_2O_3	0.00	0.00	0.00	0.01	0.00	0.00	0.00	0.01	0.01	0.00	0.00	0.00	0.00
NiO	0.42	0.11	0.10	0.21	0.31	0.25	0.22	0.08	0.04	0.00	0.15	0.12	0.14
ZnO	0.12	0.00	0.22	0.20	0.15	0.00	0.00	0.00	0.10	0.00	0.02	0.00	0.00
CoO	0.00	0.00	0.04	0.08	0.00	0.00	0.07	0.00	0.00	0.00	0.11	0.06	0.00
Total	101.03	98.11	98.10	98.12	98.94	98.02	99.87	98.29	98.56	98.01	99.02	98.06	98.08
Na	0.001	0.010	0.027	0.022	0.042	0.031	0.050	0.016	0.042	0.019	0.012	0.013	0.018
K	0.000	0.001	0.001	0.000	0.001	0.001	0.001	0.002	0.003	0.001	0.000	0.001	0.000
Ca	0.000	0.518	0.493	0.500	0.495	0.526	0.489	0.513	0.525	0.521	0.518	0.505	0.510
Al	0.000	0.009	0.038	0.024	0.069	0.038	0.070	0.020	0.150	0.073	0.049	0.052	0.096
Mn	0.003	0.002	0.004	0.000	0.005	0.000	0.002	0.001	0.001	0.000	0.000	0.003	0.000
Ti	0.000	0.000	0.002	0.001	0.004	0.002	0.003	0.001	0.001	0.000	0.001	0.002	0.002
Cr	0.000	0.002	0.004	0.000	0.008	0.003	0.009	0.000	0.009	0.000	0.000	0.004	0.006
Mg	1.753	1.261	1.253	1.250	1.240	1.244	1.251	1.271	1.185	1.234	1.259	1.273	1.229
Si	0.996	2.123	2.101	2.106	2.045	2.074	2.033	2.109	1.992	2.092	2.099	2.084	2.071
Fe^{3+}	0.000	0.000	0.000	0.000	0.000	0.000	0.000	0.000	0.000	0.000	0.000	0.000	0.000

Fe^{2+}	0.240	0.070	0.067	0.082	0.078	0.074	0.083	0.065	0.086	0.061	0.054	0.057	0.063
V	0.000	0.000	0.000	0.000	0.000	0.000	0.000	0.000	0.000	0.000	0.000	0.000	0.000
Ni	0.008	0.003	0.003	0.006	0.009	0.007	0.006	0.002	0.001	0.000	0.004	0.003	0.004
Zn	0.002	0.000	0.006	0.005	0.004	0.000	0.000	0.000	0.003	0.000	0.000	0.000	0.000
Co	0.000	0.000	0.001	0.002	0.000	0.000	0.002	0.000	0.000	0.000	0.003	0.002	0.000
Total	3.000	4.000	4.000	4.000	4.000	4.000	4.000	4.000	4.000	4.000	4.000	4.000	4.000

Sample number	SHB/19-12/37	SHB/19-12/37	SHB/19-12/37	SHB/19-12/37	SHB/18/39	SHB/18/39	SHB/18/25	SHB/18/25	SHB/18/39	SHB/18/20	SHB/18/39	SHB/18/39	SHB/18/39
Location	Maharaj-gunj	Maharaj-gunj	Maharaj-gunj	Maharaj-gunj	Kapili	Kapili	Kapili	Kapili	Kapili	Kapili	Kapili	Kapili	Kapili
EPMA point	213 / 1 .	214 / 1 .	228 / 1 .	229 / 1 .	22 / 1 .	34 / 1 .	46 / 1 .	47 / 1 .	23 / 1 .	13 / 1 .	24 / 1 .	25 / 1 .	33 / 1 .
Mineral	Clinopy-roxene	Clinopy-roxene	Clinopy-roxene	Clinopy-roxene	Mag-nesio ho-rnblende	Mag-nesio ho-rnblende	Mag-nesio ho-rnblende	Mag-nesio ho-rnblende	Actino-lite	Actino-lite	Actino-lite	Actino-lite	Actino-lite
Na_2O	0.20	0.18	0.08	0.14	1.45	1.05	0.93	0.78	0.60	0.07	0.95	1.07	0.78
K_2O	0.01	0.00	0.02	0.01	0.10	0.04	0.03	0.04	0.04	0.01	0.05	0.05	0.02
CaO	13.14	13.17	13.10	12.74	11.80	8.31	10.40	11.23	12.33	6.50	11.56	11.22	12.17
Al_2O_3	1.69	1.42	1.11	1.19	5.62	4.21	3.65	3.18	2.37	0.42	3.50	3.88	2.64
MnO	0.00	0.00	0.16	0.03	0.10	0.23	0.17	0.17	0.22	0.55	0.14	0.14	0.16
TiO_2	0.08	0.06	0.02	0.05	0.21	0.20	0.14	0.09	0.08	0.05	0.12	0.18	0.10
Cr_2O_3	0.03	0.37	0.10	0.11	0.27	0.19	0.24	0.08	0.23	0.07	0.08	0.03	0.04
MgO	23.14	23.21	23.35	23.96	19.94	20.33	23.08	23.09	21.00	23.82	20.63	20.04	20.88
SiO_2	57.96	58.10	58.11	57.75	53.76	52.77	53.22	53.19	56.13	57.04	54.82	53.91	55.09
Fe_2O_3	0.00	0.00	0.00	0.00	0.00	0.00	1.11	2.99	0.00	0.00	0.00	0.00	0.00
FeO	2.02	1.95	1.81	2.01	7.19	9.62	2.82	1.29	6.20	7.99	6.76	6.84	6.14
V_2O_3	0.00	0.00	0.03	0.02									
NiO	0.10	0.08	0.16	0.14									
ZnO	0.03	0.02	0.21	0.02									
CoO	0.00	0.11	0.00	0.08									
Total	98.40	98.66	98.26	98.23	100.43	96.95	95.80	96.11	99.21	96.52	98.59	97.34	98.03
Na	0.014	0.013	0.006	0.010	0.384	0.288	0.253	0.211	0.161	0.019	0.255	0.291	0.209
K	0.001	0.000	0.001	0.001	0.018	0.008	0.006	0.006	0.006	0.001	0.009	0.008	0.004
Ca	0.508	0.509	0.508	0.493	1.730	1.265	1.566	1.687	1.816	0.973	1.717	1.688	1.814
Al	0.072	0.060	0.047	0.050	0.906	0.704	0.605	0.525	0.384	0.069	0.571	0.642	0.433

Mn	0.000	0.000	0.005	0.001	0.012	0.028	0.020	0.020	0.026	0.065	0.016	0.016	0.019
Ti	0.002	0.002	0.001	0.001	0.022	0.021	0.015	0.009	0.008	0.006	0.012	0.019	0.011
Cr	0.001	0.010	0.003	0.003	0.029	0.021	0.027	0.008	0.025	0.007	0.009	0.003	0.005
Mg	1.245	1.247	1.260	1.289	4.068	4.303	4.836	4.826	4.303	4.960	4.262	4.195	4.332
Si	2.092	2.095	2.104	2.084	7.360	7.493	7.481	7.458	7.714	7.967	7.598	7.571	7.667
Fe^{3+}	0.000	0.000	0.000	0.000	0.000	0.000	0.118	0.315	0.000	0.000	0.000	0.000	0.000
Fe^{2+}	0.061	0.059	0.055	0.061	0.823	1.142	0.332	0.151	0.712	0.933	0.783	0.803	0.715
V	0.000	0.000	0.001	0.000									
Ni	0.003	0.002	0.005	0.004									
Zn	0.001	0.001	0.006	0.001									
Co	0.000	0.003	0.000	0.002									
Total	4.000	4.000	4.000	4.000	15.352	15.272	15.259	15.217	15.156	15.000	15.232	15.237	15.210

Sample number	SHB/18/24	SHB/18/25	SHB/18/25	SHB/18/25	SHB/18/25	SHB/18/25	SHB/19-12/78	SHB/19-12/78	SHB/19-12/78	SHB/19-12/78	SHB/19-12/78	SHB/19-12/79	SHB/19-12/79
Location	Kapili	Kapili	Kapili	Kapili	Kapili	Kapili	Kapili	Kapili	Kapili	Kapili	Kapili	Kapili	Kapili
EPMA point	37 / 1 .	41 / 1 .	42 / 1 .	43 / 1 .	48 / 1 .	50 / 1 .	153 / 1 .	161 / 1 .	175 / 1 .	184 / 1 .	185 / 1 .	31 / 1 .	32 / 1 .
Mineral	Tremolite	Tremolite	Tremolite	Tremolite	Tremolite	Tremolite	Tremolite	Tremolite	Tremolite	Tremolite	Tremolite	Tremolite	Tremolite
Na_2O	0.56	1.00	0.86	0.99	1.02	0.45	0.12	0.20	0.29	0.29	0.38	0.58	0.62
K_2O	0.04	0.03	0.02	0.04	0.03	0.02	0.02	0.01	0.00	0.02	0.00	0.02	0.02
CaO	12.96	12.30	12.01	12.08	12.08	12.94	13.38	13.29	12.90	13.10	12.50	12.75	12.89
Al_2O_3	1.13	2.92	2.66	2.87	3.09	1.15	0.28	0.38	0.62	0.66	0.91	1.39	1.54
MnO	0.01	0.00	0.05	0.15	0.00	0.04	0.18	0.02	0.12	0.08	0.13	0.10	0.12
TiO_2	0.08	0.15	0.12	0.14	0.12	0.02	0.01	0.05	0.05	0.02	0.10	0.09	0.11
Cr_2O_3	0.22	0.21	0.28	0.09	0.14	0.00	0.00	0.05	0.03	0.01	0.00	0.04	0.21
MgO	23.50	22.40	22.23	22.62	22.39	22.81	22.81	23.28	22.81	23.13	23.66	22.87	22.74
SiO_2	59.09	54.83	54.67	56.18	55.26	56.34	58.75	58.36	57.76	58.13	57.64	57.34	56.60
Fe_2O_3	0.00	0.08	0.00	0.00	0.00	0.80	0.00	0.00	0.00	0.00	0.00	0.00	0.00
FeO	2.35	3.74	3.36	3.75	3.97	2.55	2.13	2.11	2.19	2.23	2.11	2.45	2.50
V_2O_3							0.00	0.00	0.01	0.00	0.00	0.01	0.00
NiO							0.12	0.08	0.09	0.13	0.06	0.17	0.13
ZnO							0.00	0.00	0.05	0.08	0.06	0.00	0.04
CoO							0.00	0.02	0.01	0.00	0.13	0.00	0.00
Total	99.93	97.67	96.27	98.91	98.11	97.11	97.82	97.83	96.90	97.87	97.67	97.80	97.51

Na	0.144	0.268	0.233	0.262	0.273	0.121	0.032	0.053	0.076	0.076	0.102	0.155	0.164
K	0.006	0.006	0.004	0.007	0.005	0.004	0.004	0.002	0.000	0.003	0.000	0.003	0.003
Ca	1.857	1.824	1.801	1.764	1.783	1.919	1.957	1.943	1.904	1.917	1.832	1.871	1.902
Al	0.179	0.477	0.439	0.461	0.502	0.187	0.045	0.062	0.101	0.106	0.147	0.225	0.250
Mn	0.001	0.000	0.006	0.018	0.000	0.004	0.021	0.002	0.014	0.009	0.015	0.011	0.014
Ti	0.008	0.016	0.013	0.015	0.012	0.002	0.001	0.005	0.005	0.002	0.010	0.009	0.011
Cr	0.023	0.023	0.031	0.009	0.015	0.000	0.000	0.005	0.003	0.001	0.000	0.004	0.023
Mg	4.684	4.625	4.641	4.599	4.598	4.708	4.641	4.737	4.687	4.710	4.825	4.670	4.670
Si	7.901	7.593	7.654	7.661	7.611	7.801	8.018	7.965	7.961	7.941	7.885	7.853	7.796
Fe^{3+}	0.000	0.009	0.000	0.000	0.000	0.083	0.000	0.000	0.000	0.000	0.000	0.000	0.000
Fe^{2+}	0.263	0.433	0.394	0.427	0.457	0.296	0.243	0.240	0.252	0.255	0.241	0.281	0.288
V							0.000	0.000	0.001	0.000	0.000	0.001	0.000
Ni							0.013	0.008	0.010	0.014	0.006	0.019	0.014
Zn							0.000	0.000	0.005	0.008	0.006	0.000	0.004
Co							0.000	0.002	0.001	0.000	0.014	0.000	0.000
Total	15.066	15.274	15.216	15.223	15.258	15.125	14.976	15.024	15.020	15.043	15.083	15.102	15.140

Sample number	SHB/19-12/79	SHB/19-12/79	SHB/19-12/79	SHB/19-12/79	SHB/19-12/79	SHB/19-12/79	SHB/19-12/82	SHB/19-12/82	SHB/19-12/82	SHB/19-12/82	SHB/19-12/82	SHB/19-12/82	SHB/19-12/82
Location	Kapili	Kapili	Kapili	Kapili	Kapili	Kapili	Kapili	Kapili	Kapili	Kapili	Kapili	Kapili	Kapili
EPMA point	47 / 1 .	48 / 1 .	49 / 1 .	52 / 1 .	53 / 1 .	55 / 1 .	83 / 1 .	85 / 1 .	96 / 1 .	97 / 1 .	98 / 1 .	113 / 1 .	114 / 1 .
Mineral	Tremolite	Tremolite	Tremolite	Tremolite	Tremolite	Tremolite	Tremolite	Tremolite	Tremolite	Tremolite	Tremolite	Tremolite	Tremolite
Na_2O	0.64	0.62	0.60	0.57	0.61	0.65	0.79	0.70	0.55	0.66	0.55	0.65	0.16
K_2O	0.02	0.01	0.00	0.04	0.03	0.02	0.02	0.02	0.01	0.01	0.03	0.04	0.02
CaO	12.77	13.41	12.84	13.00	12.50	12.75	12.48	12.71	12.34	12.24	12.43	12.14	13.03
Al_2O_3	1.71	1.53	1.56	1.39	1.42	1.58	2.03	1.61	1.40	1.59	1.15	1.64	0.26
MnO	0.07	0.03	0.27	0.17	0.12	0.12	0.10	0.08	0.00	0.11	0.13	0.08	0.16
TiO_2	0.10	0.09	0.11	0.07	0.12	0.11	0.15	0.07	0.10	0.11	0.05	0.09	0.05
Cr_2O_3	0.36	0.28	0.06	0.10	0.14	0.29	0.02	0.20	0.09	0.05	0.32	0.10	0.04
MgO	22.66	22.69	22.47	22.81	23.08	22.82	23.16	23.09	23.39	23.60	23.13	23.49	23.73
SiO_2	56.55	55.83	56.96	56.60	56.82	56.82	55.96	56.69	55.92	56.16	56.98	56.40	58.04
Fe_2O_3	0.00	1.15	0.00	0.00	0.00	0.00	0.05	0.00	0.67	0.81	0.00	0.02	0.51
FeO	2.51	1.52	2.66	2.36	2.39	2.30	2.82	2.53	1.97	1.98	2.61	2.62	1.74
V_2O_3	0.02	0.00	0.00	0.02	0.02	0.00	0.02	0.00	0.02	0.01	0.00	0.01	0.02

NiO	0.13	0.05	0.00	0.05	0.19	0.00	0.00	0.12	0.14	0.18	0.19	0.25	0.13
ZnO	0.05	0.35	0.04	0.05	0.00	0.00	0.00	0.00	0.02	0.09	0.00	0.00	0.01
CoO	0.08	0.10	0.00	0.00	0.05	0.00	0.02	0.04	0.00	0.02	0.00	0.05	0.07
Total	97.67	97.65	97.56	97.21	97.47	97.47	97.61	97.86	96.62	97.59	97.57	97.58	97.94
Na	0.171	0.166	0.159	0.153	0.161	0.173	0.210	0.187	0.148	0.177	0.148	0.174	0.042
K	0.004	0.002	0.001	0.007	0.004	0.004	0.003	0.003	0.001	0.001	0.005	0.007	0.003
Ca	1.883	1.983	1.892	1.923	1.842	1.878	1.841	1.868	1.834	1.804	1.831	1.789	1.905
Al	0.277	0.248	0.252	0.226	0.231	0.256	0.330	0.260	0.229	0.257	0.187	0.266	0.041
Mn	0.009	0.004	0.032	0.020	0.014	0.014	0.012	0.009	0.000	0.013	0.015	0.009	0.019
Ti	0.010	0.009	0.011	0.007	0.012	0.011	0.015	0.007	0.010	0.011	0.005	0.009	0.005
Cr	0.039	0.030	0.006	0.010	0.015	0.032	0.002	0.022	0.010	0.005	0.035	0.011	0.004
Mg	4.648	4.670	4.607	4.694	4.733	4.678	4.757	4.723	4.838	4.841	4.742	4.818	4.828
Si	7.780	7.708	7.835	7.814	7.816	7.812	7.708	7.779	7.760	7.727	7.835	7.759	7.923
Fe^{3+}	0.000	0.120	0.000	0.000	0.000	0.000	0.005	0.000	0.070	0.083	0.000	0.002	0.052
Fe^{2+}	0.289	0.176	0.306	0.272	0.275	0.264	0.325	0.291	0.229	0.228	0.300	0.302	0.198
V	0.002	0.000	0.000	0.002	0.002	0.000	0.002	0.000	0.002	0.001	0.000	0.001	0.002
Ni	0.014	0.006	0.000	0.006	0.021	0.000	0.000	0.013	0.016	0.019	0.021	0.027	0.014
Zn	0.005	0.036	0.004	0.005	0.000	0.000	0.000	0.000	0.002	0.009	0.000	0.000	0.001
Co	0.009	0.011	0.000	0.000	0.005	0.000	0.002	0.004	0.000	0.002	0.000	0.005	0.007
Total	15.139	15.168	15.105	15.140	15.131	15.122	15.213	15.168	15.149	15.178	15.125	15.181	15.044

Sample number	SHB/19-12/37	SHB/19-12/37	SHB/19-12/37	SHB/19-12/37	SHB/19-12/37	SHB/19-12/37	SHB/19-12/37	SHB/19-12/37	SHB/19-12/37	SHB/18/20	SHB/18/20	SHB/18/20	SHB/18/20
Location	Maharaj-gunj	Maharaj-gunj	Maharaj-gunj	Maharaj-gunj	Maharaj-gunj	Maharaj-gunj	Maharaj-gunj	Maharaj-gunj	Maharaj-gunj	Kapili	Kapili	Kapili	Kapili
EPMA point	198 / 1 .	215 / 1 .	222 / 1 .	223 / 1 .	224 / 1 .	225 / 1 .	226 / 1 .	227 / 1 .	230 / 1 .	10 / 1 .	12 / 1 .	28 / 1 .	29 / 1 .
Mineral	Tremo-lite	Tremo-lite	Tremo-lite	Tremo-lite	Tremo-lite	Tremo-lite	Tremo-lite	Tremo-lite	Tremo-lite	Serpen-tine	Serpen-tine	Serpen-tine	Serpen-tine
Na_2O	0.18	0.14	0.17	0.18	0.24	0.19	0.12	0.16	0.22	0.02	0.03	0.03	0.00
K_2O	0.01	0.02	0.01	0.00	0.01	0.01	0.01	0.00	0.03	0.01	0.03	0.01	0.00
CaO	13.16	13.06	13.10	13.03	12.92	13.23	13.05	13.00	13.12	0.06	0.06	0.12	0.03
Al_2O_3	1.50	1.21	1.55	1.48	1.46	1.44	1.20	1.25	1.25	0.90	0.69	1.09	0.22
MnO	0.00	0.09	0.08	0.00	0.10	0.14	0.10	0.06	0.18	0.12	0.17	0.14	0.19
TiO_2	0.06	0.03	0.09	0.04	0.03	0.06	0.08	0.05	0.07	0.01	0.01	0.00	0.00
Cr_2O_3	0.42	0.00	0.10	0.00	0.24	0.00	0.23	0.00	0.06	0.07	0.03	0.00	0.06

MgO	22.89	23.43	23.06	22.89	22.73	23.02	23.16	23.20	23.23	33.32	34.47	32.93	34.65
SiO_2	57.55	58.24	57.60	57.16	57.09	57.49	57.67	57.84	57.83	49.33	50.54	49.26	45.24
Fe_2O_3	0.00	0.00	0.00	0.00	0.00	0.00	0.00	0.00	0.00				
FeO	2.07	1.75	1.87	1.81	1.86	1.98	1.84	2.15	1.85	7.16	7.09	7.57	8.53
V_2O_3	0.00	0.01	0.01	0.01	0.01	0.01	0.00	0.00	0.00				
NiO	0.12	0.01	0.06	0.07	0.24	0.01	0.07	0.04	0.00				
ZnO	0.00	0.00	0.00	0.00	0.15	0.00	0.00	0.12	0.00				
CoO	0.01	0.00	0.00	0.03	0.00	0.05	0.00	0.00	0.00				
Total	97.97	97.98	97.70	96.70	97.07	97.63	97.52	97.87	97.84	90.98	93.09	91.15	88.92
Na	0.048	0.037	0.046	0.049	0.063	0.049	0.032	0.041	0.059	0.005	0.007	0.008	0.000
K	0.002	0.003	0.002	0.000	0.001	0.002	0.001	0.000	0.005	0.002	0.005	0.002	0.000
Ca	1.923	1.900	1.916	1.924	1.907	1.939	1.912	1.900	1.917	0.008	0.008	0.017	0.005
Al	0.242	0.193	0.249	0.241	0.237	0.232	0.193	0.202	0.200	0.150	0.112	0.181	0.037
Mn	0.000	0.010	0.009	0.000	0.011	0.016	0.012	0.007	0.021	0.014	0.019	0.017	0.024
Ti	0.007	0.003	0.009	0.004	0.003	0.006	0.008	0.005	0.007	0.001	0.001	0.000	0.000
Cr	0.045	0.000	0.010	0.000	0.026	0.000	0.025	0.000	0.007	0.007	0.003	0.000	0.007
Mg	4.655	4.747	4.694	4.704	4.667	4.694	4.723	4.717	4.722	6.996	7.068	6.916	7.579
Si	7.852	7.913	7.864	7.879	7.863	7.865	7.888	7.890	7.886	6.949	6.954	6.940	6.639
Fe^{3+}	0.000	0.000	0.000	0.000	0.000	0.000	0.000	0.000	0.000				
Fe^{2+}	0.236	0.198	0.213	0.208	0.214	0.227	0.210	0.245	0.211	0.843	0.816	0.892	1.046
V	0.000	0.001	0.001	0.001	0.001	0.001	0.000	0.000	0.000				
Ni	0.013	0.001	0.006	0.007	0.027	0.001	0.007	0.005	0.000				
Zn	0.000	0.000	0.000	0.000	0.015	0.000	0.000	0.012	0.000				
Co	0.001	0.000	0.000	0.003	0.000	0.006	0.000	0.000	0.000				
Total	15.024	15.007	15.021	15.021	15.034	15.038	15.011	15.025	15.035	14.975	14.994	14.974	15.338

Sample number	SHB/18/20	SHB/19-12/78	SHB/19-12/82	SHB/19-12/82	SHB/19-12/39	SHB/19-12/39	SHB/19-12/39	SHB/19-12/39	SHB/18/24	SHB/18/36	SHB/19-12/78	SHB/19-12/79	SHB/19-12/82
Location	Kapili	Kapili	Kapili	Kapili	Maharaj-gunj	Maharaj-gunj	Maharaj-gunj	Maharaj-gunj	Kapili	Kapili	Kapili	Kapili	Kapili
EPMA point	30 / 1 .	154 / 1 .	99 / 1 .	130 / 1 .	236 / 1 .	239 / 1 .	245 / 1 .	246 / 1 .	152 / 1 .	235 / 1 .	176 / 1 .	50 / 1 .	86 / 1 .
Mineral	Serpen-tine	Serpen-tine	Serpen-tine	Serpen-tine	Serpen-tine	Serpen-tine	Serpen-tine	Serpen-tine	Chlorite	Chlorite	Chlorite	Chlorite	Chlorite
Na_2O	0.02	0.01	0.02	0.03	0.01	0.00	0.00	0.01	0.00	0.01	0.04	0.03	0.03
K_2O	0.01	0.01	0.00	0.00	0.01	0.02	0.00	0.02	0.03	0.14	0.05	0.01	0.02

CaO	0.04	0.03	0.14	0.03	0.01	0.01	0.01	0.02	0.00	0.00	0.05	0.00	0.17
Al_2O_3	1.05	0.37	0.61	0.76	0.28	0.18	0.76	0.77	17.08	17.51	15.48	11.37	11.93
MnO	0.23	0.10	0.06	0.04	0.24	0.08	0.07	0.00	0.00	0.04	0.15	0.18	0.08
TiO_2	0.02	0.00	0.00	0.01	0.01	0.00	0.02	0.04	0.00	0.12	0.05	0.05	0.05
Cr_2O_3	0.00	0.02	0.00	0.10	0.00	0.08	0.44	0.00	0.74	0.98	0.62	0.21	0.35
MgO	33.16	38.40	39.80	40.19	37.12	37.76	36.67	38.04	33.28	31.67	31.74	34.07	34.97
SiO_2	48.97	45.82	44.39	45.17	44.05	45.23	43.34	43.05	32.79	31.46	32.14	35.59	36.11
Fe_2O_3													
FeO	7.56	2.98	3.18	2.42	5.29	4.26	5.39	5.99	2.97	4.04	3.68	3.40	3.14
V_2O_3		0.01	0.00	0.01	0.01	0.01	0.01	0.00	0.00	0.02	0.02	0.02	0.02
NiO		0.06	0.02	0.12	0.00	0.00	0.00	0.00	0.13	0.00	0.00	0.00	0.05
ZnO		0.05	0.20	0.08	0.17	0.15	0.19	0.33	0.12	0.09	0.30	0.12	0.18
CoO		0.04	0.00	0.00	0.00	0.00	0.01	0.00	0.02	0.02	0.01	0.04	0.01
Total	91.05	87.89	88.42	88.95	87.20	87.77	86.90	88.25	87.15	86.11	84.33	85.09	87.10
Na	0.005	0.002	0.006	0.008	0.004	0.001	0.000	0.002	0.000	0.001	0.012	0.007	0.009
K	0.001	0.003	0.000	0.000	0.003	0.003	0.000	0.003	0.005	0.027	0.011	0.003	0.003
Ca	0.007	0.005	0.022	0.004	0.002	0.001	0.001	0.003	0.003	0.004	0.002	0.007	0.002
Al	0.174	0.063	0.104	0.127	0.048	0.030	0.133	0.133	2.973	2.943	2.801	2.026	2.077
Mn	0.027	0.012	0.007	0.005	0.030	0.010	0.009	0.000	0.000	0.006	0.019	0.022	0.010
Ti	0.002	0.000	0.000	0.001	0.001	0.000	0.002	0.004	0.000	0.014	0.006	0.006	0.006
Cr	0.000	0.003	0.000	0.011	0.000	0.009	0.052	0.000	0.087	0.237	0.075	0.025	0.041
Mg	6.977	8.267	8.572	8.558	8.183	8.203	8.125	8.341	7.324	7.138	7.259	7.674	7.696
Si	6.914	6.619	6.416	6.454	6.516	6.593	6.444	6.335	4.843	4.758	4.933	5.378	5.332
Fe^{3+}													
Fe^{2+}	0.893	0.360	0.384	0.289	0.654	0.520	0.670	0.738	0.367	0.511	0.472	0.430	0.388
V		0.000	0.000	0.001	0.001	0.000	0.000	0.000	0.000	0.001	0.001	0.001	0.001
Ni		0.006	0.002	0.013	0.000	0.000	0.000	0.000	0.014	0.000	0.000	0.000	0.005
Zn		0.006	0.023	0.009	0.020	0.017	0.023	0.038	0.014	0.011	0.037	0.015	0.021
Co		0.004	0.000	0.000	0.000	0.000	0.001	0.000	0.000	0.000	0.006	0.000	0.020
Total	15.000	15.350	15.536	15.479	15.461	15.389	15.461	15.597	15.630	15.651	15.634	15.595	15.610

Sample number	SHB/19-12/24	SHB/19-12/24	SHB/19-12/24	SHB/19-12/35	MIC/16/39	MIC/16/39	SHB/19-12/24	SHB/19-12/24
Location	Chuka Pahar	Chuka Pahar	Chuka Pahar	Maharaj-gunj	Tua Dungri	Tua Dungri	Chuka Pahar	Chuka Pahar
EPMA	72 / 1 .	73 / 1 .	82 / 1 .	140 / 1 .	17 / 1 .	20 / 1 .	71 / 1 .	81 / 1 .

point								
Mineral	Chlorite	Chlorite	Chlorite	Chlorite	Carbo-nate	Carbo-nate	Carbo-nate	Carbo-nate
Na_2O	0.00	0.06	0.06	0.00	0.00	0.02	0.02	0.02
K_2O	0.11	0.01	0.04	0.03	0.00	0.00	0.00	0.00
CaO	0.04	0.00	0.00	0.03	33.31	33.42	55.20	55.35
Al_2O_3	17.73	12.04	17.09	17.67	0.05	0.02	0.26	0.18
MnO	0.05	0.00	0.02	0.01	0.54	0.41	0.07	0.01
TiO_2	0.03	0.01	0.03	0.00	0.00	0.00	0.01	0.01
Cr_2O_3	0.65	0.69	0.62	0.57	0.05	0.06	0.00	0.03
MgO	33.08	35.68	33.19	32.96	21.46	22.01	3.52	3.30
SiO_2	31.66	35.73	31.05	32.11	0.26	0.00	3.25	3.39
Fe_2O_3								
FeO	2.49	2.59	2.49	2.87	1.69	1.69	0.40	0.40
V_2O_3	0.01	0.02	0.01	0.02	0.00	0.00	0.00	0.02
NiO	0.03	0.00	0.18	0.00	0.00	0.00	0.09	0.00
ZnO	0.13	0.21	0.29	0.10	0.00	0.02	0.00	0.00
CoO	0.04	0.07	0.02	0.00	0.07	0.00	0.00	0.05
Total	86.05	87.10	87.06	86.37	57.42	57.65	62.82	62.77
Na	0.000	0.017	0.016	0.001	0.001	0.011	0.012	0.011
K	0.021	0.002	0.007	0.005	0.000	0.000	0.001	0.000
Ca	0.006	0.011	0.002	0.000	11.174	11.173	18.111	18.173
Al	3.124	2.092	3.169	3.100	0.017	0.007	0.095	0.066
Mn	0.007	0.000	0.002	0.001	0.143	0.108	0.017	0.004
Ti	0.003	0.001	0.003	0.000	0.000	0.000	0.001	0.002
Cr	0.077	0.080	0.191	0.067	0.013	0.016	0.000	0.008
Mg	7.368	7.839	7.348	7.312	10.013	10.235	1.605	1.509
Si	4.732	5.268	4.614	4.779	0.083	0.000	0.996	1.037
Fe^{3+}								
Fe^{2+}	0.311	0.320	0.309	0.358	0.442	0.440	0.102	0.103
V	0.001	0.001	0.001	0.001	0.000	0.000	0.000	0.002
Ni	0.004	0.000	0.019	0.000	0.000	0.000	0.021	0.000
Zn	0.015	0.024	0.035	0.012	0.000	0.005	0.000	0.000
Co	0.005	0.000	0.000	0.004	0.018	0.000	0.000	0.013
Total	15.674	15.655	15.715	15.639	21.903	21.994	20.962	20.928

2.85 wt.%, CaO = 12.69 - 13.61 wt.%; $Wo_{27-29}En_{66-70}Fs_{3-5}$) in the Kapili and Maharajgunj komatiitic rocks (**Fig. 5a**).

5.1.2. Oxides

Compositions for different types of chromite grains are given in **Table 4**. Type-I chromite grains from the northern part of the greenstone belt have relatively higher MgO (2 - 3.75 wt.%), Cr_2O_3 (44.45 - 46.84 wt.%), Al_2O_3 (17.23 - 18.38 wt.%), and lower Fe_2O_3 (0.84 - 4.04 wt.%) in cores than in the outer ferritchromit (Cr_2O_3 = 26.89 - 42.54 wt.%, MgO = upto 0.68 wt.%, Fe_2O_3 = 26.89 - 42.54 wt.%, and Al_2O_3 = 0.15 - 9.95 wt.%) and chrome magnetite rims (Cr_2O_3 = 5.03 - 24.20 wt.%, MgO = 0.04 - 0.52 wt.%, Fe_2O_3 = 41.80 - 62.28 wt.%, and Al_2O_3 = 0.03 - 0.71 wt.%) (**Figs. 3g, 6a**). The non-porous cores of type-II chromites from the southern part of the greenstone belt also have relatively higher Cr_2O_3 (45.59 - 56.79 wt.%) with MgO = 1.25 - 3.13 wt.%, Fe_2O_3 = 5.54 - 14.94 wt.%, and Al_2O_3 = 2.8 - 5.16 wt.% than the porous ferritchromit (Cr_2O_3 = 16.92 - 27.03 wt.%, MgO = 0.51 - 1.55 wt.%, Fe_2O_3 = 32.26 - 44.71 wt.%, and Al_2O_3 = 0.88 - 1.72 wt.%) and chrome magnetite (Cr_2O_3 = 4.69 - 13.26 wt.%, MgO = 0.15 - 1.05 wt.%, Fe_2O_3 = 50.15 - 63.03 wt.%, and Al_2O_3 = 0.03 - 0.71 wt.%) (**Figs. 3h, 6b**) rims. In both cases, the higher (Cr /(Cr+Al) ratio in the rims reflects the extremely low Al_2O_3 contents of these zones rather than a high abundance of Cr_2O_3. The central zone of type-III chromite grains from the southernmost greenstone belt is surrounded by rims of various reflectances and porosity (**Fig. 3j**). These central zones have similar concentrations of Al_2O_3 (3.55 - 9.14 wt.%), Cr_2O_3 (41.19 - 58.06 wt.%), MgO (0.84 - 6.24 wt.%), and Fe_2O_3 (6.20 - 10.82 wt.%) to those of type-II grains (**Fig. 6c, Table 4, Appendix 1**). In contrast, the inner rims of variable reflectances show

lower concentrations of Fe_2O_3 (2.1 - 14.88 wt. %) and higher concentrations of Al_2O_3 (12.65 - 21.15 wt. %) than the inner rims of the type-I and type-II grains with Cr_2O_3 = 16.92 - 28.96 wt.% and MgO = up to 1.55 wt.% (**Fig. 6a-c**). The porous outer chrome magnetite envelope of type-III grains (Cr_2O_3 = 2.83 - 22.73 wt.%, MgO = 0.13 - 0.18 wt.%, Fe_2O_3 = 41.63 - 62.62 wt.%, and Al_2O_3 = 0.01 - 1.09 wt.%) are compositionally similar to the chrome magnetite rims of type-I and type-II varieties (**Fig. 6a-c**). These pores in the type-II and type-III grains are filled with chrome chlorite (Cr_2O_3 = 1 wt.%). The FeO concentrations are similar in cores (FeO = 22.91 - 30.65 wt. %) and rims (FeO = 27.90 - 34.26 wt.%) of all three types of zoned chromite grains (**Fig. 6a-c**). Type-IV ferritchromit grains have Cr_2O_3 = 34.20 - 42.10 wt.% and Fe_2O_3 = 17.61 - 28.47 wt.% and their abundances are similar to ferritchromit rims of type-I grains, whereas, the Al_2O_3 (1.74-2.56 wt.%) and FeO (27.68 - 29.02 wt.%) concentrations resemble those of ferritchromit rims of the type-II grains (**Table 4, Appendix 1**). The type-V chrome magnetite and magnetite grains have similar FeO (27.06 - 34.03 wt.%) and Fe_2O_3 (42.79 - 66.14 wt.%) contents to those of the chrome magnetite rims of all other types of grains with variable MgO (0.02 - 5.68 wt.%), Al_2O_3 (up to 1.61 wt.%) and Cr_2O_3 (0.92 - 19.57 wt.%) concentrations (**Table 4, Appendix 1**).

In terms of minor elements, the cores of type-I chromite grains have higher MnO (0.78 - 1.74 wt.%) and ZnO (1.63 - 2.11 wt.%) than the rims (MnO = 0.13 - 1.68 wt.% and ZnO = up to 0.88 wt.%) (**Fig. 6a**). Type-II chromites also have higher MnO (0.54 - 3.85 wt.%), ZnO (1 - 2.41 wt.%), and lower TiO_2 (0.32 - 1.51 wt.%) in their cores than in their rims (MnO = 0.19 - 2.50 wt.%, ZnO = up to 1.45 wt.%, TiO_2 = 0.13 - 2.79 wt.%) (**Fig. 6b**). Type-III chromites have relatively higher concentrations of V_2O_3 (1.23 - 1.79 wt.%), ZnO (1.64 - 5.48 wt.%), MnO (2.90 - 3.99 wt.%), and TiO_2 (4.50 -

7.46 wt.%) in inner rims than in outer porous chrome magnetite rims or chromite cores (V_2O_3 = 0.03 - 0.67 wt.%, ZnO = upto 3.03 wt.%, MnO = 0.31 - 4.40 wt.%, and TiO_2 = 0.11 - 2.50 wt.%) (**Fig. 6c**). Type-IV finer ferritchromit grains have similar TiO_2 concentrations (0.63 - 1.75 wt.%) but higher MnO (2.84 - 3.48 wt.%) and ZnO (1.29 - 1.61 wt.%) than the ferritchromit rims of type-I and type-II grains (**Table 4; Appendix 1**). Type-V chrome magnetite grains have low concentrations of ZnO (up to 0.62 wt.%) with variable TiO_2 (up to 7.67 wt.%) and MnO (up to 2.8 wt.%) content.

The cores of type-I chromites are clustered in two different places in the [Mg/(Mg + Fe^{2+})] vs. [Cr/(Cr+Al)] ratio plot, with the larger cores having relatively higher Mg/(Mg + Fe^{2+}) ratio (0.10 - 0.20) and lower Cr/(Cr+Al) ratio (0.62 - 0.64) than the smaller cores [Mg/(Mg + Fe^{2+}) = upto 0.02, Cr/(Cr+Al) = 0.97 - 0.99] (**Fig. 7a, b**). This dichotomy is also evident in the Mg/(Mg + Fe^{2+}) vs. Fe^{3+}/R^{+3} (R^{3+} = Fe^{3+}+Cr+Al) ratio plot, where the smaller type-I cores show much greater Fe^{3+} enrichment than the larger ones (**Fig. 7c**). In the same figure, the composition of chrome magnetite rims for all types of chromites and the independent type-V grains occupy the metamorphogenic chrome magnetite field of Barnes and Roeder (2001) (**Fig. 7c**). The cores of type-II grains have Mg/(Mg + Fe^{2+}) = 0.08 - 0.17 and Cr/(Cr+Al) = 0.88 - 0.91 whereas the type-III chromite cores have nearly constant Cr/(Cr+Al) ratio (0.88 - 0.91) except one data point [Cr/(Cr+Al) = 0.75] with a variable Mg/(Mg + Fe^{2+}) ratio (0.09 - 0.33) (**Fig. 7a**). Outer envelopes of type-I and type-II grains show a large variation of Cr/(Cr+Al) (0.74 - 1.00) with lower Mg/(Mg + Fe^{2+}) ratios (up to 0.08) (**Fig. 7b**). In type-III grains the inner rims have Mg/(Mg + Fe^{2+}) = 0.04 - 0.13 and Cr/(Cr+Al) = 0.45 - 0.56 (**Fig. 7b**), while the outermost chrome magnetite rims have extremely high Cr/(Cr+Al) (0.93 - 1.00) with lower Mg/(Mg + Fe^{2+}) ratios (up to 0.01). The cores of

large type-I grains have the lowest Fe^{3+}/R^{3+} ratios (0.01 - 0.05) of all types of chromite cores. The outer rims of type-I and type-II grains, and type-III chrome magnetite rims have highly variable Fe^{3+}/R^{3+} ratios (0.15 - 0.95) coupled with restricted $Mg/(Mg + Fe^{2+})$ ratio (up to 0.08) (**Fig. 7c**). The ferritchromit of type-IV grains have similar Fe^{3+}/R^{3+} ratios to the ferritchromit rims of type-I and type-II grains. Type-V chrome magnetites from all areas display a large variety of Cr/(Cr+Al) (0.69 - 1.00) and Fe^{3+}/R^{3+} ratios (0.67 - 0.98) coupled with low $Mg/(Mg + Fe^{2+})$ ratio spanning a limited range (**Fig. 7a-c**).

MnO, TiO_2, and NiO concentrations of type-I and type-II cores show restricted variation when plotted against $Mg/(Mg + Fe^{2+})$ ratio whereas type-III cores along with all the ferritchromit and chrome magnetite rims show strong variation (**Fig. 7d-f**). This is also true for type-IV ferritchromit and type-V chrome magnetite grains. In the MnO vs. Fe^{3+}/R^{3+} plot, almost all chromite rims, as well as type-IV and V grains, show two distinct, well-defined negative correlations (**Fig. 7e**). However, the chromite cores have variable concentrations of MnO with little change in Fe^{3+}/R^{3+}. The TiO_2 concentrations in type-I, type-II rims, type-III outer rims, and most type-IV and V grains show restricted variation when plotted against Fe^{3+}/R^{+3} (**Fig. 7d**). The most striking thing about this diagram is that there are two well-defined trends, one defined by type-II rims and the other by type-I and type-III rims. Type-V chrome magnetites can fall along either trend, but not in between. In the NiO vs. Fe^{3+}/R^{+3} plot, a broadly positive trend is observed. (**Fig. 7f**).

In a Fe^{3+}-Cr-Al ternary diagram, larger cores of type-I chromites with relatively higher Al plot close to the Cr-Al join and inside the greenschist facies field of Barnes and Roeder (2001) (**Fig. 7g**). In contrast, type-II and type-III chromite cores

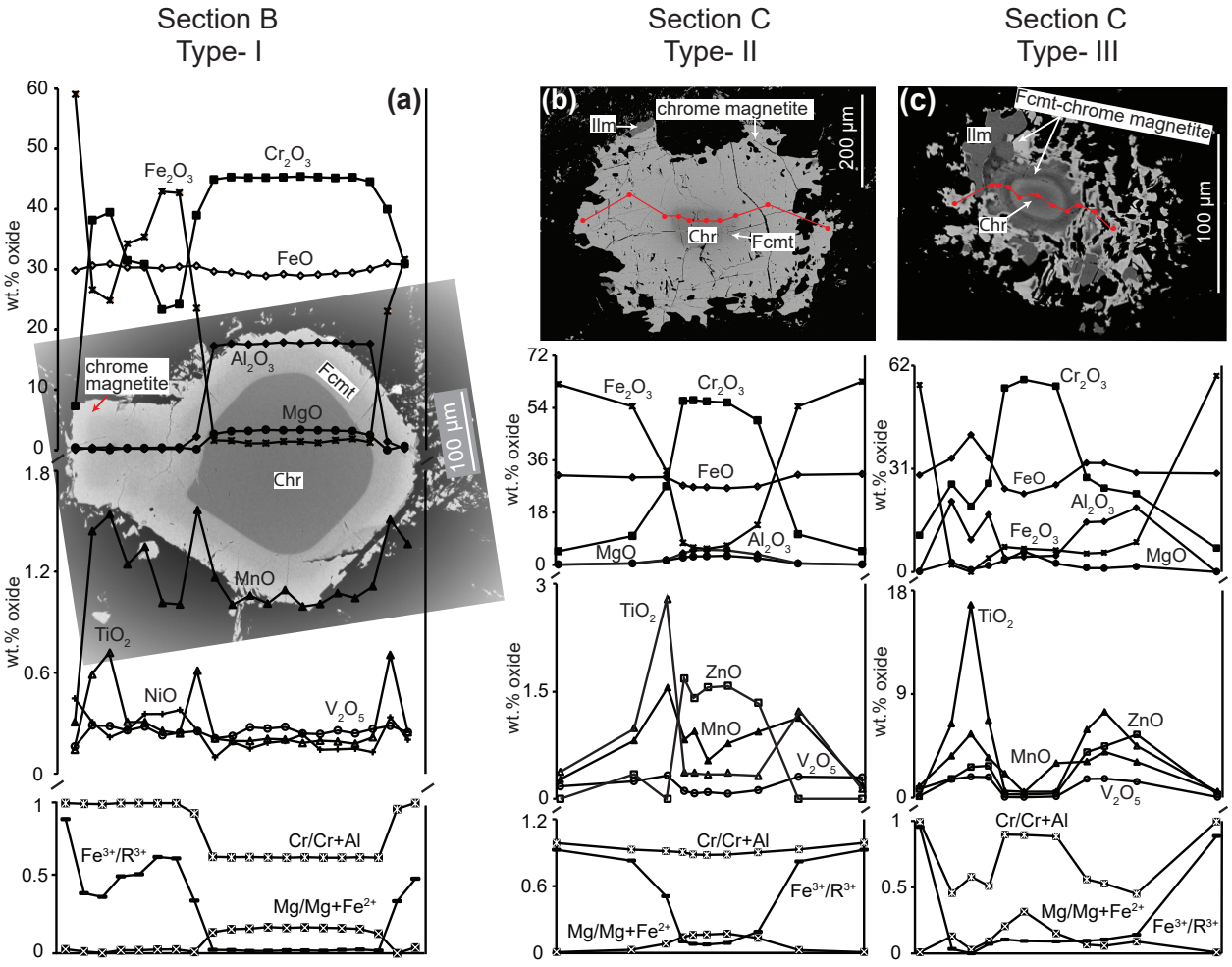

Fig. 6 Quantitative microprobe profiles of major and minor element oxides along with $Mg/Mg+Fe^{2+}$, Cr/Cr+Al, and Fe^{3+}/R^{3+} across the **a** Type-I (sample: MIC/16/39); **b** Type-II (sample: SHB/18/24); and **c** Type-III (sample: SHB/18/36) zoned chromite grains showing variation from chromite cores to ferritchromit and chrome magnetite rims. Mineral names abbreviations are from Whitney and Evans (2010).

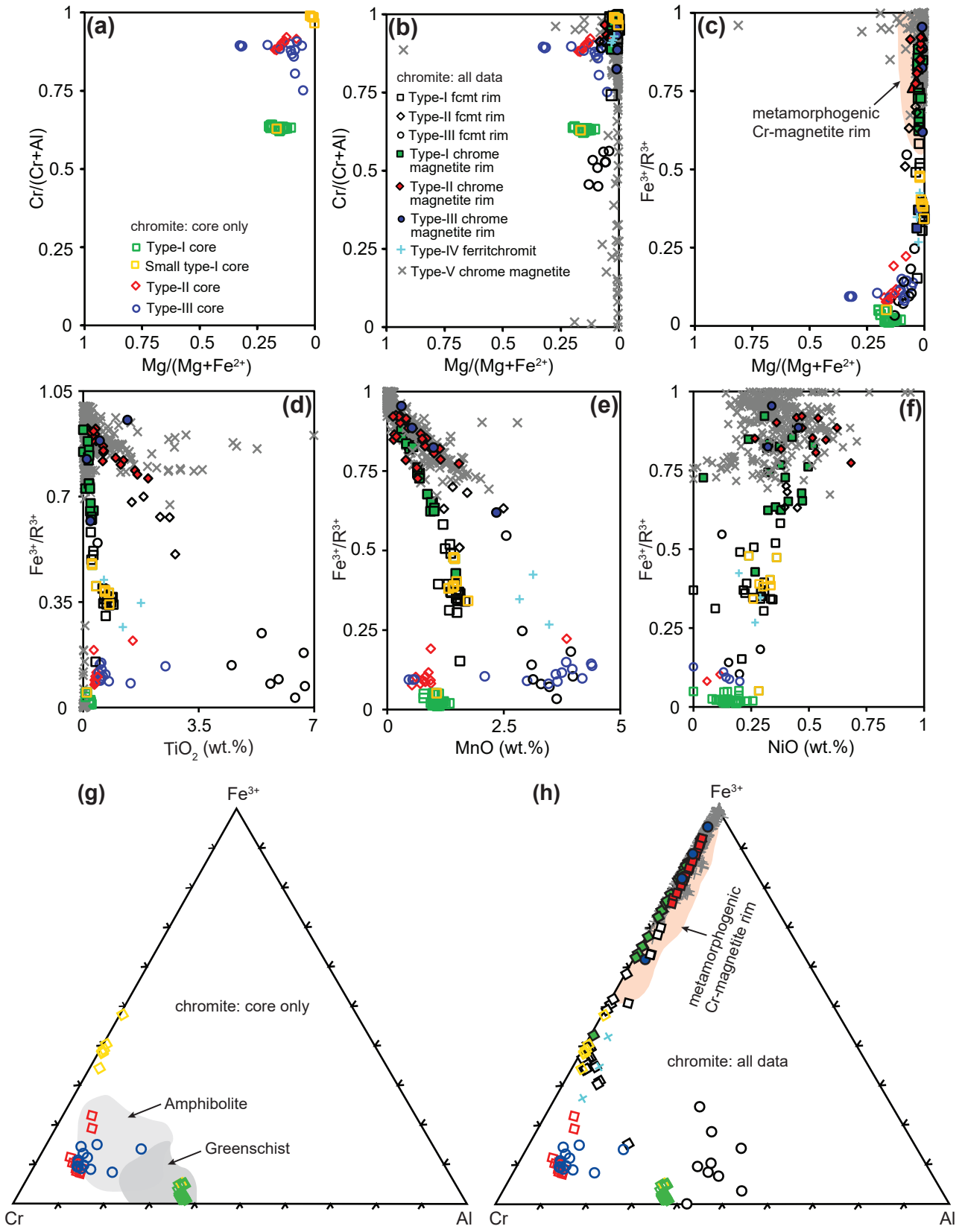

Fig. 7 Compositions of chromites from the Gorumahishani komatiitic rocks: **a, b** Mg/Mg+Fe^{2+} vs. Cr/Cr+Al and **c** Mg/Mg+Fe^{2+} vs. Fe^{3+}/(Fe^{3+} + Cr + Al) variations of the type-I, II, III, IV, and V Cr-spinels; **d, f** Variations of Fe^{3+}/(Fe^{3+} + Cr + Al) plotted against TiO_2, MnO, and NiO from all types of Cr-spinels; **g, h** Fe^{3+}, Cr, and Al variation of the type-I, II, III chromite cores, and rims along with the type-IV and type-V grains. Shaded areas are from Barnes and Roeder (2001).

Table 4 EPMA major and minor elements compositional range (wt.%) of komatiitic chromites from the Gorumahishani greenstone belt

Location	TD	TD	KL	KL	TD	KL	KL	TD	KL	KL	MG	All
Mineral	Chr	Chr	Chr	Chr	Fcmt	Fcmt	Al rich Cr-Spl	Chr mag	Chr mag	Chr mag	Fcmt	Chr mag
Type	T-I Core	S T-I core	T-II core	T-III core	T-I R1	T- II R1	T-III R1	T-I R2	T-II R2	T-III R2	T-IV	Type-V
Data (n)	36	8	11	13	22	5	8	25	16	5	3	21
Al_2O_3	17.23-18.38	0.23-0.96	2.8-5.16	3.55-9.14	0.15-9.95	0.88-1.72	12.65-21.15	0-0.19	0.03-0.71	0.01-1.09	1.74-2.56	0-1.61
MnO	0.78-1.25	1.41-1.74	0.54-3.85	0.47-4.4	1.1-1.68	1.41-2.50	2.90-3.99	0.13-1.02	0.19-1.54	0.31-2.35	2.84-3.48	0-2.8
TiO2	0.08-0.25	0.26-0.79	0.32-1.51	0.47-2.5	0.23-0.92	1.47-2.79	4.50-7.46	0-0.31	0.13-1.65	0.11-1.34	0.63-1.75	0-7.67
Cr_2O_3	44.45-46.84	33.04-44.62	45.59-56.79	41.19-58.06	26.89-42.54	16.92-27.03	23.47-28.96	5.03-24.20	4.69-13.26	2.83-22.73	34.2-42.1	0.92-19.57
MgO	2-3.75	0.04-0.35	1.25-3.13	0.84-6.24	0-0.68	0.51-1.55	0.81-2.86	0.04-0.52	0.15-1.05	0.13-0.18	0.32-0.54	0.02-5.68
SiO_2	0.09-0.30	0.23-0.27	0.08-0.17	0.05-0.15	0.08-1.46	0-0.04	0.03-0.12	0-0.47	0-0.77	0.07-0.12	0 .03-0.12	0-4.45
Fe_2O_3	0.84-4.04	22.96-32.24	5.54-14.94	6.2-10.82	26.89-42.54	32.26-44.71	2.1-14.88	41.8-62.28	50.15-63.03	41.63-62.62	17.61-28.47	42.79-66.14
FeO	26.42-30.65	29.80-30.94	25.51-27.62	22.91-27.91	29.25-31.29	28.33-30.33	29.8-34.26	29.17-30.55	28.76-31.25	27.9-31.57	27.68-29.02	27.06-34.03
V_2O_3	0.12-0.29	0.24-0.30	0.05-0.16	0.03-0.67	0.08-0.3	0.33-0.37	1.23-1.79	0.05-0.28	0.17-0.33	0.05-0.24	0.55-0.92	0-0.54
NiO	0-0.28	0.24-0.34	0.06-0.12	0-0.16	0-0.38	0.4-0.45	0.15-0.29	0.04-0.52	0.27-0.68	0.32-0.46	0.2-0.29	0-0.71
ZnO	1.63-2.11	0	1-2.41	0.28-3.03	0.52-0.88	0-1.45	1.64-5.48	0-0.38	0-0.63	0-1.16	1.29-1.61	0-0.62
CoO	0.02-0.23	0	0	0.02-0.23	0-0.16	0.12-0.27	0-0.32	0-0.14	0-0.16	0-0.07	0-0.11	0-0.31
Cation												
Al	5.387-5.867	0.084-0.343	0.989-1.747	1.231-3.108	0.055-3.408	0.323-0.618	4.260-6.617	0-0.067	0.010-0.223	0.005-0.397	0.623-0.908	0-0.589
Mn	0.175-0.311	0.365-0.446	0.130-0.976	0.110-1.092	0.280-0.431	0.313-0.654	0.702-0.952	0.034-0.263	0.049-0.400	0.080-0.616	0.736-0.885	0-0.750
Ti	0.017-0.061	0.022-0.181	0.070-0.339	0.107-0.541	0.053-0.208	0.347-0.637	0.936-1.581	0-0.072	0.031-0.379	0.025-0.311	0.143-0.402	0-1.825
Cr	9.456-9.651	8.026-9.735	10.783-12.882	9.396-12.718	6.456-9.780	4.146-6.499	5.138-6.350	1.249-5.786	1.153-3.214	0.689-5.575	8.193-10.004	0.231-4.829
Mg	0.820-1.484	0.019-1.159	0.559-1.333	0.360-2.575	0.002-0.310	0.233-0.701	0.343-1.132	0.020-0.236	0.068-0.494	0.059-0.082	0.145-0.248	0.009-2.517
Si	0.026-0.081	0.071-0.084	0.019-0.050	0.015-0.042	0.024-0.447	0-0.013	0.008-0.020	0-0.148	0-0.242	0.022-0.036	0.008-0.038	0-1.323
Fe^{3+}	5.238-7.452	0.764-7.452	1.198-3.364	1.361-2.343	2.366-9.067	7.385-10.431	0.420-3.198	9.683-14.713	11.575-14.584	9.719-14.530	3.983-6.493	9.803-15.624
Fe^{2+}	7.655-7.843	5.978-7.935	6.296-6.763	5.304-6.735	7.341-7.923	7.329-7.763	6.901-7.870	7.616-7.970	7.486-8.034	7.238-8.142	7.014-7.420	6.722-9.045
V	0.021-0.053	0.049-0.060	0.010-0.031	0.005-0.127	0.015-0.059	0.066-0.075	0.232-0.324	0.010-0.057	0.036-0.067	0.011-0.049	0.111-0.182	0-0.112
Ni	0-0.061	0.059-0.083	0.013-0.027	0-0.037	0-0.092	0.099-0.110	0.034-0.066	0.011-0.130	0.067-0.169	0.080-0.115	0.048-0.071	0-0.180
Zn	0.320-0.414	0	0.217-0.531	0.027-0.645	0.116-0.196	0-0.330	0.322-1.121	0-0.086	0-0.142	0-0.265	0.290-0.360	0-0.143
Co	0.004-0.050	0	0-0.043	0.004-0.050	0-0.038	0.028-0.067	0-0.072	0-0.034	0-0.037	0-0.018	0-0.026	0-0.079
Mg#	0.10-0.20	0-0.02	0.08-0.17	0.09-0.33	0-0.04	0.03-0.08	0.04-0.13	0-0.03	0.01-0.06	0.01	0.02-0.03	0-0.27
Cr#	0.62-0.64	0.97-0.99	0.88-0.91	0.75-0.91	0.74-0.99	0.91-0.93	0.45-0.56	0.99-1	0.92-0.99	0.93-1.00	0.91-0.93	0.69-1
Fe^{3+}/R^{3+}	0.01-0.05	0.34-0.48	0.08-0.22	0.09-0.15	0.15-0.58	0.51-0.7	0.03-0.25	0.62-0.92	0.77-0.93	0.62-0.95	0.27-0.42	0.67-0.98

TD: Tua Dungri, KL: Kapili, MG: Maharajgunj, All: All locations i.e., Maharajgunj, Chuka Pahar, Tua Dungri, and Kapili; Chr: Chromite, Fcmt: Ferritchromit, Chr mag: Chrome magnetite, Cr-Spl: Chrome spinel; T-I, II, III, IV, V: Type-I, II, III, IV, V; S T-I: Small type-I; R1: Inner rim, R2: Outer rim.

plot close to the Cr apex and amphibolite facies field of Barnes and Roeder (2001) (**Fig. 7g**). The type-IV, type-V grains and almost all ferritchromit to chrome magnetite rims show a variation along the Cr-Fe^{3+} join (**Fig. 7h**) and occupy the field of metamorphogenic ferritchromit-magnetites of Barnes and Roeder (2001). Only a few type-I ferritchromit rims and all type-III inner rims plot closer to the Cr-Al join.

5.1.3. Sulfides

Sulfide minerals are found disseminated in the spinifex zone and often in the cumulate zone of the komatiitic sequence (**Fig. 3m-o**). The modal abundance of sulfide is <1 % in the komatiitic meta-dunite and meta-peridotite samples. Sulfide minerals are analyzed by SEM-EDX (**Table 5**). The Cu-Fe bearing sulfides are plotted in the Cu-Fe-S diagram of Craig and Scott (1974) (**Fig. 8a**) and are chalcopyrite and bornite in composition. Bornite forms thin rims surrounding the chalcopyrite mineral grains (**Fig. 3n**). The Ni+Co-Fe bearing sulfides are plotted in the Ni+Co-Fe-S plot of Kullerud (1969) and these are pentlandite, cobaltian violarite, and millerite in composition (**Fig. 8b**). Pentlandite is present at the central part and is irregularly replaced by millerite with diffused contact between them (**Fig. 3o**). Along the boundary of this sulfide mineral assemblage, magnetite grains are presently sharing sharp grain contact (**Fig. 3m-o**). The chalcopyrite-bornite mineral assemblage is present at the contact of two or more chrome magnetite grains from the komatiitic meta-dunite and meta-peridotite rocks. The pentlandite, Co-violarite, and millerite mineral assemblage are disseminated in the interstitial spaces between the serpentine pseudomorphs (after olivine) forming adcumulate or mesocumulate texture in the komatiitic meta-dunite and meta-peridotite rocks.

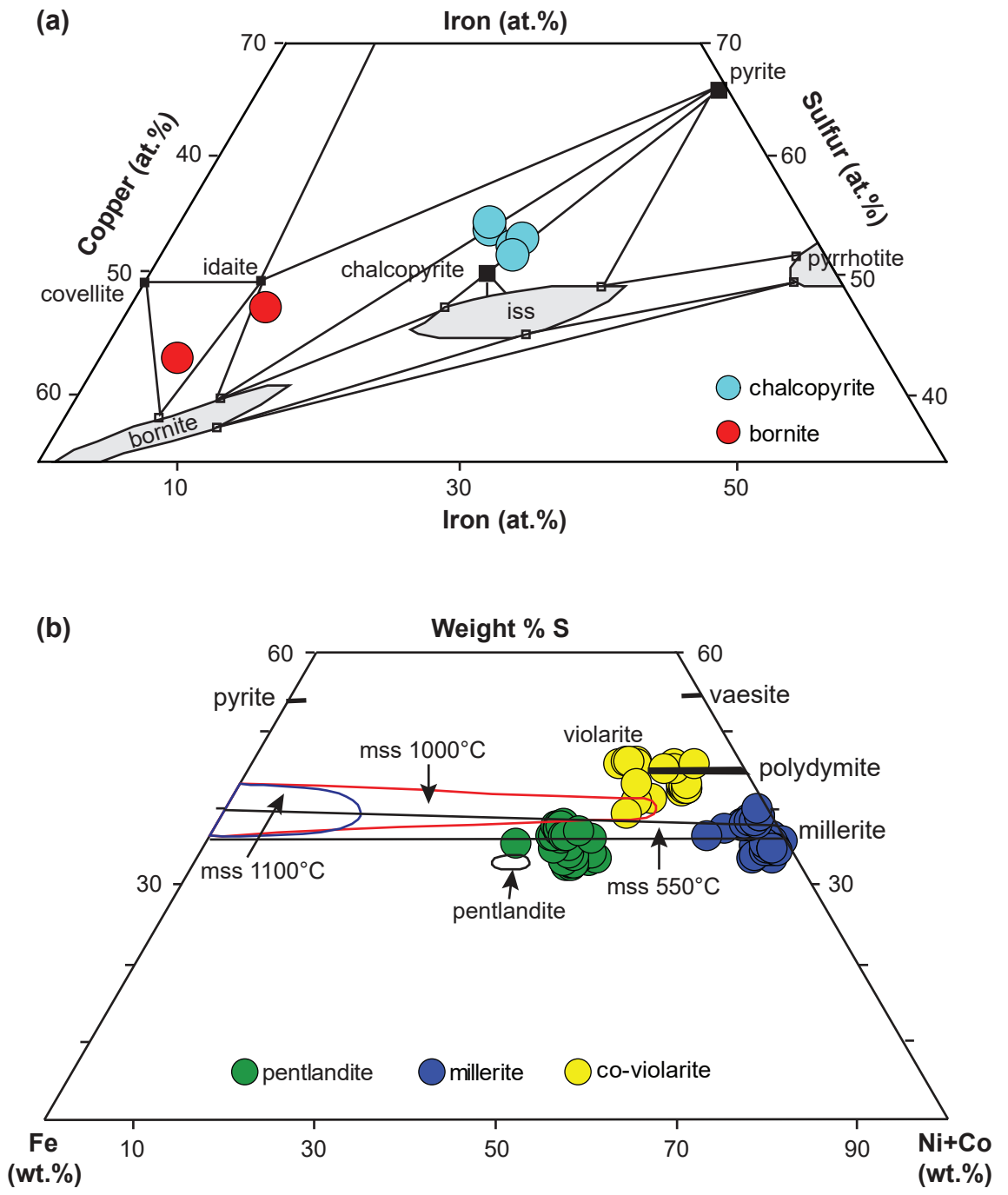

Fig. 8 Phase relationship of sulfide minerals from the Gorumahishani komatiitic rocks: **a** Cu-Fe-S ternary plot (after Craig and Scott 1974) showing the compositional field of pyrite, pyrrhotite, chalcopyrite, covellite, idaite, and bornite; iss = intermediate solid solution **b** Fe-Ni+Co-S ternary system after Kullerud et al. (1969), showing the compositional field of pyrite, pentlandite, millerite, polydymite, violarite, and vaesite; mss = monosulfide solid solution.

Table 5 EDX major and minor elements composition (wt.%) of sulfide minerals from the Gorumahishani greenstone belt

Sample Number	MIC/16/39	MIC/16/33	MIC/16/35	MIC/16/35	MIC/16/35	MIC/16/35	MIC/16/35	MIC/16/35	MIC/16/35	MIC/16/35	MIC/16/35	MIC/16/36	MIC/16/36	MIC/16/36
Mineral	Chalco-pyrite[a]	Pent-landite[a]	Pent-landite[a]	Pent-landite[a]	Pent-landite[a]	Pent-landite[a]	Pent-landite[a]	Pent-landite[a]	Pent-landite[a]	Pent-landite[a]	Pent-landite[a]	Pent-landite[a]	Pent-landite[a]	Pent-landite[a]
Data Pt.	8 / 1 .	11 / 1 .	13 / 1 .	14 / 1 .	15 / 1 .	16 / 1 .	18 / 1 .	19 / 1 .	20 / 1 .	21 / 1 .	23 / 1 .	25 / 1 .	26 / 1 .	33 / 1 .
S	36.39	32.55	33.05	31.99	32.37	32.53	32.26	32.50	32.68	31.90	32.15	32.36	33.62	32.64
Fe	10.03	22.54	23.39	25.42	24.98	24.73	21.26	25.04	25.01	24.21	24.48	23.01	22.00	24.43
Co	0.30	1.88	0.64	0.72	1.30	0.63	0.82	1.05	1.07	1.02	0.94	0.98	0.92	1.09
Ni	25.38	40.97	39.04	39.78	39.96	40.11	41.62	40.24	40.16	39.58	40.24	39.87	41.72	40.59
Cu	28.15	0.13	0.00	0.00	0.04	0.07	0.02	0.02	0.04	0.09	0.00	0.01	0.18	0.03
As	0.06	0.10	0.05	0.03	0.00	0.03	0.04	0.06	0.02	0.09	0.08	0.00	0.08	0.03
Total	100.30	98.16	96.17	97.94	98.65	98.10	96.02	98.92	98.98	96.88	97.89	96.24	98.53	98.80

Sample Number	MIC/16/36	MIC/16/36	MIC/16/36	MIC/16/36	MIC/16/35	MIC/16/36	MIC/16/39	MIC/16/39	MIC/16/39	MIC/16/39	MIC/16/39	MIC/16/39	MIC/16/39	MIC/16/39
Mineral	Pent-landite[a]	Pent-landite[a]	Pent-landite[a]	Pent-landite[a]	Co-vio-larite[a]	Co-vio-larite[a]	Co-vio-larite[a]	Co-vio-larite[a]	Co-vio-larite[a]	Co-vio-larite[a]	Co-vio-larite[a]	Co-vio-larite[a]	Co-vio-larite[a]	Co-vio-larite[a]
Data Pt.	34 / 1 .	36 / 1 .	34 / 1 .	38 / 1 .	24 / 1 .	37 / 1 .	4 / 1 .	6 / 1 .	7 / 1 .	9 / 1 .	10 / 1 .	11 / 1 .	12 / 1 .	19 / 1 .
S	32.51	33.58	32.53	33.99	40.30	39.95	41.65	42.42	42.37	42.03	41.64	41.80	41.70	41.86
Fe	24.43	25.79	23.47	24.77	11.61	13.64	8.12	7.98	7.62	7.32	7.21	7.70	7.68	7.23
Co	1.26	0.48	1.17	1.07	13.64	10.42	12.37	11.70	11.53	11.93	11.91	12.21	12.39	11.93
Ni	40.28	40.53	38.85	39.57	31.65	33.26	36.53	36.98	36.63	37.18	36.67	36.42	35.67	36.70
Cu	0.03	0.03	0.21	0.26	0.02	0.02	0.07	0.24	0.39	0.12	0.10	0.01	0.05	0.27
As	0.02	0.04	0.00	0.00	0.01	0.12	0.02	0.04	0.02	0.01	0.02	0.03	0.02	0.01
Total	98.52	100.45	96.22	99.66	97.20	97.43	98.75	99.27	98.55	98.58	97.55	98.12	97.51	97.99

Sample Number	MIC/16/39	MIC/16/39	MIC/16/35	MIC/16/33	MIC/16/33	MIC/16/33	MIC/16/33	MIC/16/33	MIC/16/33	MIC/16/39	MIC/16/39	MIC/16/39	MIC/16/39	MIC/16/39
Mineral	Co-vio-larite[a]	Co-vio-larite[a]	Co-vio-larite[a]	Mille-rite[a]	Mille-rite[a]	Mille-rite[a]	Mille-rite[a]	Mille-rite[a]	Mille-rite[a]	Mille-rite[a]	Mille-rite[a]	Mille-rite[a]	Mille-rite[a]	Mille-rite[a]
Data Pt.	20 / 1 .	22 / 1 .	24 / 1 .	5 / 1 .	6 / 1 .	7 / 1 .	8 / 1 .	9 / 1 .	12 / 1 .	13 / 1 .	14 / 1 .	16 / 1 .	17 / 1 .	18 / 1 .

S	41.81	42.23	38.06	33.01	36.27	34.24	34.24	34.66	35.97	36.38	35.28	34.55	35.07	35.20
Fe	7.26	7.24	15.35	2.61	3.83	4.86	4.57	2.19	1.92	1.20	0.81	1.21	0.75	0.51
Co	11.84	12.09	8.85	1.57	1.59	1.28	1.33	1.43	1.76	0.47	0.51	0.35	0.32	0.22
Ni	37.02	36.33	34.10	60.85	60.86	61.66	60.95	61.84	60.36	61.20	62.96	60.82	62.48	62.38
Cu	0.29	0.06	0.23	0.22	0.12	0.16	0.15	0.13	0.14	0.28	0.16	0.11	0.37	0.30
As	0.01	0.07	0.00	0.02	0.03	0.02	0.04	0.05	0.06	0.02	0.02	0.06	0.01	0.01
Total	98.22	98.02	96.58	98.24	102.71	102.22	101.27	100.29	100.22	99.50	99.71	97.10	98.98	98.61

Sample Number	MIC/16/38	MIC/16/38	MIC/16/38	MIC/16/38	MIC/16/38	MIC/16/38	MIC/16/38	MIC/16/38	MIC/16/38	MIC/16/38	MIC/16/38	MIC/16/38	MIC/16/38	MIC/16/38
Mineral	Millerite[a]	Millerite[a]	Millerite[a]	Millerite[a]	Millerite[a]	Millerite[a]	Millerite[a]	Millerite[a]	Millerite[a]	Millerite[a]	Millerite[a]	Millerite[a]	Millerite[a]	Millerite[a]
Data Pt.	45 / 1 .	46 / 1 .	47 / 1 .	48 / 1 .	49 / 1 .	50 / 1 .	52 / 1 .	53 / 1 .	55 / 1 .	57 / 1 .	58 / 1 .	60 / 1 .	61 / 1 .	63 / 1 .
S	35.10	35.44	34.89	35.32	34.93	35.83	35.15	34.59	34.13	35.18	36.17	35.09	34.39	34.67
Fe	2.40	1.57	2.36	1.75	2.06	1.57	2.78	3.06	1.81	2.67	2.37	1.97	2.08	1.71
Co	1.89	2.28	2.12	2.20	2.15	1.60	1.94	1.76	2.03	2.06	1.92	2.03	1.94	1.95
Ni	60.37	60.91	60.46	61.89	61.04	61.11	61.48	60.56	59.83	61.14	60.87	61.60	60.25	62.07
Cu	0.06	0.00	0.02	0.03	0.03	0.06	0.01	0.03	0.03	0.01	0.01	0.03	0.07	0.07
As	0.15	0.11	0.13	0.07	0.09	0.10	0.11	0.11	0.18	0.07	0.13	0.13	0.08	0.05
Total	99.97	100.31	99.98	101.25	100.24	100.27	101.45	100.11	98.01	101.13	101.47	100.86	98.81	100.52

Sample Number	MIC/16/39	MIC/16/39	MIC/16/39	MIC/16/39	MIC/16/39	MIC/16/39	MIC/16/33	MIC/16/33	MIC/16/33	MIC/16/35	MIC/16/35	MIC/16/35	MIC/16/35	MIC/16/35
Mineral	Chalcopyrite[b]	Chalcopyrite[b]	Chalcopyrite[b]	Chalcopyrite[b]	Bornite[b]	Bornite[b]	Pentlandite[b]	Pentlandite[b]	Pentlandite[b]	Pentlandite[b]	Pentlandite[b]	Pentlandite[b]	Pentlandite[b]	Pentlandite[b]
S	35.7	35.73	36.80	38.66	26.38	30.87	36.09	36.14	34.40	37.18	36.58	32.84	36.31	37.29
Fe	30.10	29.74	30.06	28.56	6.43	11.56	24.56	23.07	21.49	23.65	23.72	22.45	23.22	24.24
Co							2.21	2.01	1.83			1.52		
Ni					0.67	1.17	37.13	38.57	36.17	37.08	36.97	36.10	38.33	38.28
Cu	30.75	30.34	30.53	32.63	62.2	54.52								
B														
O	2.28	3.07	2.04		3.65	1.44			4.75		2.52	5.25	2.00	
Mg		0.37			0.31	0.25			0.86			1.15		

Si	0.19	0.26	0.16	0.15	0.35	0.19		0.21	0.51	0.27	0.20	0.68	0.14	0.19
Na														
Ca	0.30													
Cr	0.67	0.49	0.41											
Total	100.00	100.00	100.00	100.00	100.00	100.00	100.00	100.00	100.00	100.00	100.00	100.00	100.00	100.00

Sample Number	MIC/16/35	MIC/16/35	MIC/16/35	MIC/16/35	MIC/16/35	MIC/16/35	MIC/16/35	MIC/16/35	MIC/16/35	MIC/16/35	MIC/16/35	MIC/16/35	MIC/16/35	MIC/16/35
Mineral	Pent-landite[b]	Pent-landite[b]	Pent-landite[b]	Pent-landite[b]	Pent-landite[b]	Pent-landite[b]	Pent-landite[b]	Pent-landite[b]	Pent-landite[b]	Pent-landite[b]	Pent-landite[b]	Pent-landite[b]	Pent-landite[b]	Pent-landite[b]
S	36.79	35.35	34.84	34.46	35.57	36.60	35.88	36.56	33.40	36.17	35.75	36.40	37.20	34.65
Fe	24.78	22.87	24.47	25.93	24.93	25.15	24.16	25.43	28.17	23.54	22.84	23.91	24.12	21.22
Co									1.55		1.50			
Ni	38.29	37.08	36.59	36.81	36.76	38.25	37.66	38.01	32.11	36.08	35.71	37.33	38.09	35.06
Cu														
B														
O		3.63	3.31	2.42	2.52		2.30		4.67	3.99	3.26	2.22		5.29
Mg		0.62	0.45								0.49		0.31	1.11
Si	0.14	0.46	0.33	0.38	0.22				0.11	0.22	0.45	0.13	0.28	0.83
Na														
Ca														
Cr														
Total	100.00	100.00	100.00	100.00	100.00	100.00	100.00	100.00	100.00	100.00	100.00	100.00	100.00	100.00

Sample Number	MIC/16/35	MIC/16/35	MIC/16/38	MIC/16/38	MIC/16/38	MIC/16/38	MIC/16/38	MIC/16/33	MIC/16/35	MIC/16/35	MIC/16/35	MIC/16/35	MIC/16/35	MIC/16/38
Mineral	Pent-landite[b]	Pent-landite[b]	Pent-landite[b]	Pent-landite[b]	Pent-landite[b]	Pent-landite[b]	Pent-landite[b]	Co-vio-larite[b]	Co-vio-larite[b]	Co-vio-larite[b]	Co-vio-larite[b]	Co-vio-larite[b]	Co-vio-larite[b]	Co-vio-larite[b]
S	37.32	36.42	35.15	41.51	36.56	36.46	35.87	44.98	45.58	44.14	45.26	45.29	43.85	45.29
Fe	24.43	22.98	20.61	12.39	24.23	23.86	21.52	7.22	11.28	12.93	11.19	12.34	11.73	7.69
Co			1.92	2.25	2.00	2.02	2.09	18.19	12.49	9.63	12.65	11.37	10.94	19.87
Ni	38.05	36.85	39.35	39.96	37.20	37.50	37.01	28.07	29.22	29.75	29.37	29.41	28.59	27.02
Cu														

B														
O		2.94	2.73	2.97			2.88		1.25	3.55	1.34	1.43	3.58	
Mg		0.41					0.34						0.72	
Si	0.19	0.40	0.23	0.92		0.16	0.30		0.18		0.19	0.15	0.57	
Na														
Ca														
Cr														
Total	100.00	100.00	100.00	100.00	100.00	100.00	100.00	100.00	100.00	100.00	100.00	100.00	100.00	100.00

Sample Number	MIC/16/38	MIC/16/39	MIC/16/33	MIC/16/33	MIC/16/33	MIC/16/38	MIC/16/38	MIC/16/38	MIC/16/38	MIC/16/38	MIC/16/38	MIC/16/38	MIC/16/38	MIC/16/38
Mineral	Co-violarite[b]	Co-violarite[b]	Millerite[b]	Millerite[b]	Millerite[b]	Millerite[b]	Millerite[b]	Millerite[b]	Millerite[b]	Millerite[b]	Millerite[b]	Millerite[b]	Millerite[b]	Millerite[b]
S	45.27	44.27	33.78	35.38	35.33	34.59	32.75	34.34	37.19	36.13	36.97	34.23	37.79	37.31
Fe	8.77	5.04	2.83	2.11	3.25	3.06	1.80	2.66	2.20	3.81	2.11	2.53	2.78	2.53
Co	17.32	6.63	1.33	1.48	1.14	1.85	1.37	1.91	1.90	1.72	2.20	1.93	2.07	2.03
Ni	28.65	40.51	51.56	53.05	53.51	51.83	48.89	51.39	55.88	53.94	54.69	50.83	56.07	55.82
Cu														
B														
O		3.01	9.67	7.14	6.78	7.61	12.08	8.93	2.84	4.26	3.88	9.22	1.14	2.31
Mg														
Si		0.18				0.14				0.14	0.16	0.11	0.15	
Na			0.84	0.83		0.93	3.10	0.77				1.14		
Ca		0.35												
Cr														
Total	100.00	100.00	100.00	100.00	100.00	100.00	100.00	100.00	100.00	100.00	100.00	100.00	100.00	100.00

Sample Number	MIC/16/38	MIC/16/38	MIC/16/38	MIC/16/38	MIC/16/38	MIC/16/38	MIC/16/38	MIC/16/38	MIC/16/38	MIC/16/38	MIC/16/38	MIC/16/38	MIC/16/38	MIC/16/38
Mineral	Millerite[b]	Millerite[b]	Millerite[b]	Millerite[b]	Millerite[b]	Millerite[b]	Millerite[b]	Millerite[b]	Millerite[b]	Millerite[b]	Millerite[b]	Millerite[b]	Millerite[b]	Millerite[b]
S	37.86	37.90	38.70	36.19	37.64	38.74	36.91	35.80	36.94	37.08	37.00	37.47	34.97	33.59
Fe	3.62	2.93	1.74	2.00	1.89	1.77	5.91	8.06	2.38	3.35	2.66	1.82	1.90	1.93

Co	2.00	2.06	2.10	1.67	1.54	1.99	1.88	1.70	1.55	1.60	1.79	1.86	1.89	1.68
Ni	55.46	55.40	57.33	54.21	56.07	57.34	53.91	52.18	54.61	55.27	54.76	55.83	52.83	50.29
Cu														
B														
O	0.94	1.57		5.74	2.66		1.27	2.14	4.35	2.49	3.08	2.88	7.55	9.93
Mg														
Si	0.12	0.14	0.13	0.18	0.19	0.17	0.14	0.12	0.16	0.20	0.25	0.15	0.13	0.14
Na													0.73	2.43
Ca														
Cr														
Total	100.00	100.00	100.00	100.00	100.00	100.00	100.00	100.00	100.00	100.00	100.00	100.00	100.00	100.00

Sample Number	MIC/16/39	MIC/16/39	MIC/16/39	MIC/16/33	MIC/16/35	MIC/16/35	MIC/16/38
Mineral	Mille-rite[b]	Mille-rite[b]	Mille-rite[b]	Barite[b]	Barite[b]	Barite[b]	Barite[b]
S	36.23	36.03	37.76	18.26	8.77	11.18	9.64
Fe	1.18	1.21	1.17	3.54	7.28	8.99	0.78
Co	0.48	0.50	0.41	8.90			0.60
Ni	54.51	54.41	55.15	13.28	11.24	14.15	18.01
Cu							
B				55.98	71.64	64.48	66.85
O	7.17	7.86	5.50		1.05	1.16	3.69
Mg							
Si	0.13			0.04	0.03	0.04	0.02
Na							0.40
Ca	0.30						
Cr							
Total	100.00	100.00	100.00	100.00	100.00	100.00	100.00

[a] Data analyzed from Department of Geology, Banaras Hindu University, India.

[b] Data analyzed from Department of Geology and Geophysics, Indian Institute of Technology, Kharagpur, India.

Chalcopyrite grains from the Gorumahishani komatiite have Cu = 30.34 - 32.63 wt.%, Fe = 28.54 - 30.10 wt.%, and S = 35.7 - 38.66 wt.% while bornite have Cu = 54.52 - 62.20 wt.%, Fe = 6.43 - 11.46 wt.%, and S = 26.38 - 30.87 wt.% with Ni = 0.67 - 1.17 wt.% (**Table 5**). The pentlandite grains from the Ni+Co-Fe bearing sulfide assemblages have Ni = 38.85 - 41.72 wt.%, Fe = 21.26 - 25.79 wt.%, and S = 31.90 - 33.99 wt.% whereas patches of millerite have Ni = 59.83 - 62.96 wt.%, Fe = 0.5 - 4.86 wt.%, and S = 33 - 36.38 wt.% (**Table 5**). Pentlandite grains have a higher concentration of Co (0.5 - 2.25 wt.%) and Cobaltian violarites have high Co (8.85 - 13.64 wt.%) with Ni = 31.65 – 37.18 wt.%, Fe = 7.21 - 15.35 wt.%, and S = 38.06 - 42.42 wt.% (**Table 5**).

5.2. *In-situ* LA-ICPMS of oxides: Trace and Platinum-Group element (PGE)

5.2.1. Trace elements

In-situ trace element analysis by LA-ICPMS of Cr-oxides of type-I and type-II show significant compositional variations across the grains (**Table 6**; **Fig. 9a-d**). Type-III and type-IV grains were not analyzed because they are either highly porous (type-III) or small and fractured (type-IV) (**Fig. 3j, k**). On the other hand, the type-V chrome magnetite grains are selected for their high modal abundance and large grain size over small, locally abundant, and fractured type-IV grains (**Fig. 3l**). The type-I zoned chromites from the northern part and the type-II grains from the southern part of the greenstone belt can easily demonstrate the change of metamorphic grade and degree of hydrothermal alteration. The cores of type-I chromites from the serpentinized peridotite of Tua Dungri have higher concentrations of Sc = 2.62 - 5.40 ppm, V = 864 - 1040 ppm, Zn = 16,866 - 18,124 ppm, and Ga = 10.4 - 23.5 ppm than

their corresponding rims (Sc = 0.01 - 0.96 ppm, V = 15.8 - 959 ppm, Zn = 196 - 8346 ppm, and Ga = 0.04 - 2.25 ppm; **Fig. 9a**, **b**). In comparison, Ti (41.2 - 2370 ppm), Mn (196 - 11,522 ppm), and Ni (30.94 - 1945 ppm) are higher in the ferritchromit and chrome magnetite rims than the core (Ti = 535 - 1475 ppm, Mn = 6447 - 9947 ppm, and Ni = 1782 - 4812 ppm; **Fig. 9a**, **b**). The core regions of type-II chromites in the meta-peridotite from the spinifex zone of Kapili have higher concentrations of Sc = 3.39 - 5.68 ppm, Ti = 20,759 - 36,413 ppm, V = 3338 - 7165 ppm, Mn = 27,181 - 45,891 ppm, Co = 1744 - 2586 ppm, Ni = 4513 - 10,583 ppm, Zn = 11,665 - 15,757 ppm, and Ga = 49.8 - 83.7 ppm than the chrome magnetite rim (Sc = 0.22 - 0.92 ppm, Ti = 1845 - 6248 ppm, V = 808 - 2317 ppm, Mn = 2107 - 6122 ppm, Co = 196 - 541.5 ppm, Ni = 1628 - 4705 ppm, Zn = 627 - 1746 ppm, and Ga = 6.64 - 18.9 ppm; **Fig. 9c, d**). Type-V chrome magnetite grains show highly variable concentrations of Ti = 451 - 7856 ppm, V = 661 - 7609 ppm, Mn = 661 - 7609 ppm, Co = 12.5 - 668 ppm, Ni = 848 - 6689 ppm, and Zn = 580 - 3159 ppm with Ga = 0.05 - 29.4 ppm and Sc = 0.10 - 2.47 ppm (**Table 6**).

In $Mg/(Mg + Fe^{2+})$ versus trace elements plots, Ga, Sc concentrations of the type-I chromite cores show a positive correlation from the outer to the inner core, whereas Ni, Co, Mn, Zn, and Ti show a negative trend (**Fig. 10a-g**). Nevertheless, given the limited number of measurements generalizations must be viewed with caution.

Trace element diagrams (spidergrams) following the order of elements suggested by Colás et al. (2014) and Park et al. (2017), and normalized to chromite compositions from East Pacific Rise MORB (Pagé and Barnes 2009), are shown in **figure 11**. In the trace element spidergram, the average core compositions of the

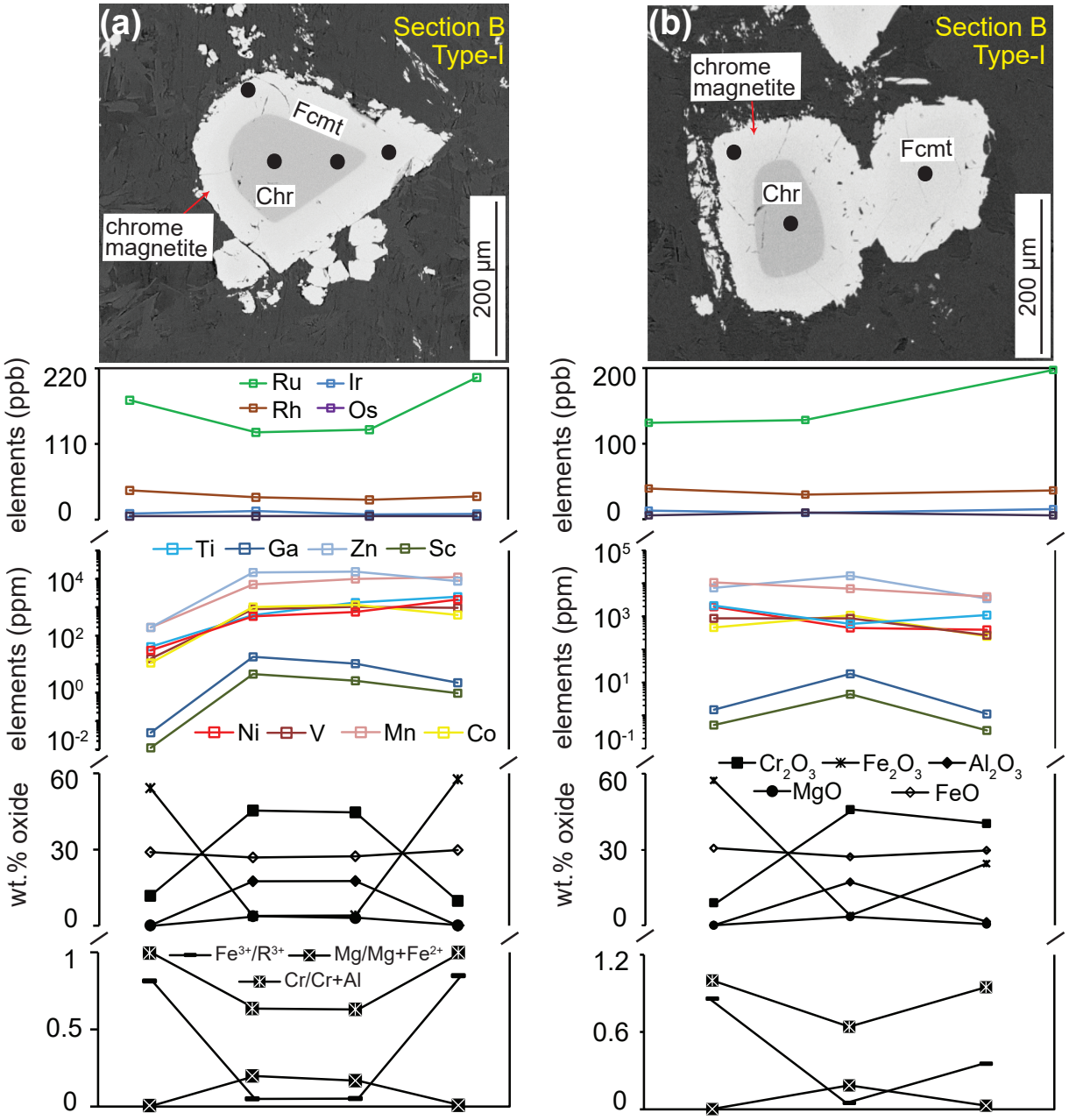

Fig. 9 Quantitative *in situ* LA-ICPMS profiles of trace and platinum-group elements along with major elements Cr_2O_3, Al_2O_3, MgO, Fe_2O_3, FeO and Mg/Mg+Fe^{2+}, Cr/Cr+Al, Fe^{3+}/R^{3+} across the **a, b** Type-I and (sample: MIC/16/39), **c, d** Type-II (sample: SHB/19-12/82) zoned chromites. Laser spots indicate data points showing variation from chromite core to ferritchromit and chrome magnetite rims. Mineral names abbreviations are from Whitney and Evans (2010).

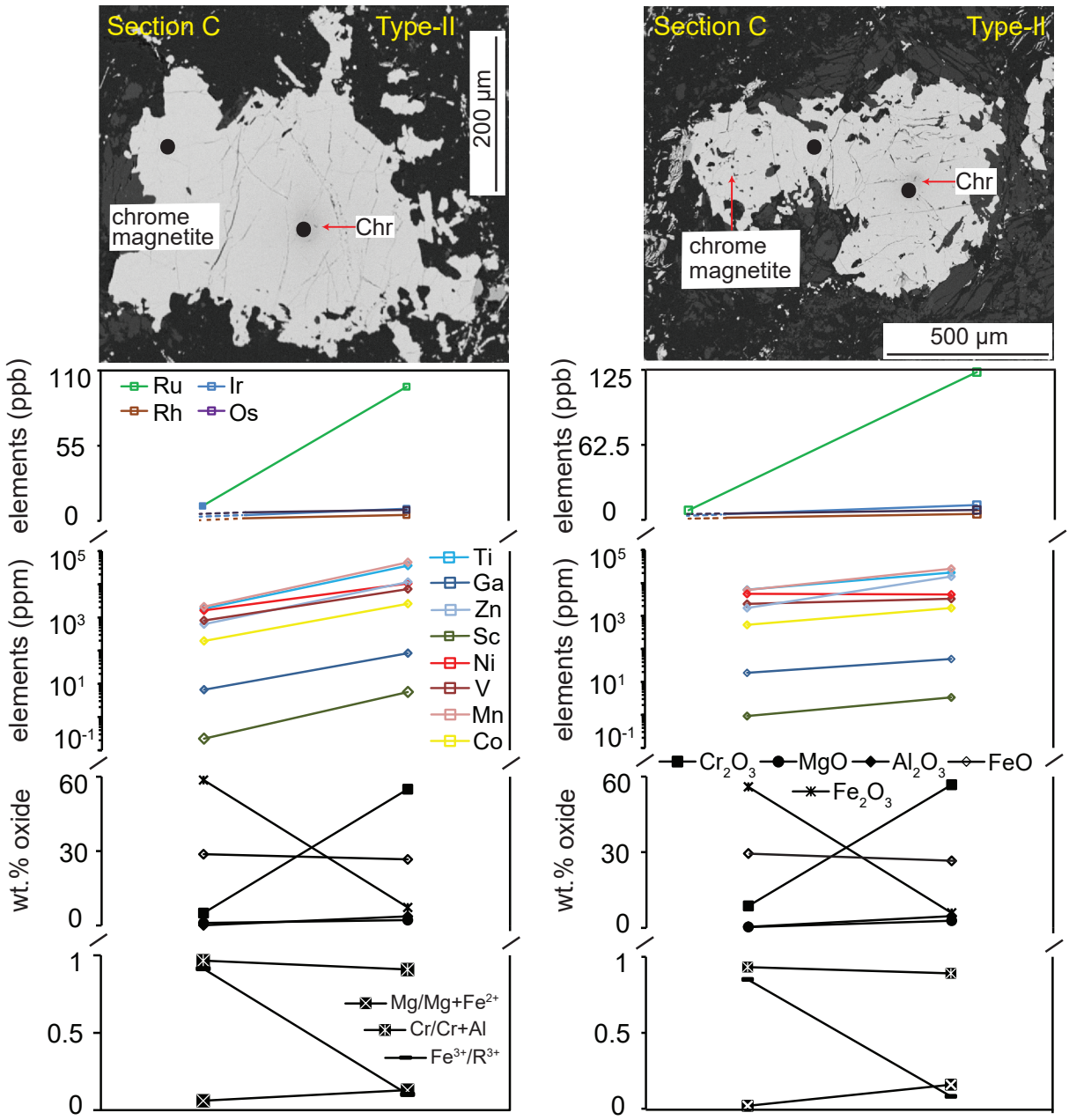

Fig. 9 Continued.

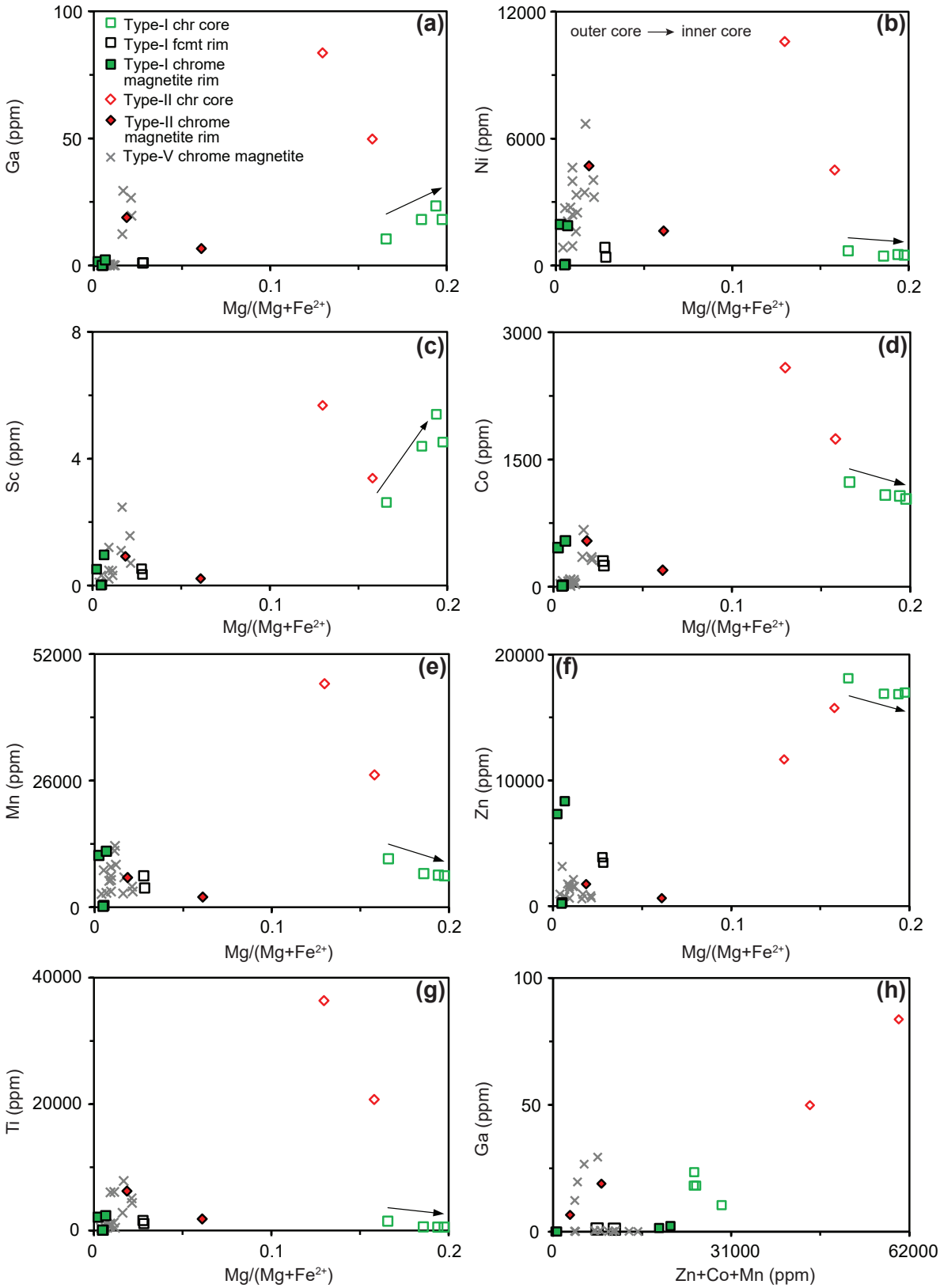

Fig. 10 Compositional variations of the type-I, type-II, and type-V Cr-spinel grains from **a-g** Mg/Mg+Fe^{2+} vs. Ga, Ni, Sc, Co, Mn, Zn, and Ti plots, **h** Zn+Co+Mn vs. Ga plot.

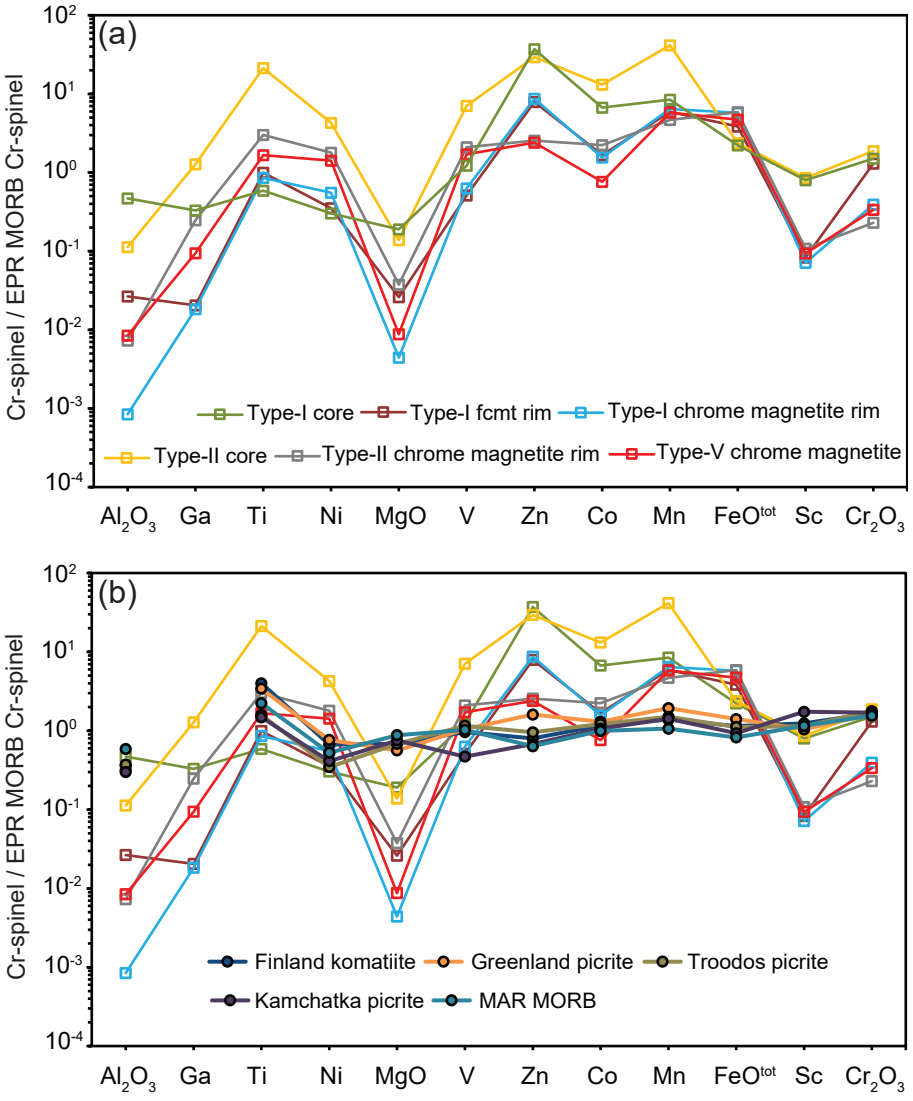

Fig. 11 EPR MORB Cr-spinel (after Pagé and Barnes, 2009) normalized spidergrams: **a** Average major and trace elements compositional variation of the type-I, type-II, and type-V Cr-spinels and, **b** Comparison of the type-I, type-II, and type-V Cr-spinels with the least altered chromites from Finland komatiite (˜2.05 Ga) and Greenland (˜62 Ma), Troodos (˜90 Ma), and Kamchatka (˜88 Ma) picrite (Page´ and Barnes 2009; Park et al. 2012, 2017; Kamenetsky et al. 2015).

Table 6 *In situ* LA-ICPMS trace elements composition (ppm) of komatiitic chromites from the Gorumahishani greenstone belt

Sample number	MIC/16/39	MIC/16/39	MIC/16/39	MIC/16/39	MIC/16/39	MIC/16/39	MIC/16/39	MIC/16/39	MIC/16/39	MIC/16/39	SHB/19-12/82	SHB/19-12/82	SHB/19-12/82
Location	Tua Dungri	Tua Dungri	Tua Dungri	Tua Dungri	Tua Dungri	Tua Dungri	Tua Dungri	Tua Dungri	Tua Dungri	Tua Dungri	Kapili	Kapili	Kapili
LA point	1	3	8	9	5	6	2	4	7	10	25	34	26
EPMA point	28/1.	24/1.	9/1.	6/1.	21/1.	27/1.	29/1.	26/1.	14/1.	2/1.	103/1.	118/1.	100/1.
Mineral	Chro-mite	Chro-mite	Chro-mite	Chro-mite	Ferrit-chromit	Ferrit-chromit	Chr mag-netite	Chr mag-netite	Chr mag-netite	Chr mag-netite	Chro-mite	Chro-mite	Chr mag-netite
Type	Type-I core	Type-I core	Type-I core	Type-I core	Type-I inner rim	Type-I inner rim	Type-I outer rim	Type-I outer rim	Type-I outer rim	Type-I outer rim	Type-II core	Type-II core	Type-II outer rim
Sc	5.40	4.40	4.52	2.62	0.35	0.53	0.02	0.51	0.01	0.96	5.68	3.39	0.22
Ti	554.31	594.17	534.70	1474.71	1097.34	1576.23	74.79	2116.70	41.20	2369.50	36412.54	20758.92	1845.19
V	878.10	871.55	863.76	1040.39	270.13	489.53	28.31	865.91	15.77	958.93	7165.42	3337.90	807.58
Mn	6600.85	6909.01	6447.34	9946.79	3950.50	6453.32	362.46	10635.74	196.29	11521.59	45891.24	27180.67	2107.26
Co	1071.21	1081.90	1037.17	1234.52	248.19	304.79	17.43	461.77	11.12	539.76	2585.57	1744.47	195.86
Ni	514.42	447.66	488.12	688.55	394.70	851.14	58.95	1944.89	30.94	1876.10	10582.87	4512.85	1627.49
Cu	0.09	0.57	2.38	1.68	0.04	0.34	0.03	2.06	0.03	0.64	0.23	3.13	0.17
Zn	16865.87	16884.20	16987.22	18124.18	3454.17	3898.71	296.45	7324.89	196.33	8346.21	11664.55	15757.33	627.38
Ga	23.48	18.16	18.13	10.44	1.11	1.04	0.06	1.49	0.04	2.25	83.70	49.83	6.64
Cr_2O_3	44.16	45.77	45.39	44.61	40.27	37.50	16.31	8.98	11.78	9.78	55.00	56.79	5.02
Al_2O_3	17.61	17.53	17.14	17.32	1.48	0.49	0.06	0.00	0.05	0.02	3.69	4.68	0.12
MgO	3.04	3.71	3.47	3.57	0.48	0.46	0.09	0.04	0.08	0.11	2.23	2.79	1.05
FeO	26.42	27.09	26.88	27.30	29.69	29.03	29.32	30.50	28.97	29.76	26.69	26.54	28.76
Fe_2O_3	3.94	3.87	3.82	4.00	24.45	27.44	50.11	57.33	54.15	57.70	7.27	5.92	58.60
Mg#	0.19	0.19	0.20	0.17	0.03	0.03	0.01	0.00	0.00	0.01	0.13	0.16	0.06
Fe^{3+}/R^{3+}	0.05	0.05	0.05	0.05	0.35	0.41	0.74	0.86	0.81	0.85	0.10	0.08	0.91
Cr#	0.63	0.64	0.63	0.63	0.95	0.98	0.99	1.00	0.99	1.00	0.91	0.89	0.97

Sample number	SHB/19-12/82	SHB/19-12/82	SHB/19-12/82	SHB/19-12/82	SHB/19-12/82	SHB/19-12/35	SHB/19-12/35	SHB/19-12/35	SHB/19-12/35	SHB/19-12/35	SHB/19-12/35	SHB/19-12/24	SHB/19-12/24
Location	Kapili	Kapili	Kapili	Kapili	Kapili	Maha-	Maha-	Maha-	Maha-	Maha-	Maha-	Chuka	Chuka

LA point	33	24	29	30	31	rajgunj 16	rajgunj 17	rajgunj 19	rajgunj 20	rajgunj 21	rajgunj 22	Pahar 11	Pahar 12
EPMA point	121/1.	110/1.	89/1.	92/1.	94/1.	146/1.	145/1.	148/1.	149/1.	133/1.	143/1.	69/1.	68/1.
Mineral	Chr mag-netite	Chr mag-netite	Chr mag-netite	Chr mag-netite	Chr mag-netite	Chr mag-netite	Chr mag-netite	Chr mag-netite	Chr mag-netite	Chr mag-netite	Chr mag-netite	Chr mag-netite	Chr mag-netite
Type	Type-II outer rim	Type-V	Type-V	Type-V	Type-V	Type-V	Type-V	Type-V	Type-V	Type-V	Type-V	Type-V	Type-V
Sc	0.92	2.47	1.57	0.70	1.10	0.10	0.10	0.21	0.10	0.10	0.32	0.32	0.48
Ti	6247.98	7855.66	5098.91	4378.72	2822.38	649.75	1097.50	876.69	462.76	450.83	2112.30	6110.31	6022.85
V	2316.46	3102.78	1921.67	1602.08	1639.54	1040.52	1388.39	1258.69	645.25	477.59	1263.45	2307.15	1539.36
Mn	6121.52	6158.82	4228.22	3257.71	2834.59	5421.29	6441.65	5599.25	2964.66	2761.42	7608.79	12582.50	8288.06
Co	541.47	668.12	347.37	318.45	352.45	62.77	86.16	78.72	33.90	32.41	67.62	50.74	39.39
Ni	4705.06	6688.57	4035.50	3233.99	3444.45	2743.15	4623.81	3980.73	2083.78	847.92	2700.03	3328.77	2404.06
Cu	0.32	0.22	0.03	0.03	0.08	0.03	0.07	0.03	0.03	0.03	0.03	0.20	0.04
Zn	1746.30	938.86	821.11	658.30	580.29	1762.25	1656.77	1525.22	775.48	952.62	3159.17	2126.80	1323.33
Ga	18.88	29.39	26.61	19.61	12.32	0.39	0.52	0.46	0.25	0.17	0.38	0.11	0.08
Cr_2O_3	8.69	7.47	6.74	5.68	5.34	13.71	12.35	11.22	12.51	12.84	12.20	15.92	15.08
Al_2O_3	0.42	0.35	0.37	0.22	0.21	0.61	0.93	0.43	0.43	0.38	0.92	0.23	0.16
MgO	0.31	0.28	0.36	0.36	0.27	0.14	0.16	0.16	0.11	0.07	0.09	0.19	0.15
FeO	29.43	29.61	29.66	29.45	29.58	29.67	29.69	29.85	29.82	29.57	29.72	28.67	28.85
Fe_2O_3	55.93	57.48	58.19	60.31	59.97	52.47	53.25	55.10	53.80	54.03	50.72	49.37	49.99
Mg#	0.02	0.02	0.02	0.02	0.02	0.01	0.01	0.01	0.01	0.00	0.01	0.01	0.01
Fe^{3+}/R^{3+}	0.85	0.87	0.88	0.91	0.91	0.77	0.79	0.81	0.80	0.79	0.78	0.74	0.76
Cr#	0.93	0.93	0.92	0.95	0.94	0.94	0.90	0.91	0.95	0.96	0.90	0.98	0.98

Sample number	SHB/19-12/24	SHB/19-12/24	SHB/19-12/24
Location	Chuka Pahar	Chuka Pahar	Chuka Pahar
LA point	13	14	15
EPMA point	58/1.	78/1.	75/1.
Mineral	Chr mag-netite	Chr mag-netite	Chr mag-netite

Type	Type-V	Type-V	Type-V
Sc	0.47	0.10	1.20
Ti	1232.64	456.03	674.97
V	2300.21	1798.71	660.52
Mn	11590.42	8754.33	3254.69
Co	77.06	32.58	12.45
Ni	1606.87	2492.89	922.90
Cu	0.07	0.09	0.03
Zn	1559.11	1579.29	626.47
Ga	0.12	0.05	0.10
Cr_2O_3	16.55	15.59	16.91
Al_2O_3	0.17	0.11	0.13
MgO	0.18	0.15	0.20
FeO	28.91	28.87	28.27
Fe_2O_3	48.75	50.11	48.94
Mg#	0.01	0.01	0.01
Fe^{3+}/R^{3+}	0.73	0.75	0.73
Cr#	0.99	0.99	0.99

Chr magnetite: Chrome magnetite,
Mg#: $Mg/(Mg+Fe^{2+})$, R^{3+}: $Fe^{3+}+Cr+Al$, Cr#: $Cr/(Cr+Al)$

type-I (n = 4) and type-II (n = 2) chromites show a minor negative Sc anomaly (0.79 - 0.86 × EPR MORB Cr-spinel) with high abundances of Zn, Co, and Mn (6.70 - 41.47 × EPR MORB Cr-spinel; **Fig. 11a**). The ferritchromit and chrome magnetite rims of the type-I grains (n = 6) also show moderately high abundances of Zn and Mn (5.90 - 8.69 × EPR MORB Cr-spinel) with a strong negative Sc anomaly (0.07 - 0.08 × EPR MORB Cr-spinel; **Fig. 11a**). The M-shaped positive anomaly in the segment Zn-Co-Mn (ZCM anomaly; Colás et al. 2014) is more prominent for the rims relative to the cores of the type-I grains (**Fig. 11a**). Chrome magnetite rims of the type-II grains (n = 2) and the average type-V grains (n = 15) have similar patterns, with negative anomalies of Sc (0.09 - 0.10 × EPR MORB Cr-spinel) and minor ZCM anomalies (1 - 5.79 × EPR MORB Cr-spinel) (**Fig. 11a**). The least altered volcanic chromites from other occurrences do not have any such ZCM anomalies and overall show a fat pattern (**Fig. 11b**).

5.2.2. Platinum-Group Element (PGE)

Platinum-Group Elements (PGE) are analyzed *in situ* by LA-ICPMS in the cores and rims of type-I and type-II zoned chromites, and type-V chrome magnetite grains (**Fig. 9a-d**; **Table 7**). Type-III and type-IV chromites are avoided for the reasons explained above. Os, Ir, Ru (IPGE), and Rh concentrations were determined successfully while Pt and Pd were below the detection limits in all analyzed grains (**Table 7**). Despite the mostly uniform count rates of IPGE + Rh, a few grains of the type-V chrome magnetite from the Chuka Pahar (2 points) and Maharajgunj areas (3 points) show anomalous Ru, Rh signals from the time-resolved LA-ICP-MS spectra (**Table 7**; **Fig. 12**). This may be due to the presence of PGE microinclusions in the chromites. The

concentrations for the three data points from Maharajgunj are determined by excluding the Ru and Rh spikes, however, the 2 data points from Chuka Pahar are not corrected by excluding the PGE spikes (Ir, Os, Rh), and are not used in the plots (Ru = 128 - 140 ppb, Rh = 4.8 - 8.9 ppb, Os = 22.5 - 25.6 ppb, Ir = 20.8 - 23.8 ppb). The type-V chrome magnetites in the komatiitic sequence from the Maharajgunj-Chuka Pahar and Kapili sectors show a distinct variation (**Table 7**). The type-V grains from the Kapili have Os, Ir, Rh below the detection limit with Ru = 8 - 46 ppb except for one data point (Ru = 211.5 ppb, Rh = 14.4 ppb, Os = 7.3 ppb, and Ir = 13.5 ppb) compared to the type-V grains from the Maharajgunj-Chuka Pahar sector which have higher PGE contents (Ru = 72.2 - 110 ppb, Rh = 2.9 - 8.9 ppb, Os = 19.7 - 29.8 ppb, Ir = 12.4 - 23.8 ppb). The cores of the analyzed type-I chromites have Ru (127 - 163.2 ppb), and Rh (28.9 - 32.6 ppb) contents similar to or slightly lower than those of its respective ferritchromit and chrome magnetite rims (Ru = 116.9 - 206.7 ppb, Rh = 29 - 44.8 ppb) (**Fig. 9a**). Osmium is detected in one laser point of the type-I chromite core (Os = 8.8 ppb). In comparison with the type-I grains, the type-II chromite cores have lower concentrations of Ru (98.1 - 123.1 ppb), Rh (4.4 - 4.9 ppb), and nearly similar Ir (8.9 - 12.3 ppb), and Os (8 - 8.3 ppb) content (**Fig. 9**). The chrome magnetite rims of the type-II grains have a lower concentration of Ru = 8 - 11 ppb than their respective cores with Rh, Os, and Ir below the detection limit (**Fig. 9b**). Cores of type-I and type-II zoned chromites from the Gorumahishani belt have generally lower IPGE + Rh contents than volcanic chromites of komatiites and picrites from Finland and picrites from Greenland, Kamchatka, Troodos, and the Emeishan province, with ranges of Ru = 87 - 336 ppb, Rh = 7 - 95 ppb, Ir = 14 - 101 ppb, and Os = 5 - 54 ppb (Pagé and Barnes 2009; Park et al. 2012, 2017; Kamenetsky et al. 2015).

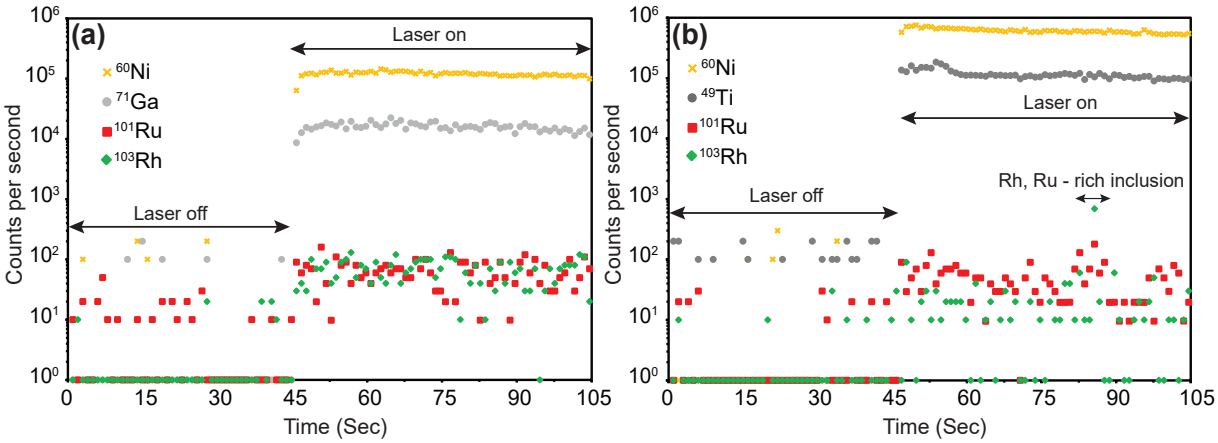

Fig. 12 Representative time-resolved spectra of LA-ICP-MS analyses on the komatiitic chromites from **a** Sample MIC/16/39 (type-I chromite, Tua Dungri) showing homogeneous PGE spectra. **b** Sample SHB/19-12/35 (type-V chromite, Maharajgunj) with Rh, Ru spikes indicating the probable presence of Rh, Ru-bearing micro-inclusions.

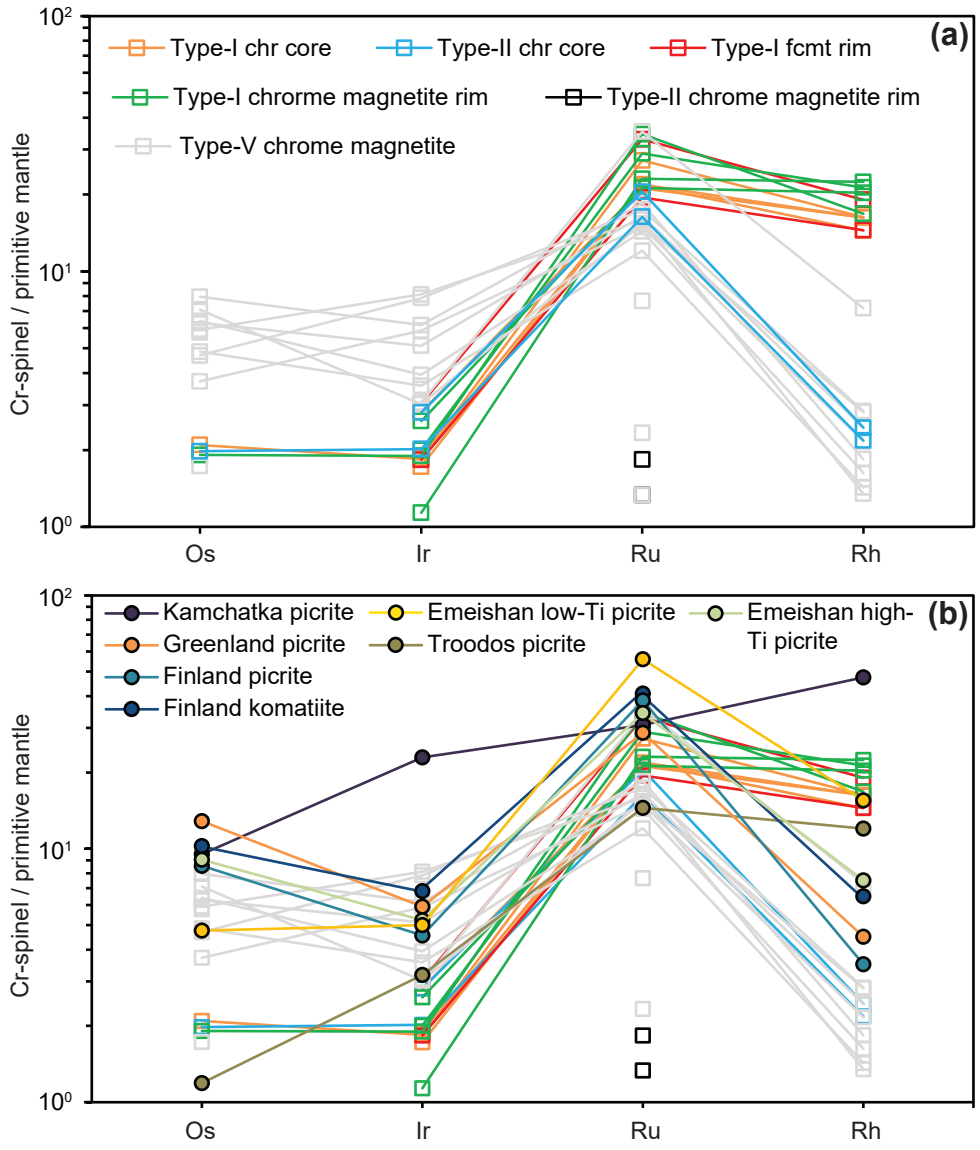

Fig. 13 Primitive Mantle (PM) normalized Rh and IPGE plot of **a** Type-I, type-II, and type-V Cr-spinel grains from the Gorumahishani komatiitic rocks and **b** Comparison of type-I, type-II, and type-V Cr-spinels with the least altered chromites from the Finland komatiite (˜2.05 Ga) and Greenland (˜62 Ma), Troodos (˜90 Ma), Finland (˜2.05 Ga), Emeishan (˜256 Ma), and Kamchatka picrites (˜88 Ma) (Page´ and Barnes 2009; Park et al. 2012, 2017; Kamenetsky et al. 2015). Primitive Mantle values are from Barnes et al. (1988).

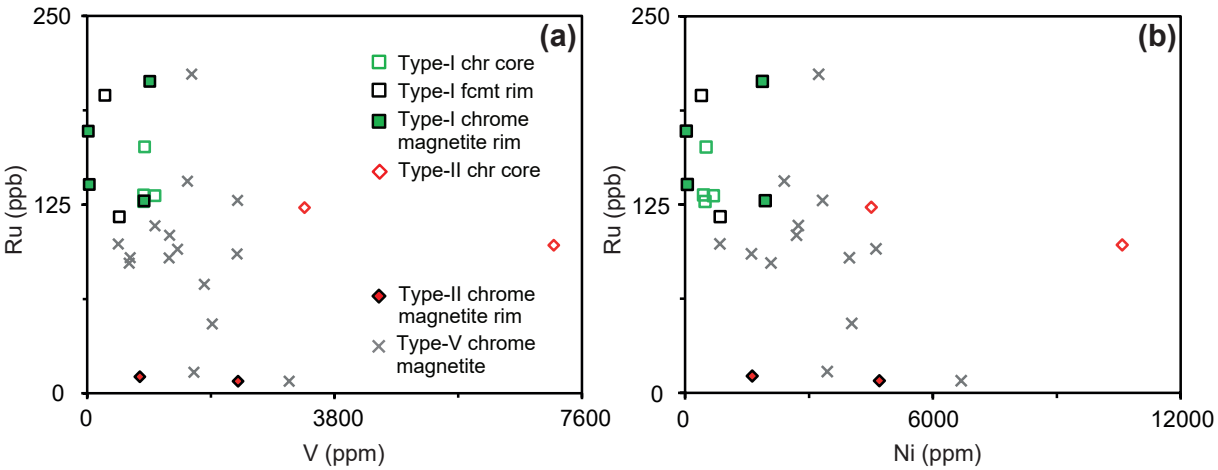

Fig. 14 Compositional variations of trace and platinum-group elements in the type-I, type-II, and type-V Cr-spinel grains in **a** V vs. Ru. **b** Ni vs. Ru plots.

Table 7 *In situ* LA-ICPMS Platinum-Group element (PGE) composition (ppm) of komatiitic chromites from the Gorumahishani greenstone belt

Sample number	MIC/16/39	MIC/16/39	MIC/16/39	MIC/16/39	MIC/16/39	MIC/16/39	MIC/16/39	MIC/16/39	MIC/16/39	MIC/16/39	SHB/19-12/82	SHB/19-12/82	SHB/19-12/82
Location	Tua Dungri	Tua Dungri	Tua Dungri	Tua Dungri	Tua Dungri	Tua Dungri	Tua Dungri	Tua Dungri	Tua Dungri	Tua Dungri	Kapili	Kapili	Kapili
EPMA point	28/1.	24/1.	9/1.	6/1.	21/1.	27/1.	29/1.	26/1.	14/1.	2/1.	103/1.	118/1.	100/1.
LA point	1	3	8	9	5	6	2	4	7	10	25	34	26
Mineral	Chro-mite	Chro-mite	Chro-mite	Chro-mite	Ferrit-chromit	Ferrit-chromit	Chr ma-gnetite	Chr ma-gnetite	Chr ma-gnetite	Chr ma-gnetite	Chro-mite	Chro-mite	Chr ma-gnetite
Type	Type-I core	Type-I core	Type-I core	Type-I core	Type-I inner rim	Type-I inner rim	Type-I outer rim	Type-I outer rim	Type-I outer rim	Type-I outer rim	Type-II core	Type-II core	Type-II outer rim
Os	<5	8.8	<5	<5	<5	<5	<5	<5	<5	<5	8.0	8.3	<5
Ir	8.1	8.1	12.4	7.6	13.4	8.1	5	11.4	8.8	8.3	8.9	12.3	<3
Ru	163.2	131.4	127.0	130.9	197.4	116.9	138.3	127.5	173.7	206.7	98.1	123.1	11.0
Rh	32.6	32.5	32.5	28.9	38.1	29.0	44.8	40.6	42.6	33.6	4.4	4.9	<1
Pt	<2	<2	<2	<2	<2	<2	<2	<2	<2	<2	<12	<12	<12
Pd	<14	<14	<14	<14	<14	<14	<14	<14	<14	<14	<14	<14	<14
Rh_N/Os_N	7.79									8.79	1.10		
Rh_N/Ir_N	8.84	8.78	5.77	8.39	6.28	7.92	19.72	7.83	10.64	8.87	1.08	0.87	
Rh_N/Ru_N	0.60	0.74	0.77	0.66	0.58	0.74	0.97	0.96	0.74	0.49	0.13	0.12	
Ru_N/Os_N	12.99									18	8.27		
Ru_N/Ir_N	14.75	11.83	7.52	12.66	10.84	10.64	20.28	8.19	14.46	18.15	8.10	7.31	
Ir_N/Os_N	0.88									0.99	1.02		
Cr_2O_3	44.16	45.77	45.39	44.61	40.27	37.50	16.31	8.98	11.78	9.78	55	56.79	5.02
Al_2O_3	17.61	17.53	17.14	17.32	1.48	0.49	0.06	0.00	0.05	0.02	3.69	4.68	0.12
MgO	3.04	3.71	3.47	3.57	0.48	0.46	0.09	0.04	0.08	0.11	2.23	2.79	1.05
FeO	26.42	27.09	26.88	27.30	29.69	29.03	29.32	30.50	28.97	29.76	26.69	26.54	28.76
Fe_2O_3	3.94	3.87	3.82	4.00	24.45	27.44	50.11	57.33	54.15	57.70	7.27	5.92	58.60
Mg#	0.19	0.19	0.20	0.17	0.03	0.03	0.01	0.00	0.00	0.01	0.13	0.16	0.06
Fe^{3+}/R^{3+}	0.05	0.05	0.05	0.05	0.35	0.41	0.74	0.86	0.81	0.85	0.10	0.08	0.91
Cr#	0.63	0.64	0.63	0.63	0.95	0.98	0.99	1.00	0.99	1.00	0.91	0.89	0.97

Sample number	SHB/19-12/82	SHB/19-12/82	SHB/19-12/82	SHB/19-12/82	SHB/19-12/82	SHB/19-12/35	SHB/19-12/35	SHB/19-12/35	SHB/19-12/35	SHB/19-12/35	SHB/19-12/35	SHB/19-12/24	SHB/19-12/24
Location	Kapili	Kapili	Kapili	Kapili	Kapili	Maharaj-gunj	Maharaj-gunj	Maharaj-gunj	Maharaj-gunj	Maharaj-gunj	Maharaj-gunj	Chuka Pahar	Chuka Pahar
EPMA point	121/1.	110/1.	89/1.	92/1.	94/1.	146/1.	145/1.	148/1.	149/1.	133/1.	143/1.	69/1.	68/1.
LA point	33	24	29	30	31	16	17	19	20	21	22	11	12
Mineral	Chr ma-gnetite	Chr ma-gnetite	Chr ma-gnetite	Chr ma-gnetite	Chr ma-gnetite	Chr ma-gnetite	Chr ma-gnetite	Chr ma-gnetite	Chr ma-gnetite	Chr ma-gnetite	Chr ma-gnetite	Chr ma-gnetite	Chr ma-gnetite
Type	Type-II outer rim	Type-V	Type-V	Type-V	Type-V	Type-V	Type-V	Type-V	Type-V	Type-V	Type-V	Type-V	Type-V
Os	<5	<5	<5	7.3	<5	24.2	33.4	24.8	15.6	26.9	26.4	25.6	22.5
Ir	<3	<3	<3	13.5	<3	27.1	35.7	25.8	17.3	22.5	34.6	23.8	20.8
Ru	8.0	8.0	46.0	211.5	14.0	110.9	95.5	89.7	86.2	98.9	104.6	127.7	140.6
Rh	<1	<1	<2	14.4	<1	3.7	2.7	4.3	3.2	4.9	5.7	8.9	4.8
Pt	<12	<12	<12	<12	<12	<12	<12	<12	<12	<12	<12	<12	<12
Pd	<14	<14	<14	<14	<14	<14	<14	<14	<14	<14	<14	<14	<14
Rh_N/Os_N				1.90		0.15	0.08	0.17	0.21	0.18	0.22	0.35	0.21
Rh_N/Ir_N				2.34		0.30	0.17	0.37	0.41	0.48	0.36		
Rh_N/Ru_N				0.07		0.03	0.03	0.05	0.04	0.05	0.05	0.07	0.03
Ru_N/Os_N				29.11		4.58	2.86	3.61	5.52	3.68	3.97	4.98	6.25
Ru_N/Ir_N				11.48		2.99	1.96	2.55	3.65	3.22	2.22		
Ir_N/Os_N				1.86		1.12	1.07	1.04	1.11	0.84	1.31	0.93	0.92
Cr_2O_3	8.69	7.47	6.74	5.68	5.34	13.71	12.35	11.22	12.51	12.84	12.20	15.92	15.08
Al_2O_3	0.42	0.35	0.37	0.22	0.21	0.61	0.93	0.43	0.43	0.38	0.92	0.23	0.16
MgO	0.31	0.28	0.36	0.36	0.27	0.14	0.16	0.16	0.11	0.07	0.09	0.19	0.15
FeO	29.43	29.61	29.66	29.45	29.58	29.67	29.69	29.85	29.82	29.57	29.72	28.67	28.85
Fe_2O_3	55.93	57.48	58.19	60.31	59.97	52.47	53.25	55.10	53.80	54.03	50.72	49.37	49.99
Mg#	0.02	0.02	0.02	0.02	0.02	0.01	0.01	0.01	0.01	0.00	0.01	0.01	0.01
Fe^{3+}/R^{3+}	0.85	0.87	0.88	0.91	0.91	0.77	0.79	0.81	0.80	0.79	0.78	0.74	0.76
Cr#	0.93	0.93	0.92	0.95	0.94	0.94	0.90	0.91	0.95	0.96	0.90	0.98	0.98

Sample number	SHB/19-12/24	SHB/19-12/24	SHB/19-12/24
Location	Chuka Pahar	Chuka Pahar	Chuka Pahar
EPMA point	58/1.	78/1.	75/1.
LA point	13	14	15
Mineral	Chr magnetite	Chr magnetite	Chr magnetite
Type	Type-V	Type-V	Type-V
Os	19.7	29.8	20.4
Ir	13.3	15.7	12.4
Ru	92.3	72.2	89.9
Rh	5.6	2.9	4.9
Pt	<12	<12	<12
Pd	<14	<14	<14
Rh_N/Os_N	0.29	0.10	0.24
Rh_N/Ir_N	0.93	0.40	0.88
Rh_N/Ru_N	0.06	0.04	0.06
Ru_N/Os_N	4.69	2.43	4.41
Ru_N/Ir_N	5.09	3.38	5.32
Ir_N/Os_N	0.68	0.53	0.61
Cr_2O_3	16.55	15.59	16.91
Al_2O_3	0.17	0.11	0.13
MgO	0.18	0.15	0.20
FeO	28.91	28.87	28.27
Fe_2O_3	48.75	50.11	48.94
Mg#	0.01	0.01	0.01
Fe^{3+}/R^{3+}	0.73	0.75	0.73
Cr#	0.99	0.99	0.99

Chr magnetite: Chrome magnetite, Mg#: $Mg/(Mg+Fe^{2+})$, R^{3+}: $Fe^{3+}+Cr+Al$, Cr#: $Cr/(Cr+Al)$

Primitive mantle normalized plots of Ru, Rh, Os, and Ir show fractionated PGE patterns for all three types of chromites with all being strongly enriched in Ru. In nearly all cases, Ir_N/Os_N ratios are close to 1 (**Fig. 13a; Table 7**). Type-I chromite cores, ferritchromit, and chrome magnetite rims are particularly enriched in both Ru and Rh (15 - 34 × PM). The cores and ferritchromit rims of the type-I chromites tend to have less fractionated PGE ratios than the type-I chrome magnetite rims (**Table 7**), though given the small number of points it is difficult to generalize. The type-II chromite cores show strong positive anomalies for Ru (16 - 21 × PM) with lower Rh abundances than the type-I grains (**Fig. 13a**). The type-V chrome magnetites are enriched in Os and Ir (Os = 2 - 8 × PM) compared to the other types of chromites (**Fig. 13a**). They also have low Rh abundances, similar to those of the type-II chromite cores. The least altered volcanic chromites from Troodos, Greenland, Finland, Emeishan picrite, and Finland komatiite (Park et al. 2017) show similar PGE patterns of the type-V chrome magnetite grains except for Kamchatka picrite (**Fig. 13b**). They have higher Ru anomaly (15 - 56 × PM) but a similar abundance of Os, Ir, and Rh (**Fig. 13b**). No distinct relationships are observed in V, Ni vs. Ru plots for the type-I, type-II, and type-V grains (**Fig. 14a-b**).

5.3. Bulk-rock geochemistry

5.3.1. Major and trace elements

The Gorumahishani komatiites from the three sections (section A: Chuka Pahar - Maharajgunj; section B: Tua Dungri; section C: Kapili) of the greenstone belt are geochemically classified based on $(Fe_2O_3 + TiO_2)$ - Al_2O_3 - MgO triangular diagram of Jensen (1976) (**Fig. 15a**). The samples of the komatiitic meta-dunite and meta-

peridotite from the cumulate and spinifex zones occupy the komatiite field in the diagram except one sample from section C (SHB/18/39) with MgO = 20.90 wt.%. The samples of the komatiitic meta-basalt from the upper part of the sequence occupy the komatiitic basaltic field except for a few samples from sections B and C (**Fig. 15a**). These samples are plotted at the boundary between komatiitic basalt and tholeiitic basalt. Al_2O_3 and TiO_2 are two important elements for komatiite classification because of their relatively low mobility. Nesbitt and Sun (1976) and Sun and Nesbitt (1978) classified komatiites into Al-depleted with low and sub-chondritic Al_2O_3/TiO_2 (<15) and Al-undepleted with chondritic Al_2O_3/TiO_2 (~22). Jahn et al. (1982) classified the komatiites with high Al_2O_3/TiO_2 (>25) as an Al-enriched type. Arndt et al. (2008) classified the komatiites by comparing them with the type areas. Low Al_2O_3/TiO_2 varieties are named 'Barberton-type' komatiite, chondritic Al_2O_3/TiO_2 varieties are termed as 'Munro-type' komatiite, and high Al_2O_3/TiO_2 varieties as 'Gorgona-type' komatiites. In the Al_2O_3 vs. TiO_2 diagram, (**Fig. 15b**) the komatiitic meta-dunite, meta-peridotite, and komatiitic meta-basalt from sections B and C occupy the Al-depleted field except for a few komatiitic meta-basalt (**Fig. 15b**). The composition of the komatiitic meta-dunite and meta-peridotite from section A occupy the Ti-depleted field except for one meta-basalt sample (SHB/19-12/39) from the upper part of the komatiitic sequence of section A (**Fig. 15b**). The high Al_2O_3/TiO_2 type is termed as the Ti-depleted komatiite with their very low TiO_2 = 0.02 - 0.13 wt.% content and Al_2O_3 = 0.31 - 5.62 wt.% that are close to the range of Al-depleted ones (Al_2O_3 = 1.42 - 6.88 wt.%, TiO_2 = 0.1 - 0.54 wt.%; e.g. Kamber and Tomlinson 2019).

The Gorumahishani komatiitic suite of rocks were metamorphosed under the greenschist-amphibolite facies. To evaluate the effects of metamorphism and

alteration, major and trace elements of meta-dunite, meta-peridotite, and meta-basalt are plotted against LOI (Loss on Ignition) (**Fig. 16a-h**). MgO and Ni show a positive relation with LOI whereas TiO_2, Al_2O_3, Ga, V, Cr, and Y show negative relations (**Fig. 16a-h**). Samples of komatiitic meta-basalt show a more scattered nature at a restricted LOI in comparison with the komatiitic meta-dunite and meta-peridotite. Chromium concentrations for all the samples from the three sections show a highly scattered distribution (**Fig. 16f**).

Correlations in the different variation diagrams based on bulk-rock major and trace element geochemistry of the Gorumahishani komatiitic rocks reflect the modal variation of minerals across the sequence (**Fig. 17a-l**). Major element oxides (Na_2O+K_2O), SiO_2, TiO_2, $FeO_{(T)}$, and Al_2O_3 show a negative relation with MgO for samples of the meta-dunite, meta-peridotite, and meta-basalt (**Fig. 17a, b, e, f**). The meta-dunite and meta-peridotite have low concentrations of (Na_2O+K_2O) and show a minor change with decreasing MgO (**Fig. 17b**)**.** The meta-dunite and meta-peridotite from section A have a lower concentration of $FeO_{(T)}$ (6.34 - 10.19 wt.%), and TiO_2 (0.02 - 0.13 wt.%) compared to the samples from section B and C ($FeO_{(T)}$ = 9.51 - 14.67 wt.%, TiO_2 = 0.01 - 0.43 wt.%) (**Fig. 17e, f**). CaO shows a negative correlation with MgO for the samples of the meta-dunite and meta-peridotite while the samples of the meta-basalt show a positive relation (**Fig. 17d**). In the MgO vs. SiO_2 plot, the komatiitic rocks show the olivine fractionation trend (Grove and Parman 2004) (**Fig. 17a**). In the MgO vs. Sc, Sr, and V plots the meta-dunite and meta-peridotite show a distinct negative correlation (**Fig. 17g, h, l**). The samples of the meta-basalt show a negative relation in MgO vs. Sr and V plots whereas Sc shows no correlation with MgO (**Fig. 17g, h, l**). Trace elements Ni and Co show a positive relation with MgO for

the samples of the meta-dunite, meta-peridotite, and meta-basalt of sections B and C (**Fig. 17i, j**). The samples of section A show no such correlation in the MgO vs. Ni and Co plots (**Fig. 17i, j**). The concentration of Cr increases with MgO from meta-dunite to meta-peridotite and decreases in the meta-basalt (**Fig. 17k**). The meta-dunite and meta-peridotite of section A have lower Ni and Co and higher Cr than sections B and C (**Fig. 17i-k**). In the MgO vs. other major and trace elements plots the compositions of the Gorumahishani komatiitic rocks show a close resemblance with the early Archean komatiites from different cratons (**Fig. 17a-l**).

The chondrite normalized rare-earth elements for the Gorumahishani komatiitic rocks show a flat to a minor LREE enriched pattern (**Fig. 18a-d**). The samples of the meta-dunite and meta-peridotite of section A are sub-chondritic and more depleted in LREE (La_n/Sm_n = 0.62 - 0.94) than the samples of sections B and C (La_n/Sm_n = 0.62 - 3.93; **Fig. 18a-c**). The HREEs are below the detection limit for the komatiitic meta-peridotite of section A (**Fig. 18a; Table 8**). The samples of the komatiitic meta-basalts from all the sections have a variable LREE enriched pattern (La_n/Sm_n = 0.52 - 1.99, Gd_n/Yb_n = 0.93 - 1.82; **Fig. 18a-c**). The chondrite normalized REE data for the Gorumahishani komatiitic rocks are compared with the early Archean komatiitic rocks from the Western Dharwar and Singhbhum Cratons (**Fig. 18d**). It is observed that the Gorumahishani meta-dunites and meta-peridotites show a similarity with the komatiitic rocks of the Tomka-Daitari greenstone belt, Singhbhum Craton and the Sargur type older greestone belt, Western Dharwar Craton (**Fig. 18d**). The Daitari komatiites show a similar REE pattern with the komatiitic samples of section A, whereas, the Badampahar komatiites have an REE enriched pattern than all the three sections of the Gorumahishani greenstone belt.

Average komatiitic basalts from both Badampahar and Daitari have similar REE patterns except a little depletion in LREE than the Gorumahishani komatiitic basalts from the three sections (**Fig. 18d**). The REE patterns of the Gorumahishani komatiitic rocks are also compared with the early to late Archean komatiites from the Kaapvaal, Pilbara, Zimbabwe, Karelian, and Superior Cratons (**Fig. 18d**). The meta-dunite and meta-peridotite from section A show a relatively depleted REE pattern (with higher depletion in Nd) when compared to the global database (**Fig. 18d**). The meta-basalts from the three sections have enriched LREE and HREE than other early Archean komatiitic basalt but relatively depleted in comparison to the late Archean komatiites (**Fig. 18d**).

In the chondrite normalized multielement plot, meta-dunite, and meta-peridotite from the three sections show a flat to little LILE enriched pattern (**Fig. 18e-h**) with a distinct negative Rb anomaly (0.04 - 0.52 × chondrite) except one sample (SHB/18/37; 1.13 × chondrite). A few samples of the meta-dunite and meta-peridotite from three sections show a little negative Nb anomaly (0.42 - 5.42 × chondrite) along with Y and Yb anomalies (0.57 - 6.83 × chondrite) from sections B and C (**Fig. 18e-g**). The meta-basalts from the three sections show a minor LILE-enriched pattern. The meta-basalts from sections B and C are more LREE enriched than section A (**Fig. 18e-g**). Two samples (SHB/19-12/56, 57) of the komatiitic meta-basalts from section B have relatively higher concentrations of Th, U than the other samples indicating the presence of Th, U bearing mineral like monazite or incorporation of these elements during alteration (**Fig. 18f**). In the chondrite normalized multielement plot the Gorumahishani komatiites show similar LILE and HFSE pattern with the other global occurrences except a negative Nd and Zr

anomalies for samples of section A (**Fig. 18h**). The Gorumahishani komatiitic meta-dunite and meta-peridotite show similar multi-element pattern like the komatiitic rocks from the Tomka-Daitari greenstone belt and the Sargur type older greenstone belt from the Western Dharwar Craton (**Fig. 18h**). However, the komatiitic samples from the Badampahar greenstone belt have higher HFSE than most of the Gorumahishani komatiitic samples. The Badampahar komatiitic meta-basalts have a similar LILE and HFSE pattern to the rest of the meta-basalt samples while Daitari meta-basalts show a depleted pattern (**Fig. 18h**).

The Nb/Ta ratios of the meta-dunites, meta-peridotites (Nb/Ta = 1 - 13), and the meta-basalts (Nb/Ta = 5 - 17) from three sections are highly variable compared to the primitive mantle (Nb/Ta = 17; McDonough and Sun 1995). This low and variable Nb/Ta ratio for most of the samples may indicate the effect of crustal input. To understand the assimilation of crustal materials by the Gorumahishani komatiites during emplacement, the data are plotted in the Zr vs. TiO_2, La vs. Sm, and Th vs. Yb plots (**Fig. 19a-c**). Besides positive correlation, komatiitic rocks follow the primitive mantle (e.g. McDonough and Sun 1995) trend except for a few komatiitic meta-basalt samples from sections B and C The data field of the early Archean mafic proto-crust from the ca. 3.7 - 3.8 Ga meta-basalt and amphibolite of the Isua supracrustal belt, Greenland (Polat et al. 2002, 2003; Frei et al. 2004; Polat and Frei 2005; Furnes et al. 2009; Hoffmann et al. 2010) coincides with the Zr/TiO_2, La/Sm, and Th/Yb ratios of the Gorumahishani komatiitic rocks (**Fig. 19a-c**). This indicates probable contamination of the komatiites by the older mafic proto-crust. The mafic contaminants are not highly evolved like those of the bulk continental crust (e.g.

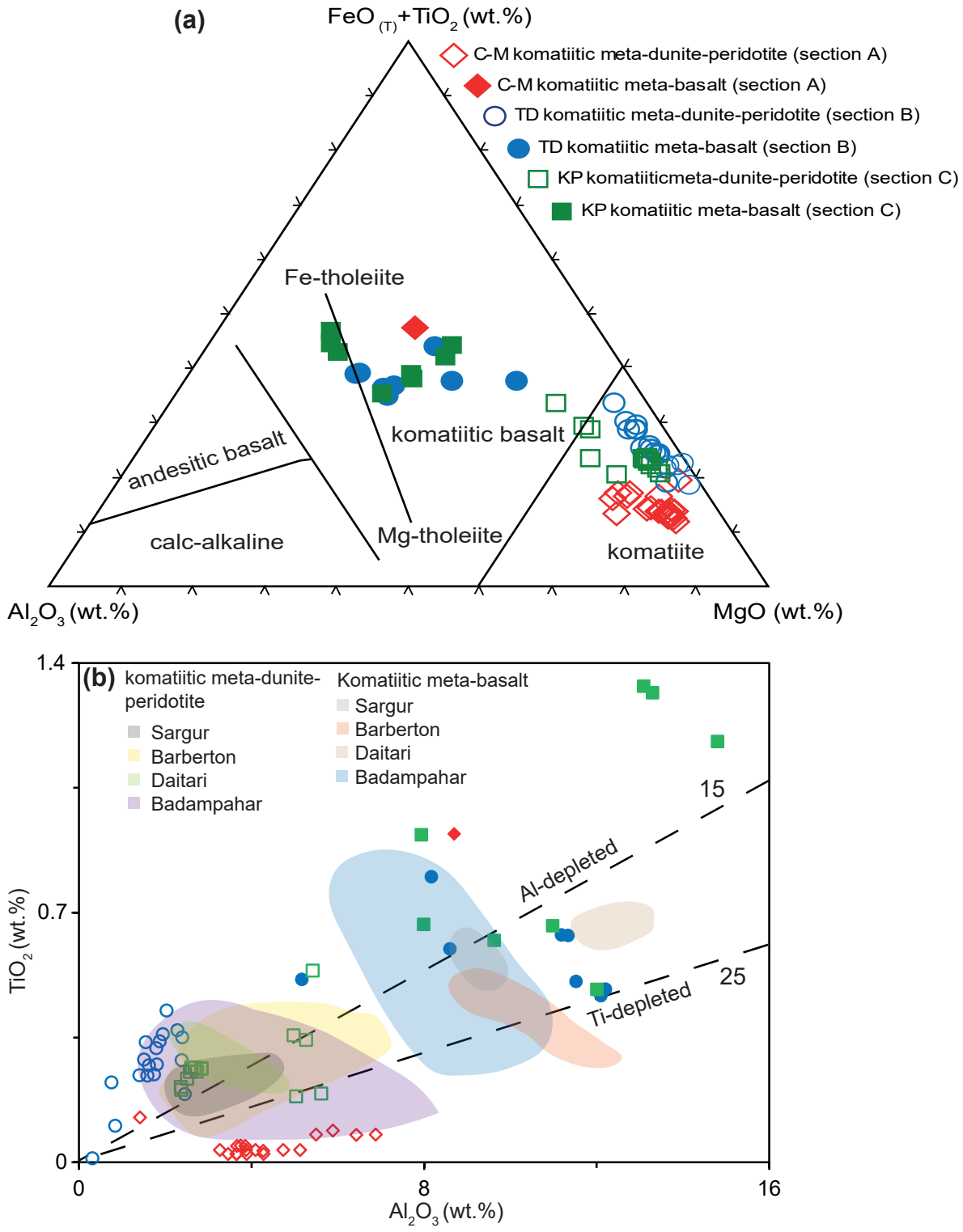

Fig. 15 a Al_2O_3-MgO-$FeO_{(T)}$+TiO_2 classification plot (after Jensen 1976) of the Gorumahishani komatiites. **b** Al_2O_3 vs. TiO_2 classification diagram for the Gorumahishani komatiites. The dotted lines indicate the limit of the Al_2O_3/TiO_2 ratio for Al-depleted and Ti-depleted komatiites. The early Archean Badampahar, Daitari, Sargur, and Barberton komatiites and komatiitic basalts are also plotted for comparison. Other data from Jayananda et al. (2008); Robin-Popieul et al. (2012); Puchtel et al. (2013); Tushipokla and Jayananda (2013); Schneider et al. (2019); Ghosh et al. (2019); Bachhar et al. (2021); and Adhikari et al. (2021a).

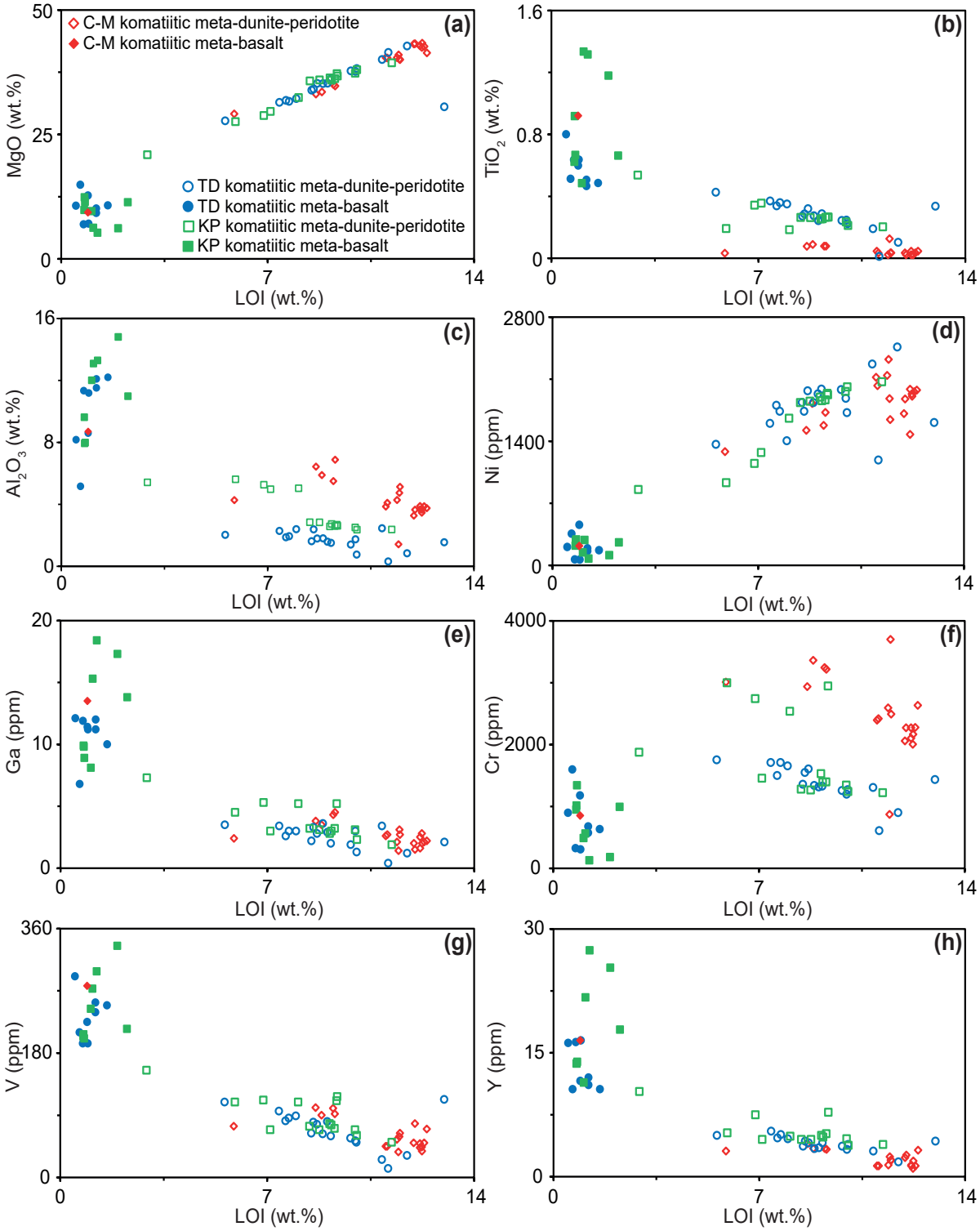

Fig. 16 Variation diagrams for selected major (anhydrous basis) and trace elements with LOI **a** LOI vs. MgO, **b** MgO vs. TiO_2, **c** LOI vs. Al_2O_3, **d** LOI vs. Ni, **e** LOI vs. Ga, **f** LOI vs. Cr, **g** LOI vs. V, and **h** LOI vs. Y.

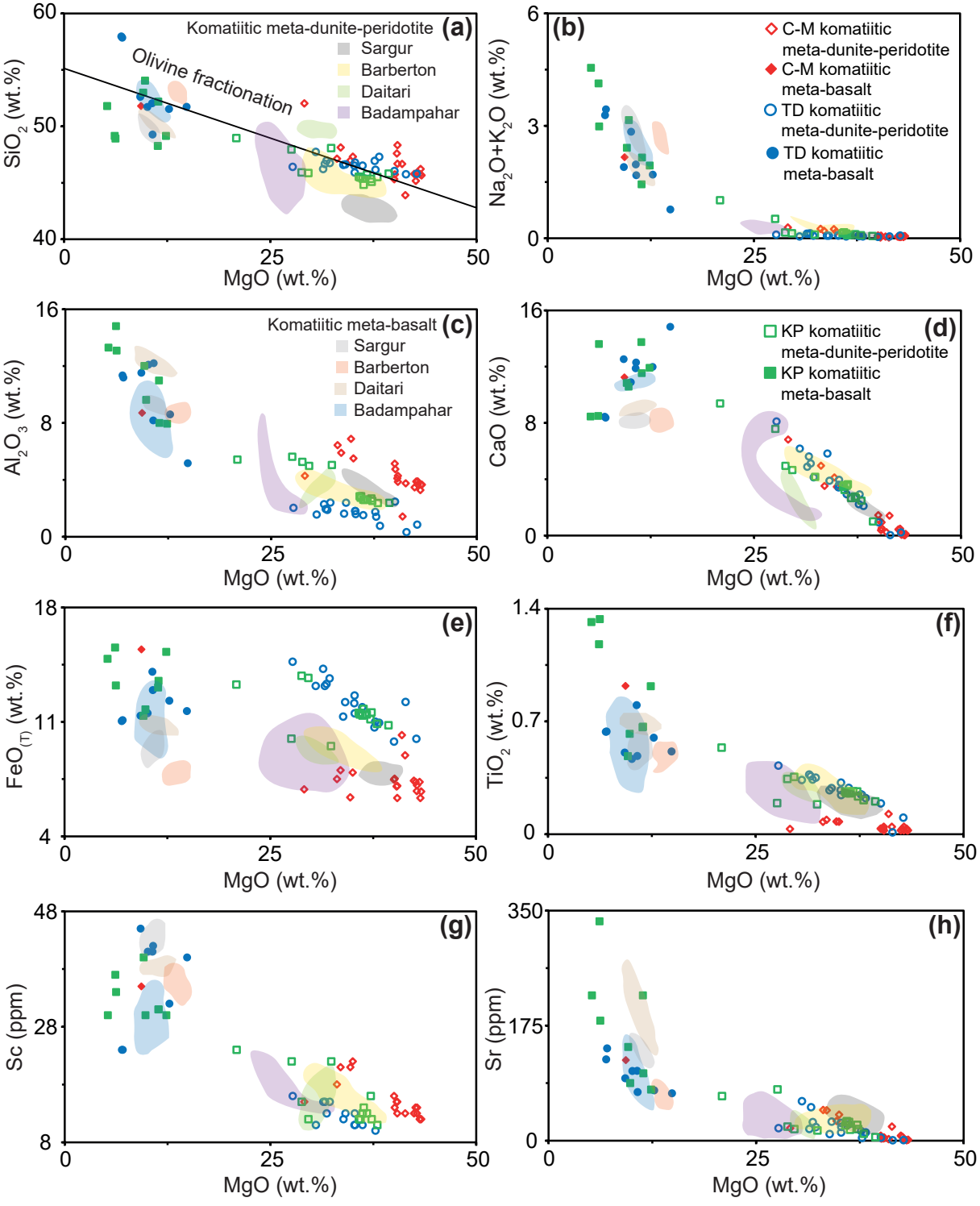

Fig. 17 Variation diagrams for selected major (anhydrous basis) and trace elements with MgO **a** MgO vs. SiO_2, **b** MgO vs. $Na_2O + K_2O$, **c** MgO vs. Al_2O_3, **d** MgO vs. CaO, **e** MgO vs. $FeO_{(T)}$, **f** MgO vs. TiO2, **g** MgO vs. Sc, **h** MgO vs. Sr, **i** MgO vs. Ni, **j** MgO vs. Co, **k** MgO vs. Cr, **l** MgO vs. V. The Gorumahishani komatiite and komatiitic basalt samples are compared with the early Archean Badampahar, Daitari, Sargur, and Barberton komatiites and komatiitic basalts. Other data from Jayananda et al. (2008); Robin-Popieul et al. (2012); Puchtel et al. (2013); Tushipokla and Jayananda (2013); Schneider et al. (2019); Ghosh et al. (2019); Bachhar et al. (2021); and Adhikari et al. (2021a).

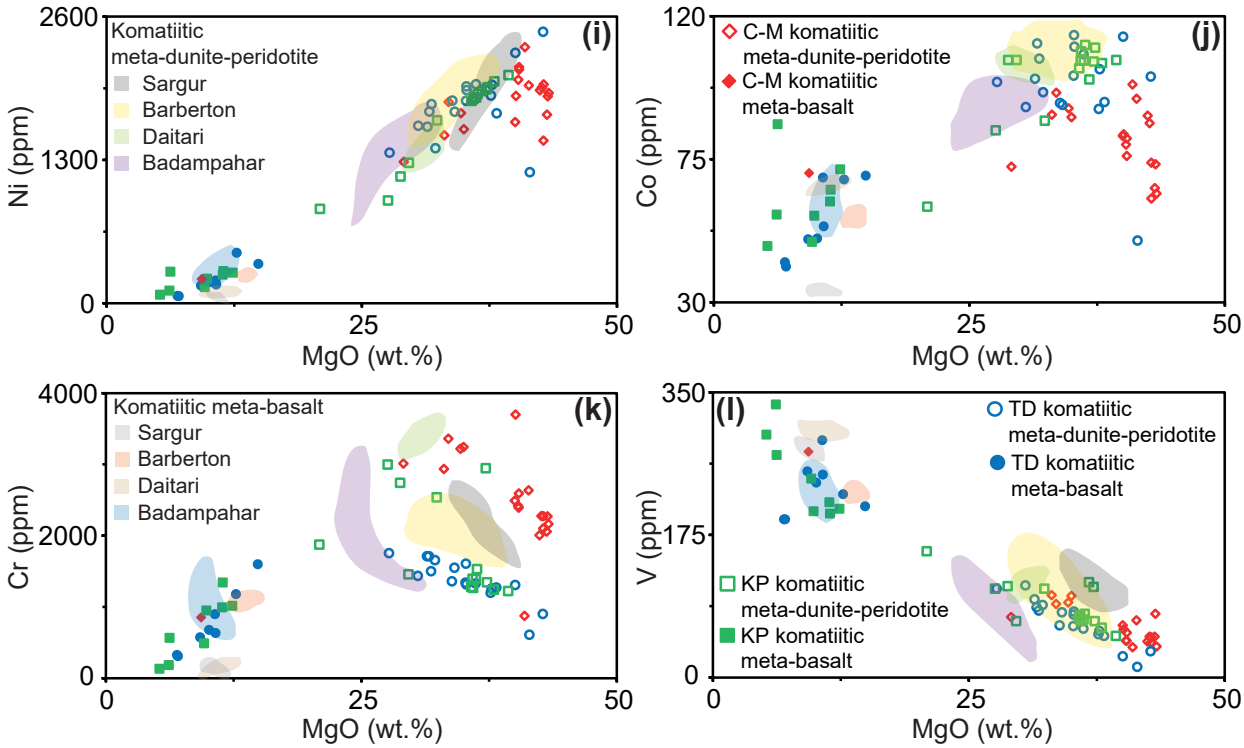

Fig. 17 Continued.

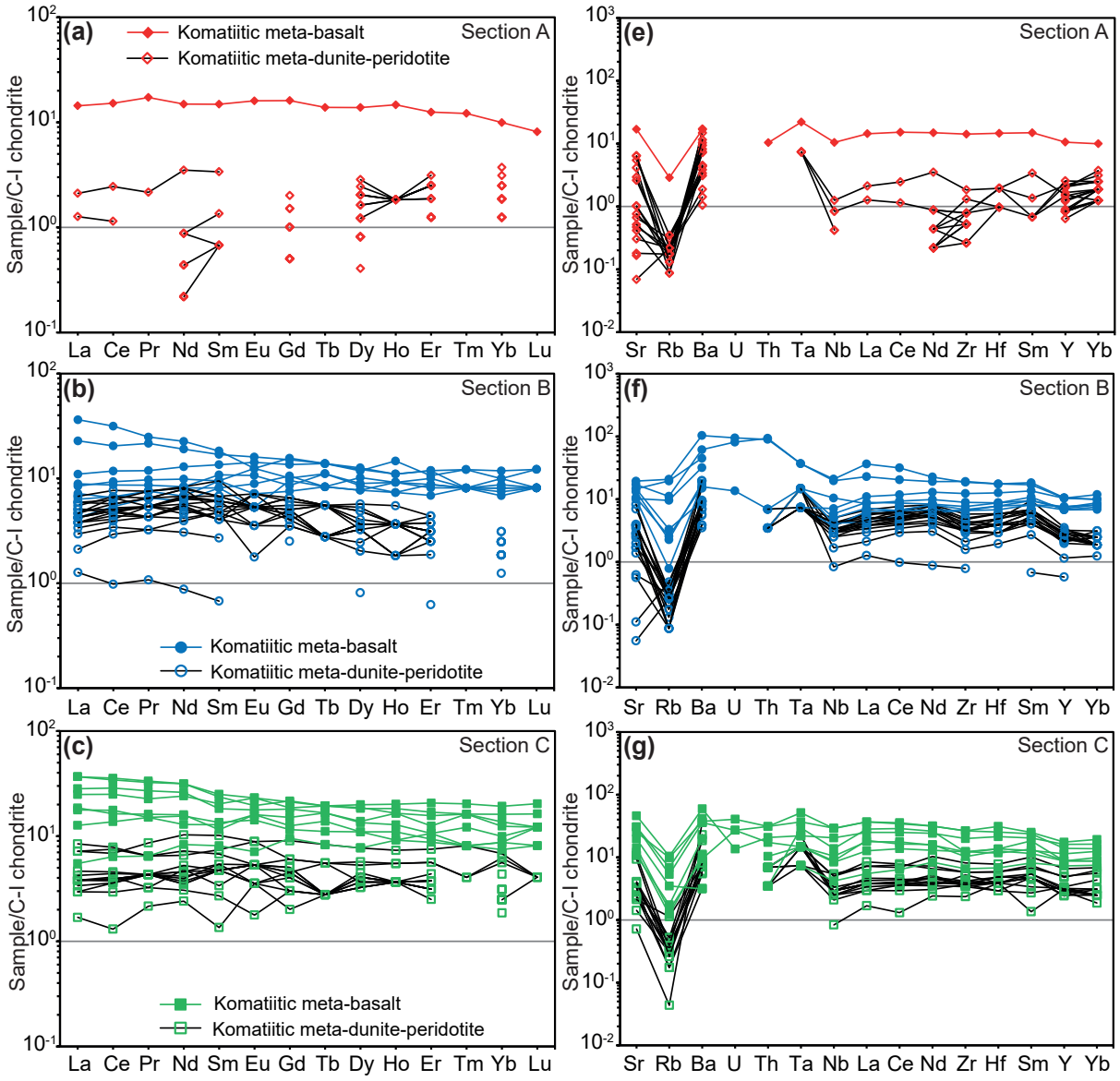

Fig. 18 Chondrite normalized (McDonough and Sun 1995) REE and multielement diagrams of the Gorumahisani komatiitic rocks from **a, e** Maharajgunj-Chuka Pahar (Section A); **b, f** Tua Dungri (Section B); and **c, g** Kapili (Section C) areas. **d, h** Comparison of the Gorumahisani komatiitic rocks with the early to late Archean komatiites from the Kaapvaal, Pilbara, Zimbabwe, Karelian, and Superior Craton as well as from the early Archean Badampahar, Daitari (Singhbhum Craton), and Sargur (Western Dharwar Craton) greenstone belts. Other data from Lahaye et al. (1995); Puchtel et al. (1998, 2004, 2009a, 2009b, 2013); Blichert-Toft et al. (2004); Shimizu et al. (2005); Puchtel and Humayun (2005); Jayananda et al. (2008); Maier et al. (2009); Robin-Popieul et al. (2012); Tushipokla and Jayananda (2013); Sossi et al. (2016); Schneider et al. (2019); Ghosh et al. (2019); Bachhar et al. (2021); and Adhikari et al. (2021a). Komatiitic meta-basalt: Section A Section B Section C; Komatiitic meta-dunite-peridotite: Section A Section B Section C

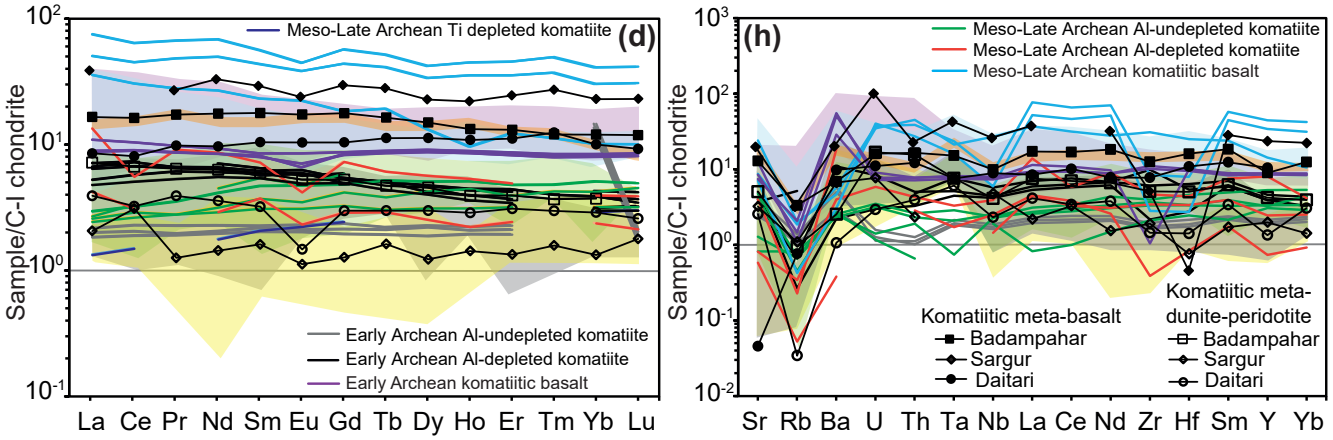

Fig. 18 Continued.

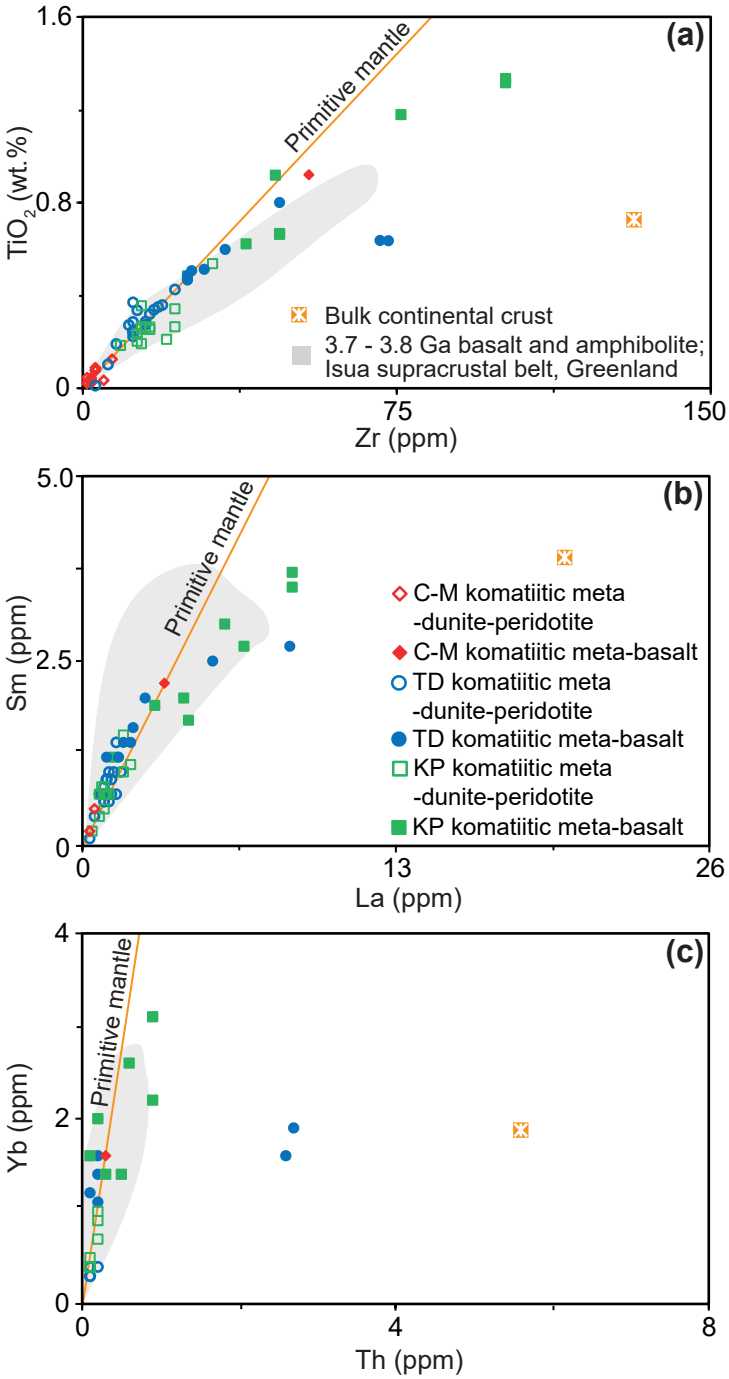

Fig. 19 Plots of **a** Zr vs. TiO_2, **b** La vs. Sm, and **c** Th vs. Yb for the Gorumahishani komatiitic rocks. The saffron colour line illustrates the primitive mantle (McDonough and Sun 1995) ratio of the trace elements. Data of ca. 3.7 - 3.8 Ga basalt and amphibolite rocks (Isua supracrustal belt, Greenland; Polat et al. 2002, 2003; Frei et al. 2004; Polat and Frei 2005; Furnes et al. 2009; Hoffmann et al. 2010) have been incorporated here to check the crustal contamination status of the komatiitic rocks. The bulk continental crust value is from Rudnick and Gao (2014).

Table 8 Bulk-rock major elements data on anhydrous basis (wt.%) and trace elements (ppm) data of komatiitic rocks from the Gorumahishani greenstone belt

Location	Section A	Section A	Section A	Section A	Section A	Section A	Section A	Section A	Section A	Section A	Section A	Section A
Rock Type	Komatiitic meta-peridotite	Komatiitic meta-peridotite	Komatiitic meta-peridotite	Komatiitic meta-peridotite	Komatiitic meta-peridotite	Komatiitic meta-peridotite	Komatiitic meta-peridotite	Komatiitic meta-peridotite	Komatiitic meta-peridotite	Komatiitic meta-peridotite	Komatiitic meta-peridotite	Komatiitic meta-peridotite
Sample	SHB/19-12/20	SHB/19-12/22	SHB/19-12/23	SHB/19-12/24	SHB/19-12/25	SHB/19-12/26	SHB/19-12/27	SHB/19-12/28	SHB/19-12/29	SHB/19-12/30	SHB/19-12/31	SHB/19-12/33
Wt.%												
SiO_2	46.96	47.60	48.33	43.90	46.68	45.82	45.78	45.17	45.77	45.90	46.22	45.66
TiO_2	0.08	0.03	0.05	0.05	0.02	0.05	0.02	0.03	0.03	0.02	0.02	0.02
Al_2O_3	6.88	4.10	3.86	3.76	4.28	3.67	3.46	3.88	3.27	3.89	3.65	3.66
FeO (T)	6.38	7.05	6.34	8.95	7.08	7.12	7.40	7.31	7.32	6.76	6.34	6.74
Cr_2O_3	0.52	0.38	0.38	0.42	0.43	0.36	0.33	0.36	0.33	0.35	0.37	0.37
MnO	0.10	0.10	0.08	0.11	0.09	0.09	0.09	0.09	0.08	0.09	0.10	0.06
MgO	34.71	40.34	40.41	41.37	40.42	42.82	42.44	42.64	43.14	42.80	43.22	43.32
CaO	4.12	0.37	0.52	1.41	0.93	0.05	0.42	0.48	0.02	0.11	0.01	0.10
Na_2O	0.22	0.02	0.05	0.02	0.07	0.03	0.05	0.03	0.03	0.05	0.06	0.06
BaO												
K_2O	0.02											
P_2O_5												
Total	99.99	100.00	100.00	99.99	100.00	100.00	100.00	100.00	100.00	99.98	100.00	99.99
ppm												
LI	2.10	2.50	2.70	1.30	3.20	2.80	2.20	1.60	1	1	0.90	0.90
Be					0.08	0.07	0.07			0.06	0.07	0.08
Cd	0.03		0.03		0.04	0.04	0.04					0.03
Ge	0.84	0.89	0.75	0.67	0.8	0.66	0.71	0.63	0.68	0.72	0.62	0.73
In	0.01											
Sc	21	15	13	13	15	14	13	14	12	13	12	12
V	92	45	45	70	55	49	44	50	50	43	78	38
Cr	3217	2417	2392	2634	2591	2271	2004	2275	2057	2101	2270	2164
Co	91	79.60	81.50	94	76	73.90	88.70	86.30	65.90	62.60	73.40	64.20
Ni	1723.90	2026.30	2119.30	1975.10	2140.90	1984.80	1931.60	1955.50	1710	1475.10	1876.40	1906.90

Cu		1.20	1.20	3.30	0.90	2.30	1.40	4.50	2.10	1.60	2.80	
Ag	0.01							0.10			0.02	0.01
Zn	47	39	33	46	37	36	32	38	44	30	43	30
Ga	4.50	2.70	2.60	2.20	2.10	2.50	2.80	2.10	2	1.60	1.50	2
Rb	0.20	0.50	0.70	0.40	0.40	0.40	0.30	0.50	0.50	0.70	0.30	
Sr	29.80	3.40	4.80	21.20	3.70	1.30	7.40	5.50	0.50			1.20
Y	3.30	1.30	1.30	3.20	1.40	1.40	1	1.30	2.30	1.30	2.60	1.90
Zr	3	2	2	1	1			2	2	1	1	2
Nb					0.20		0.10					
Mo												
Cs		0.10	0.10	0.10	0.30		0.30	0.10		0.20	0.10	
Ba	40.90	4.50	10.60	35.30		22.40	17.70	9.20	10.80	7.40	24.70	2.50
La												
Ce												
Pr												
Nd	0.10	0.10		0.10		0.10	0.10		0.10	0.20		
Sm									0.10			
Eu												
Gd	0.20	0.10	0.10	0.20	0.10	0.10			0.20			0.10
Tb												
Dy	0.50	0.20	0.20	0.40	0.20	0.20	0.10	0.20	0.40	0.20	0.30	0.30
Ho	0.10			0.10					0.10			
Er	0.40	0.20	0.20	0.40	0.20	0.20	0.20	0.20	0.30	0.20	0.20	0.20
Tm												
Yb	0.40	0.20	0.30	0.40	0.30	0.20	0.20	0.20	0.30	0.20	0.30	0.30
Lu												
Hf				0.10								
Ta							0.10			0.10	0.10	
Pb	1.90	1.30	1.20	1.10	2.10	3.30	0.80	1.40	0.70			0.60
Sb	0.22	0.30	0.31	0.26	0.16	0.21	0.30	0.33	0.31	0.33	0.24	0.39
Bi	0.04	0.04	0.04	0.02	0.03	0.03	0.02	0.03	0.02	0.02	0.02	0.01
Th												
U												

Location	Section A	Section A	Section A	Section A	Section A	Section A	Section A	Section A	Section B	Section B	Section B	Section B
Rock Type	Komatiitic meta-peridotite	Komatiitic meta-peridotite	Komatiitic meta-peridotite	Komatiitic meta-peridotite	Komatiitic meta-peridotite	Komatiitic meta-peridotite	Komatiitic meta-peridotite	Komatiitic meta-basalt	Komatiitic meta-peridotite	Komatiitic meta-peridotite	Komatiitic meta-peridotite	Komatiitic meta-peridotite
Sample	SHB/19-12/34	SHB/19-12/35	SHB/19-12/36	SHB/19-12/37	SHB/19-12/39	SHB/19-12/18	SHB/19-12/19	SHB/19-12/21	SHB/18/12	MIC/16/31	MIC/16/32	MIC/16/33
Wt.%												
SiO_2	48.12	52.02	45.31	45.74	46.67	47.30	47.13	51.79	45.79	46.75	47.73	47.29
TiO_2	0.09	0.03	0.03	0.03	0.13	0.08	0.08	0.92	0.10	0.35	0.34	0.22
Al_2O_3	5.89	4.27	5.13	4.74	1.42	5.50	6.43	8.70	0.84	2.40	1.55	0.76
FeO (T)	8.03	6.87	7.46	7.52	10.19	7.90	7.50	15.43	9.96	13.66	13.19	10.94
Cr_2O_3	0.54	0.47	0.41	0.63	0.14	0.43	0.45	0.12	0.15	0.25	0.24	0.19
MnO	0.10	0.11	0.09	0.10	0.15	0.12	0.11	0.23	0.10	0.19	0.15	0.19
MgO	33.52	29.12	40.02	40.10	40.98	35.01	33.09	9.33	42.76	32.21	30.53	38.22
CaO	3.51	6.82	1.44	1.07	0.24	3.46	4.96	11.24	0.22	4.13	6.17	2.09
Na_2O	0.19	0.27	0.07	0.07	0.05	0.17	0.23	1.81	0.06	0.07	0.05	0.04
BaO								0.01				
K_2O	0.01	0.02				0.01	0.02	0.35	0.01			
P_2O_5					0.02		0.01	0.06		0.01	0.05	0.01
Total	100.00	100.00	99.96	100.00	99.98	99.97	100.00	100.00	99.99	100.00	100.00	99.96
ppm												
LI	2	2.50	2.30	2.80	3.50	1.90	1.80	2.30		0.90	1.20	1.50
Be	0.13	0.08			0.09			0.32	0.16	0.18	0.12	0.12
Cd	0.07	0.05			0.03		0.03	0.06		0.04	0.07	
Ge	0.92	0.86	0.66	0.73	0.95	0.68	0.63	0.94	0.93	0.86	0.91	1.36
In	0.01	0.01	0.01	0.01	0.01	0.01	0.02	0.06	0.01	0.02	0.02	
Sc	21	15	16	14		22	18	35		15	11	
V	90	74	64	59	37	100	101	277	32	89	113	51
Cr	3361	3010	2490	3699	872	3243	2935	852	900	1656	1434	1271
Co	95.90	72.60	82.30	82.80	98.50	88.20	89	70.60	101	96.10	91.40	93
Ni	1824.90	1281.30	1642.30	1879.00	2321.50	1578.10	1522.10	218.80	2461.7	1405.30	1609.60	1722.60
Cu	14.10			3	2.80	1.30	3.30	91.70		80.40	157.50	20.40

Ag	0.02	0.03	0.03	0.01	0.02			0.01	0.05		0.04	
Zn	59	74	35	63	52	43	45	110	46	79	57	92
Ga	3.50	2.40	2.70	3.10	1.40	4.30	3.80	13.50	1.2	3	2.10	1.30
Rb	0.50	0.40	0.40	0.20	0.50	0.80	0.30	6.60	1.1	0.30	0.60	0.40
Sr	45.90	18.80	7.30	3	2.20	39.40	46.40	122.40	0.8	20.50	59.90	12.30
Y	3.40	3.10	2	2	2.40	3.40	4	16.50	1.8	4.60	4.30	3.90
Zr	3	2	5	2	7	3	3	54	6	18	13	12
Nb	0.20	0.10			0.30			2.50	0.4	1	0.70	0.70
Mo					0.1			0.2				
Cs	0.30		0.40	0.30	0.30	0.30	0.20	0.30	0.5		0.20	0.10
Ba	17.20	19.50	27.60	10.40	3.40	8.10		40	19.6	17	21.60	8.40
La	0.30				0.50			3.40	0.5	1.20	1	0.90
Ce	0.70				1.50			9.30	1.8	2.90	3.20	2.50
Pr					0.20			1.60	0.3	0.50	0.50	0.50
Nd	0.40	0.40	0.20	0.20	1.60	0.20	0.40	6.80	1.4	3.10	2.90	2.10
Sm	0.20				0.50	0.10	0.10	2.20	0.4	0.90	0.90	0.80
Eu								0.9		0.30	0.30	0.30
Gd	0.20	0.10	0.10	0.20	0.40	0.30	0.30	3.20	0.5	1	1.10	0.90
Tb								0.50		0.20	0.20	0.10
Dy	0.60	0.50	0.30	0.30	0.50	0.50	0.70	3.40	0.5	1	1.20	0.90
Ho	0.10	0.10		0.10		0.10	0.10	0.80		0.20	0.20	0.20
Er	0.50	0.40	0.20	0.30	0.30	0.40	0.40	2.00	0.1	0.50	0.50	0.50
Tm								0.30				
Yb	0.50	0.60	0.30	0.30	0.20	0.40	0.40	1.60	0.2	0.30	0.40	0.30
Lu								0.20				
Hf	0.20		0.10		0.20	0.20	0.10	1.50	0.2	0.60	0.40	0.30
Ta	0.10			0.10	0.10			0.30	0.2	0.10	0.10	
Pb	2.40	0.80	2.20	0.80	0.50	0.70	0.90	1.30		0.70	0.90	0.90
Sb	2.29	0.25	1.71	1.21	0.67	0.24	0.25	0.16	0.54	1.11	0.98	1.60
Bi	0.06	0.03		0.01	0.04	0.02	0.03	0.04	0.02	0.08	0.05	0.14
Th								0.30		0.10	0.10	
U												

Location	Section B	Section B	Section B	Section B	Section B	Section B	Section B	Section B	Section B	Section B	Section B	Section B
Rock Type	Komatiitic meta-peridotite	Komatiitic meta-peridotite	Komatiitic meta-peridotite	Komatiitic meta-peridotite	Komatiitic meta-peridotite	Komatiitic meta-peridotite	Komatiitic meta-peridotite	Komatiitic meta-peridotite	Komatiitic meta-peridotite	Komatiitic meta-peridotite	Komatiitic meta-peridotite	Komatiitic meta-peridotite
Sample	MIC/16/34	MIC/16/35	MIC/16/36	MIC/16/37	MIC/16/38	MIC/16/39	MIC/16/40	MIC/16/41	MIC/16/42	MIC/16/43	MIC/16/44	SHB/18/16
Wt.%												
SiO_2	46.52	46.95	46.63	46.52	46.04	46.79	46.21	45.75	46.96	46.67	46.59	46.15
TiO_2	0.29	0.25	0.29	0.27	0.19	0.24	0.37	0.01	0.34	0.36	0.27	0.24
Al_2O_3	1.51	1.74	2.39	1.81	2.46	1.59	2.29	0.31	1.88	1.95	1.62	1.41
FeO (T)	11.89	10.66	12.20	12.14	9.79	11.51	14.24	12.21	13.32	13.19	11.32	11.01
Cr_2O_3	0.21	0.19	0.23	0.22	0.20	0.21	0.25	0.10	0.24	0.25	0.22	0.20
MnO	0.20	0.19	0.18	0.20	0.17	0.19	0.20	0.08	0.17	0.21	0.20	0.20
MgO	36.19	37.66	34.11	35.21	40.05	35.28	31.43	41.45	31.84	31.63	33.87	37.76
CaO	2.93	2.21	3.89	3.42	0.93	3.95	4.88	0.02	5.11	5.61	5.82	2.92
Na_2O	0.04	0.06	0.07	0.08	0.03	0.08	0.11	0.04	0.13	0.11	0.07	0.06
BaO											0.01	
K_2O							0.01			0.01		
P_2O_5	0.01	0.01	0.01	0.01	0.01	0.00	0.02		0.01	0.02	0.01	0.01
Total	99.79	99.92	99.98	99.86	99.87	99.84	100.00	99.98	100.00	100.00	99.99	99.96
ppm												
LI	1.40	1.10	1.10	0.90	1.10	1	1.30	0.30	1.10	2	2.10	1.10
Be	0.06	0.08	0.08	0.09	0.07	0.07	0.17	0.19	0.11	0.16	0.11	0.10
Cd		0.03	0.07	0.02		0.03	0.06		0.06	0.07	0.02	0.02
Ge	1	1.17	1.40	0.87	0.85	0.79	1.04	1.59	1.05	1.04	1.16	0.73
In	0.02	0.02	0.02	0.02	0.02	0.02	0.03		0.02	0.02	0.01	
Sc	11		13	11		11	15		13	15	12	10
V	60	53	80	63	26	81	96	13	82	86	64	57
Cr	1328	1197	1548	1339	1306	1316	1710	608	1501	1710	1358	1257
Co	108	90.80	92.10	101.30	113.50	110.40	100.30	49.40	106.60	111.40	92.70	103.30
Ni	1986.10	1883.60	1736.90	1834.60	2270	1932.90	1601.10	1188	1805.30	1738	1837.80	1980.60
Cu	10.80	14.20	116.10	14.30	9.20	24.60	18.50	29.60	49.80	42.90	12.70	
Ag		0.02		0.02		0.05		0.01	0.02			0.02

Zn	78	74	68	76	72	73	85	50	70	59	72	101
Ga	2	3	3.30	3.60	3.40	2.90	3.40	0.40	2.60	3	2.20	1.90
Rb	0.80	0.20	0.60	0.20	0.70	0.20	0.60	0.60	0.70	0.80	0.50	0.20
Sr	24.90	14.40	28.70	26.80	4.50	20.80	17.70	0.40	28	50.70	10	4.10
Y	4.10	3.30	4.30	3.40	3.10	3.50	5.50	0.90	4.70	5.10	3.70	3.70
Zr	15	12	12	15	8	12	12	3	17	19	11	12
Nb	0.80	0.70	0.70	0.80	0.60	0.80	1	0.20	0.90	1	0.70	0.60
Mo					0.1							
Cs	0.60	0.30	0.20	0.40	0.30	0.50	0.20	0.20	0.20	0.30	0.40	0.40
Ba	22.40	47.30	9.30	21.90	13.70	13.20	16.30	36	46.70	19.70	23	16.70
La	1	0.80	1	1.10	0.70	0.90	1.40	0.30	1.40	1.30	1.20	0.90
Ce	3	2.40	3	4	2.10	2.90	3.80	0.60	3.50	4.10	3.10	2.70
Pr	0.50	0.40	0.40	0.50	0.30	0.40	0.70	0.10	0.60	0.60	0.50	0.40
Nd	3	1.90	2.60	2.30	1.80	2.40	3.80	0.40	3.60	3.60	2.60	2.50
Sm	0.90	0.70	0.90	0.60	0.70	0.60	1.40	0.10	0.70	1	0.70	0.60
Eu	0.20	0.20	0.30	0.20	0.10	0.30	0.30		0.40	0.30	0.30	0.40
Gd	1	0.90	0.80	0.70	0.70	1	1.30		1.20	1.30	0.90	0.80
Tb	0.10	0.10	0.20	0.10	0.10	0.10	0.20		0.20	0.20	0.10	0.10
Dy	0.80	0.90	0.80	0.90	0.50	0.80	1.20	0.20	0.90	1.30	0.80	0.60
Ho	0.10	0.20	0.10	0.20	0.10	0.10	0.20		0.20	0.20	0.20	0.20
Er	0.50	0.40	0.50	0.60	0.30	0.40	0.70		0.60	0.60	0.40	0.40
Tm												
Yb	0.30	0.40	0.40	0.40	0.30	0.50	0.30		0.40	0.40	0.30	0.30
Lu												
Hf	0.50	0.40	0.40	0.40	0.30	0.30	0.50		0.40	0.60	0.30	0.40
Ta		0.10		0.10		0.10	0.10	0.20	0.20	0.10	0.20	0.10
Pb	0.80	0.90	0.90	0.90	0.90	0.80	1	0.60	0.60	0.90	1	0.60
Sb	1.31	1.66	1.55	1.16	1.29	1.57	0.83	1.51	0.51	0.47	0.20	0.12
Bi	0.13	0.18	0.13	0.11	0.04	0.03	0.30	0.81	0.02	0.03		0.01
Th				0.20					0.10	0.10	0.10	
U												

Location	Section B	Section B	Section B	Section B	Section B	Section B	Section B	Section B	Section B	Section B	Section C	Section C

Rock Type	Komatiitic meta-peridotite	Komatiitic meta-peridotite	Komatiitic meta-basalt	Komatiitic meta-basalt	Komatiitic meta-basalt	Komatiitic meta-basalt	Komatiitic meta-basalt	Komatiitic meta-basalt	Komatiitic meta-basalt	Komatiitic meta-basalt	Komatiitic meta-peridotite	Komatiitic meta-peridotite
Sample	SHB/18/17	SHB/18/18	MIC/16/30	SHB/18/14	SHB/19-12/52	SHB/19-12/53	SHB/19-12/56	SHB/19-12/57	SHB/19-12/58	SHB/19-12/59	SHB/18/20	SHB/18/21
Wt.%												
SiO_2	45.90	46.40	51.72	52.04	51.54	52.61	57.85	57.95	49.27	51.71	45.92	45.86
TiO_2	0.32	0.43	0.51	0.80	0.60	0.51	0.64	0.64	0.49	0.47	0.34	0.36
Al_2O_3	1.80	2.03	5.17	8.17	8.60	11.52	11.19	11.34	12.20	12.10	5.27	4.98
FeO (T)	12.61	14.67	11.66	14.06	12.29	11.37	11.10	11.05	12.94	11.52	13.82	13.69
Cr_2O_3	0.24	0.28	0.22	0.12	0.17	0.08	0.04	0.05	0.10	0.10	0.43	0.46
MnO	0.19	0.20	0.21	0.21	0.23	0.20	0.17	0.18	0.24	0.20	0.20	0.18
MgO	35.25	27.72	14.87	10.69	12.74	9.24	7.07	6.96	10.75	10.11	28.80	29.62
CaO	3.60	8.10	14.83	11.87	11.98	12.53	8.37	8.44	12.29	10.89	4.94	4.64
Na_2O	0.07	0.09	0.68	1.62	1.43	1.68	2.13	2.47	1.09	1.82	0.13	0.11
BaO			0.01	0.01	0.01	0.01	0.03	0.02	0.02	0.02		
K_2O		0.01	0.08	0.34	0.26	0.21	1.30	0.81	0.59	1.02	0.02	0.02
P_2O_5	0.01	0.02	0.03	0.06	0.15	0.03	0.10	0.09	0.03	0.03	0.04	0.03
Total	99.98	99.94	100.00	100.00	100.00	100.00	100.00	100.00	100.00	100.00	99.91	99.96
ppm												
LI	1.30	1	5.80	9.70	7.30	7.90	9.20	7.20	32.50	23.70	1.2	1.50
Be	0.09	0.17	0.19	0.23	9.59	0.76	0.82	0.92	0.15	0.74	0.21	0.16
Cd	0.02	0.04	0.08	0.13	0.09	0.06	0.08	0.13	0.10	0.04	0.09	0.06
Ge	0.81	1.02	1.51	1.19	1.94	1.10	1.30	1.40	0.96	1.17	0.87	0.71
In	0.01	0.02	0.04	0.05	0.05	0.05	0.04	0.04	0.04	0.04	0.03	0.02
Sc	13	16	40	41	32	45	24	24	42	41	15	12
V	77	109	210	291	225	253	194	194	249	239	112	69
Cr	1607	1754	1597	898	1179	573	308	326	633	677	2742	1457
Co	114	99.30	69.80	69.20	68.60	49.80	41.20	42.60	53.90	50.10	106.2	106.20
Ni	1967.20	1364.40	356.30	207.20	457.90	160	65.40	66.60	170.30	191.20	1149.7	1272.70
Cu	2.80	5	86.60	55.50	28.80	29.40	68.50	43.30	53.30	66.10	63	58.60
Ag		0.02			0.05	0.04	0.02	0.01	0.12	0.02	0.09	
Zn	73	65	73	107	102	83	80	82	88	76	81	83

Ga	2.80	3.50	6.80	12.10	11.40	12	11.20	11.90	10	11.20	5.3	3
Rb	1	0.60	1.80	7.60	5.90	5.20	47.70	25.50	22	44.80	1.2	0.70
Sr	12.20	19	71.90	106.10	76.50	94.90	140.30	123.60	73.90	105.80	21.2	17.60
Y	4.10	5	10.60	16.20	11.60	12	16.50	16.30	10.60	11.10	7.5	4.50
Zr	16	22	29	47	34	26	71	73	25	25	22	14
Nb	1	1.20	1.40	1.70	2.50	0.90	5	4.70	1	1.20	1.2	0.60
Mo			0.1	0.1	0.2	0.3	0.5	0.2		0.1		
Cs	0.40	0.20	0.10		0.20	0.20	0.70	0.40	0.90	1	0.6	0.30
Ba	22.30	9.20	39.70	22.50	37.80	43	248	147.50	76.30	107.30	54.9	20.10
La	1.10	1.60	2.10	2.60	2	1.50	8.60	5.40	1	1.70	2	0.90
Ce	3.50	4.70	5.30	7.20	5.70	4.10	19.30	12.50	3.30	4	4.8	2.30
Pr	0.60	0.70	0.80	1.10	0.90	0.70	2.30	2	0.60	0.70	0.6	0.40
Nd	3.10	3.70	3.80	5.90	4.50	3.70	10.30	8.70	2.80	3.10	3	1.90
Sm	1	1	1.60	2	1.40	1.20	2.70	2.50	1.20	1.40	1.1	0.70
Eu	0.30	0.40	0.60	0.80	0.70	0.50	0.70	0.90	0.30	0.40	0.5	0.30
Gd	1	1.30	1.70	2.70	2	2.10	3.10	3	1.90	1.50	1.2	0.80
Tb	0.20	0.20	0.40	0.50	0.40	0.30	0.50	0.50	0.30	0.30	0.2	0.10
Dy	0.90	1.40	2.10	3	2.20	2.50	3.10	2.90	1.90	1.90	1.4	0.90
Ho	0.20	0.30	0.40	0.60	0.50	0.50	0.60	0.80	0.40	0.50	0.3	0.20
Er	0.50	0.70	1.10	1.90	1.40	1.60	1.90	1.70	1.40	1.30	0.9	0.50
Tm			0.20	0.20	0.20	0.20	0.30	0.30	0.20	0.20	0.1	
Yb	0.30	0.50	1.10	1.60	1.40	1.30	1.60	1.90	1.20	1.30	1	0.30
Lu			0.20	0.20	0.20	0.20	0.30	0.30	0.20	0.20	0.1	
Hf	0.50	0.60	0.90	1.30	0.90	0.80	1.80	1.80	0.70	0.80	0.6	0.50
Ta		0.10		0.10	0.20	0.10	0.50	0.50	0.20	0.20	0.2	0.20
Pb		0.60	0.90	1.20	1.20	1.30	4.30	3.50	1	1.20	0.7	0.80
Sb	0.34	0.13	0.12	0.09	0.12	0.28	0.74	0.58	0.20	0.34	0.11	0.13
Bi	0.02	0.02	0.01	0.04	0.31	0.29	0.03	0.03	0.08	0.16	0.01	0.01
Th		0.10	0.20	0.20	0.20		2.60	2.70	0.10		0.2	
U					0.10		0.70	0.60				

Location	Section C	Section C	Section C	Section C	Section C	Section C	Section C	Section C	Section C	Section C	Section C	Section C
Rock	Komatiitic	Komatiitic	Komatiitic	Komatiitic	Komatiitic	Komatiitic	Komatiitic	Komatiitic	Komatiitic	Komatiitic	Komatiitic	Komatiitic

Type	meta-peridotite	meta-peridotite	meta-peridotite	meta-peridotite	meta-peridotite	meta-peridotite	meta-peridotite	meta-peridotite	meta-peridotite	meta-peridotite	meta-peridotite	meta-peridotite
Sample	SHB/18/22	SHB/18/23	SHB/18/24	SHB/18/25	SHB/18/36	SHB/19-12/77	SHB/19-12/78	SHB/19-12/79	SHB/19-12/80	SHB/19-12/81	SHB/19-12/82	SHB/18/37
Wt.%												
SiO_2	45.51	45.34	45.38	47.95	45.81	45.53	45.72	44.82	45.09	45.49	45.48	48.07
TiO_2	0.21	0.27	0.26	0.19	0.20	0.26	0.27	0.25	0.23	0.26	0.25	0.18
Al_2O_3	2.37	2.68	2.60	5.62	2.38	2.85	2.62	2.58	2.51	2.84	2.73	5.04
FeO (T)	10.87	11.16	11.39	9.97	10.79	11.54	11.45	11.79	11.57	11.54	11.45	9.51
Cr_2O_3	0.20	0.22	0.21	0.48	0.20	0.21	0.23	0.23	0.21	0.21	0.21	0.38
MnO	0.17	0.15	0.15	0.13	0.16	0.15	0.16	0.17	0.16	0.16	0.15	0.15
MgO	37.98	37.19	36.21	27.58	39.37	35.75	36.74	36.33	37.30	35.94	35.89	32.39
CaO	2.48	2.77	3.53	7.57	0.99	3.45	2.65	3.64	2.67	3.23	3.57	4.16
Na_2O	0.08	0.09	0.12	0.49	0.06	0.13	0.09	0.08	0.10	0.15	0.14	0.08
BaO										0.01		
K_2O		0.01		0.02								0.02
P_2O_5	0.02	0.02	0.01	0.00	0.01	0.02	0.02	0.02	0.01	0.02	0.02	0.01
Total	99.88	99.89	99.87	100.00	99.97	99.90	99.93	99.89	99.85	99.86	99.91	100.00
ppm												
LI	0.70	1.70	1.30	2.20	5.70	1.80	1.60	1.20	0.80	1.20	1.30	1.80
Be		0.05	0.09	0.06	0.12	0.08	0.05	0.06	0.07	0.08	0.08	
Cd	0.03	0.02		0.03	0.02	0.04		0.02		0.05	0.03	0.05
Ge	0.69	0.79	0.74	0.90	0.81	0.73	0.91	0.84	0.81	0.77	0.72	0.75
In	0.01	0.02	0.02	0.02	0.02	0.01	0.02	0.02	0.01	0.02	0.02	0.01
Sc	11	16	13	22		12	13	14	12	12	12	22
V	61	111	71	109	51	74	117	78	69	69	76	109
Cr	1241	2946	1397	2997	1223	1279		1529	1346	1266	1393	2537
Co	105.20	105.70	106	84.10	106.20	103.60	100.10	110.90	110.10	108.90	106	87.10
Ni	2011.60	1938.30	1865.30	932.30	2069.50	1834.80	1924.10	1897.20	1959.70	1850.90	1855.50	1658.60
Cu	31.20	13.70	20.60	7.80	5.10	10.60	2.10	45.10	1.30	4.60		18.20
Ag	2.92			0.02	0.06	0.01			0.01	0.01		
Zn	56	52	54	60	64	49	59	62	55	48	50	53
Ga	2.30	5.20	3.20	4.50	1.90	3.20		2.80	3.10	3.10	3	5.20

Rb	0.70	1	0.70	0.90	0.10	0.40		0.80	0.40	1.20	0.90	2.60
Sr	10.30	23.90	28.30	77.80	5.20	23.10		16.60	17.60	29.60	27.90	15.30
Y	3.80	7.80	5.20	5.30	3.90	4.50		5	4.60	4.50	4.80	4.90
Zr	20	22	14	14	13	16		16	13	15	14	9
Nb	0.60	1.30	0.70	0.50	0.70	0.70		0.70	0.70	0.80	0.60	0.20
Mo												
Cs	0.40	0.40	0.60	0.60	0.80	0.60		0.50	0.50	0.60	0.50	1.40
Ba	17.20	26.60	20.90	13.50	86.20	7.60		14.30	13.10	16.90	44.40	17.40
La	0.70	1.70	0.90	0.70	0.90	1.10		0.90	0.90	1	0.80	0.40
Ce	2.20	4.60	2.40	1.80	2.40	2.80		2.50	2.40	2.70	2.20	0.80
Pr	0.40	0.60	0.40	0.30	0.40	0.40		0.30	0.40	0.40	0.40	0.20
Nd	1.60	3.30	2.10	1.40	1.60	1.70		2.20	2.40	2.10	1.80	1.10
Sm	0.70	1	0.80	0.40	0.70	0.70		0.50	0.70	0.70	0.80	0.20
Eu	0.20	0.30	0.30	0.10	0.30	0.20		0.30	0.30	0.30	0.20	0.20
Gd	0.80	1.20	1	0.60	0.60	0.60		0.90	1	0.90	0.90	0.40
Tb	0.10	0.20	0.10	0.10	0.10	0.10		0.10	0.10	0.10	0.20	0.10
Dy	0.80	1.30	1	0.90	0.80	1		1	1.10	1	0.90	0.80
Ho	0.20	0.30	0.20	0.20	0.20	0.20		0.20	0.20	0.20	0.20	0.20
Er	0.40	0.90	0.70	0.60	0.50	0.60		0.60	0.50	0.60	0.60	0.50
Tm		0.10					0.50		1.30			
Yb	0.50	0.90	0.40	0.70	0.40	0.40		0.50	0.40	0.50	0.40	0.40
Lu		0.10					0.50					0.10
Hf	0.40	0.60	0.50	0.30	0.30	0.50		0.40	0.40	0.40	0.40	0.40
Ta		0.10	0.10	0.10	0.20	0.20			0.20	0.20	0.30	
Pb	0.60	0.70	0.90	0.80	1.30	0.60	0.90	0.80	0.50	0.60	0.50	1
Sb					0.82							0.41
Bi	0.02	0.03		0.05	0.08	0.02		0.02	0.05	0.03	0.01	0.02
Th		0.20	0.10	0.20		0.10		0.10	0.10			
U							7					

Location	Section C	Section C	Section C	Section C	Section C	Section C	Section C	Section C	Section C
Rock Type	Komatiitic meta-	Komatiitic meta-	Komatiitic meta-	Komatiitic meta-	Komatiitic meta-	Komatiitic meta-	Komatiitic meta-	Komatiitic meta-	Komatiitic meta-

Sample	peridotite SHB/18/39	basalt SHB/18/31	basalt SHB/19-12/83	basalt SHB/19-12/84	basalt SHB/19-12/60	basalt SHB/19-12/61	basalt SHB/18/27	basalt SHB/19-12/73	basalt SHB/19-12/76
Wt.%									
SiO_2	48.95	52.19	48.26	52.98	49.14	48.92	49.14	51.79	54.04
TiO_2	0.54	0.67	0.66	0.48	0.92	1.33	1.18	1.32	0.62
Al_2O_3	5.42	7.99	10.98	12.01	7.94	13.09	14.81	13.29	9.63
FeO (T)	13.28	13.51	13.09	11.36	15.27	13.22	15.54	14.85	11.76
Cr_2O_3	0.28	0.20	0.15	0.07	0.15	0.08	0.03	0.02	0.14
MnO	0.21	0.24	0.22	0.19	0.25	0.41	0.26	0.21	0.19
MgO	20.90	11.44	11.38	9.61	12.37	6.25	6.16	5.24	9.84
CaO	9.38	11.54	13.74	10.84	11.92	13.61	8.50	8.45	10.57
Na_2O	0.97	2.01	0.96	2.17	1.61	2.23	3.44	4.03	3.02
BaO		0.01	0.02	0.01	0.01	0.02	0.02	0.02	0.01
K_2O	0.04	0.14	0.48	0.24	0.32	0.75	0.69	0.52	0.13
P_2O_5	0.03	0.07	0.06	0.03	0.09	0.08	0.10	0.13	0.06
Total	100.00	100.00	100.00	100.00	100.00	100.00	99.86	99.88	100.00
ppm									
LI	1.10	2.30	20.40	4.80	7.50	17	23.10	9.20	2.40
Be	0.11	0.31	0.33	0.12	0.46	1.22	0.30	0.99	0.26
Cd	0.09	0.10	0.04	0.08	0.11	0.12	0.13	0.11	0.06
Ge	1.19	1.19	0.94	1.27	1.17	1.22	0.66	1.11	1.12
In	0.03	0.05	0.08	0.04	0.06	0.06	0.08	0.07	0.05
Sc	24	31	31	40	30	34	37	30	30
V	155	201	215	244	207	273	335	298	204
Cr	1875	1341	992	489	1014	564	183	131	950
Co	60.10	65.40	61.70	49	71.80	86	57.60	47.70	57.20
Ni	855	292	259.70	146	276.90	286.10	113.90	77.20	222.80
Cu	75.30	63.90	1.80	20.40	109	92.90	94.40	124.50	39.70
Ag	0.02	0.06	0.05	0.02	0.02	0.03	0.12	0.07	0.07
Zn	84	101	81	75	104	123	112	123	86
Ga	7.30	8.90	13.80	8.10	9.80	15.30	17.30	18.40	9.90
Rb	0.60	3.30	15.80	8	4	22.60	23.90	12.20	2.80

Sr	67.80	102.40	221	142.40	77.60	182.40	333.50	220.90	87.50
Y	10.30	13.90	17.80	11.40	13.70	21.70	25.30	27.40	13.70
Zr	31	47	47	25	46	101	76	101	39
Nb	1.20	2.50	2	1	3.30	6.90	4.90	7	2.10
Mo			0.10			0.30	0.20	0.40	0.40
Cs	0.20	0.20	0.50	0.40	0.20	0.90	0.80	0.30	
Ba	19.40	22.70	99.80	7.50	47.60	89.70	142.50	85.80	25.90
La	1.70	4.20	3	1.30	6.70	8.70	5.90	8.70	4.40
Ce	4.20	10.80	8.40	3.90	17.60	21	15.30	21.80	10
Pr	0.80	1.40	1.40	0.60	2.50	3	2.10	3.10	1.50
Nd	4.70	7.10	5.90	3.80	11.90	14.40	11	14.40	7.30
Sm	1.50	2	1.90	1.20	2.70	3.50	3	3.70	1.70
Eu	0.50	0.80	0.90	0.40	1	1.10	1.30	1.30	0.90
Gd	1.80	2.30	3	1.90	3.60	4.30	3.70	4.20	2.50
Tb	0.30	0.40	0.60	0.30	0.60	0.70	0.70	0.70	0.50
Dy	1.90	2.70	3.40	1.90	3.30	4.60	4.50	4.90	2.70
Ho	0.40	0.60	0.90	0.50	0.70	0.90	1	1.10	0.50
Er	1.20	1.50	2	1.40	1.70	2.50	2.70	3.30	1.70
Tm	0.20	0.20	0.40	0.20	0.30	0.40	0.40	0.50	0.20
Yb	1.10	1.40	2	1.20	1.60	2.20	2.60	3.10	1.40
Lu	0.10	0.20	0.30	0.20	0.30	0.30	0.40	0.50	0.30
Hf	0.80	1.20	1.40	0.70	1.40	2.60	2.20	3.20	1.30
Ta	0.20	0.20	0.20	0.10	0.40	0.70	0.30	0.50	0.20
Pb	0.60	1.30	1.90	0.60	1.10	4	3.40	2.80	1.20
Sb		0.07	0.55	0.07	0.10	0.19	0.19	0.15	0.06
Bi	0.02	0.02	0.04		0.04	0.33	0.03	0.05	0.06
Th	0.20	0.50	0.20		0.10	0.90	0.60	0.90	0.30
U		0.20				0.30	0.10	0.20	

Rudnick and Gao 2014), and a drastic change in komatiite composition is not expected even after enough contamination of the komatiitic magma (**Fig. 19a-c**).

5.3.2. Platinum-Group element (PGE)

The bulk-rock PGE data of the Gorumahishani komatiitic suite of rocks are plotted against MgO (**Fig. 20a-r**). Section A meta-dunite and meta-peridotite rocks show a weak negative trend in the MgO vs. Pd plot whereas other PGEs show no such correlation with MgO (**Fig. 20a, d, g, j, m, p**). Section B komatiitic meta-dunite, meta-peridotite, and meta-basalt samples also show a negative correlation in MgO vs. Pt, Pd plots (**Fig. 20b, e**). A positive correlation is observed in MgO vs. Ru and Ir plots of section B samples (**Fig. 20h, k**). No such distinct correlation is observed in MgO vs. Pd, Rh, and Os plots for the section C komatiitic rocks, however, Pt and Ru show a positive relation with MgO (**Fig. 20c, f, i, l, r**).

The meta-dunite and meta-peridotites from section A show a weak positive relation in Cr vs. Ir and Ru plots (**Fig. 21j, m**). The komatiitic rocks from section B show a positive relation in the Cr vs. Ru plot and a weak negative relation in the Cr vs. Pt and Pd plots (**Fig. 21b, e, k, n**). The meta-dunite, meta-peridotite, and meta-basalt from section C show a positive relation in Cr vs. Ru, Ir, and Pt plots (**Fig. 21c, l, o**). Os and Rh show no such distinct relationship with Cr for the komatiitic rocks from the three sections (**Fig. 21g-i, p-r**).

PGE ratios like Pd/Ir, Pd/Ru, and Pd/Pt are plotted against MgO and Cr (**Fig. 22a-f**). Pd/Ir and Pd/Ru of the komatiitic rocks from all three sections show negative co-relation with MgO (**Fig. 22b, c**). Pd/Pt shows no such correlation with MgO (**Fig. 22a**). $Pd/Ir_{average}$ = 3.3 and $Pd/Ru_{average}$ = 3.6 are higher in the komatiitic meta-basalts

compared to the komatiitic meta-dunite and meta-peridotite ($Pd/Ir_{average}$ = 1.5, $Pd/Ru_{average}$ = 1.1). All these values from the Gorumahishnai komatiitic rocks are higher than the primitive mantle ratio ($Pd/Ir_{primitive\ mantle}$ = 1, $Pd/Ru_{primitive\ mantle}$ = 0.7; Barnes et al. 1988) indicating their fractionated character. Pd/Ru and Pd/Ir of komatiitic meta-dunite, meta-peridotite, and meta-basalt show a negative correlation with Cr from the samples of the three sections (**Fig. 22e, f**). No such convincing correlation is observed in the Pd/Pt vs. Cr plot (**Fig. 22 d**). The komatiitic rocks from the three sections show a negative trend in the Pd/Ir vs. Ni/Cu plot (**Fig. 22d**) where Ni/Cu is high in komatiitic meta-dunites and meta-peridotites (10.2 - 1689) than the komatiitic meta-basalts (0.62 - 144.3).

The PGEs and their ratios along with MgO, Cr, Ni, Cu, Co, and S concentrations are plotted across the komatiitic sequence in the three sections (**Fig. 23**). Section A komatiitic rocks do not show visible sulfide minerals. Only one meta-dunite sample (SHB/19-12/18) has minor S (0.02 wt.%, **Table 9**) with concentrations of Ni, Cu, Co, and PGEs similar to other samples from this section. Meta-dunite sample SHB/19-12/19 also have marked peaks in Pt (= 8 ppb) and Pd (= 11 ppb) without any S (**Fig. 23**). In contrast, eleven komatiitic meta-dunite and meta-peridotite samples from the cumulate and spinifex zones of sections B and C have visible sulfide minerals. The bulk-rock S for these samples varies from 0.01 to 0.07 wt.% (**Table 9**). From section B komatiitic meta-dunite, the sample MIC/16/34 shows small peaks in Ni (= 1986.1 ppm) and Co (= 108 ppm) and a distinct peak in S (= 0.07 wt.%) but the PGE concentrations are similar to other samples (**Table 9**). On the other hand, meta-dunite sample MIC/16/37 has peaks only in Pt (= 19 ppb) and S (= 0.03 wt.%) whereas meta-peridotite sample MIC/16/41 has peaks in Pt (= 64 ppb),

Pd (= 29 ppb), Rh (= 6 ppb), and Ru (= 8 ppb) without any S (**Fig. 23, Table 9**). Like section B, komatiitic meta-peridotite sample SHB/19-12/79 from section C has a well-defined peak in Cu (= 45.1 ppm) and S (= 0.03 wt.%) but the PGE concentrations are similar to the rest of the samples (**Fig. 23, Table 9**). On the contrary, meta-peridotite samples SHB/18/23 and SHB/18/37 have peaks in platinum-group elements (Pd = 6 ppb, Rh = 4 ppb, Ru = 5 ppb, and Ir = 5 ppb) without any S (**Fig. 23, Table 9**). Komatiitic meta-peridotite sample SHB/19-12/78 from section C also shows a high concentration of S (= 0.04 wt.%) alongside sharp peaks in Pt (= 16 ppb), Pd (= 6 ppb), Ru (= 5 ppb), and Os (= 2 ppb) but Ni, Co, and Cu concentrations are similar to rest of the samples (**Fig. 23, Table 9**). All the meta-basalt samples except two samples from section C (SHB/18/27, SHB/19-12/73; S = 0.05 - 0.06 wt.%) do not have any sulfide minerals in them (**Fig. 23, Table 9**).

In the primitive mantle normalized PGE plots the meta-dunite and meta-peridotite from the three sections show variable enrichment in Pd-group of PGE (PPGE: Pt, Pd, Rh = 0.2 - 2.1 × primitive mantle) and Ir-group of PGE (IPGE: Ru, Ir, Os = 0.2 - 1.1 × primitive mantle) except one sample with anomalously high PPGE (MIC/16/41; PPGE = 3 - 6.9 × primitive mantle; **Fig. 24a-c**). The meta-basalt samples from the three sections show more depletion in IPGE (0.2 - 0.5 × primitive mantle) and similar PPGE (0.2 - 2 × primitive mantle) compared to the meta-dunite and meta-peridotite (**Fig. 24a-c**). Overall the PGEs from most of the meta-dunites, meta-peridotites, and meta-basalts show depleted character (**Fig. 24a-c**). In the meta-dunite and meta-peridotite samples from the three sections, a negative Pt anomaly is observed (0.3 - 0.9 × primitive mantle) except for two samples from section B and one sample from section C (**Fig. 24a-c**). All the komatiitic suite of rocks from three

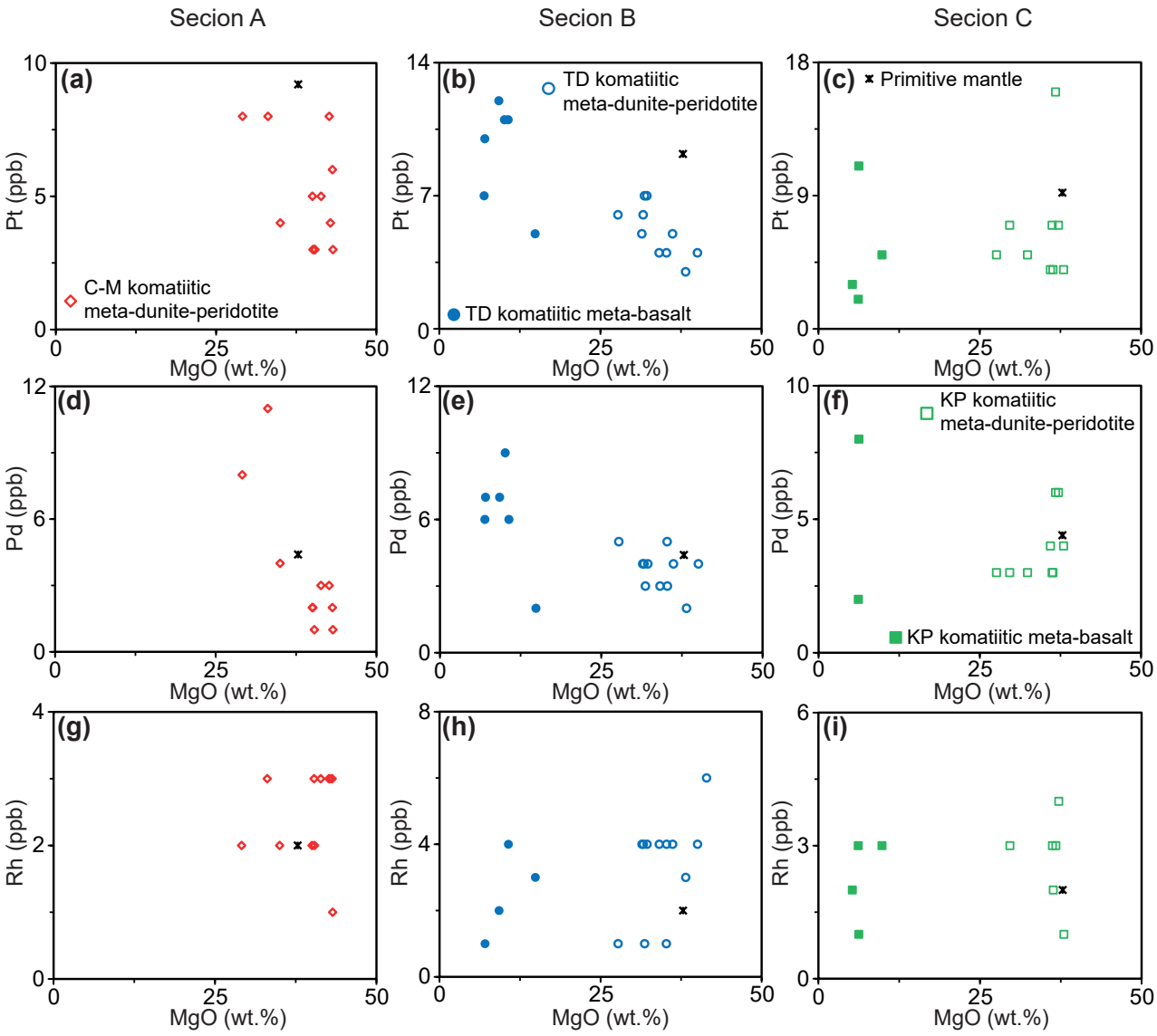

Fig. 20 MgO vs. **a-c** Pt, **d-f** Pd, **g-i** Rh, **j-l** Ru, **m-o** Ir, and **p-r** Os plots for the Gorumahishani komatiitic rock samples from Maharajgunj-Chuka Pahar (Section A), Tua Dungri (Section B), and Kapili (Section C) areas. Primitive mantle values are from McDonough and Sun (1995) and Barnes et al. (1988).

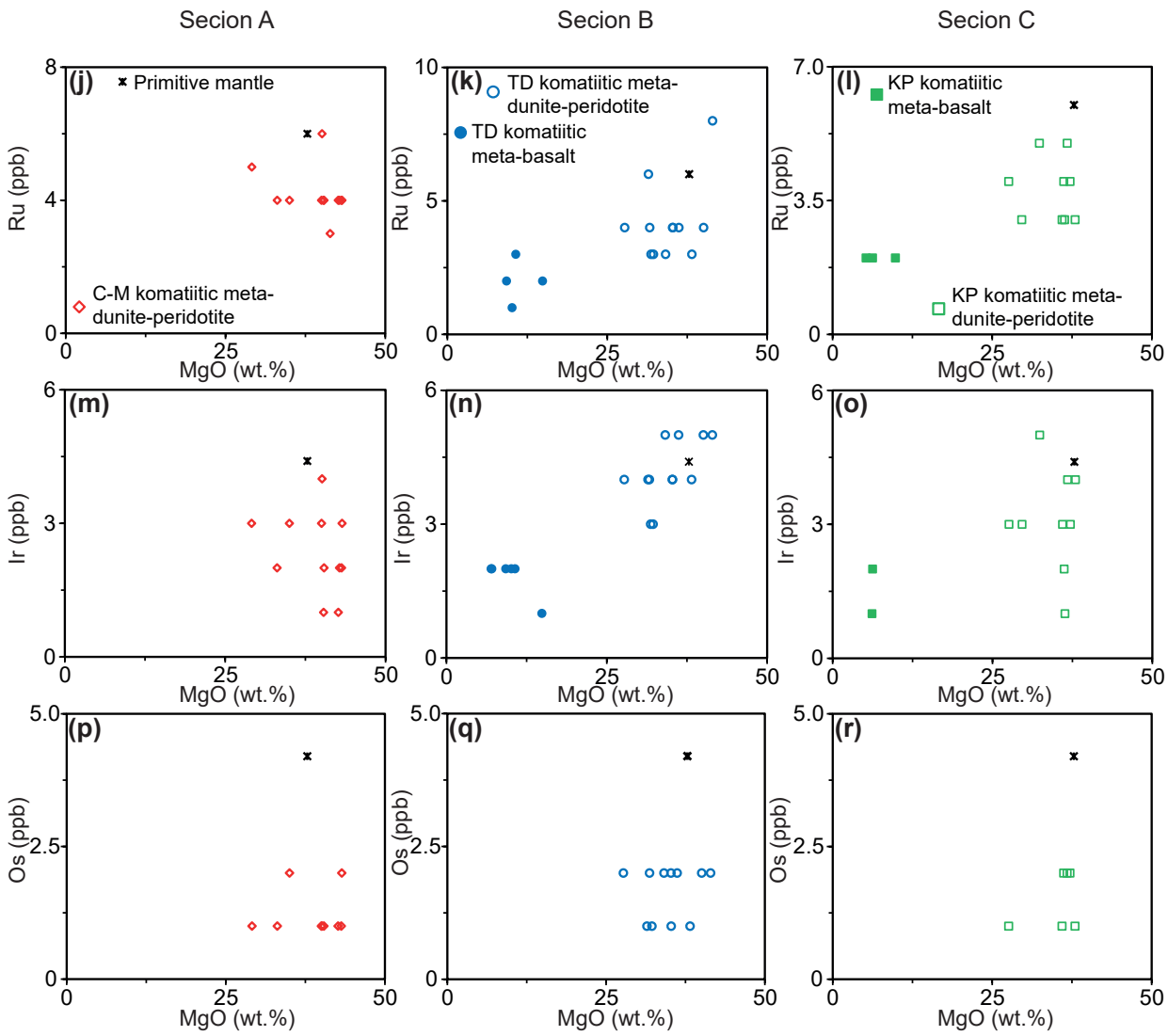

Fig. 20 continued.

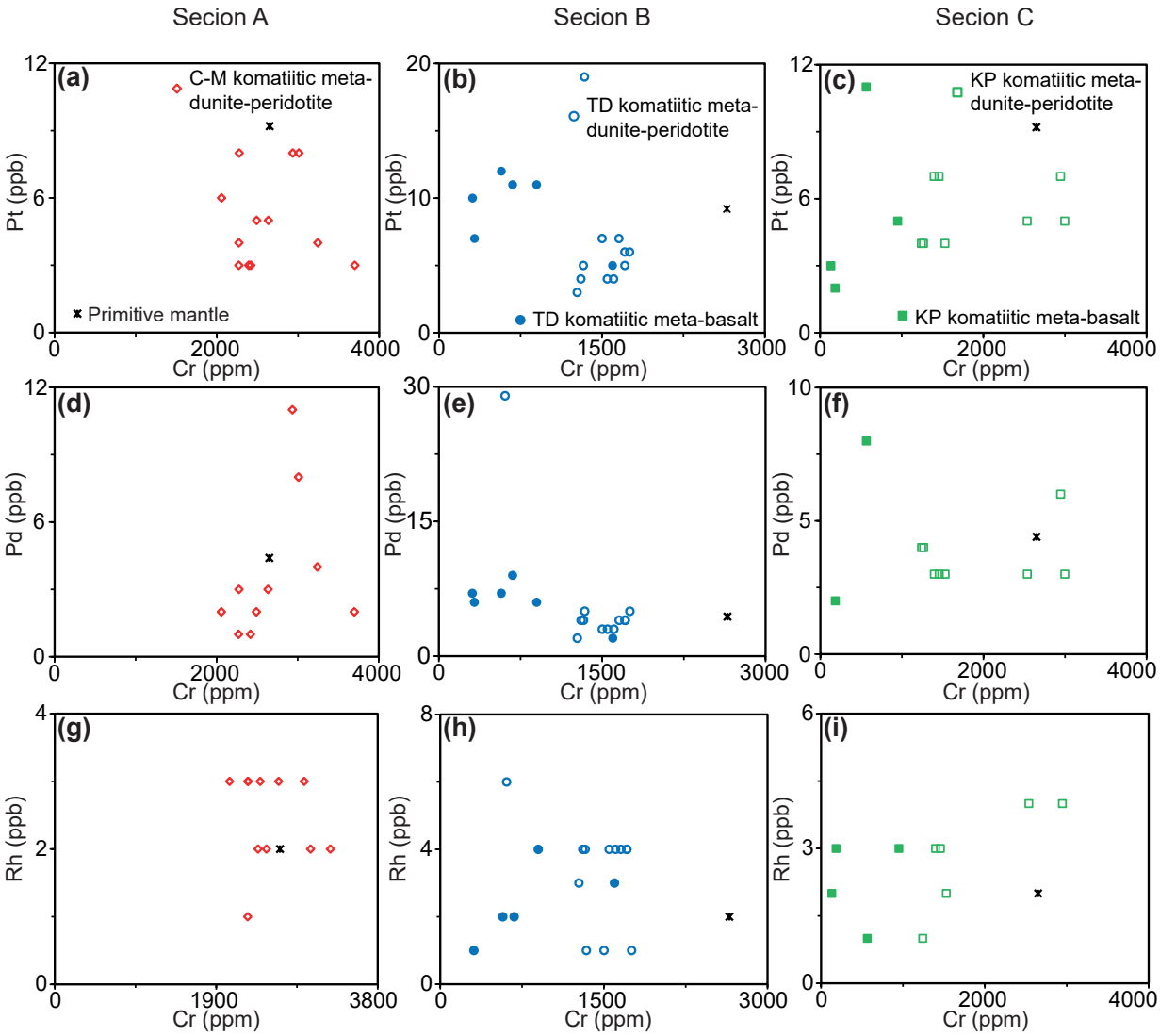

Fig. 21 Cr vs. **a-c** Pt, **d-f** Pd, **g-i** Rh, **j-l** Ru, **m-o** Ir, and **p-r** Os plots for the Gorumahishani komatiitic rock samples from Maharajgunj-Chuka Pahar (Section A), Tua Dungri (Section B), and Kapili (Section C) areas. Primitive mantle values are from McDonough and Sun (1995) and Barnes et al. (1988).

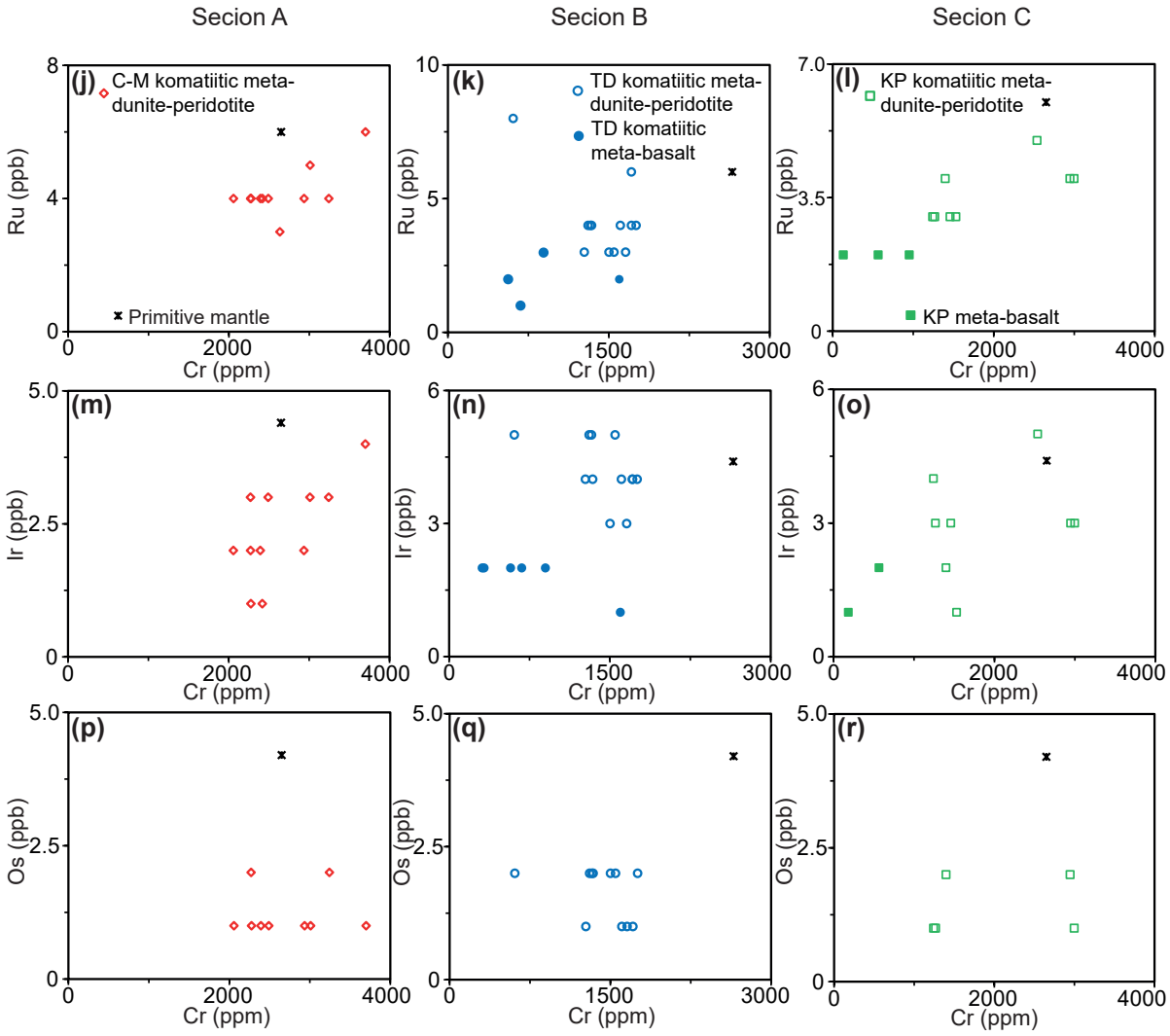

Fig. 21 continued

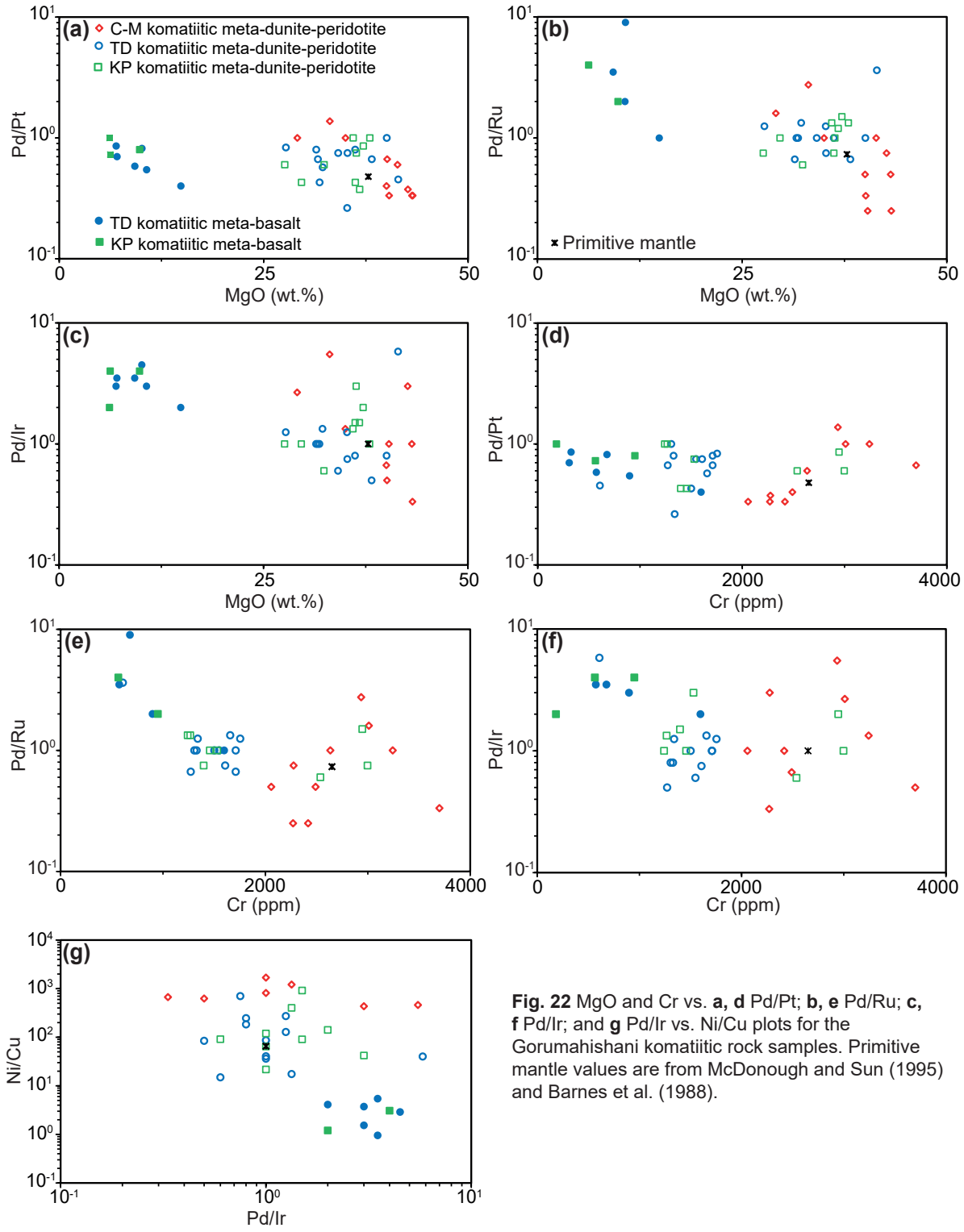

Fig. 22 MgO and Cr vs. **a, d** Pd/Pt; **b, e** Pd/Ru; **c, f** Pd/Ir; and **g** Pd/Ir vs. Ni/Cu plots for the Gorumahishani komatiitic rock samples. Primitive mantle values are from McDonough and Sun (1995) and Barnes et al. (1988).

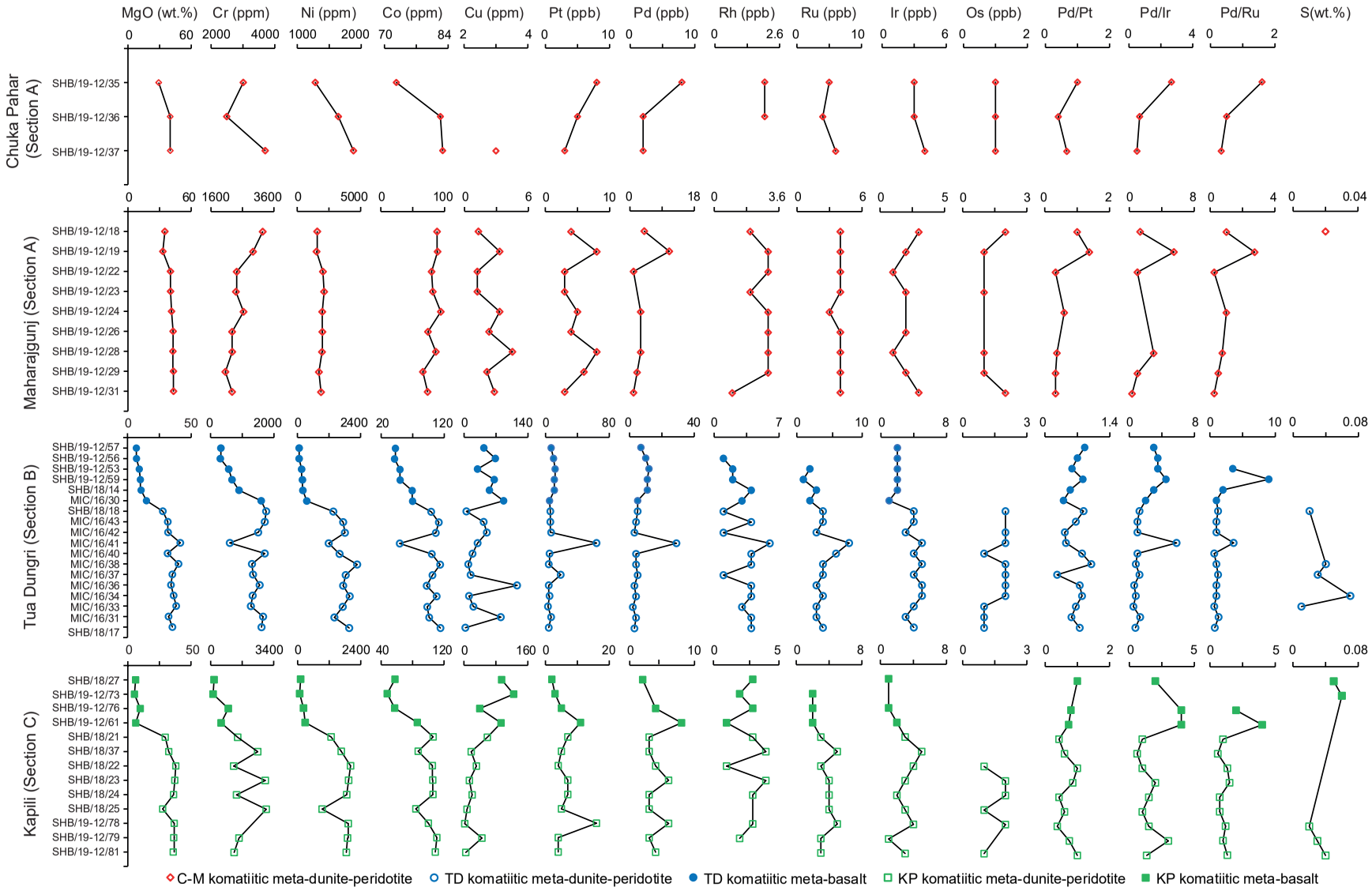

Fig. 23 Plot of MgO, Cr, Ni, Cu, Co, Pt, Pd, Rh, Ru, Ir, Os, and S concentrations and Pd/Pt, Pd/Ir, and Pd/Ru ratios against the stratigraphic distribution of the komatiitic rock samples from Maharajgunj-Chuka Pahar (Section A), Tua Dungri (Section B), and Kapili (Section C) areas.

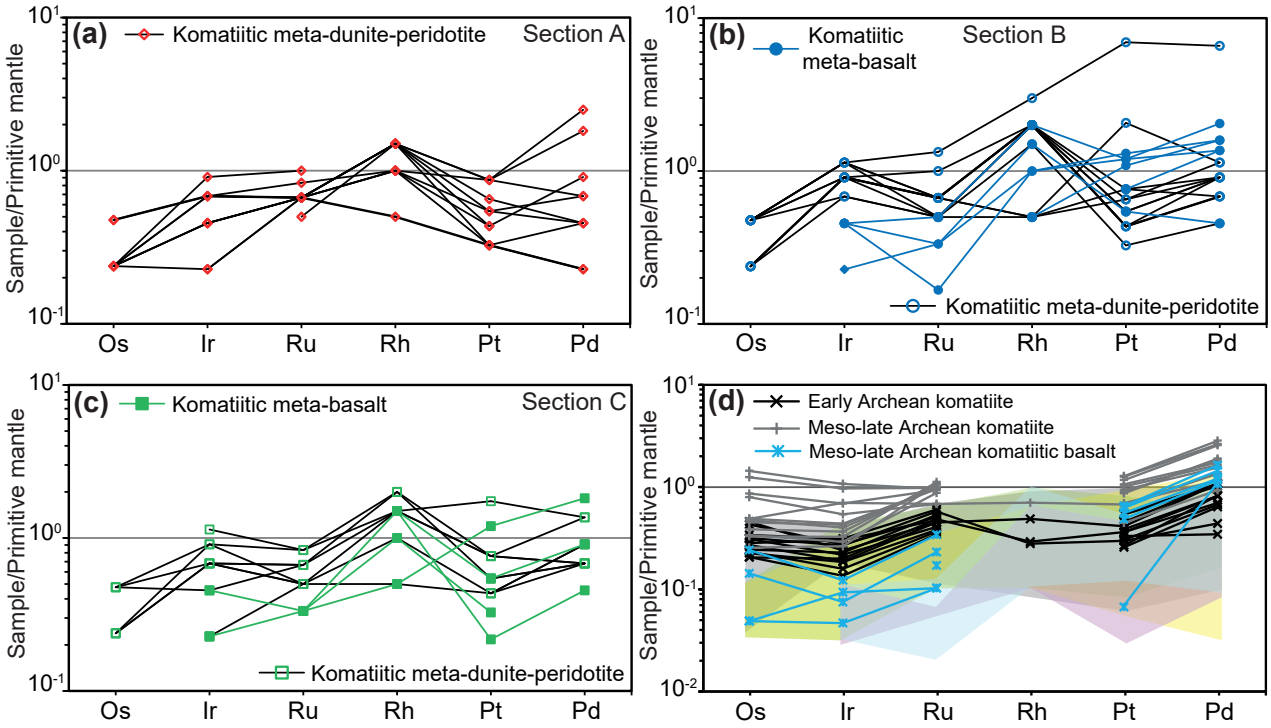

Fig. 24 Primitive mantle-normalized platinum-group elements pattern for the Gorumahishani komatiitic suite of rocks from **a** Maharajgunj-Chuka Pahar (Section A), **b** Tua Dungri (Section B), and **c** Kapili (Section C) areas. **d** Samples from all the sections are compared with early to late Archean komatiites from the Yilgarn, Kaapvaal, Pilbara, Karelia, Superior, and Dharwar craton. Normalized values are from Barnes et al. (1988). Other data from Puchtel et al. (2004, 2009a, 2009b, 2013); Puchtel and Humayun (2005); Maier et al. (2009); Mukherjee et al. (2014); Schneider et al. (2019); and Dutta et al. (2021b). Komatiitic meta-dunite-peridotite: Section A Section B Section C. Komatiitic meta-basalt: Section B Section C.

Table 9 Bulk-rock Platinum-Group element (PGE) (ppb) and S (wt.%) data of komatiitic rocks from the Gorumahishani greenstone belt

Location	Section A	Section A	Section A	Section A	Section A	Section A	Section A	Section A	Section A	Section A	Section A	Section A
Rock Type	Komatiitic meta-peridotite	Komatiitic meta-peridotite	Komatiitic meta-peridotite	Komatiitic meta-peridotite	Komatiitic meta-peridotite	Komatiitic meta-peridotite	Komatiitic meta-peridotite	Komatiitic meta-peridotite	Komatiitic meta-peridotite	Komatiitic meta-peridotite	Komatiitic meta-peridotite	Komatiitic meta-peridotite
Sample	SHB/19-12/22	SHB/19-12/23	SHB/19-12/24	SHB/19-12/26	SHB/19-12/28	SHB/19-12/29	SHB/19-12/31	SHB/19-12/35	SHB/19-12/36	SHB/19-12/37	SHB/19-12/18	SHB/19-12/19
ppb												
Os		1			1	1	2	1	1	1	2	1
Ir	1	2		2	1	2	3	3	3	4	3	2
Ru	4	4	3	4	4	4	4	5	4	6	4	4
Rh	3	2	3	3	3	3	1	2	2		2	3
Pt	3	3	5	4	8	6	3	8	5	3	4	8
Pd	1		3		3	2	1	8	2	2	4	11
wt.%												
S											0.02	

Location	Section B	Section B	Section B	Section B	Section B	Section B	Section B	Section B	Section B	Section B	Section B	Section B
Rock Type	Komatiitic meta-peridotite	Komatiitic meta-peridotite	Komatiitic meta-peridotite	Komatiitic meta-peridotite	Komatiitic meta-peridotite	Komatiitic meta-peridotite	Komatiitic meta-peridotite	Komatiitic meta-peridotite	Komatiitic meta-peridotite	Komatiitic meta-peridotite	Komatiitic meta-peridotite	Komatiitic meta-peridotite
Sample	MIC/16/31	MIC/16/33	MIC/16/34	MIC/16/35	MIC/16/36	MIC/16/37	MIC/16/38	MIC/16/39	MIC/16/40	MIC/16/41	MIC/16/42	MIC/16/43
ppb												
Os	1	1	2		2	2	2		1	2	2	
Ir	3	4	5		5	4	5		4	5	3	4
Ru	3	3	4		3	4	4		6	8	3	4
Rh	4	3	4		4	1	4		4	6	1	4
Pt	7	3	5		4	19	4		5	64	7	6
Pd	4	2	4		3	5	4		4	29	3	4
wt.%												
S		0.01	0.07	0.02		0.03	0.04	0.04				

Location	Section B	Section B	Section B	Section B	Section B	Section B	Section B	Section B	Section C	Section C	Section C	Section C
Rock Type	Komatiitic meta-peridotite	Komatiitic meta-peridotite	Komatiitic meta-basalt	Komatiitic meta-basalt	Komatiitic meta-basalt	Komatiitic meta-basalt	Komatiitic meta-basalt	Komatiitic meta-basalt	Komatiitic meta-peridotite	Komatiitic meta-peridotite	Komatiitic meta-peridotite	Komatiitic meta-peridotite
Sample	SHB/18/17	SHB/18/18	MIC/16/30	SHB/18 14	SHB/19-12/53	SHB/19-12/56	SHB/19-12/57	SHB/19-12/59	SHB/18/20	SHB/18/21	SHB/18/22	SHB/18/23
ppb												
Os	1	2									1	2
Ir	4	4	1	2	2	2	2	2		3	4	3
Ru	4	4	2	3	2			1		3	3	4
Rh	4	1	3	4	2	1		2		3	1	4
Pt	4	6	5	11	12	10	7	11		7	4	7
Pd	3	5	2	6	7	7	6	9		3	4	6
wt.%												
S		0.02							0.02	0.01	0.03	0.04

Location	Section C	Section C	Section C	Section C	Section C	Section C	Section C	Section C	Section C	Section C	Section C	Section C
Rock Type	Komatiitic meta-peridotite	Komatiitic meta-peridotite	Komatiitic meta-peridotite	Komatiitic meta-peridotite	Komatiitic meta-peridotite	Komatiitic meta-peridotite	Komatiitic meta-peridotite	Komatiitic meta-peridotite	Komatiitic meta-peridotite	Komatiitic meta-basalt	Komatiitic meta-basalt	Komatiitic meta-basalt
Sample	SHB/18/24	SHB/18/25	SHB/19-12/77	SHB/19-12/78	SHB/19-12/79	SHB/19-12/80	SHB/19-12/81	SHB/19-12/82	SHB/18/37	SHB/19-12/61	SHB/18/27	SHB/19-12/73
ppb												
Os	2	1		2			1					
Ir	2	3		4	1		3		5	2	1	
Ru	4	4		5	3		3		5	2		2
Rh	3			3	2				4	1	3	2
Pt	7	5		16	4		4		5	11	2	3
Pd	3	3		6	3		4		3	8	2	
wt.%												
S	0.05		0.02	0.02	0.03	0.04	0.04	0.02			0.06	0.05

Location	Section C
Rock Type	Komatiitic meta-basalt
Sample	SHB/19-12/76
ppb	
Os	
Ir	1
Ru	2
Rh	3
Pt	5
Pd	4
wt.%	
S	

sections also show distinct negative Os anomaly (0.2 - 0.5 × primitive mantle). The meta-basalt samples of section B have minor Pt and Pd enrichments (0.4 - 2 × primitive mantle) than the meta-basalts from section C (0.2 - 1.8 × primitive mantle; **Fig. 24b, c**). The komatiitic rocks from sections B and C also show a distinct negative Ru anomaly (0.5 - 0.8 × primitive mantle) except for two samples, however, no such negative anomaly is observed for the samples of section A (**Fig. 24a-c**).

In the primitive mantle normalized PGE plot, the data for the komatiitic samples from the Gorumahishani greenstone belt are compared with the early to late Archean komatiitic rocks from the Yilgarn, Kaapvaal, Pilbara, Karelia, Superior, and Dharwar Cratons (**Fig. 24d**). The meta-dunite and meta-peridotite samples have similar normalized PGE patterns, however, the PGE concentration in the late Archean is relatively higher than the early Archean komatiites (**Fig. 24d**; e.g. Maier et al. 2009).

5.3.3. Sm-Nd isotope systematics

The komatiitic suite of rocks from the three sections of the Gorumahishani greenstone belt, define an eighteen-point errorchron corresponding to an age of 3472 ± 260 Ma (MSWD = 107, initial $^{143}Nd/^{144}Nd$ = 0.50813 ± 0.00034) (**Fig. 25c**). The data of the Tua Dungri area (section B) define an eight-point errorchron corresponding to an age of 3353 ± 830 Ma (MSWD = 211, initial $^{143}Nd/^{144}Nd$ = 0.5083 ± 0.0011) (**Fig. 25b**). However, more realistic and best-fit correlation line for the Gorumahishani komatiites is observed from the section C samples of the Kapili area. An eight-point errorchron is obtained for these rocks corresponding to an age of 3508 ± 190 Ma (MSWD = 41, initial $^{143}Nd/^{144}Nd$ = 0.50808 ± 0.00025) and $\varepsilon_{Nd(T)}$ value

of 0.1 (**Fig. 25d**). The $\varepsilon_{Nd(T)}$ is considered from this errorchron to calculate the initial $^{143}Nd/^{144}Nd$. The regression lines are calculated and plotted using the isoplot program for Excel by Ludwig (2008). The least erroneous age is well within the error limits of the other two errorchrons (**Fig. 25b, c**). Therefore, this particular age is considered the emplacement age of the parental magma of the Gorumahishani komatiitic suite of rocks (**Fig. 25d**).

Although the komatiitic rocks from the Kapili area do not show significant disturbance of their isotopic ratios as indicated by the negative co-relation in $^{143}Nd/^{144}Nd$ vs. (La_n/Sm_n) plot (e.g. Zindler et al. 1979), however, the high error in age data is quite distinct (**Fig. 25a**). The (La_n/Sm_n) ratio serves as an indicator of element mobility during metamorphic alteration events. Significant degrees of metamorphism and hydrothermal alteration can redistribute the highly mobile element La and cause a low (La_N/Sm_N) ratio but it can not redistribute the robust Nd. Therefore, a negative relation between these elements indicates the robustness of the Nd isotope systematics. Low to moderate spread of $^{143}Nd/^{144}Nd$ (0.5118 - 0.5129) and $^{147}Sm/^{144}Nd$ (0.16 - 0.20) values from the Kapili area (section C) or all eighteen samples ($^{143}Nd/^{144}Nd$ = 0.5118 - 0.5132, $^{147}Sm/^{144}Nd$ = 0.16 - 0.22) may also be responsible for the high error in age. The well-defined regression line for the samples of section C, $\varepsilon_{Nd(T)}$ value of 0.1 from the errorchron, and the average $\varepsilon_{Nd(T)}$ value of -0.17 $\pm$ 1.85 from the eighteen samples overall indicate that the Nd isotopic signature does not deviate much from the chondritic value (Jacobsen and Wasserberg 1980). The calculated CHUR model ages (T_{CHUR}) from the Kapili komatiite samples vary between 3.34 and 3.98 Ga (**Table 10**). The lower limit of T_{CHUR} is well within the error limit of the emplacement age of the komatiitic magma as yielded by the errorchrons,

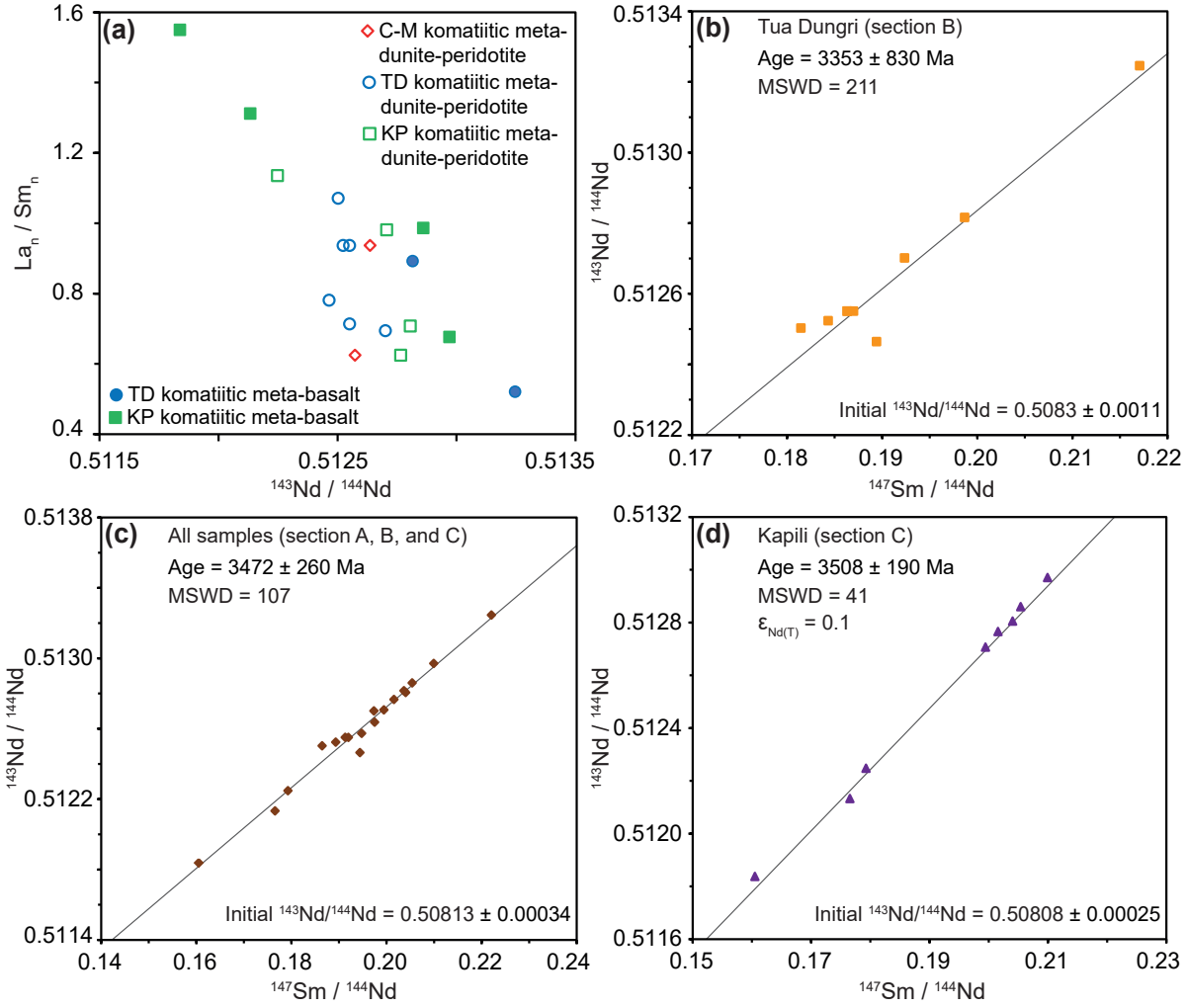

Fig. 25 a $^{143}Nd/^{144}Nd$ vs. La_n/Sm_n bivariate plot for the komatiitic rocks from the Gorumahishani greenstone belt. Normalized values are from McDonough and Sun (1995). **b** Whole-rock Sm-Nd errochron of the Gorumahishani komatiitic rocks from Tua Dungri area (section A). **c** Whole-rock Sm-Nd errochron of Gorumahishani komatiitic rocks from Chuka Pahar-Maharajgunj, Tua Dungri, and Kapili areas (Section A, B, and C respectively). **d** Whole-rock Sm-Nd errorchron of Gorumahishani komatiitic rocks from Kapili area (section A).

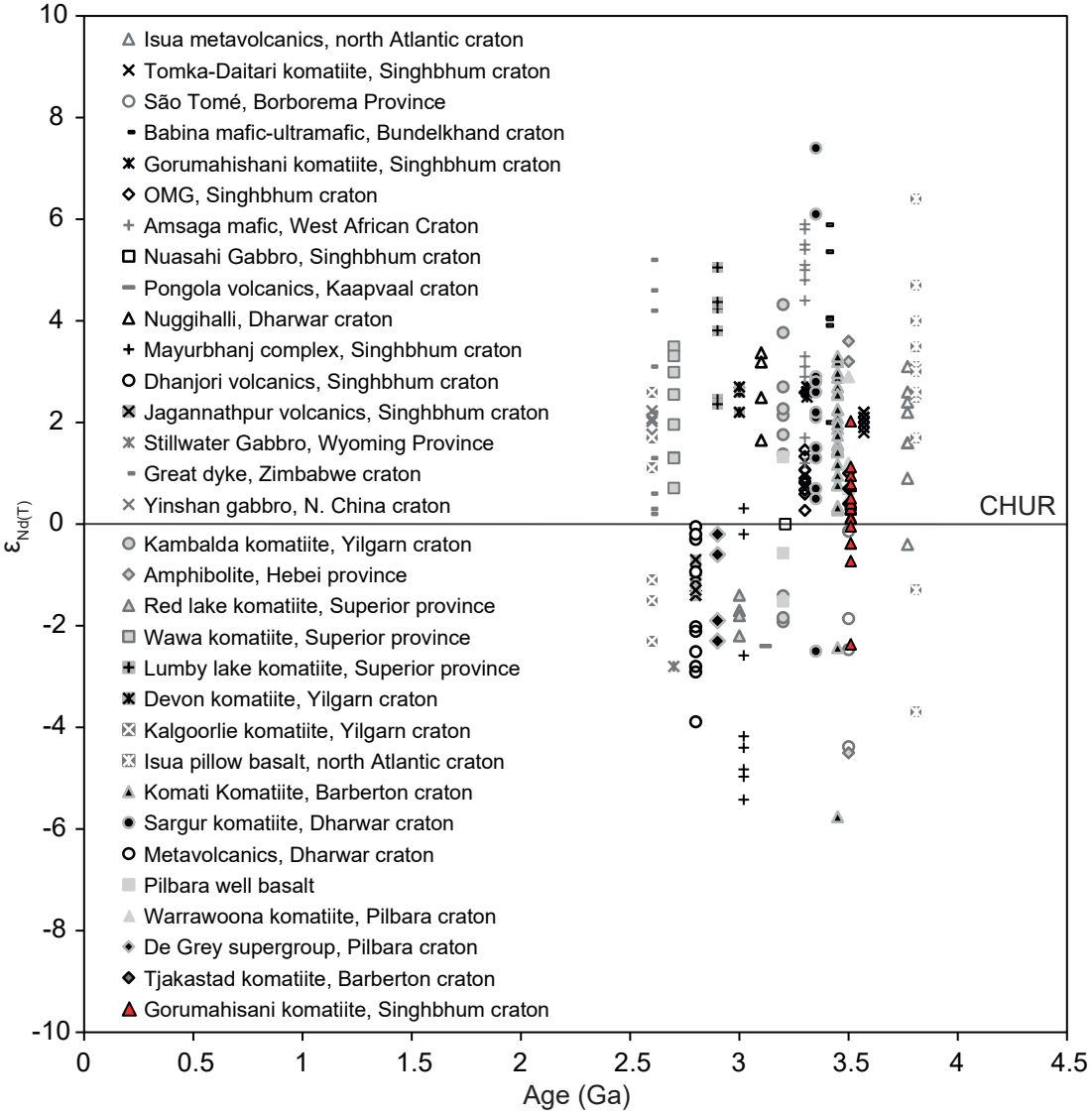

Fig. 26 Age vs. $\varepsilon_{Nd(T)}$ plot for ultramafic-mafic rocks from the Archean greenstone belts of different cratons around ca. 3.8 - 2.6 Ga. Data of the Singhbhum komatiitic rocks (this study) is compared with the data from other ultramafic-mafic rocks of the Singhbhum Craton as well as other Cratons worldwide. The global data from Hamilton et al. (1979); DePaolo and Wasserburg (1979); Hamilton et al. (1983); Hegner et al. (1984); Chauvel et al. (1985); Huang et al. (1986); Sharma et al. (1994); Kumar et al. (1996); Tomlinson et al. (1998); Polat et al. (1999); Blichert-Toft et al. (1999); Hollings and Wyman (1999); Bateman et al. (2001); Oberthür et al. (2002); Augé et al. (2003); Frei and Jensen (2003); Misra and Johnson (2005); Chavagnac (2004); Jayananda et al. (2008); Van Kranendonk et al. (2010); Mukherjee et al. (2012); Wang et al. (2015); Ruiz et al. (2019); Singh et al. (2019); Wainwright et al. (2019); Adhikari et al. (2021a, b); and Hasenstab et al. (2021).

however, the upper limit represents a much older age. The Sm-Nd data of the Gorumahishani komatiitic rocks are compared with other early to late Archean ultramafic-mafic rocks from the Singhbhum Craton and other different Archean greenstone belts in the age (Ga) vs. $\varepsilon_{Nd(T)}$ plot (**Fig. 26**) to understand the evolution of the mantle through ages.

Table 10 Bulk-rock Sm-Nd isotopic data of komatiitic suite of rocks from the Gorumahishani greenstone belt

Location	Rock type	Sample	Sm (ppm)	2 std err	Nd (ppm)	2 std err	$^{147}Sm/^{144}Nd$	$^{143}Nd/^{144}Nd$	$(^{143}Nd/^{144}Nd)_{3508\ Ma}$	T_{CHUR}	ε_{Nd} (3508 Ma)
Section A	Komatiitic meta-peridotite	SHB/19-12/39	0.37	0.000076	1.16	0.000158	0.19477	0.51257	0.508054		
Section A	Komatiitic meta-peridotite	SHB/19-12/34	0.13	0.000036	0.40	0.000041	0.19750	0.51264	0.508054		-0.38
Section B	Komatiitic meta-peridotite	MIC/16/32	0.98	0.000175	3.01	0.000111	0.19734	0.51270	0.508121		0.95
Section B	Komatiitic meta-peridotite	MIC/16/35	0.70	0.000240	2.22	0.001582	0.19131	0.51255	0.508111	2.45	0.75
Section B	Komatiitic meta-peridotite	MIC/16/39	0.68	0.000202	2.17	0.000678	0.18931	0.51252	0.508130	2.35	1.12
Section B	Komatiitic meta-peridotite	MIC/16/44	0.83	0.000182	2.69	0.000302	0.18645	0.51250	0.508176	2.00	2.02
Section B	Komatiitic meta-peridotite	SHB/18/12	0.43	0.000076	1.34	0.000167	0.19440	0.51246	0.507953		-2.37
Section B	Komatiitic meta-peridotite	SHB/18/16	0.69	0.000097	2.16	0.000216	0.19198	0.51255	0.508095	2.80	0.44
Section B	Komatiitic meta-basalt	SHB/19-12/52	1.21	0.000176	3.58	0.000651	0.20366	0.51282	0.508090	3.86	0.32
Section B	Komatiitic meta-basalt	SHB/19-12/58	0.96	0.000198	2.61	0.000557	0.22206	0.51325	0.508092	3.62	0.38
Section C	Komatiitic meta-peridotite	SHB/18/20	0.95	0.000183	3.20	0.001686	0.17926	0.51225	0.508088	3.38	0.29
Section C	Komatiitic meta-peridotite	SHB/19-12/77	0.69	0.000271	2.09	0.000634	0.19944	0.51271	0.508079	3.81	0.11
Section C	Komatiitic meta-peridotite	SHB/19-12/82	0.63	0.000102	1.88	0.000361	0.20156	0.51277	0.508089	3.98	0.30
Section C	Komatiitic meta-peridotite	SHB/18/39	1.36	0.000315	4.03	0.000566	0.20402	0.51281	0.508071	3.46	-0.04
Section C	Komatiitic meta-basalt	SHB/18/31	1.87	0.000294	6.38	0.001857	0.17655	0.51213	0.508036	3.78	-0.73

Section C	Komatiitic meta-basalt	SHB/19-12/83	1.98	0.000629	5.80	0.001957	0.20539	0.51286	0.508094	3.86	0.41
Section C	Komatiitic meta-basalt	SHB/19-12/84	1.07	0.000263	3.08	0.002590	0.20993	0.51297	0.508099	3.80	0.51
Section C	Komatiitic meta-basalt	SHB/19-12/60	3.03	0.000643	11.41	0.002622	0.16050	0.51184	0.508113	3.34	0.79

Chapter 6

Discussion

6. Discussion

6.1. Modification of chromite to ferritchromit and chrome magnetite

Zones of various reflectances around chromite cores of all types (**Fig. 3h-j**) mainly reflect compositional variation in the rims between ferritchromit and chrome magnetite resulting from prograde (Evans and Frost 1975; Burkhard 1993; Loferski 1986; Fleet et al. 1993; Barnes 2000; Mondal et al. 2006; Mukherjee et al. 2010, 2015; Staddon et al. 2021; Datta and Mondal 2021a; Kang et al. 2022; Barnes et al. 2023) or retrograde metamorphism (Proenza et al. 2004; Gervilla et al. 2012, 2019; Colás et al. 2014, 2017, 2019, 2020; Bussolesi et al. 2022; Roy et al. 2022). The ferritchromit formation is contemporaneous with the modification of the primary mineral assemblages of komatiitic meta-dunites and meta-peridotites (olivine, orthopyroxene, clinopyroxene) from cumulate and spinifex zones to serpentine, tremolite, chlorite, and carbonates. The CO_2-rich fluid at low metamorphic grade drives the formation of talc and carbonate minerals (e.g. Barnes 2006). The komatiitic chromites from the Gorumahishani belt were modified during the metamorphism of the entire greenstone sequence and became depleted in Mg, Al, and Cr, and enriched in Fe^{3+} at the boundaries (**Fig. 6a-c**). Chrome chlorite is formed during this metamorphic process, incorporating Cr and Al released from chromites (e.g. Evans and Frost 1975; Burkhard 1993; Barnes 2000). The enrichment of Fe^{3+} during prograde metamorphism has produced the ferritchromit as the inner rim and chrome magnetite as the outer rim in the modified chromites (type-I and type-II grains; **Fig. 3g-i, 6a-c**). The type-III chromites from the northern Kapili are different from type-I and type-II grains, showing complex zoning patterns with a highly porous character (**Fig. 6c**). The porous chrome magnetite rims of the type-II and type-III

grains suggest significant mass loss due to elemental exchange with silicates without any changes in grain size during metamorphism (**Fig. 6b, c**). The type-III grains have broadly higher Cr# (0.87 - 0.92) and lower Mg# (0.08 - 0.17) in their cores relative to type-I varieties (**Fig. 6c**). Lower Fe_2O_3 (2.1 - 14.88 wt.%) and Fe^{3+}/R^{3+} in the type-I and II inner rims relative to the outer rims suggest the presence of an oxidizing environment. Overall concentration difference of TiO_2, V_2O_5, NiO, and CoO between type-I core and rims are quite less except for MnO in both areas (**Fig. 6a**). This indicates a restricted modification of type-I chromite core at a low metamorphic grade (e.g. Kimball 1990; Barnes 2000). The mineral assemblage, serpentine + tremolite + chlorite ± calcite ± dolomite in the Tua Dungri komatiites (**Fig. 4**, **Table 3**) confirms this and supports modification under the greenschist to greenschist-amphibolite transition facies metamorphism with the involvement of CO_2 rich fluids (**Fig. 27**). In comparison, type-II chromites have a more homogenized core with high concentrations of ZnO and MnO but significantly low Al_2O_3, MgO (**Fig. 6b**). Higher enrichment of low mobile elements with slower diffusion rates like Ti (e.g. Rollinson 1995) is also observed in the chrome magnetite rim part relative to the type-I grains (**Fig. 6a, b**). This high concentration of high-mobile elements like Zn, and Mn in the type-II core and low-mobile elements like Ti in the type-II rim indicates that a higher metamorphic grade is suffered by the type-II chromites compared to the type-I grains (e.g. Barnes 2000). Mineral assemblages of serpentine + tremolite + hornblende + chlorite ± actinolite ± carbonate from the Kapili area (**Fig. 4**) in association with type-II chromite grains point towards metamorphism under amphibolite facies (**Fig. 27**). Compared to type-II grains, type-III grains from the Kapili area have inner rims of variable reflectances with a high concentration of MnO,

ZnO alongside TiO_2, and V_2O_5 (**Fig. 6c**). This is due to the diffusion of these elements from the core to the inner rims after complete homogenization of core composition (type-II) at high metamorphic grade (Barnes 2000). Mineral assemblage associated with the type-III chromites is nearly similar to the association with type-II grains except for the low modal abundance of chlorite (**Fig. 4**). This suggests that the reverse diffusion of certain elements from core to inner rims took place during metamorphism under the amphibolite facies condition (e.g. Barnes 2000) (**Fig. 27**). The higher Al_2O_3 in the inner rims of the type-III grains might be due to the breakdown of chlorite under this high metamorphic grade (e.g. Loferski 1986). The type-IV grains from Maharajgunj are intensely fractured small ferritchromit grains suggesting deformation during metamorphism (**Fig. 3j**). The concentrations of major and minor elements in the type-IV grains are mostly similar to those in the ferritchromit rims of the type-I and type-II grains (**Table 4; Appendix 1**). The mineral assemblage of serpentine + chlorite + carbonate + tremolite ± talc from the northern Maharajgunj-Chuka Pahar indicates a low metamorphic grade close to the greenschist-amphibolite transition facies (**Fig. 4**). The type-V chrome magnetite grains have a wide-ranging major and minor element concentration (**Fig. 7b-f; Table 4**) and the geochemical diversity reflects the differing degrees of metamorphism related to the development of the chrome magnetite grains. Finer-grained type-V magnetites were formed during the alteration of the primary ferromagnesian silicates like olivine due to hydration of the komatiitic rocks under the low-grade metamorphism (e.g. Bach et al. 2004; Alt et al. 2007; Gahlan et al. 2006; Eslami et al. 2018). Considering the olivine core (Fo_{88}) from the Kapili area (**Fig. 3a**) and the associated chromite core, the geothermometers of Roeder et al.

(1979) and Fabriès (1979) yield re-equilibration temperatures in the range of 409 - 619°C, consistent up to amphibolite facies metamorphism. However, these olivine grains might have a metamorphic origin because under the amphibolite facies serpentine breaks down to form metamorphic olivine (e.g. Evans and Trommsdorff 1974; Kunugiza et al. 1986; Barnes 2006). Thermometric calculations are also performed using chrome magnetite-ilmenite pairs of the Maharajgunj (1 pair) and Kapili area (3 pairs) following the method of Spencer and Lindsley (1981) and Lepage (2003). The calculated temperature from the northern part of the greenstone belt (Maharajgunj area) is 384°C suggesting greenschist facies metamorphism at $X(CO_2) < 0.05$ in the stability field of serpentine, tremolite, chlorite, and carbonate (e.g. Barnes 2006). On the other hand, the calculated temperatures from the southern part of the greenstone belt (Kapili area) range from 443 to 502°C suggesting a greenschist-amphibolite transition to amphibolite facies metamorphism at $X(CO_2) < 0.05$ in the stability field of serpentine, tremolite, hornblende, chlorite ± metamorphic olivine, which is consistent with the present observations (e.g. Barnes 2006). In Barnes and Roeder's (2001; **Fig. 7g**) chromite compositional discrimination fields, the Gorumahishani komatiitic chromite cores for type-I grains occupy the greenschist field and type-II and type-III cores occupy the amphibolite field. To understand the lowest equilibration temperature of the assemblage, chlorite thermometry has been employed following the method of Cathelineau and Nieva (1985) where: $T = 319 \times Al_{IV}^{Corrected} - 69$ and $Al_{IV}^{Corrected} = Al_{IV} + 0.1 \times (Fe/Fe+Mg)$. The calculation reveals the lowest temperature of re-equilibration of the komatiitic mineral assemblage is ~337 - 237°C from the northern part and ~357 - 243°C from the southern part of the Gorumahishani greenstone belt.

6.2. Fractionation of trace elements and PGE during metamorphism of chromites

6.2.1. Trace elements

Zoned chromites from the Gorumahishani greenstone belt show inter and intra-grain major and minor element variations, developed due to greenschist to amphibolite facies metamorphism. Similar variations are apparent in trace element abundances determined by LA-ICPMS. The positive relationships of Ga, Sc with $Mg/(Mg+Fe^{2+})$ for the non-porous cores of type-I chromites indicate relatively pristine core compositions (**Fig. 10a, c**). However, the sum of Zn+Co+Mn remains almost constant with decreasing Ga (**Fig. 10h**). This indicates a greater role for metamorphism than for H_2O, CO_2-rich fluid activity because hydrothermal re-equilibration might have affected the Zn+Co+Mn content of type-I cores but not Ga (e.g. Colás et al. 2014). Ga and Sc are not compatible in olivine but may enter into the chlorite structure in substitution for Al during the metamorphic modification of the assemblage (Nelson and Roy 1958; Colás et al. 2014; Chu et al. 2020).

The type-II porous chromites have a higher concentration of Ga and similar Sc compared to the type-I grains (**Fig. 10a, c; Table 6**). The higher concentrations of Ga and lower modes of chlorite in the pores of chrome magnetite rims from Kapili suggest a lower degree of substitution of Ga for Al in chlorite (e.g. Colás et al. 2014; Chu et al. 2020). Lower Al_2O_3 content in the type-II cores and rims than in the type-I variety supports this observation as Al has migrated to chlorite (Fleet et al. 1993; Barnes 2000; Merlini et al. 2009) (**Table 4**). The concentrations of Zn in the type-II cores are similar but Co and Mn are higher compared to the type-I cores (**Table 6; Fig. 10d-f**). This is related to the higher metamorphic grade, i.e. up to amphibolite

facies metamorphism of the komatiitic rocks from Kapili, and therefore, the higher diffusion rate of the trace elements (e.g. Sievwright et al. 2020). The ZCM anomaly in the type-I and type-II chromite cores (**Fig. 11a, b**) was likely due to modification during metamorphism when Zn, Co, and Mn were diffused into the chromite structure from altered silicate minerals such as olivine, clinopyroxene, and the associated carbonate phases (e.g. Colás et al. 2014).

The microprobe data are consistent with the LA-ICPMS data and show greater contrast between core and rim in the type-III grains than in the type-II grains, with the inner rims of the former having higher concentrations of Mn, Zn, Ni, Ti, and V than the cores (**Table 6**). This transition from homogenized type-II cores towards enriched type-III inner rims indicates the reverse diffusion of these elements from the core to the inner rims of the type-III grains under the amphibolite facies conditions (e.g. Barnes 2000) (**Fig. 27**).

The LA-ICPMS data show that the type-II cores have higher concentrations of Ni (4513 - 10,583 ppm) and Ti (20,759 - 36,413 ppm) at similar $Mg/(Mg+Fe^{2+})$ (0.13 - 0.16) and higher Fe^{3+}/R^{3+} ratio (0.08 - 0.10) than the type-I cores (**Fig. 9a-d; Table 4, 6**). Ti^{4+} is less mobile to incorporate into the spinel structure than the +2 ions (e.g. Wylie et al. 1987; Barnes 2000; Nielsen and Beard 2000), therefore, its higher concentration in type-II cores indicates a modified core composition compared to the type-I cores under a higher grade of metamorphism (**Fig. 9a-d; Table 6**). With an increasing Fe^{3+}/ R^{3+} ratio, bivalent ions begin to occupy octahedral sites of the inverse spinel structure (e.g. Barnes 2000; Gervilla et al. 2012). As the homogenized type-II cores have higher Fe^{3+}/R^{3+} ratios, their higher Ni concentrations may therefore result from the substitution of Ni^{2+} for the bivalent ions (Fe^{2+}, Mg^{2+}) in the

divalent octahedral sites and Ti^{4+} for Fe^{3+} in the tetrahedral sites (e.g. Barnes 1998, 2000).

The type-V chrome magnetite grains show variable degrees of enrichment of Zn and Co with lower Mg/(Mg+Fe^{2+}) and higher Fe^{3+}/R^{3+} ratios (**Fig. 10d, f; Table 4, 6**), indicating different degrees of involvement of metamorphism. However, the overall negative relationship between Fe^{3+}/R^{3+} and MnO mainly from the type-V grains (**Fig. 7e**) indicates the bivalent tetrahedral site occupancy of Mn was decreased in the inverse spinel structure. Fe^{3+} occupies the tetrahedral site in the inverse spinel structure, limiting the possibility of Mn occupying this site (e.g. Sack and Ghiorso 1991; González Jiménez et al. 2009; Gervilla et al. 2012; Davis et al. 2013). The type-V chrome magnetite grains also show variable enrichment of Ni and Ti with Mg/(Mg+Fe^{2+}) and Fe^{3+}/R^{3+} (**Fig. 10b, g; Table 4, 6**). This is due to different degrees of metamorphic modification coupled with a variable Fe^{2+}-Fe^{3+} re-ordering (e.g. Barnes 2000; Nielsen and Beard 2000; Gervilla et al. 2012).

6.2.2. Platinum-Group element (PGE)

Previous studies using in situ LA-ICPMS analysis of natural chrome spinels from volcanic ultramafic-mafic rocks have documented higher concentrations of Rh, Os, Ir, and Ru that are considered to be present as solid solutions in the spinel structure (Locmelis et al. 2011; Park et al. 2012, 2017; Pagé et al. 2012; Pagé and Barnes 2016; Schoneveld et al. 2022). Platinum-group elements were also found to exist as micro-nuggets in chromite grains (Tredoux et al. 1995; Ballhaus and Sylvester 2000; Park et al. 2012, 2017; Kamenetsky et al. 2015; Arguin et al. 2016; González-Pérez et al. 2021; Cabri et al. 2022). Inclusions of PGE-bearing phases, such as laurite (RuS_2),

IPGE (Ir, Os, Ru)-alloys, and Pt-alloys, are common in chromites from mafic layered intrusions and ophiolitic complexes (Garuti et al. 2002; Ahmed 2007; Fonseca et al. 2009; Habtoor et al. 2017; Prichard et al. 2017; Mondal et al. 2019; Garuti et al. 2021; Bussolesi et al. 2022; Zaccarini et al. 2022). Experimental studies considering silicate melt and chrome spinel have shown higher partition coefficients of Rh and IPGEs (Os, Ir, Ru) in chrome spinels than Pt, Pd (Capobianco and Drake 1990; Nell and O'Neill 1997; Righter and Downs 2001; Brenan et al. 2012; Prasek 2022). *In situ* LA-ICPMS analysis of type-I, type-II, and type-V grains show high Ir, Os, Ru, and Rh concentrations with strong positive Ru anomalies (**Fig. 13a**), as observed in other volcanic chromites from different tectonic settings (**Fig. 13b**) (e.g. Pagé and Barnes 2009; Park et al. 2012, 2017; Kamenetsky et al. 2015). However, the concentrations of Rh, Ir, Os, and Ru differ between the types of altered chromite grains and are also highly variable in different zones within a single grain (**Fig. 9a-d; Table 7**). The type-I chromite cores from Tua Dungri have lower Ru and similar Ir and Os to the ferritchromit and chrome magnetite rims (**Fig. 9a, b**). The Rh concentrations are also slightly lower in the cores of the type-I grains than in the corresponding outer ferritchromit and chrome magnetite rims (**Fig. 9a, b; Table 7**). The petrological evidence reveals that the type-I chromite grains were modified under greenschist-amphibolite transition facies conditions. The modification of existing chromite to ferritchromit and chrome magnetite rims was accompanied by the development of an inverse spinel structure surrounding the core. Among the PGEs, Rh^{2+} might have diffused towards the ferritchromit and chrome magnetite rims as these elements prefer to occupy divalent octahedral sites of inverse spinel (e.g. Borisov and Palme 1995; Brenan et al. 2003; Park et al. 2017). However, such a process, if it occurred,

must have been quite limited as the difference between the Rh abundances of the core and the rim are minimal (**Fig. 9a, b**). Ru shows no relationship with Ni or V contents even though these trace elements also tend to occupy the divalent octahedral sites in an inverse spinel structure (**Fig. 14a, b**) (e.g. Barnes 2000; Park et al. 2017). Ruthenium exists both as Ru^{2+} and Ru^{3+} depending on the fO_2 condition of the magma (e.g. Brenan et al. 2012; Park et al. 2012; Locmelis et al. 2018). If Ru occupied the divalent octahedral site as Ru^{2+}, the type-I chromite grains should have crystallized from a reduced parental melt. However, the Fe^{3+} enrichment and development of an inverse spinel structure during the formation of the ferritchromit and chrome magnetite rims were due to post-magmatic oxidation during metamorphism and not a magmatic process. Therefore, possibly Ru was initially present as a +2 ion in the reduced komatiitic melt of the early Archean Gorumahishani greenstone belt and thus preferred to occupy the divalent octahedral sites (Ru^{2+}) in the primary magmatic chromites. The enrichment of Ru^{2+} in the outer rims took place during metamorphic modification of the grains when Ru^{2+} preferentially diffused to the octahedral sites in the inverse spinel structure of the rims (**Fig. 9a, b**). High temperature (1275°C, 1 atm) experimental study between basaltic melt and magnetite also indicates a greater degree of the partitioning of Ru, Rh towards the inverse spinel structure (e.g. Capobianco et al. 1994). However, it should be noted that the existing PGE characters of the different altered zones of the komatiitic chromites from the Gorumahishani greenstone belt took place under the low-temperature metamorphic condition. Vanadium (V) is a redox-sensitive element, and during metamorphic modification of chromites, the concentrations should be increased in the altered outer rims; however, there is no such correlation of V with

Ru concentrations in the zoned chromites (**Fig. 14a**). This suggests a reduced mantle source for the Gorumahishani komatiites and supports the existence of a global heterogeneity in mantle redox conditions as suggested from the study of the early Archean komatiites (e.g. Nicklas et al. 2019). As noted above, there may also be some IPGE-bearing phases present as inclusions (e.g. laurite, erlichmanite, IPGE alloys; Kamenetsky et al. 2015) which result in the IPGE-enrichment in chrome spinels (e.g. Fiorentini et al. 2004). A minor IPGE spike (Rh, Ru rich inclusion) is observed from the laser ablation (LA) spots in the type-I grains (**Fig. 12b**); however, only a limited number of spots were analyzed and no specific platinum-group mineral (PGM) phase was identified during the SEM study (**Fig. 12a, b**). In addition, the observation of Ru (and Rh) enrichments in the outer rims on both sides of the central cores of the type-I grains strongly suggests that in the studied spots Ru is hosted as a solid solution in the spinel structure rather than in IPGE bearing inclusions (**Fig. 9a, b**). The type-II chromite cores have lower Os, Ir, Ru, and Rh than the type-I chromite cores (**Fig. 9c, d; Table 7**). In addition, the chrome magnetite rims of the type-II grains have a negligible amount of Ru with no traceable Rh, Os, and Ir (**Fig. 9c, d; Table 7**). The petrological evidence reveals that the type-II chromite grains were modified up to amphibolite facies conditions. Therefore, the enrichment of Ru and Rh in the thick chrome magnetite rims relative to the cores should have been even higher than in the type-I grains. The very low abundances of these elements in both type-II cores and rims are thus surprising, and may reflect faster diffusion under the higher metamorphic grade (**Fig. 27**). The chalcophile character of PGEs might have facilitated the partitioning of these elements into the co-existing sulfide phases (e.g. chalcopyrite, pentlandite, millerite) or platinum-group minerals

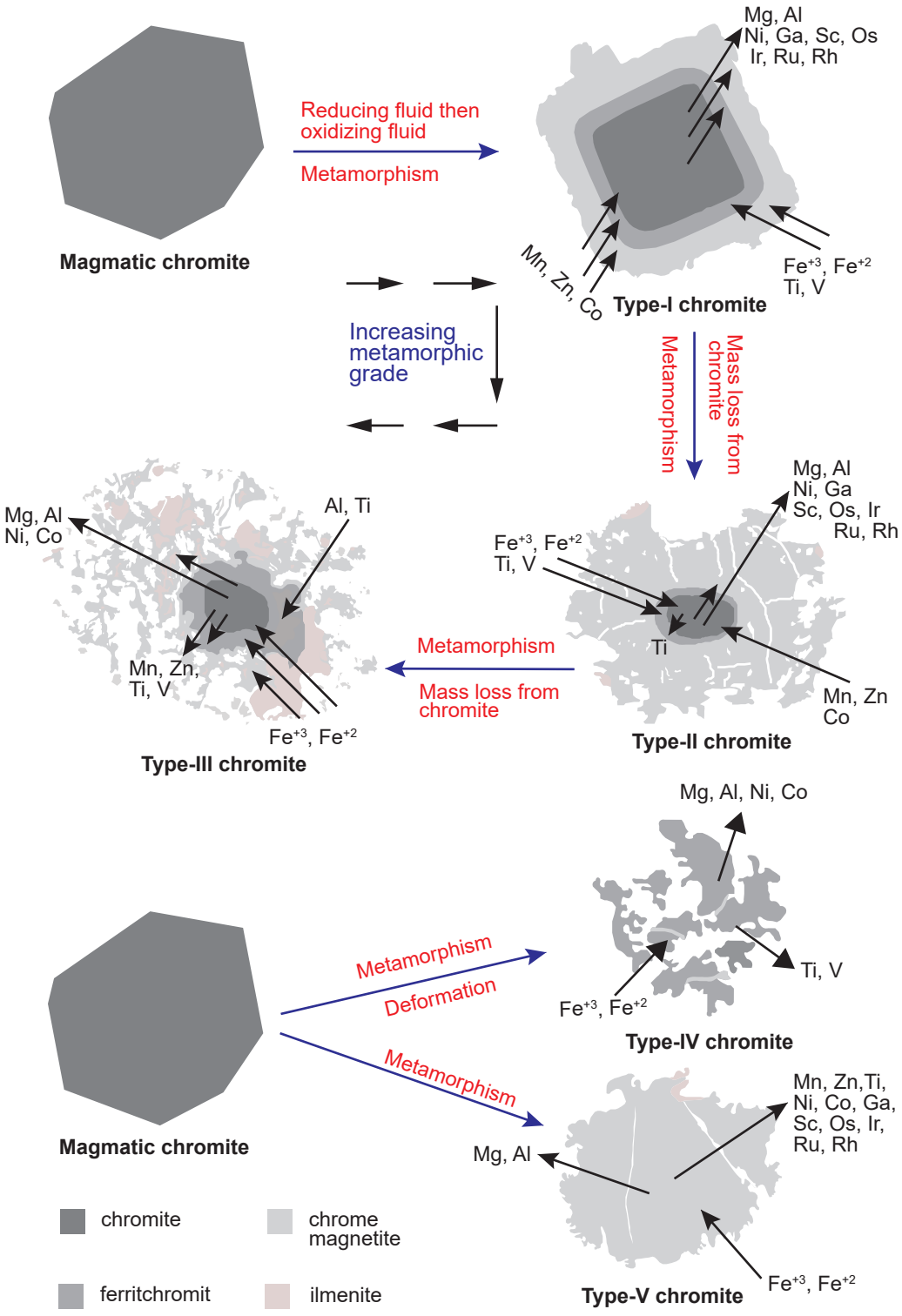

Fig. 27 Schematic illustration of microstructural and chemical (major, trace, and platinum-group elements) changes in the five types of Cr-spinel grains during prograde metamorphism of the komatiitic rocks from the Gorumahishani greenstone belt.

(e.g. laurite, erlichmanite, IPGE alloy) that may be present in the komatiitic rocks or as inclusions in chromites (Peach and Mathez 1996; Andrews and Brenan 2002; Fiorentini et al. 2004; Fonseca et al. 2009; Park et al. 2012, 2017; Pagé and Barnes 2016; Locmelis et al. 2018). The isolated type-V chrome magnetite grains have higher Os, Ir, and lower Rh content with a wider range of Ru concentration than the cores and rims of type-I and type-II grains (**Table 7**). The IPGE and Rh concentrations of type-V grains vary spatially in the greenstone belt. Only Ru is detected in type-V grains from the southern Kapili area whereas higher IPGE and Rh contents are found in those from the northernmost Maharajgunj and Chuka Pahar areas (**Table 7**). It indicates an increase in the diffusion of PGEs from the chromite grains to associated sulfides (e.g. chalcopyrite, pentlandite, millerite) or platinum-group minerals with increasing metamorphic grade from the northern to the southern part of the greenstone belt as discussed earlier. The overall enrichment of Os and Ir in the type-V grains (**Fig. 13a-b; Table 7**) is due to the stronger affinity of these elements towards the VI-fold coordination of the inverse spinel structure (e.g. Brenan et al. 2012).

6.2.3. Mass balance calculation and partitioning behaviour of PGE

Chrome spinel plays a significant role in controlling the PGE budget, and several trace elements in plutonic and volcanic ultramafic-mafic rocks that formed under different geological conditions (Pagé and Barnes 2009; Park et al. 2012; Colás et al. 2014; Kamenetsky et al. 2015; Park et al. 2017; Chu et al. 2020; Schoneveld et al. 2022; Zaccarini et al. 2022). Thus understanding the partitioning of these elements between ultramafic-mafic silicate melt and co-existing chrome spinels during early

magmatic processes is of great importance. This is a challenging exercise for the Gorumahishani komatiitic chromites owing to their extensive metamorphic alteration and therefore, only the core compositions of the least altered chromites were considered for mass balance and partitioning calculations. The compositions of the Al-depleted meta-peridotite (**Table 7**) from Tua Dungri (sample MIC/16/44) and Kapili (sample SHB/18/25) are considered to be equivalent to the parental komatiitic melt compositions of the type-I (Tua Dungri) and type-II (Kapili) chromites, respectively.

The mass fraction of chromite in komatiitic rocks from the least altered chromite cores of type-I (sample MIC/16/39, meta-peridotite) and type-II grains (sample SHB/19-12/82, spinifex-textured meta-peridotite) are calculated following the equation proposed by Pagé and Barnes (2016): **% Cr-spinel in sample = ($Cr_2O_3^{WR}$ / $Cr_2O_3^{Cr\text{-}spinel}$) × 100 × 0.75** where $Cr_2O_3^{WR}$ = whole-rock Cr_2O_3 content in wt.% and $Cr_2O_3^{Cr\text{-}spinel}$ = Cr_2O_3 content of Cr-spinel in wt.%. The calculation assumes that 75% of Cr in the whole rock is hosted by chromite (e.g. Arguin et al. 2016), with the rest being hosted by silicate phases dominated by olivine with some pyroxene and chlorite (e.g. Pagé et al. 2012; Pagé and Barnes 2016). Using the Cr_2O_3 abundances of the least altered chromite cores and the Cr_2O_3 contents of the corresponding rocks, we find that the proportions of chromite in the komatiitic rocks ranged from 0.33 to 0.61% (**Tables 11, 12**) which is similar to the lower limit of chromite modal abundances obtained by Pagé and Barnes (2016) for volcanic samples. The weight fraction of chromite in the studied samples was used to estimate the fractions of trace elements and IPGE + Rh in the whole rock contributed by chromite, following the equation of Pagé and Barnes (2016):

$\mathbf{F_i^{Cr\text{-}spinel}\ (\%) = 100 \times (\ C_i^{Cr\text{-}spinel} \times F^{Cr\text{-}spinel}) \,/\, C_i^{WR}}$ where $F_i^{Cr\text{-}spinel}$ = contribution of element 'i' from chromite in the whole rock, $C_i^{Cr\text{-}spinel}$ = element 'i' concentration in chromite, $F^{Cr\text{-}spinel}$ = proportion of Cr-spinel in our sample, and C_i^{WR} = concentration of element 'i' in the whole-rock. The mass balance calculation for the Tua Dungri komatiites indicates that chromite hosts mass fractions of Sc = 0.12 - 0.15%, Ti = 0.04%, Ni = 0.08 - 0.10%, V = 4.46%, Ga = 2.71 - 3.62%, Mn = 0.83 - 0.87% and Co = 3.7 - 3.92%. The proportions for the Kapili komatiites are Sc = 0.09 - 0.16%, Ti = 3.89 - 7.05%, Ni = 2.88 - 6.97%, Ga = 6.58 - 11.41%, Mn = 9.62 - 16.78%, Co = 12.33 - 18.87% and V = 18.20 - 40.34% (**Tables 11, 12**). These values can be compared with the F_{Sc} and F_{Ni} values of the least modified komatiitic chromites (F_{Sc} = 23.21%, F_{Ni} = 47.98%) of Park et al. (2017) and the bulk rock data of Törmänen et al. (2016). Assuming that our choices for the bulk melt compositions are appropriate, the data show that low and variable fractions of the considered minor and trace elements are hosted by chromites in the Gorumahishani komatiites, unlike the much higher fractions of these elements hosted by chromites in the other komatiites (e.g. Park et al. 2017). This suggests that the distribution of these elements in the komatiitic rocks is mainly controlled by the modally abundant silicate plus carbonate minerals in combination with the metamorphic modification of the primary assemblages.

Calculations based on global komatiitic and ultramafic-mafic volcanic rocks (e.g. Pagé et al. 2012; Pagé and Barnes 2016; Park et al. 2017) reveal that about 15 - 40% of the whole-rock Os, Ir, Rh budgets and nearly 100% of the Ru budget are represented by accessory chromites or the PGE-rich micro-inclusions they contain. In contrast, the type-I chromite cores from the Gorumahishani komatiites account for 15 - 20% Ru, 11 - 12% Rh, 2% Os, and 1 - 2% Ir in the whole-rock budgets while the

type-II chromite cores represent even lower proportions of these elements (Ru = 8 - 10%, Rh = 2%, Os = 2%, and Ir = 1%; **Tables 11, 12**). The lower values from both types of grains relative to those calculated from the global dataset partly reflect the redistribution of PGEs during metamorphic modification of the komatiitic chromites. Metamorphic redistribution may include the diffusion of IPGE and Rh from chromites to co-existing sulfide phases (e.g. chalcopyrite, pentlandite, millerite). In addition, part of the whole-rock PGE budget may be held by micro-inclusions of PGE alloys or PGE minerals in the zoned chrome spinels, although such phases have not yet been identified in the laser spot analyses of our samples.

The empirical partition coefficients for trace elements and PGEs are calculated considering the chromite core compositions and the bulk rock compositions of the selected komatiitic rocks (**Table 11**). To obtain the composition of the melt with which the Cr-spinel equilibrated, it is necessary to exclude the portion of each element hosted by this phase from the bulk rock composition. The mass balance equation of Pagé and Barnes (2016) is used to do this. The equation is: $\mathbf{C_i^{Melt} = [(C_i^{WR} \times 100) - (C_i^{Cr\text{-}spinel} \times \% \text{ Cr-spinel})] / (100 - \% \text{ Cr-spinel})}$ where C_i^{Melt} = content of element 'i' in the silicate melt. We then used these calculated melt compositions to determine empirical partition coefficients ($D = C_i^{Cr\text{-}spinel} / C_i^{Melt}$) for Sc, Ti, V, Mn, Co, Ni, Ga, IPGEs, and Rh for the least altered type-I and type-II cores. Type-I chromite cores have values of D_{Sc} = 0.37 - 0.45, D_{Ni} = 0.24 - 0.28, D_{Ti} = 0.12 - 0.13, and D_{Co} = 11.58 - 12.10 (**Table 11**) similar to or lower than the previous empirical values for volcanic chromites as well as experimentally determined values, e.g. D_{Sc} = 0.36 - 0.57, D_{Ni} = 3.5 - 6.8 and D_{Ti} = 0.4 - 3.5, D_{Co} = 3.1 - 29.6 (Horn et al. 1994; Sattari et al. 2002; Righter et al. 2006; Pagé and Barnes 2009; Park et al. 2012). The other trace

elements from type-I chromite cores show a restricted range of values: D_V = 14.08 - 14.38, D_{Mn} = 2.51 - 2.69, and D_{Ga} = 8.44 - 11.04 (**Table 11**). The type-II chromites have higher empirical partition coefficients for D_{Co} (23.52 - 37.66) than the type-I values, and even higher than the volcanic chromites determined by previous workers (Horn et al. 1994; Sattari et al. 2002; Righter et al. 2006; Pagé and Barnes 2009; Park et al. 2012). The other trace elements, except for Sc, also show higher values than the type-I values (**Table 11**). Nevertheless, accessory chromites in komatiitic rocks have re-equilibrated with co-existing modally abundant silicate minerals during metamorphism, so the empirically determined partition coefficients should differ from the true magmatic values.

Empirical partition coefficients calculated for IPGEs and Rh for type-I chromite cores are D_{Os} = 4.45, D_{Ir} = 2.54 - 4.18, D_{Ru} = 49.79 - 67.86, and D_{Rh} = 32.21 - 36.94 (**Table 12**). Coefficients for type-II chromite cores are D_{Ir} = 2.23 - 3.1, D_{Ru} = 35.51 - 45.43, and D_{Rh} = 4.4 - 4.94, which are lower than the values obtained for the type-I grains except for D_{Os} = 8.18 - 8.45 (**Table 12**). Previous studies (e.g. Pagé et al. 2012; Park et al. 2017) of komatiitic chromites yielded D_{Os} = 9.6 - 18, D_{Ir} = 11 - 11.8, D_{Ru} = 5.64 - 100, and D_{Rh} = 13 - 18.1. The calculated D_{Os} and D_{Ir} from this study are somewhat lower while D_{Ru} falls within the wide range of published values. D_{Rh} shows lower values in type-II cores but higher in type-I cores compared to the published data. Experiments by Brenan et al. (2012) using synthetic iron-bearing basalt at 0.1 MPa and 2 GPa at 1400 - 1900°C, fO_2 = IW + 1.6 to IW + 2.1 yielded lower partition coefficient values for these elements (D_{Ru} = 4, $D_{Rh,\ Ir}$ = 0.04 - 1). However, the values were higher (D_{Ir} = 186.9, D_{Ru} = 37.9, and D_{Rh} = 89) under more oxidizing conditions, e.g. fO_2 = IW + 3.1 to IW + 7.2. Other researchers (e.g. Capobianco and

Drake 1990; Capobianco et al. 1994; Righter et al. 2004) determined the experimental partition coefficients under much more oxidizing conditions (NNO to HM buffer), obtaining exceedingly high values of D_{Ir} = 5 - 22,000, D_{Ru} = 20 - 4000, and D_{Rh} = 41 - 530. Natural chrome spinels crystallized from an oxidized basaltic magma from Ambae volcano, Vanuatu at fO_2 = QFM + 2.5 (Park et al. 2012) yielded D_{Os} = 288, D_{Ir} = 472, D_{Ru} = 2448, and D_{Rh} = 641, which are comparable to the values determined experimentally under highly oxidizing conditions. Brenan et al. (2012) emphasized that the high D (Ru Ir, Rh) values obtained for experiments performed under oxidizing conditions were due to the presence of ferric iron in the spinels. In this context, it is significant that some of the zoned chromites from the Gorumahishani belt have Fe^{3+}-rich outer rims with elevated Ru and Rh contents. Similarly, many of the type-V chrome magnetites have higher IPGE contents than the other chromites (**Table 7**). Although the fO_2 values of the Gorumahishani komatiite parental melts are poorly constrained, the empirical partition coefficients ($D_{IPGE, Rh}$) of this study and comparison with other natural or experimental values suggest that the accessory chromites we studied might have crystallized from magma under relatively low fO_2 conditions. The low calculated D values for Os, Ir, Ru, and Rh are consistent with the low Fe^{3+}/R^{3+} values of the type-I and type-II chromite cores, with both suggesting reducing conditions. These findings corroborate the study of Nicklas et al. (2019). These workers observed the global heterogeneity in early Archean mantle redox conditions and found the change of estimated fO_2 conditions for komatiitic melts from reducing to oxidizing since the early Archean (3.48 Ga: 0.11 ± 0.30 ΔQFM log units to 1.87 Ga: 1.22 ± 0.31 ΔQFM log units). Finally, even though the cores are the least altered chromite available, their trace element and PGE abundances may still

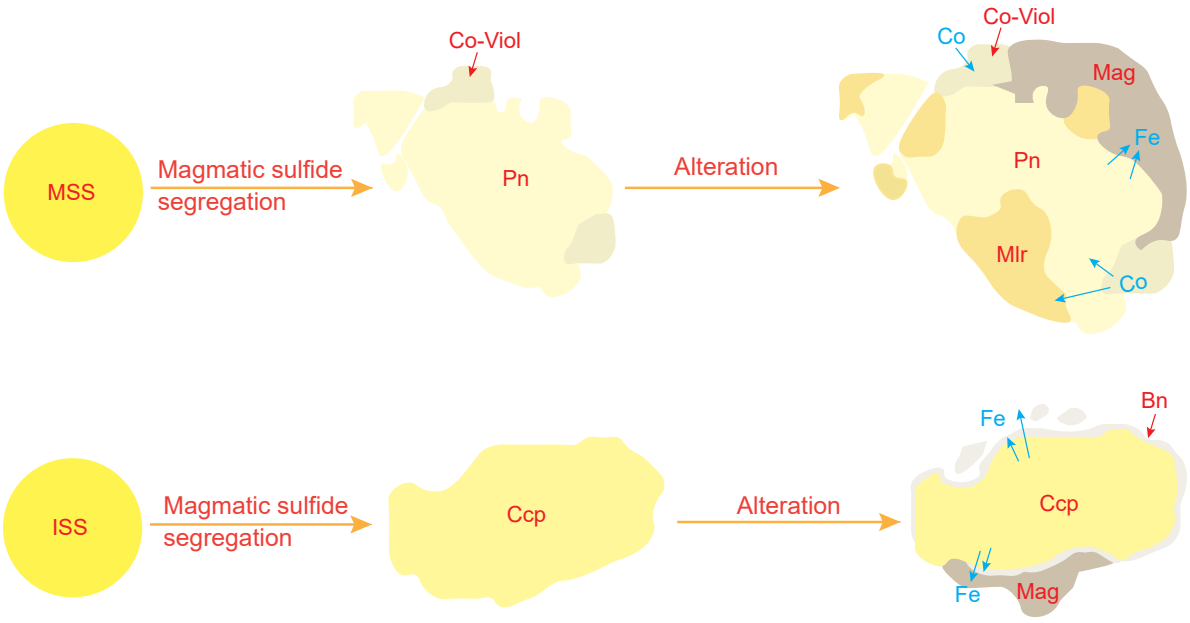

Fig. 28 Schematic illustration representing textural and chemical (major and minor elements) changes of sulfide minerals from the Gorumahishani greenstone belt during alteration. Mineral names abbreviations are from Whitney and Evans (2010).

Table 11 Empirical partition coefficient of trace elements ($D_{Cr\ spinel\text{-}silicate\ melt}$) from the Gorumahishani komatiites

Sample	MIC/16/39			SHB/19-12/82	
Type	Type-I Core	Type-I Core	Type-I Core	Type-II Core	Type-II Core
Location	Tua Dungri	Tua Dungri	Tua Dungri	Kapili	Kapili
D_{Sc}	0.37	0.45	0.38	0.26	0.15
D_{Ti}	0.13	0.12	0.12	12.28	6.77
D_{V}	14.21	14.34	14.08	109.52	37.21
D_{Mn}	2.69	2.57	2.51	32.65	17.81
D_{Co}	12.10	11.99	11.58	37.66	23.52
D_{Ni}	0.24	0.28	0.26	12.13	4.95
D_{Ga}	8.46	11.04	8.44	20.87	11.78

Table 12 Empirical partition coefficient of IPGE (Os, Ir, Ru) and Rh ($D_{Cr\ spinel\text{-}silicate\ melt}$) from the Gorumahishani komatiites

Sample	MIC/16/39				SHB/19-12/82	
Type	Type-I Core	Type-I Core	Type-I Core	Type-I Core	Type-II Core	Type-II Core
Location	Tua Dungri	Tua Dungri	Tua Dungri	Tua Dungri	Kapili	Kapili
D_{Ru}	67.86	51.73	49.79	51.74	35.51	45.43
D_{Rh}	36.94	36.66	36.71	32.21	4.40	4.94
D_{Os}		4.45			8.18	8.45
D_{Ir}	2.72	2.73	4.18	2.54	2.23	3.10

have been modified by metamorphism. Therefore, the calculated magmatic partition coefficients may represent minimum values. This is particularly true for the type-II cores from the southern area (Kapili), which experienced higher-grade metamorphism and are less likely to represent magmatic compositions.

6.3. Significance of different correlation trends in bulk-rock geochemistry

The various relations of bulk-rock major and trace element geochemistry of the entire komatiite sequence from three sections of the Gorumahishani greenstone belt reflect the modal variation of minerals across the lithology of the komatiitic suite of rocks (**Fig. 17a-l**). The cumulate and spinifex zones are extensively serpentinized, and serpentine consumes H_2O in the samples (e.g. Lamadrid et al. 2017). As a result, a positive correlation in MgO vs. LOI is observed. (**Fig. 16a**). The plots of other major and trace elements vs. LOI show little or no influence of metamorphic modification on the major and trace element geochemistry of the komatiitic rocks (**Fig. 16a-h**). Both Al_2O_3 and TiO_2 are less mobile and show a negative correlation when plotted against LOI (**Fig. 16b, c**) supporting that their concentrations were not disturbed due to metamorphic modification of the komatiites. Similarly, trace elements like Ga, Cr, V, and Y vs LOI of the meta-dunites and meta-peridotites also show a negative correlation indicating their robustness during metamorphic modification (**Fig. 16e-h**). Ni shows a positive relation with LOI in the meta-dunites and meta-peridotites which is due to higher modes of olivine (altered to serpentine) in the rocks (**Fig. 16d**). The meta-basalts show variable major and trace elements concentration without any change in LOI indicating their robust character during metamorphic modification of the rocks (**Fig. 16a-h**). Thus, the komatiitic rocks show little effect of metamorphic

modification on bulk-rock major and trace element mobility. Therefore the plots of major and trace elements are used to understand the primary magmatic processes responsible for these early Archean komatiitic rocks (**Fig. 17a-l**).

The Gorumahishani komatiitic suite of rocks shows a distinct variation in its mineral modes from the meta-dunite at the bottom to the komatiitic meta-basalt at the top. A negative relation in the MgO vs. SiO_2 plot (**Fig. 17a**) and the alignment of the bulk-rock data along the olivine fractionation trend indicate olivine-control magma fractionation (e.g. Grove and Parman 2004). The negative relations in the MgO vs. Al_2O_3, CaO, Sc, and Sr plots are due to the incompatibility of these elements during olivine crystallization from the komatiitic magma (**Fig. 17c, d, g, h**). Petrographic study shows that the chromite mode is relatively higher in the meta-peridotite from the spinifex zone than in the lower cumulate zone which is also reflected in the bulk-rock Cr concentration variation across the komatiitic sequence (**Figs. 4, 17k**). In the meta-basalt, the oxide mineralogy is dominated by magnetite, therefore, the Cr concentration drops with decreasing MgO (**Fig. 4**). The magma evolution trends of the Gorumahishani komatiitic rocks are best matched with the early Archean Barberton komatiites of South Africa (Robin-Popieul et al. 2012; Puchtel et al. 2013; **Fig. 17a-l**). It is observed that despite following the same trend, the samples of section A have a low concentration of $FeO_{(T)}$, and TiO_2 and higher concentrations of Al_2O_3, and Cr than the other two sections (**Fig. 17c, e, g, j**). As there is no such variation in mineral assemblage or mineral modal abundance from section A komatiitic suite of rocks than sections B and C, the change in elemental concentrations reflects the difference in the mantle source chemistry (e.g. Waterton et al. 2017, 2021).

The bulk-rock PGE geochemistry can be used as a tracer of the chemical character of the mantle source as well as the processes involved during magma evolution (e.g. Khatun et al. 2014; Mukherjee et al. 2014; Mondal et al. 2019). The bulk-rock PGEs show characteristic trends for the Gorumahishani komatiitic rocks (**Fig. 20, 21**). The positive correlations between MgO, Cr vs. Ru, Ir (**Fig. 20j-o, 21j-o**) and the negative relations in the MgO, Cr vs. Pd/Ru, Pd/Ir plots (**Fig. 22b, c, e, f**) are due to the early crystallization of chromites during the formation of the dunite-peridotite sequence and magnetite during the formation of the komatiitic basalt. Experimental works also demonstrate the high partition coefficients of IPGEs and Rh to chromite structure from silicate melt. However, these partition coefficient values can vary depending on the fO_2 condition of the magma (e.g. Capobianco and Drake 1990; Capobianco et al. 1994; Righter et al. 2004; Brenan et al. 2012; Park et al. 2012). Brenan et al. (2012) conducted experiments at 0.1 MPa and 2 GPa pressure and 1400 - 1900°C temperature with fO_2 = IW + 1.6 to IW + 2.1. Their experiments yielded partition coefficient values for D_{Ru} = 4 and $D_{Rh, Ir}$ = 0.04 - 1. On the other hand, these partition coefficient values were higher at more oxidizing conditions (fO_2 = IW + 3.1 to IW + 7.2) where D_{Ir} = 186.9, D_{Ru} = 37.9, and D_{Rh} = 89 (Brenan et al. 2012). Other experimental works also determined the high partition coefficient values of D_{Ir} = 5 - 22,000, D_{Ru} = 20 - 4000, and D_{Rh} = 41 - 530 at fO_2 varies between NNO to HM buffer (Capobianco and Drake 1990; Capobianco et al. 1994; Righter et al. 2004). Park et al. (2012) determined the partition coefficients between basaltic magma and Cr-spinels from the Ambae volcano, Vanuatu, with fO_2 = QFM + 2.5 and yielded D_{Os} = 288, D_{Ir} = 472, D_{Ru} = 2448, and DRh = 641. Overall, a weak negative correlation of Pd and Pt with MgO and Cr (**Fig. 20 a-f, 21a-f**) indicates the incompatibility of these

PPGEs with early fractionated phases (olivine and chromite). However, Pt in the samples of section A shows a positive correlation with Cr (**Fig. 21a**) which may be due to the presence of Pt-bearing phases (alloys or sulfides) as micro-inclusion in the early fractionated chromite grains (e.g. Borisov and Palme 1995, 2000; Lorand et al. 1999, 2013; Fonseca et al. 2012). There is a weak negative relation between Pd/Ir and Ni/Cu for the samples of the three sections (**Fig. 22g**). Olivine prefers Ni over Cu and chromite prefers Ir over Pd (e.g. Barnes et al. 1988; Mukherjee et al. 2015). Thus early crystallization of olivine and chromite decreases the Ni/Cu ratio and increases the Pd/Ir ratio in the fractionated melt.

The Gorumahishani komatiitic rocks contain very minor to negligible Ni-Cu-Co-bearing sulfides in a few samples from the cumulate and spinifex zones (**Fig. 3m-p**). In a silicate melt-sulfide liquid system the PGEs show a strong preference towards base metal sulfides with the sulfide-silicate partition coefficient ranging from ~10^3 to ~10^6 as observed from the experiments and natural occurrences (e.g. Peach et al. 1990, 1994; Fleet et al. 1996; Andrews and Brenan 2002; Fonseca et al. 2009; Mungall and Brenan 2014). Cr, Ni, Co, Cu, and S along with PGEs and their ratios are plotted across the komatiitic sequence from the three sections (**Fig. 23**). The sulfide minerals chalcopyrite, pentlandite, Co-violarite, millerite, and bornite are present in a few samples from the cumulate and spinifex zones of the komatiitic rocks (**Fig. 3m-p**). If the sulfide phases were responsible for fractionating the PGEs in the komatiitic sequence then there must be a harmonious peak in the concentration of PGEs along with S, Ni, Cu, or Co. The sulfide-bearing samples MIC/16/37 and SHB/19-12/78 from sections B and C show peaks in S along with Pt, Pd, Ru, or Os concentrations indicating a localized control of sulfide minerals on the PGE fractionation (**Fig. 23**).

Two sulfide-bearing komatiitic basalt samples from the section C (SHB/19-12/73 and SHB/18/27) have peaks in S and Cu concentrations but not in PGEs indicating no relation with Cu-bearing sulfides and the PGEs in the rocks (**Fig. 23**). Four samples from the three sections do not have sulfide minerals but show notable peaks in PGE concentrations which may be due to the presence of platinum-group minerals (PGM) or alloys in the rocks. The presence of PGM inclusions (e.g. laurite, erlichmanite, IPGE alloys) in the chromite grains also causes PGE anomalies (e.g. Fiorentini et al. 2004, 2008; Finnigan et al. 2008; Locmelis et al. 2011; Pagé et al. 2012; Mondal et al. 2019; Haugaard et al. 2021), however, so far these phases are not identified in the chromites or the studied komatiitic rocks from the Gorumahishani belt.

6.4. Chemical character of the mantle source and origin of the komatiitic magma

Based on the bulk-rock geochemistry of the Gorumahishani komatiitic suite of rocks are classified as Ti-depleted (in section A) and Al-depleted komatiites (in sections B and C (**Fig. 15b**). The composition of these komatiites are compared with the other Archean komatiitic suite of rocks from Indian cratons as well as from different parts of the world (**Fig. 15b, 29a**). It is observed that the Archean komatiites from the Badampahar greenstone belt in the Singhbhum Craton also show two distinct geochemical characteristics like the Gorumahishani komatiites (**Fig. 15b, 29a**). This is a common observation for other global occurrences where Al-depleted, Al-undepleted, or Ti-depleted komatiites are present and systematically studied (**Fig. 15b**; Lahaye et al. 1995; Puchtel et al. 2004, 2009a; Blichert-Toft et al. 2004; Maier et al. 2009; Robin-Popieul et al. 2012; Sossi et al. 2016). It has been proposed that the Al-depleted komatiites are generated from a garnet-peridotite mantle source with

majorite garnet retained at the residue (e.g. Nesbitt et al. 1982; Xie and Kerrich 1994; Arndt et al. 2008; Robin-Popieul et al. 2012). These studies showed that Al_2O_3 and Yb are more compatible in majorite garnet during the melting of a garnet peridotite mantle source. The komatiitic rocks from sections B and C are characterized by low Al_2O_3/TiO_2 (<15) and high Gd_n/Yb_n indicating an origin from a garnet peridotite source (**Fig. 15b, 29a**; (e.g. Xie and Kerrich 1994; Arndt et al. 2008; Robin-Popieul et al. 2012; Netshidzivhe et al. 2023). The samples from section A are Ti-depleted with a very low Gd_n/Yb_n ratio (**Fig. 29a**). This possibly indicates their origin from a previously depleted mantle source (e.g. Wilson 2019; Waterton et al. 2021).

Existing models for the origin of Al-depleted komatiites propose the generation of high-Mg silicate melt from a rising plume of garnet-peridotitic material at P ≥ 6 GPa and T ≥ 1600°C (e.g. Walter 1998; Asahara et al. 1998; Herzberg and O'Hara 2002; Arndt 2003). High-Mg silicate melt formed by partial melting at this high pressure is more compressible than their solid residue and the density difference becomes minimal (e.g. Ohtani 1984; Ridgen et al. 1984; Miller et al. 1991). Therefore, the mantle plume at this depth must produce a significant amount of partial melt to escape to the surface. It is less likely that the Ti-depleted komatiites of section A generated by a second stage of melting of this depleted plume source at the garnet-peridotite stability field because of their HREE-depleted character (**Fig. 18a-d**) and almost similar Al_2O_3 content (1.42 - 6.88 wt.%) compared to the Al-depleted samples (Al_2O_3 = 0.31 - 5.62 wt.%). The second stage of melting of a garnet peridotite residue would require a high degree of partial melting. This might have resulted in high HREE and Al_2O_3 in the Ti-depleted komatiitic rocks but this is not true for the section A samples (**Fig. 18a-d**). In this context, a second stage of melting of

the same depleted mantle plume at a shallower depth similar to the spinel peridotite stability field (P < 4 GPa and T < 1500°C) might be a more possible mechanism to generate the Ti-depleted komatiites of section A (e.g. Robinson and Wood 1998; Arndt 2003; Wilson 2019; Waterton et al. 2021). This process could produce MgO-rich (29.12 - 43.32 wt.%) and highly Ti-depleted (0.02 - 0.13 wt.%) melt than the first stage of melting of a garnet peridotite mantle source (MgO = 20.90 - 42.76 wt.%, TiO_2 = 0.10 - 0.54 wt.%; **Table 8**). The density difference between melt and residue is much less than in the previous case and melt can escape from the depleted mantle source by a high degree of partial melting (e.g. Arndt et al. 1997; Arndt 2003). The depleted LREE pattern of section A komatiites compared to sections B and C along with low $FeO_{(T)}$ and high Cr content also support the origin from a depleted mantle source (**Fig. 18a-d, Table 8**). Chromium is compatible with garnet during high-pressure melting of a garnet peridotite source (e.g. Klemme et al. 2009). Therefore, the komatiitic melt generated due to a high degree of partial melting of a depleted mantle source should release more Cr than the previous melting.

To quantify two extreme ends of komatiite melt generation in the Gorumahishani greenstone belt, a two-stage melting of the mantle plume has been modeled based on a non-modal batch melting equation (Shaw 1970). The first stage of melting is considered to take place at the garnet peridotite source containing garnet, olivine, orthopyroxene (Opx), and clinopyroxene (Cpx). 10 %, 20 %, 30 %, and 40 % non-modal batch melting has been performed at the plume source by varying their mineralogical composition from 5 % garnet to 10 %, 15 %, and 20 % garnet in every melting stage (**Fig. 29b**). The second stage of melting is considered to take place at the spinel peridotite source containing olivine, orthopyroxene, and spinel

with 10 %, 20 %, 30 %, 40 %, and 50 % non-modal batch melting (**Fig 29c**). Non-modal batch melting lines of these two stages of melting are produced based on the partitioning of (Gd/Yb) and TiO_2 between the source mantle and the komatiitic melt (McKenzie and O'Nions 1991). In the first stage, it is observed that the Al-depleted komatiitic melt can be produced by 27 % partial melting of a plume at a garnet peridotite depth with 15 % garnet (**Fig. 29b**). Although the melt % varies with the change of garnet modal %; the consideration of 15 modal % garnet at the source of Al-depleted komatiite is consistent with the previous works (e.g. Arndt 2003; Robin-Popieul et al. 2012). After the first stage of melting, the depleted mantle plume ascends to a shallower level and the second stage of melting takes place at the spinel peridotite stability field. To produce a Ti-depleted komatiite, like section A, a high degree of partial melting (~45 %) is required (**Fig. 29c**). In the proposed model, spinifex textured komatiites from the Gorumahishani belt are considered as the parental komatiitic melt composition (e.g. Barnes et al. 1995). There are experimental studies as well as models based on natural komatiites that showed ~40 % - 50 % partial melting of a depleted mantle source to generate komatiitic melts similar to those occurring in different parts of the world (e.g. Herzberg 1992; Walter 1998; Robin-Popieul et al. 2012; Sossi et al. 2016).

Alternative theories are available to explain the high degree of partial melting (~40 % - 50 %) of a spinel peridotite mantle source to generate komatiitic magma. One of the theories proposes a hydrous melting of the source mantle (e.g. Allègre 1982; Echeverría 1982; Grove and Parman 2004; Fiorentini et al. 2008; Sobolev et al. 2016). After originating from the plume source, the komatiitic melt rises to the surface via rift zones generated within the proto-crust. The rift basin gradually

transforms into an ocean basin where water can percolate through the rift axis like the modern-day mid-ocean ridge settings (e.g. Langmuir and Forsyth 2007). In this setting, a high degree of melting of the depleted shallow mantle source under a hydrous condition might have generated the komatiites similar to that of section A within the Gorumahishani greenstone belt (e.g. Echeverría 1982). Sobolev et al. (2016) proposed the existence of a hydrous deep-mantle reservoir based on the study of hydrous melt inclusions in magnesian olivine in the Archean komatiites from the Abitibi greenstone belt in Canada. Water-bearing wadsleyite [$Mg_4O(Si_2O_7)$] or ringwoodite [$(Mg, Fe^{2+})_2SiO_4$] acts as a source of water when the plume passes through the mantle transition zone at ~410 km depth (Sobolev et al. 2016). Although, H_2O bearing fluid inclusions in the pristine olivine grains are not identified from the metamorphosed komatiites of the Gorumahishani greenstone belt, such supply of water from the deep mantle to the plume source is still possible which can expedite the high degree of partial melting at the second stage. Fiorentini et al. (2008) reported hydromagmatic primary amphiboles from the Pechenga ferropicrites and interpreted that the source of volatiles might be either a metasomatized subcontinental lithospheric mantle or a hydrous plume. However, the primary magmatic amphibole is not identified in the metamorphosed komatiites (**Fig. 3f, g**) or as inclusions in chromite, olivine, or pyroxene from the Gorumahishani belt.

Besides the plume origin of the komatiitic suite of rocks, Allègre (1982) proposed a hydrous melting of an undifferentiated peridotitic oceanic proto-crust at a shallow mantle depth (40 - 70 km) in a subduction environment. According to their model, the hydrated peridotitic oceanic crust had gone through a high degree of partial melting when intersecting the wet-solidus at a high Archean geothermal

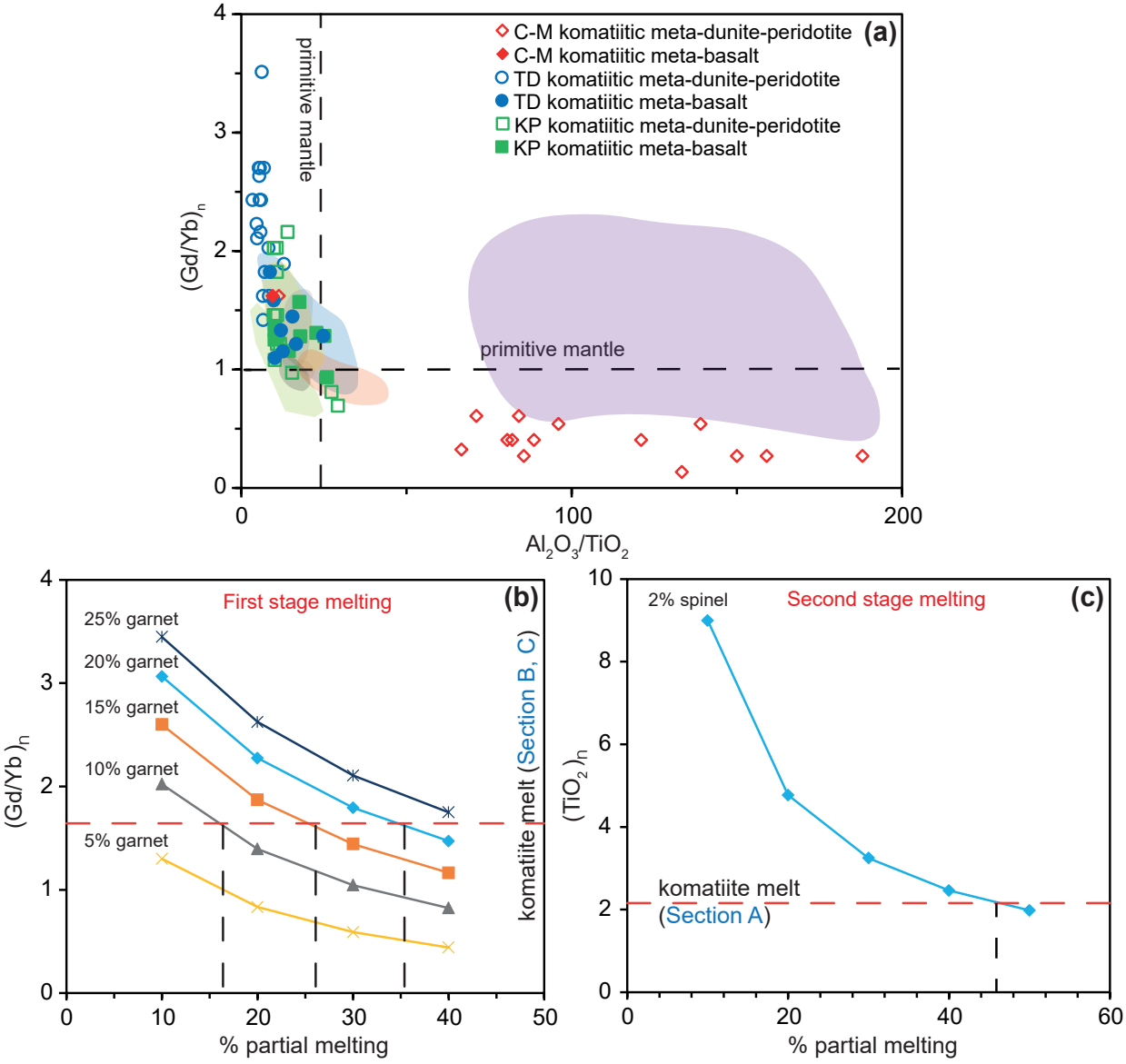

Fig. 29 a Al_2O_3/TiO_2 vs. Gd_n/Yb_n diagram for the Gorumahishani komatiitic rocks. Gd and Yb concentrations are normalized to the primitive mantle values of McDonough and Sun (1995). Gorumahishani komatiite and komatiitic basalt samples are compared with early Archean Badampahar, Daitari, Sargur, and Barberton komatiites and komatiitic basalts. Other data from Jayananda et al. (2008); Robin-Popieul et al. (2012); Puchtel et al. (2013); Tushipokla and Jayananda (2013); Schneider et al. (2019); Ghosh et al. (2019); Bachhar et al. (2021); Adhikari et al. (2021a). **b-c** Al_2O_3/TiO_2 vs. Gd_n/Yb_n plots showing a two-stage melting of the Gorumahishani komatiitic rocks from sections B and C (first stage), and section A (second stage). Komatiitic meta-dunite-peridotite: Sargur Daitari Barberton Badampahar; Komatiitic meta-basalt: Sargur Daitari Barberton Badampahar.

gradient. An experimental study by Parman et al. (1997) also pointed to a subduction origin of the ˜3.5 Ga Barberton komatiites. They compared the composition of igneous pyroxene from the olivine spinifex unit with pyroxene from a laboratory experiment at 0.1 MPa under anhydrous conditions or 100 - 200 MPa under hydrous conditions. This comparison showed that the pyroxene minerals contained 6 wt.% magmatic water, and the H_2O in komatiitic magma might sourced from a subducted oceanic crust. Based on the experimental study, Parman et al. (2001) proposed that the Archean Barberton komatiitic basalts are equivalent to modern boninites and were generated by a hydrous melting process in a subduction zone. Higher SiO_2, lower TiO_2, positive anomalies in Zr and Hf, and a U-shaped REE pattern of the komatiitic rocks also showed some similarity with boninites, along with petrographic evidence for high magmatic H_2O contents. Extraction of Barberton komatiitic melt gave rise to a depleted mantle residue as represented by part of the material forming the Kaapvaal cratonic keel (e.g. Parman et al. 2001, 2004; Grove and Parman 2004).

6.5. PGE geochemical and Sm-Nd isotopic constraints on the mantle source and the melting processes

Primitive mantle normalized PGE plots of the 3.5 Ga komatiitic rocks from the Gorumahishani greenstone belt show a PGE-depleted character (**Fig. 24a-d**). The PGE patterns are compared with the early to late Archean komatiites from other cratons e.g. Yilgarn, Kaapvaal, Pilbara, Karelia, Superior, and Western Dharwar Cratons (**Fig. 24d**). The Gorumahishani komatiites show a similar depleted character to other early Archean komatiites. Based on the PGE geochemistry of komatiites of different ages,

Maier et al. (2009) showed that there is a gradual enrichment of PGEs in the late Archean komatiites (**Fig. 24d**). Maier et al. (2009) hypothesized this character as evidence of progressive mixing of PGE-rich chondritic materials with the Earth's mantle during the late heavy meteorite bombardment (˜4.5 Ga - 3.8 Ga; Chou 1978). The early Archean komatiites were formed during the slow accretion of the PGE-rich cosmic material and bear a depleted PGE character that was generated due to early core segregation (e.g. Stevenson 1981; Maier and Mundl-Petermeier 2023). The relatively younger komatiites (Mesoarchean to Late Archean) show PGE-enriched character due to the slow and gradual mixing of the chondritic materials and a homogenous mixing was completed by 2.9 Ga (Maier et al. 2009). Puchtel et al. (2004, 2014, 2016) explained the change in PGE characters in komatiites with time as a consequence of the heterogeneous mantle source domain in terms of PGE geochemistry. They proposed the existence of Pt-enriched and Pt-depleted mantle domains during the major silicate differentiation of the Earth (e.g. Stevenson 1981). Recent research by Waterton et al. (2017, 2021) showed that the Paleoproterozoic Winnipegosis komatiites (ca. 1.9 Ga), Canada, have a depleted PGE character that questions the gradual PGE enrichment of the Earth's mantle during progressive mixing with the PGE-rich chondritic component (e.g. Maier et al. 2009).

According to Waterton et al. (2021), Ru is a good tracer to study the PGE partitioning behaviour of the evolving Earth. In the fertile mantle xenoliths, PGEs are concentrated in base metal sulfides (e.g. Lorand and Alard 2001) and retain as alloy phases in the depleted mantle after the complete exhaustion of sulfides due to a high degree of partial melting (e.g. Luguet and Pearson 2019). If the mantle peridotite is critically melted at a high temperature (~1650°C), the initial melt after

~10 % partial melting contains a low Ru concentration because high-temperature sulfides are still present in the mantle source (Waterton et al. 2021). After high degrees of partial melting (~20 % - 25 %) at the same temperature, these sulfides are completely exhausted from the mantle and Ru content increases in the melt (e.g. Waterton et al. 2021). The melting model indicates that komatiitic melt can be generated during the first stage of melting at garnet peridotite depth by 27 % of partial melting of a rising plume (**Fig. 29b**). Therefore, the mantle source probably reaches sulfide exhaustion and the Ru in sections B and C komatiitic rocks of the Gorumahishani greenstone belt may have a concentration in the range of 3 - 8 ppb. The lower values of Ru in komatiitic rocks possibly indicate early Ru removal from the silicate melt as alloy phases (e.g. Lorand et al. 2013). The upper limit of these values is closely similar to the primitive mantle Ru content of 7 ppb (e.g. Becker et al. 2006) and may indicate a complete sulfide exhaustion from the source. After complete sulfide exhaustion during a high degree of partial melting at the first stage, Ru concentration in the second stage melt should be low (e.g. Waterton et al. 2021). The Ti-depleted komatiite of section A within the Gorumahishani belt has Ru content in the range of 3 - 5 ppb which can be explained by the model proposed by Waterton et al. (2021). However, the possibility of early removal of Ru-bearing alloys from the silicate melts may be another possible mechanism for Ru-depletion in the komatiites (e.g. Lorand et al. 2013). In addition, a low concentration of Ru in the Ti-depleted komatiite is possible if the melt is generated from a reduced mantle source where D^{Ru} is relatively higher towards the silicate melt (e.g. Waterton et al. 2021; Zhou et al. 2023).

In the normalized PGE plots most of the komatiitic samples of sections B and C from the Gorumahishani belt have negative Os, Ru, and Pt anomalies and a sample from section A has a negative Ir anomaly (**Fig. 24a-c**). Although the komatiitic rocks from the entire belt contain chromites, these negative anomalies of Os, Ru, and Pt (and Ir) strongly suggest early removal of PGE alloys before the onset of chromite crystallization from the rising komatiitic melt or retention of PGE-alloys in the mantle residue during high-degree of partial melting. Based on an experimental study at 1300°C, Fonseca et al. (2012) proposed that the Os-Ir alloys can precipitate directly from a silicate melt, which is found in the mantle rocks. Ru, Os, and Ir have low solubility in the silicate melts and their sulfide matte/silicate-melt partition coefficients are quite high (Brenan and Rose 2002; Fonseca et al. 2012). Thus, partial melting and extraction of sulfur into the silicate melt from the base-metal-sulfide matte in the mantle can lead to a decrease in the fS_2 condition of the mantle. This low fS_2 condition may lead to the exsolution of IPGE or Pt-alloys from the refractory matte because of the decrease in solubility of PGEs (e.g. Borisov and Palme 1995, 2000; Fonseca et al. 2012). Lorand et al. (1999) from the study of Pyrenean orogenic lherzolites showed that Pt along with Ir and Ru can reside in the mantle as melting-resistant atomic clusters or micro alloys after significant melt extraction. In another study, Lorand et al. (2013) discussed that the platinum-group minerals (PGM) may present as a refractory residue of platinum-iridium-osmium alloys as found in many sulfide-free residual mantle peridotites. Mantle xenoliths from the Slave Craton and the Kaapvaal Craton also show evidence of the presence of PGM or alloy phases (Irvine et al. 2003; Luguet et al. 2007). A late-stage sulfur saturation of the Gorumahishani komatiitic melt and their S-undersaturated character before the

eruption to the surface may be the reason for the early crystallization and precipitation of PGE phases. Wittig et al. (2010) proposed that the Ru (Os, Ir)-rich alloys can be eliminated from their mantle source by dissolving into the S-free, Si-poor komatiitic melt at a temperature of 1600 - 1700°C. However, it is difficult to incorporate the PGEs in melts during mantle melting (e.g. Alard et al. 2000) because the PGM or alloy phases might have reprecipitated from the komatiitic melt close to the melting site.

The Sm-Nd errorchron of the 3.5 Ga Gorumahishani komatiites gives an $\varepsilon_{Nd(T)}$ value of 0.1 for the section C samples whereas the calculated values for eighteen samples give an average $\varepsilon_{Nd(T)}$ = - 0.17 ± 1.85. Overall, the Sm-Nd isotopic character of the Gorumahishani komatiites shows similarity with the primitive mantle. Most of the samples have positive $\varepsilon_{Nd(T)}$ values ($\varepsilon_{Nd(T)}$ = +0.11 to +2.02), other than the five samples that yielded negative $\varepsilon_{Nd(T)}$ values ($\varepsilon_{Nd(T)}$ = -0.04 to -2.37) (**Table 10**). The positive $\varepsilon_{Nd(T)}$ values may indicate a slightly depleted mantle source domain and agree with the PGE geochemical constraints on the mantle source (**Fig. 24a-d**). On the other hand, the five negative $\varepsilon_{Nd(T)}$ values may indicate a little perturbation of the Sm-Nd isotopic systematic due to metamorphism (e.g. Blichert-Toft et al. 1999). However, the $^{143}Nd/^{144}Nd$ vs. La_n/Sm_n plot reveals no such isotopic disturbance due to metamorphic modification of the rocks (**Fig. 25a**). Alternatively, this may be due to little heterogeneity of the mantle source in terms of incompatible trace element concentrations (e.g. Lahaye et al. 1995; Jayananda et al. 2008). In the age vs. $\varepsilon_{Nd(T)}$ plot (**Fig. 26**), the Gorumahishani komatiites show an $\varepsilon_{Nd(T)}$ value well within the range of the early Archean komatiites worldwide like Barberton komatiite, Kaapvaal Craton (South Africa), Warrawoona Group komatiite, Pilbara Craton (Australia),

Sargur group komatiite, Western Dharwar Craton (India), and Daitari komatiite, Singhbhum Craton (India). Most Early Archean komatiites and other rock samples from different parts of the world exhibit positive $\varepsilon_{Nd(T)}$ values, indicating a depleted mantle character (e.g. Bennett et al. 1993; Nebel et al. 2014) (**Fig. 26)**. In Mesoarchean to late Archean, komatiites and other rock samples show an increase in negative $\varepsilon_{Nd(T)}$ values, which may indicate a shift towards horizontal tectonics and subsequent mantle metasomatism or crustal contamination event (e.g. Jahn and Condie 1995; Roy et al. 2004; Mukherjee et al. 2012) (**Fig. 26**).

6.6. Geodynamic implications

Available geochronological studies on komatiitic and felsic volcanic rocks from the three IOG greenstone belts in the Singhbhum Craton e.g. Tomka-Daitari, Noamundi-Jamda-Koira and Gorumahishani-Badampahar greenstone belts (**Fig. 1a**) revealed the ages around 3.6 to 3.5 Ga (e.g. Basu et al. 2008; Mukhopadhyay et al. 2008; Adhikari et al. 2021a; Jodder et al. 2021). The current study on the Gorumahishani komatiitic suite of rocks also yielded a whole rock Sm-Nd errorchron age of ~3.5 Ga. This study along with other recent research works on the Singhbhum Craton confirm that the rocks of the Older Metamorphic Group, Older Metamorphic Tonalite Gneiss, older phases of the Singhbhum Granitic Complex, and the three greenstone belts are more or less coeval within a period of ~3.6 Ga - 3.3 Ga (e.g. Sharma et al. 1994; Goswami et al. 1995; Mishra et al. 1999; Tait et al. 2011; Upadhyay et al. 2014; Dey et al. 2017; Chakraborti et al. 2019; Pandey et al. 2019).

The current research proposes that the Gorumahishani komatiites with two distinct compositional types were formed from the rising plume of peridotitic

materials where melting took place in two different depth fields. The first-stage melt generation was restricted at the garnet peridotite stability depth that generated the Al-depleted komatiite whereas the Ti-depleted komatiitic melt was generated due to the second-stage melting of the same depleted plume source at a shallow depth (**Fig. 29b, c**). According to this model, the komatiitic melts erupted through an older mafic proto-crust (older than 3.6 Ga) (**Fig. 19a-c**). The Hadean to early Archean geochronology of the Singhbhum Craton is evidenced by the presence of detrital and xenocrystic zircons of ca. 4.2 - 3.6 Ga (e.g. Chaudhuri et al. 2018; Miller et al. 2018; Olierook et al. 2019; Sreenivas et al. 2019; Bhattacharjee et al. 2021). Based on Re-Os isotope systematics of chromites from the Sukinda and Nuasahi ultramafic-mafic complexes in the Singhbhum Craton, Mondal et al. (2007) reported a mantle depletion age of ~3.7 Ga. This indicates that the initial melting of a primitive mantle started as early as ˜3.7 Ga in the Singhbhum Craton and suggested the probable existence of a contemporary ancient crust.

Petrological and geochemical studies indicate that the Gorumahishani komatiites were generated from the hot mantle plume at different depths and erupted at the surface through rift basins similar to many other komatiites worldwide (e.g. Glikson 1971; Fyfe 1978; Bickle 1993; Arndt 2003; Robin-Popieul et al. 2012; McKenzie 2020; Waterton et al. 2021) (**Fig. 30**). There are several alternative hypotheses for the generation of komatiitic magma in various tectonic settings. Researchers (e.g. Shimizu et al. 2001; Sobolev et al. 2016) suggested that komatiitic melts might have been generated from the hydrous plume source and the hydrous phases were added to the plume from the mantle transition zone or the upper mantle. Wilson et al. (2003) proposed that the komatiite genesis begins by

melting of a hot mantle plume at a deeper depth to produce Al-depleted komatiites and the residual depleted mantle may be melted again at a relatively shallower depth under an H_2O saturated condition within a subduction setting to produce the low TiO_2/Al_2O_3 komatiites. According to Parman et al. (2001, 2004) and Grove and Parman (2004), komatiitic magma might be generated due to hydrous mantle melting within a subduction setting.

The Archean greenstone belts are closely associated with tonalite-trondhjemite-granodiorite-granitic rocks (TTG) of similar age. Moyen and Martin (2012) summarized the origin of the TTG suite of rocks by (i) melting at the base of a thick oceanic plateau over the upwelling mantle plume, (ii) melting of the delaminated mafic crust at the downwelling part of the convective mantle, and (iii) melting of the subducted mafic oceanic crust. The early Archean greenstone belts of the Singhbhum Craton are mostly associated with the felsic batholithic plutons of the Singhbhum Granite Complex. In addition, TTG rocks of the OMTG are also present at different places in the craton **(Fig. 1b).** The ~3.5 Ga tonalitic enclave known as the Patna tonalite is located near the Gorumahishani greenstone belt. These TTG are characterized by high-HREE concentrations (Dey et al. 2017). The low-HREE TTG rocks are also located in the Champua area (~3.5 Ga, Sharma et al. 1994). Both the high-HREE and low-HREE TTG rocks from the Singhbhum Craton are characterized by low Mg# along with low Cr and Ni concentrations indicating that their parental melts can not be generated from a subducted oceanic crust (e.g. Saha 1994; Sharma et al. 1994; Dey et al. 2017). If melting of the subducted mafic crust produced the parental melts of the TTG then it must have passed through the overlying mantle wedge whereby their Mg# along with MgO, Cr, and Ni concentrations should be increased

(e.g. Smithies 2000; López et al. 2006). Geochemical modeling and experimental studies also point towards the melting of ultramafic-mafic crust at different depths to produce parental melt of the high- and low-HREE TTG rocks (e.g. Rapp and Watson 1995; Moyen 2011). According to these researchers, the trace element composition of the tonalite-trondhjemite-granodioritic rocks is strongly controlled by the mineralogy of the source and the depth of melting. Parental magma for the low-HREE tonalite-trondhjemite-granodioritic rocks can be generated at the deeper crustal depth where garnet is stable with pressure-temperature varies between 10 kbar at 700°C to 15 kbar at 1200°C (Moyen and Martin 2012). On the other hand, parental magma for the high-HREE tonalite-trondhjemite-granodioritic rocks can be generated by melting of the mafic-crust at a shallow to moderate depth (~8 - 10 kbar) (e.g. Moyen and Stevens 2006) where plagioclase, pyroxene, and amphibole are stable. Therefore, it may be possible that the parental magmas of the early Archean tonalite-trondhjemite-granodioritic rocks of the Singhbhum Craton generated by the melting of the mafic proto-crust at different depths (e.g. Champion and Smithies 2007; Moyen et al. 2007; Dey et al. 2017) (**Fig. 30**).

The supracrustal rocks of the Older Metamorphic Group (OMG; Saha 1994) are present as enclaves along with the OMTG rocks within the Singhbhum granite batholithic complex**.** Saha (1994) reported that the amphibolites of the OMG are LREE enriched without HREE depletion indicating their probable origin related to the melting of a mafic primordial crust at a moderate depth (**Fig. 30**). Saha and Ray (1984), Mukhopadhyay (2001), and Chaudhuri et al. (2022) also postulated that the OMG amphibolites have a komatiitic to tholeiitic affinity and pointed to their

fractional crystallization origin from an ultramafic parental magma like those of the upper komatiitic/ tholeiitic/ picritic basalts of the Iron Ore Group supracrustal unit.

The voluminous older phases of the Singhbhum granites (phase-I and phase-II; Saha 1994) are the most prominent felsic magmatic units in the Singhbhum Craton. The phase-I granitic rocks are mostly granodiorites-trondhjemites and the phase-II rocks are granodiorites grading to adamellitic granites (e.g. Saha 1994). The emplacement of the different phases of the Singhbhum granite batholithic complex during the early Archean points toward a continuous mantle plume activity (e.g. Saha 1994; Dey et al. 2017). Underplating and intraplating of plume-generated ultramafic-mafic magma in several episodes resulted in repeated crustal reworking (Dey et al. 2017; **Fig. 30**). Low K_2O and FeO_{total}/MgO, and high Cr/Ni of the phase-I and phase-II granitic rocks compared to the phase-III variety indicate their origin by repetitive melting of the ultramafic-mafic crustal component (Saha 1994). Therefore, it may be possible that the ultramafic-mafic proto-crust of the Singhbhum Craton was melted during the emplacement of the high-temperature komatiitic magma at different depths in different degrees to produce the parental magmas of the older phases of the Singhbhum granite batholithic complex (phase-I and II) and the tonalite-trondhjemite-granodiorite suite of rocks of the OMTG (**Fig. 30**). Fractionation of these magmas resulted in variations in the older phases of the Singhbhum granites and the tonalite-trondhjemite-granodiorite.

Based on Archean komatiite formation along with the associated TTG, this study proposes a geodynamic model for the early crustal evolution of the Singhbhum Craton (**Fig. 30**). The continuous heat conduction from a hot mantle plume generated a soft and ductile crust that induced sagging of the overlying crustal

materials and formation of a basinal environment (e.g. Dey et al. 2017). Komatiitic magmas were emplaced within these basins through rifting and the rift basins gradually transformed into ocean basins (e.g. Rosendahl 1987; Leroy et al. 2004). Pillow basalts that are located at the top of the komatiitic sequence from the Gorumahishani, Badampahar, and Daitari areas (e.g. Ghosh et al. 2019; Bachhar et al. 2021; Jodder et al. 2021, 2023) and also cross-laminated sedimentary units, graded bedding, and ripple lamination from the top of the volcano-sedimentary sequences of the greenstone belts indicate subaqueous environment (e.g. Mazumder and Chaudhuri 2019; Jodder et al. 2021, 2023). The continuous rifting process of the ocean floor, therefore, leads to the subduction of oceanic lithosphere under the continental lithosphere in an active continental margin setting. The Mesoarchean to late Archean ultramafic-mafic intrusive rocks (e.g. Nuasahi-Sukinda-Mayurbhanj Complexes) and the volcanic rocks of the younger greenstone belts (e.g. Dhanjori-Simlipal-Dalma-Jagannathpur-Malangtoli belts) are thought to be formed from the magmas that were originated in the lithospheric mantle wedge by hydrous melting within active continental margin settings (**Figs. 1a;** Mondal et al. 2021; Bhattacharjee et al. 2022). The emplacement of these magmas adjacent to the early Archean greenstone belts (~3.6-3.5 Ga) supplied the heat required for the metamorphism of these rocks. The voluminous younger felsic plutonic rocks (Mayurbhanj-Nilgiri-Bonai granitic complexes) were formed from the felsic magmas that were generated by melting and reworking of the early Archean TTG crust during the emplacement of the ultramafic-mafic magmas from the continental lithospheric mantle wedge (e.g. Mondal et al. 2021; Bhattacharjee et al. 2022). In addition to supplying the heat, the younger igneous intrusions acted as the source of the pressure for the

metamorphism of the early Archean rock suites in the craton. Evidence of compressional deformation on the komatiitic and tonalite-trondhjemite-granodiorite-granite suite of rocks is provided by many researchers. Saha et al. (2021) have studied the Singhbhum granite phase-I and phase-II rocks around the Gorumahishani-Badampahar greenstone belt and reported inclined to reclined folds with steep NE-SW trending axial plane and steeply plunging mineral elongation-lineations that indicate high strain zones in these areas. Similarly, Singhbhum granite phase-II rocks show foliation and lineation fabrics along the contact with the Gorumahishani-Badampahar volcano-sedimentary strata (Saha et al. 2021). A more prominent signature of a compressional deformation is represented by the NE trending tight to overturned synforms and antiforms as observed in the Gorumahishani-Badampahar volcano-sedimentary sequence (Saha et al. 2021).
The researchers (e.g. De wit et al. 1992; Rodgers 1996; Bleeker 2003) proposed the possibility of the existence of an early Archean supercraton considering the global occurrence of the 3.6 Ga - 3.3 Ga komatiitic magmatism. Nearly ca. 35 cratonic blocks are considered at the early Archean (e.g. Bleeker 2003). However, a correlation was not possible because of the multiple break-up and dispersal events by convective plumes (e.g. Taylor and McLennan 1985; Pollack 1997; Bleeker 2003). It has been considered that the Archean Earth had twice the heat production than today (e.g. Lambert 1980; Richter 1985) and was characterized by vigorous mantle convection with smaller, faster plates**.** High geothermal gradient and high convection rate of the Archean mantle implied a lower viscosity and, therefore, a thinner lithosphere or thinner thermal boundary layer, which might not have the strength to behave rigidly and gave rise to frequent break up of the Archean continental or

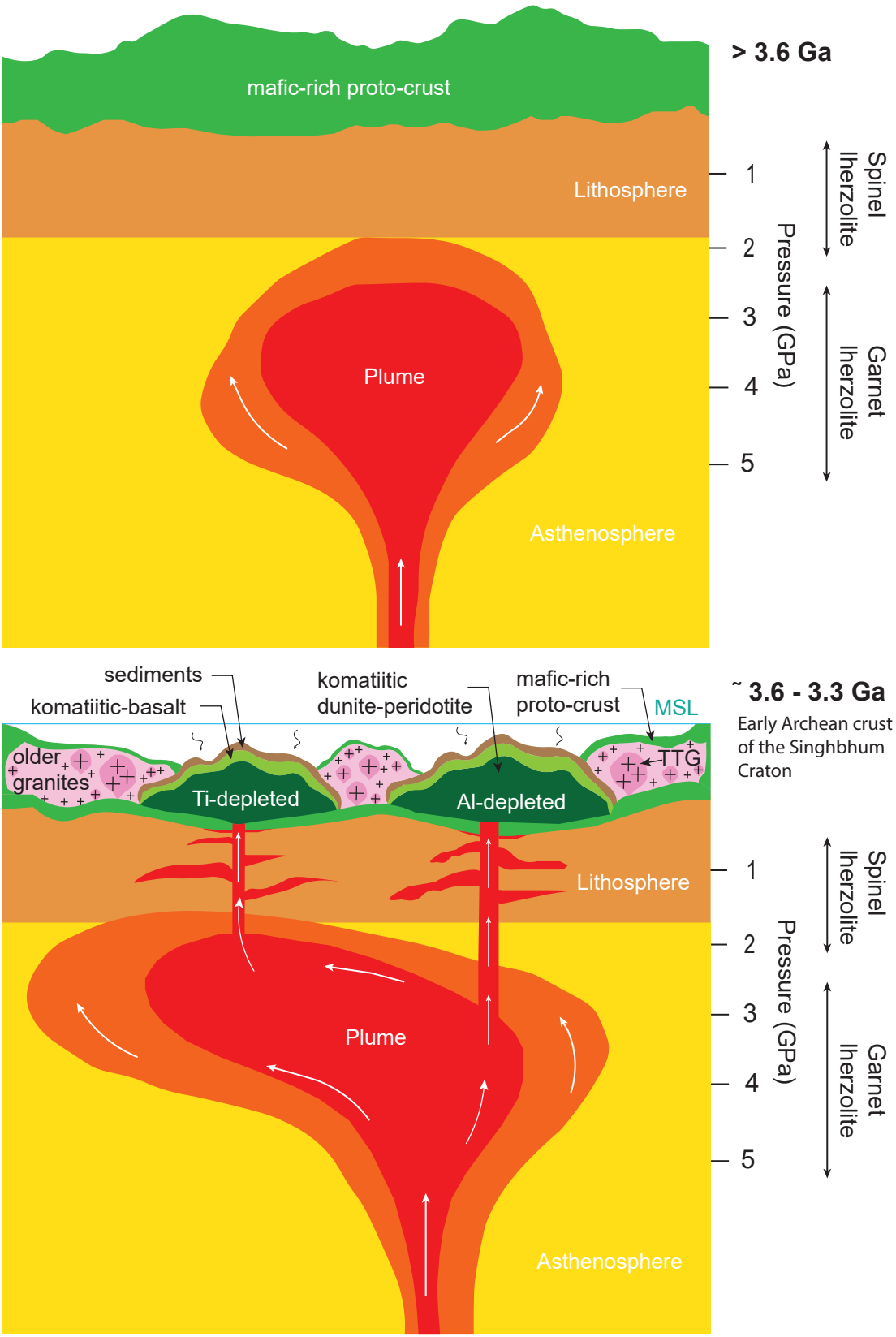

Fig. 30 Models showing a probable geodynamic setting for the formation of the komatiitic suite of rocks and contemporaneous tonalite-trondhjemite-granodiorite (TTG), and older phases of the Singhbhum granite rocks in the Gorumahishani greenstone belt, Singhbhum Craton. Models illustrate that the komatiitic magma is generated by a two stage melting of the mantle plume and associated TTG and older granitic rocks are generated by melting of a mafic-rich proto-crust. Ti-depleted komatiite is from Maharajgunj-Chuka Pahar (section A) and Al-depleted komatiite is from Tua Dungri and Kapili (sections B and C). Spinel and garnet lherzolite fields are from McDonough and Rudnick (1998).

oceanic plates into smaller ones (e.g. Davies 2007; Ernst 2017). Under this condition, smaller, transient continental aggregations as supercratons were more likely than the formation of a single large supercontinent. The ca. 3.5 Ga Vaalbara supercraton (e.g. De wit et al. 1992; Rodgers 1996; Bleeker 2003) is one such hypothetical supercraton, and the Singhbhum Craton might be a part of this. Petrological and geochemical similarities of the early Archean Kaapvaal, Pilbara, Singhbhum, and Dharwar Cratons (e.g. Nelson et al. 1999; Hofmann et al. 2016; Kumar et al. 2017) possibly indicate their coexistence in the ancestral supercraton assembly. The presence of ~3.6 - 3.5 Ga komatiitic magmatism event, ~3.3 Ga voluminous TTG activity, ~ 3.0 - 2.7 Ga large-scale magmatic events as evidenced by igneous intrusive and extrusive complexes and dyke-sills, and rifted margins of the Proterozoic age therefore, possibly indicate the Kaapvaal, Pilbara, Singhbhum, and Dharwar cratons are mere fragments of the Vaalbara supercraton. The similarity of paleomagnetic data between the Archean dyke swarms from these cratons also indicates their proximity to each other (e.g. Kumar et al. 2017).

Chapter 7

Conclusions

7. Conclusions

The major conclusions of this research are

a) The komatiitic suite of rocks in the Gorumahishani greenstone belt were metamorphosed under greenschist to amphibolite facies. As a result, the primary mineral assemblages of olivine, clinopyroxene, and plagioclase were altered to an assemblage of serpentine, tremolite, chlorite, hornblende, epidote, and carbonate minerals. Mineral assemblages like serpentine + tremolite + chlorite ± calcite ± dolomite from the Maharajgunj-Chukapahar (section A) and Tua Dungri areas (section B) indicate the effect of greenschist-amphibolite transition facies metamorphism. From the Kapili area (section C), the silicate and carbonate mineral assemblages like serpentine + tremolite + hornblende + chlorite ± actinolite ± carbonate indicate metamorphism under amphibolite facies.

b) The accessory chromite grains from the metamorphosed komatiitic dunite-peridotites within the greenstone sequence show optical and compositional zoning patterns (classified as type I, II, III chromite grains) due to modification with a relatively unaltered central core surrounded by ferritchromit to chrome-magnetite rims. With increasing metamorphic grade from the northern (section A, B) to the southern (section C) parts of the greenstone belt, the type-II and type-III chromite cores, found in section C, display greater extents of diffusive equilibration of trace elements such as Zn, Co, and Mn with associated silicate or carbonate minerals than the type-I chromite cores from section B. Increasing Os, Ir, Ru and Rh concentrations from the type-I cores to rims and lower concentrations of these elements in the type-II chromite cores to undetectable concentrations in the type-II rims are also related to the increasing metamorphic

grade towards the southern part of the greenstone belt. The co-existing sulfide or platinum-group mineral phases might control the diffusion of Os, Ir, Ru, and Rh from the chromite grains.

c) Disseminated base metal sulfide minerals e.g. chalcopyrite, pentlandite, and violarite in the komatiitic suite of rocks were modified during late-stage alteration events. A thin bornite rim is observed surrounding the chalcopyrite grain by replacing Fe^{2+} with Cu. Pentlandite shows replacement by millerite that occurs as patches and can be explained by the replacement of Fe^{2+} by Ni from the secondary alteration. The Fe^{2+} ions probably precipitate as magnetite surrounding the sulfide mineral assemblages in the presence of oxidizing fluid.

d) Mass balance calculation shows that the cores of the type-I chromite contribute < 1 % Sc, Ti, Ni, and Mn, and 2-5 % V, Ga, and Co to the whole-rock trace elements budget. The type-II chromite cores contribute < 1-19 % Sc, Ti, Ni, Mn, Ga, Co, and 18-40 % V, indicating a significant control of the modally abundant silicate minerals on the whole-rock budget of these trace elements. In terms of Os, Ir, Ru (IPGE), and Rh the type-I chromite cores contribute ≤ 20 %, and the type-II chromite cores contribute ≤ 10 % of the whole-rock IPGE+Rh budget, indicating the effect of metamorphism or equilibration with other PGE-bearing phases. Calculation of empirical partition coefficients (D) of trace and platinum-group elements based on the least altered cores of the type-I and type-II grains and komatiitic whole-rock compositions yield values broadly comparable to the low-end of the published natural and experimental $D_{IPGE+Rh}$ values as a result of metamorphic modification. However, these interpretations should be viewed

cautiously because of the limited number of *in situ* LA-ICP-MS PGE and trace elements data.

e) The whole-rock major and trace elements across the komatiitic sequence reflect the changing modes of the minerals during the magmatic crystallization process. The fractionation of PGEs was controlled by the accessory chromites for the lower meta-dunite-peridotite unit, whereas, by the accessory magnetite for the upper meta-basalt. In addition, localized control of PGEs by disseminated sulfide minerals is also observed in the meta-dunite-peridotites as evident by the congruous peaks of PGEs with S, Ni, Cu, and Co across the komatiitic sequence.

f) The bulk-rock geochemical characteristics of the Gorumahishani komatiites reveal two compositional types: (i) komatiites from section A are Ti-depleted, whereas, (ii) from sections B and C are Al-depleted. Geochemical modeling suggests that the Al-depleted komatiites were generated from a rising plume of garnet-peridotite mantle source by 27 % partial melting with 15 % garnet in the residue. Modeling also indicates that ~45 % partial melting of this rising depleted mantle plume at the spinel-peridotite stability field might produce the Ti-depleted komatiitic melt.

g) Sm-Nd isotopic study of the Gorumahishani komatiites yields an errorchron for the samples from section C (Kapili area). An eight-point errorchron yielded an age of 3508 ± 190 Ma (MSWD = 41, initial $^{143}Nd/^{144}Nd = 0.50808 \pm 0.00025$) with $\varepsilon_{Nd(T)} = 0.1$. The calculated $\varepsilon_{Nd(T)}$ is - 0.17 ± 1.85 for eighteen samples representing the entire greenstone belt. Overall, the $\varepsilon_{Nd(T)}$ values of the Gorumahishani komatiites are similar to the primitive mantle, however, the

effect of crustal contamination or the presence of a slightly depleted mantle source can not be ignored.

h) The chondrite-normalized REE plots and primitive mantle-normalized PGE plots of the Gorumahishani komatiites show a depleted character. The depleted PGE patterns of the early Archean Gorumahishani komatiites are similar to the other early Archean komatiites from different greenstone belts worldwide. The PGE patterns indicate the extraction of the komatiitic melt from the PGE-depleted primitive mantle. The depleted character of the primitive mantle source represents the early removal of PGEs during core segregation of the Earth within a magma ocean. Distinct negative Os, Ru, and Pt anomalies of the Gorumahishani komatiites may be due to the retention of Pt-Ru-rich micro nuggets, such as isoferroplatinum (Pt_3Fe), osmiridium (Os-Ir alloy), and Ru-Ir rich alloys in the residual mantle or the early segregation of these PGE-bearing phases from the ascending komatiitic magma.

i) Based on this study, a geodynamic model has been proposed for the early Archean crustal evolution of the Singhbhum Craton. According to this model the komatiitic magma generated within a rising plume from different depths forming Al-depleted and Ti-depleted komatiites that were erupted within a rift setting under sub-aqueous conditions. During the emplacement, the high-temperature komatiitic magma supplied heat for the melting of the mafic-rich proto-crust in different depths that generated parental magmas for the early Archean TTG and an older granitic suite of rocks in the Singhbhum Craton. The initial rift basin gradually converted into an ocean basin, and the continuous rifting process led to the beginning of subduction of the early formed crust in an

active continental margin setting. The Mesoarchean to late Archean ultramafic-mafic intrusive and the extrusive rocks in the Singhbhum Craton were formed from the magmas that originated in the lithospheric mantle wedge within an active continental margin setting. In this setting, the rising ultramafic-mafic magmas supplied the heat to melt the early Archean TTG-granitic crust and generated the parental felsic magmas from which the voluminous younger granitic intrusions were formed.

References

Acharya S K (1984) Stratigraphy and structural evolution of the rocks of the iron ore basin in Singhbhum-Orissa Iron Ore Province. In Proc. Sem. on Crustal evolution of the Indian shield and its bearing on metallogeny. Indian Journal Earth Science v:19-27.

Acharyya S K (1993) Greenstones from Singhbhum craton, their Archaean character, oceanic crustal affinity and tectonics. The Proceedings of the National Academy of Sciences, India Sec A 63(1):211-222.

Acharyya S K, Gupta A, Orihashi Y (2010a) New U-Pb zircon ages from Paleo Mesoarchean TTG gneisses of the Singhbhum Craton, eastern India. Geochemical Journal 44:81-88.

Acharyya S K, Anupendu Gupta, Y Orihashi (2010b) Neoarchean-Paleoproterozoic stratigraphy of the Dhanjori basin, Singhbhum Craton, Eastern India: And recording of a few U-Pb zircon dates from its basal part. Journal of Asian Earth Sciences 39(6): 527-536.

Adhikari A, Mukherjee S, Vadlamani R (2021a) A plume-mantle interaction model for the petrogenesis of komatiite-komatiitic basalt-basalt-basaltic andesite volcanism from the Paleoarchean (3.57-3.31 Ga) Iron Ore Group greenstone belts, Singhbhum craton, India: Constraints from trace element geochemistry and Sm-Nd geochronology. Lithos 398-399:106315.

Adhikari A, Nandi A, Mukherjee S, Vadlamani R (2021b) Petrogenesis of Neoarchean (2.80-2.75 Ga) Jagannathpur volcanics and the Ghatgaon and Keshargaria dyke swarms, Singhbhum craton, eastern India: Geochemical, Sr-Nd isotopic and Sm-Nd geochronologic constraints for interaction of enriched-DMM

derived magma with metasomatised subcontinental lithospheric mantle. Lithos 400-401:106373.

Adhikari A, Vadlamani R (2022) Petrogenesis of the Mesoarchean (~3.05 Ga) mafic volcanics from the western Iron Ore Group volcano-sedimentary succession, Singhbhum craton, eastern India: constraints from geochemical modelling and Sm-Nd geochronology. Lithos 412-413:106596.

Ahmed A H (2007) Diversity of platinum-group minerals in podiform chromitites of the late Proterozoic ophiolite, eastern Desert, Egypt: genetic implications. Ore Geology Reviews 32:1-19.

Alard O, Griffin W L, Lorand J P, Jackson S E, O'Reilly S Y (2000) Non-chondritic distribution of the highly siderophile elements in mantle sulphides. Nature 407(6806):891-894.

Allègre C J (1982) Genesis of Archaean komatiites in a wet ultramafic subducted plate. In: Arndt N T, Nisbet E G (Eds.) Komatiites: London, George Allen and Unwin, pp. 495-500.

Alt J C, Shanks W C, Bach W, Paulick H, Garrido C J, Beaudoin G (2007) Hydrothermal alteration and microbial sulfate reduction in peridotite and gabbro exposed by detachment faulting at the Mid-Atlantic Ridge, 15°20'N (ODP Leg 209): a sulfur and oxygen isotope study. Geochemistry Geophysics Geosystems 8:Q08002.

Alvi S H, Mir A R, Bhat I M (2019) Geochemistry of Dalma metavolcanic Suite from Proterozoic Singhbhum Mobile Belt, Eastern India: Implications for Petrogenesis and Tectonic Setting. Journal of the Geological Society of India 94:351-358.

Andrews D R, Brenan J M (2002) The solubility of ruthenium in sulfide liquid: implications for platinum group mineral stability and sulfide melt-silicate melt partitioning. Chemical Geology 192(3-4):163-181.

Arguin J -P, Pagé P, Barnes S -J, Yu S -Y, Song X -Y (2016) The effect of chromite crystallization on the distribution of osmium, iridium, ruthenium and rhodium in picritic magmas: an example from the Emeishan large igneous province, Southwestern China. Journal of Petrology 57:1019-1048.

Arndt N T, Naldrett A J, Pyke D R (1977) Komatiitic and iron-rich tholeiitic lavas of Munro Township, northeast Ontario. Journal of Petrology 18:319-369.

Arndt N T, Nisbet E G (1982). Komatiites. Cambridge University Press, xvii + 526 pp.

Arndt N T, Kerr A C, Tarney J (1997) Dynamic melting in plume heads: the formation of Gorgona komatiites and basalts. Earth and Planetary Science Letters 146(1-2):289-301.

Arndt N (2003) Komatiites, kimberlites, and boninites. Journal of Geophysical Research 108:2293.

Arndt N T, Lesher C M, Barnes S J (2008) Komatiite. Cambridge University Press, 488 pp.

Asahara Y, Ohtani E, Suzuki A (1998) Melting relations of hydrous and dry mantle compositions and the genesis of komatiites. Geophysical research letters 25(12):2201-2204.

Augé T, Cocherie A, Genna A, Armstrong R, Guerrot C, Mukherjee, M M, Patra R N (2003) Age of the Baula PGE mineralization (Orissa, India) and its implications concerning the Singhbhum Archaean nucleus. Precambrian Research 121(1-2):85-101.

Bachhar P, Saha D, Santosh M, Liu, H -D, Kwon S, Banerjee A, Patranabis-Deb S, Deb G K (2021) Mantle heterogeneity and crust-mantle interaction in the Singhbhum craton, India: New evidence from 3340 Ma komatiites. Lithos 382-383:105931.

Bach W, Garrido C J, Paulick H, Harvey J, Rosner M (2004) Seawater peridotite interactions: first insights from ODP Leg 209, MAR 15N. Geochemistry Geophysics Geosystems.

Baksi A K, Archibald D, Sarkar S, Saha A (1987) ^{40}Ar-^{39}Ar incremental heating study of mineral separates from the early Archean east Indian craton: implications for the thermal history of a section of the Singbhum Granite batholithic complex. Canadian Journal of Earth Sciences 24:1985-1993.

Ballhaus C, Sylvester P (2000) Noble metal enrichment processes in the Merensky Reef, Bushveld Complex. Journal of Petrology 41(4):545-561.

Bandyopadhyay P, Chakrabarti A, Deomurari M, Misra S (2001) 2.8 Ga old anorogenic granite-acid volcanics association from western margin of the Singhbhum-Orissa Craton, eastern India. Gondwana Research 4:465-475.

Bandyopadhyay, N. (2003) Metamorphic history of the rocks in the southeastern sector of the Proterozoic Singhbhum shear zone and its environs. Ph.D. Thesis, University of Calcutta, Calcutta, India.

Bandopadhyay P C, Eriksson P G, Roberts R J (2010) A vertic paleosol at the Archean-Proterozoic contact from the Singhbhum-Orissa craton, eastern India. Precambrian Reseach 177:277-290.

Banerji A K (1969) A reinterpretation of the geological history of the Singhbhum shear zone, Bihar. Journal of the Geological Society of India 10:49-55.

Banerji A K (1981) Ore genesis and its relationship to volcanism, tectonism, granitic activity, and metasomatism along the Singhbhum shear zone, eastern India. Economic Geology 76:905-912.

Banerjee R, Mondal S K, Reisberg L, Park J -W (2022) Fractionation of trace and platinum-group elements during metamorphism of komatiitic chromites from the early Archean Gorumahishani greenstone belt, Singhbhum Craton (eastern India). Contributions to Mineralogy and Petrology 177(8):75.

Banerjee R, Biswas B K, Mondal S K (2023) Origin of Alteration Patterns in Accessory Chromites from the Kudada Metaperidotites, East Singhbhum District (Jharkhand, India). Journal of the Geological Society of India 99(3):345-356.

Barnes S -J, Naldrett A J, Gorton M P (1985) The origin of the fractionation of platinum-group elements in terrestrial magmas. Chemical Geology 53(3-4):303-323.

Barnes S J, Naldrett A J (1986) Geochemistry of the J-M Reef of the Stillwater Complex, Minneapolis Adit Area II. Silicate Mineral Chemistry and Petrogenesis. Journal of Petrology 27(4):791-825.

Barnes S -J, Boyd R, Korneliussen A, Nilsson L P, Often M, Pedersen R B, Robins B (1988) The use of mantle normalization and metal ratios in discriminating be tween the effects of partial melting, crystal fractionation and sulphide segregation on platinum group elements, gold, nickel, and copper: example from Norway. In: Prichard H M, Potts P J, Cripp S J (Eds.) Geoplatinum 87, Elsevier Applied Sciences, London:pp. 113-143.

Barnes S -J, Picard C P (1993) The behaviour of platinum-group elements during partial melting, crystal fractionation, and sulphide segregation: An example from the Cape Smith Fold Belt, northern Quebec. Geochimica et Cosmochimica Acta 57(1):79-87.

Barnes S J, Lesher C M, Keays R R (1995) Geochemistry of mineralised and barren komatiites from the Perseverance nickel deposit, Western Australia. Lithos 34(1-3):209-234.

Barnes S J (1998) Chromite in komatiites, I. Magmatic controls on crystallization and composition. Journal of Petrology 39:1689-1720.

Barnes S J, Brand N W (1999) The distribution Cr, Ni, and chromite in komatiites, and application to exploration for komatiite-hosted nickel sulfide deposits. Economic Geology 94(1):129-132.

Barnes S J (2000) Chromite in komatiites, II. Modifcation during greenschist to mid amphibolite facies metamorphism. Journal of Petrology 41:387-409.

Barnes S J, Roeder P L (2001) The Range of Spinel Compositions in Terrestrial Mafic and Ultramafic Rocks. Journal of Petrology 42(12):2279-2302.

Barnes S J (2006) Komatiites: petrology, volcanology, metamorphism, and geochemistry. Economic Geology Special Publication 13:13-49.

Barnes S J, Fiorentini M (2012) Komatiite Magmas and Sulfide Nickel Deposits: A Comparison of Variably Endowed Archean Terranes. Economic Geology 107:755-780.

Barnes S J, Cruden A R, Arndt N, Saumur B M (2016) The mineral system approach applied to magmatic Ni-Cu-PGE sulphide deposits. Ore Geology Reviews 76:296-316.

Barnes S J, Ryan C, Moorhead G, Latypov R, Maier W D, Yudovskaya M, Godel B, Schoneveld L E, Le Vaillant M, Pearce M B (2021) Spatial association between platinum minerals and magmatic sulfides imaged with the Maia Mapper and implications for the origin of the chromite-sulfide-PGE association. The Canadian Mineralogist 59(6):1775-1799.

Barnes S -J, Mansur E T, Maier W D, Prevec S A (2023) A comparison of trace element concentrations in chromite from komatiites, picrites, and layered intrusions: implications for the formation of massive chromite layers. Canadian Journal of Earth Sciences 60(2):97-132.

Basu A R, Ray S L, Saha A K, Sarkar S N (1981) Eastern Indian 3800-million-year-old crust and early mantle differentiation. Science 212:1502-1506.

Basu A, Sharma M, Premo W (1996) U-Pb age of an older Metamorphic Group mica schist: earliest terrain of the eastern Indian Craton. Recent Researches in Geology and Geophysics of the Precambrians 16:93-102.

Basu A R, Bandyopadhyay P K, Chakrabarty R, Zhou H (2008) Large 3.4 Ga Algoma Type BIF in the Eastern Indian Craton. In: Goldschmidt Conference Abstracts, Vancouver. Geochimica et Cosmochimica Acta 72:A59.

Bateman R, Costa S, Swe T, Lambert D (2001) Archaean mafic magmatism in the Kalgoorlie area of the Yilgarn Craton, Western Australia: a geochemical and Nd isotopic study of the petrogenetic and tectonic evolution of a greenstone belt. Precambrian Research 108(1-2):75-112.

Becker H, Horan M F, Walker R J, Gao S, Lorand J -P, Rudnick R L (2006) Highly siderophile element composition of Earth's primitive upper mantle:

Constraints from new data on peridotite massifs and xenoliths. Geochimica et Cosmochimica Acta 70:4528-4550.

Bhattacharya H, Chakraborty I, Ghosh K K (2007) Geochemistry of some banded iron-formations of the archean supracrustals, Jharkhand-Orissa region, India. Journal of Earth System Science 116:245-259.

Bhattacharya H, Nelson D, Thern E, Altermann W (2015) Petrogenesis and geochronology of the Arkasani granophyre and felsic Dalma volcanic rocks: Implications for the evolution of the Proterozoic North Singhbhum Mobile Belt, east India. Geological Magazine 152(3):492-503.

Bhattacharjee S, Mulder J A, Roy S, Chowdhury P, Cawood P A, Nebel O (2021) Unravelling depositional setting, age and provenance of the Simlipal volcano-sedimentary complex, Singhbhum craton: Evidence for Hadean crust and Mesoarchean marginal marine sedimentation. Precambrian Research 354:106038.

Bhattacharjee C, Mondal S K (2021) Geochemistry of Fe-Ti oxide and sulfide minerals in gabbroic rocks and magnetitite of the Archean Mayurbhanj mafic complex (eastern India): Magma fractionation, thermometry and oxygen fugacity of re-equilibration, and implications for Ni-Cu mineralization. Ore Geology Reviews 131:104005.

Bhattacharjee C, Mondal S K, Reisberg L C (2022) Petrogenesis of the~ 3.1 Ga Mayurbhanj Gabbro-Anorthosite Complex, Singhbhum Craton (India): Magmatism in an active continental margin setting. AGU 2023 abstract.

Bickle M (1993) Plume origin for komatiites. Nature 365(6445):390-391.

Bickle M J, Hawkesworth C J, Martin A, Nisbet E G, O'NIONS R K (1976) Mantle composition derived from the chemistry of ultramafic lavas. Nature 263:577-580.

Blackburn W, Srivastava D (1994) Geochemistry and tectonic significance of the Ongarbira metavolcanic rocks, Singhbhum District, India. Precambrian Research 67:181-206.

Bleeker W (2002) Archaean tectonics: a review, with illustrations from the Slave craton. Geological Society, London, Special Publications 199(1):151-181.

Bleeker W (2003) The late Archean record: a puzzle in ca. 35 pieces. Lithos 71(2-4):99-134.

Blichert-Toft J, Albarède F, Rosing M, Frei R, Bridgwater D (1999) The Nd and Hf isotopic evolution of the mantle through the Archean. Results from the Isua supracrustals, West Greenland, and from the Birimian terranes of West Africa. Geochimica et Cosmochimica Acta 63(22):3901-3914.

Blichert-Toft J, Arndt N T, Gruau G (2004) Hf isotopic measurements on Barberton komatiites: Effects of incomplete sample dissolution and importance for primary and secondary magmatic signatures. Chemical Geology 207(3-4):261-275.

Borisov A, Palme H (1995) Solubility of iridium in silicate melts: New data from experiments with $Ir_{10}Pt_{90}$ alloys. Geochimica et Cosmochimica Acta 59:481-485.

Borisov A, Palme H (2000) Solubilities of noble metals in Fe-containing silicate melts as derived from experiments in Fe-free systems. American Mineralogist 85(11-12):1665-1673.

Bose P K, Mazumder R, Sarkar S (1997) Tidal sandwaves and related storm deposits in the transgressive Protoproterozoic Chaibasa Formation, India. Precambrian Research 84:63-81.

Bose M K (2009) Precambrian mafic magmatism in the Singhbhum Craton, Eastern India. Journal of the Geological Society of India 73:13-35.

Bourdeau J E, Hayes B, Zhang S E, Logue A, Bybee G M (2022) Origin and significance of noritic blocks in layered anorthosites in the Bushveld Complex, South Africa. Contributions to Mineralogy and Petrology 177:11.

Brandon A D, Walker R J, Morgan J W, Norman M D, Prichard H M (1998) Coupled ^{186}Os and ^{187}Os evidence for core-mantle interaction. Science 280(5369):1570-1573.

Brenan J M, Rose L A (2002) Experimental constraints on the wetting of chromite by sulfide liquid. The Canadian Mineralogist 40(4):1113-1126.

Brenan J M, McDonough W F, Dalpe C (2003) Experimental constraints on the partitioning of rhenium and some platinum-group elements between olivine and silicate melt. Earth and Planetary Science Letters 212(1-2):135-150.

Brenan J M, Finnigan C F, McDonough W F, Homolova V (2012) Experimental constraints on the partitioning of Ru, Rh, Ir, Pt and Pd between chromite and silicate melt: the importance of ferric iron. Chemical Geology 302:16-32.

Bridgwater D, Collerson K D (1976) The major petrological and geochemical characters of the 3,600 m.y. Uivak gneisses from Labrador. Contributions to Mineralogy and Petrology 5:43-59.

Burkhard D J M (1993) Accessory chromian spinels: their coexistence and alteration in serpentinites. Geochim Cosmochim Acta 57:1297-1306.

Bussolesi M, Grieco G, Zaccarini F, Cavallo A, Tzamos E, Storni N (2022) Chromite compositional variability and associated PGE enrichments in chromitites from the Gomati and Nea Roda ophiolite, Chalkidiki, Northern Greece. Miner Deposita 57:1323-1342.

Cabri L J, Oberthür T, Keays R R (2022) Origin and depositional history of platinum-group minerals in placers-A critical review of facts and fiction. Ore Geology Reviews 144:104733.

Canil D (2002) Vanadium in peridotites, mantle redox and tectonic environments: Archean to present. Earth and Planetary Science Letters 195:75-90.

Capobianco C J, Drake M J (1990) Partitioning of ruthenium, rhodium, and palladium between spinel and silicate melt and implications for platinum group element fractionation trends. Geochimica et Cosmochimica Acta 54(3):869-874.

Capobianco C J, Hervig R L, Drake M J (1994) Experiments on crystal/liquid partitioning of Ru, Rh and Pd for magnetite and hematite solid solutions crystallized from silicate melt. Chemical Geology 113(1-2):23-43.

Cathelineau M, Nieva D (1985) A chlorite solid solution geothermometer the Los Azufres (Mexico) geothermal system. Contributions to mineralogy and petrology 91:235-244.

Cawood P A, Hawkesworth C J, Pisarevsky S A, Dhuime B, Capitanio F A, Nebel O (2018) Geological archive of the onset of plate tectonics. Philosophical Transactions of the Royal Society A 376(2132):20170405.

Chakraborty K L, Majumder T (1986) Geological aspects of the banded iron-formation of Bihar and Orissa. Journal of the Geological Society of India 28(2&3):109-133.

Chakraborti T M, Ray A, Deb G K, Upadhyay D, Chakrabarti R (2019) Evidence of crustal reworking in the Mesoarchean: Insights from geochemical, U-Pb zircon and Nd isotopic study of a 3.08-3.12 Ga ferro-potassic granite-gneiss from north-eastern margin of Singhbhum Craton, India. Lithos 330-331:16-34.

Champion D C, Smithies R H (2007) Geochemistry of Paleoarchean granites of the East Pilbara terrane, Pilbara craton, Western Australia: implications for Early Archean crustal growth. Developments in Precambrian geology 15:369-409.

Chatterjee S, Mondal S, Gain D, Baidya T K, Mazumdar D (2018) Interpretation of magnetic fabrics in the Dalma volcanic rocks and associated metasediments of the Singhbhum mobile belt. Journal of Earth System Science 127(11):89.

Chauvel C, Dupré B, Jenner G A (1985) The Sm-Nd age of Kambalda volcanics is 500 Ma too old!. Earth and Planetary Science Letters 74(4):315-324.

Chaudhuri T, Mazumder R, Arima M (2015) Petrography and geochemistry of Mesoarchaean komatiites from the eastern Iron Ore belt, Singhbhum craton, India, and its similarity with 'Barberton type komatiite.' Journal of African Earth Sciences 101:135-147.

Chaudhuri T, Satish-Kumar M, Mazumder R, Biswas S (2017) Geochemistry and Sm-Nd isotopic characteristics of the Paleoarchean Komatiites from Singhbhum Craton, Eastern India and their implications. Precambrian Research 298:385-402.

Chaudhuri T, Wan Y, Mazumder R, Ma M, Liu D (2018) Evidence of enriched, Hadean mantle reservoir from 4.2-4.0 Ga zircon xenocrysts from Paleoarchean TTGs of the Singhbhum Craton, Eastern India. Scientific Reports 8:7069.

Chaudhuri T, Kamei A, Das M, Mazumder R, Owada M (2022) Evolution of the Archean felsic crust of Singhbhum Craton, India: A reassessment. Earth-Science Reviews 231:104067.

Chavagnac V (2004) A geochemical and Nd isotopic study of Barberton komatiites (South Africa): implication for the Archean mantle. Lithos 75(3-4):253-281.

Chou C L (1978) Fractionation of siderophile elements in the earth's upper mantle. Proceedings of the 9th Lunar and Planetary Science Conference. Geochimica et Cosmochimica Acta Supplement: pp. 219-230.

Chowdhury S, Pal D C, Papineau D, Lentz D R (2020) Major and trace element and multiple sulfur isotope composition of sulfides from the Paleoproterozoic Surda copper deposit, Singhbhum shear Zone, India: Implications for the mineralization processes. Ore Geology Reviews 120:103396.

Chu G, Zhang S, Zhang X, Xiao B, Han J, Zhang Y, Cheng J, Feng Y (2020) Chlorite chemistry of Tongshankou porphyry-related Cu-Mo-W skarn deposit, Eastern China: Implications for hydrothermal fluid evolution and exploration vectoring to concealed orebodies. Ore Geology Reviews 122:103531.

Colás V, González-Jiménez J M, Grifn W L, Fanlo I, Gervilla F, O'Reilly S Y, Pearson N J, Kerestedjian T, Proenza J A (2014) Fingerprints of metamorphism in chromite: new insights from minor and trace elements. Chemical Geology 389:137-152.

Colás V, Padrón-Navarta J A, González-Jiménez J M, Fanlo I, López Sánchez-Vizcaíno V, Gervilla F, Bolibar R (2017) The role of silica in the hydrous metamorphism of chromite. Ore Geology Reviews 90:274-286.

Colás V, González-Jiménez J M, Camprubí A, Proenza J A, Griffin W L, Fanlo I, O'Reilly S Y, Gervilla F, González-Partida E (2019) A reappraisal of the metamorphic

history of the Tehuitzingo chromitite, Puebla state, Mexico. International Geology Review 61(7):1706-1727.

Colás V, Subias I, González-Jiménez J M, Proenza J, Fanlo I, Camprubí A, Grifn W, Gervilla F, O'Reilly S, Escayola M (2020) Metamorphic fingerprints of Fe-rich chromitites at Eastern Pampean Ranges. Boletín de la Sociedad Geológica Mexicana 72(3):A080420.

Condie K C (1967) Geochemistry of early Precambrian graywackes from Wyoming. Geochimica et Cosmochimica Acta 31(11):2135-2149.

Condie K C (1981) Archean greenstone belts. Elsevier.

Craig J R, Scott S D (1974) Sulfifide phase equilibria. In: Ribbe P H (ed.) Sulfifide Mineralogy. Mineralogical Society of America, Short Course Notes 1:CS1-S110.

Datta P, Mondal S K (2021a) Compositional variations, thermometry, and probable parental magmas of Archean chromite from the Sargur greenstone belt, Western Dharwar Craton (India). Lithos 380-381:105867.

Datta P, Mukherjee R, Mondal S K, Lingadevaru M (2021b) Origin of Ni-Cu-(PGE + Au) sulfides in late-Archean komatiitic suite of rocks in the Shankaraghatta belt, Western Dharwar Craton (India). Ore Geology Reviews 138:104375.

Davies G F (2007) Dynamics of the Hadean and Archaean mantle. Developments in Precambrian Geology 15:61-73.

Davis F A, Humayun M, Hirschmann M M, Cooper R S (2013) Experimentally determined mineral/melt partitioning of first-row transition elements (FRTE) during partial melting of peridotite at 3 GPa. Geochimica et Cosmochimica Acta 104:232-260.

De S, Mazumder R, Ohta T, Hegner E, Yamada K, Bhattacharyya T, Chiarenzelli J, Altermann W, Arima M (2015) Geochemical and Sm-Nd isotopic characteristics of the Late Archaean-Palaeoproterozoic Dhanjori and Chaibasa metasedimentary rocks, Singhbhum craton, E. India: Implications for provenance, and contemporary basin tectonics. Precambrian Research 256:62-78.

de Wit M J, Ashwal L D (1995) Greenstone belts: what are they?. South African Journal of Geology 98(4):505-520.

de Wit M J, Tredoux M (1988) PGE in the 3·5 Ga Jamestown Ophiolite Complex, Barberton Greenstone Belt, with Implications for PGE Distribution in Simatic Lithosphere. Geo-platinum 87:pp. 319-341.

de Wit M J, de Ronde C E, Tredoux M, Roering C, Hart R J, Armstrong R A, Green R W, Peberdy E, Hart R A (1992) Formation of an Archaean continent. Nature 357(6379):553-562.

Debaille V, O'Neill C, Brandon A D, Haenecour P, Yin Q -Z, Mattielli N, Treiman A H (2013) Stagnant-lid tectonics in early Earth revealed by 142Nd variations in late Archean rocks, Earth and Planetary Science Letters 373:83-92.

DePaolo D J, Wasserburg G J (1979) Sm-Nd age of the Stillwater Complex and the mantle evolution curve for neodymium. Geochimica et Cosmochimica Acta 43(7):999-1008.

Dey S, Topno A, Liu Y, Zong K (2017) Generation and evolution of Palaeoarchaean continental crust in the central part of the Singhbhum craton, eastern India. Precambrian Research 298:268-291.

Dey S, Mitra A, Nandy J, Mondal S, Topno A, Liu Y, Zong K (2019) Chapter 30 - Early Crustal Evolution as Recorded in the Granitoids of the Singhbhum and Western Dharwar Cratons. In: Van Kranendonk M J, Bennett V C, Hoffmann J E (Eds.) Earth's Oldest Rocks (Second Edition), pp. 741-792.

Dey A, Mondal S K (2021) Origin of Fe-Ni-Cu (Co) sulfide and Fe–Ti oxide minerals in the c. 1.77 Ga dolerite dyke, Singhbhum Craton (eastern India). Geological Society, London, Special Publications 518(1):553-574.

Donaldson C H (1982) Spinifex-textured komatiites: a review of textures, compositions and layering. In: Arndt N T, Nisbet E G (eds.) Komatiites. Allen & Unwin:pp. 213-244.

Droop G (1987) A general equation for estimating Fe^{3+} concentrations in ferromagnesian silicates and oxides from microprobe analyses, using stoichiometric criteria. Mineralogical Magazine 51:431-435.

Dunn J A (1940) The stratigraphy of south Singhbhum. Memoir of the Geological Survey of India 63: 303-369.

Dunn J A, Dey A K (1942) The geology and petrology of eastern Singhbhum and surrounding areas. Memoir of the Geological Survey of India 69:281-450.

Echeverría L M (1982) Komatiites from Gorgona Island, Colombia. In: Arndt N T, Nisbet E G (eds.) Komatiites. London, George Allen & Unwin: pp. 199-210.

Elias M (2007) Lateritic nickel mineralization of the Yilgarn Craton. In: Barnes S J (ed) Nickel deposits of the Yilgarn Craton. Society of Economic Geologists, Special Publication 13:195-209.

Eriksson P G, Mazumder R, Sarkar S, Bose P K, Altermann W V, Van der Merwe R (1999) The 2.7-2.0 Ga volcano-sedimentary record of Africa, India and

Australia: evidence for global and local changes in sea level and continental freeboard. Precambrian Research 97(3-4):269-302.

Ernst W G (2017) Earth's thermal evolution, mantle convection, and Hadean onset of plate tectonics. Journal of Asian Earth Sciences 145:334-348.

Eslami A, Arai S, Miura M, Mackizadeh M A (2018) Metallogeny of the peridotite-hosted magnetite ores of the Nain ophiolite, Central Iran: Implications for Fe concentration processes during multi-episodic serpentinization. Ore Geology Reviews 95:680-694.

Evans B W, Trommsdorff V (1974) On elongate olivine of metamorphic origin. Geology 2(3):131-132.

Evans B W, Frost B R (1975) Chrome-spinel in progressive metamorphism- a preliminary analysis. Geochim Cosmochim Acta 39:959-972.

Evans D M (2015) Metamorphic modifications of the Muremera mafic-ultramafic intrusions, eastern Burundi, and their effect on chromite compositions. Journal of African Earth Sciences 101:19-34.

Fabriès J (1979) Spinel-olivine geothermometry in peridotites from ultramafc complexes. Contributions to Mineralogy and Petrology 69:329-336.

Finnigan C S, Brenan J M, Mungall J E, McDonough W F (2008) Experiments and models bearing on the role of chromite as a collector of platinum group minerals by local reduction. Journal of Petrology 49(9):1647-1665.

Fiorentini M L, Stone W E, Beresford S W, Barley M E (2004) Platinum-group element alloy inclusions in chromites from Archaean mafic-ultramafic units: evidence from the Abitibi and the Agnew-Wiluna Greenstone Belts. Mineralogy and Petrology 82:341-355.

Fiorentini M L, Beresford S W, Barley M E (2008) Ruthenium-chromium variation: A new lithogeochemical tool in the exploration for komatiite-hosted Ni-Cu-(PGE) deposits. Economic Geology 103(2):431-437.

Fiorentini M L, Barnes S J, Lesher C M, Heggie G J, Keays R R, Burnham O M (2010) Platinum group element geochemistry of mineralized and nonmineralized komatiites and basalts. Economic Geology 105(4):795-823.

Fiorentini M L, Barnes S J, Maier W D, Burnham O M, Heggie G (2011) Global Variability in the Platinum-group Element Contents of Komatiites. Journal of Petrology 52(1):83-112.

Fleet ME, Angeli N, Pan Y (1993) Oriented chlorite lamellae in chromite from the Pedra Branca Mafc-Ultramafc Complex, Ceari, Brazil. American Mineralogist 78:68-74.

Fleet M E, Crocket J H, Stone W E (1996) Partitioning of platinum-group elements (Os, Ir, Ru, Pt, Pd) and gold between sulfide liquid and basalt melt. Geochimica et Cosmochimica Acta 60(13):2397-2412.

Fonseca R O, Campbell I H, O'Neill H S, Allen C M (2009) Solubility of Pt in sulphide mattes: Implications for the genesis of PGE-rich horizons in layered intrusions. Geochimica et Cosmochimica Acta 73(19):5764-5777.

Fonseca R O, Laurenz V, Mallmann G, Luguet A, Hoehne N, Jochum K P (2012) New constraints on the genesis and long-term stability of Os-rich alloys in the Earth's mantle. Geochimica et Cosmochimica Acta 87:227-242.

Frei R, Polat A, Meibom A (2004) The Hadean upper mantle conundrum: Evidence for source depletion and enrichment from Sm-Nd, Re-Os, and Pb isotopic

compositions in 3.71 Gy boninite-like metabasalts from the Isua Supracrustal Belt, Greenland. Geochimica et Cosmochimica Acta 68(7):1645-1660.

Frei R, Jensen B K (2003) Re-Os, Sm-Nd isotope-and REE systematics on ultramafic rocks and pillow basalts from the Earth's oldest oceanic crustal fragments (Isua supracrustal belt and Ujaragssuit nunat area, W Greenland). Chemical geology 196(1-4):163-191.

Friend C R, Nutman A P (2019) Tectono-stratigraphic terranes in Archaean gneiss complexes as evidence for plate tectonics: The Nuuk region, southern West Greenland. Gondwana Research 72:213-237.

Furnes H, Rosing M, Dilek Y, De Wit M (2009) Isua supracrustal belt (Greenland)-A vestige of a 3.8 Ga suprasubduction zone ophiolite, and the implications for Archean geology. Lithos 113(1-2):115-132.

Fyfe W S (1978) The evolution of the Earth's crust: modern plate tectonics to ancient hot spot tectonics? Chemical Geology 23(1-4):89-114.

Gahlan H A, Arai S, Ahmed A H, Ishida Y, Abdel Aziz Y M, Rahimi A (2006) Origin of magnetite veins in serpentinite from the Late Proterozoic Bou-Azzer ophiolite, Anti-Atlas, Morocco: an implication for mobility of iron during serpentinization. Journal of African Earth Sciences 46:318-330.

Garuti G, Pushkarev E V, Zaccarini F (2002) Composition and paragenesis of Pt alloys from chromitites of the Uralian-Alaskan-type Kytlym and Uktus complexes, northern and central Urals, Russia. The Canadian Mineralogist 40(4):1127-1146.

Garuti G, Pushkarev E V, Gottman I A, Zaccarini F (2021) Chromite-PGM Mineralization in the Lherzolite Mantle Tectonite of the Kraka Ophiolite Complex (Southern Urals, Russia). Minerals 11(11):1287.

Gervilla F, Padrón-Navarta J, Kerestedjian T, Sergeeva I, González-Jiménez J, Fanlo I (2012) Formation of ferrian chromite in podiform chromitites from the Golyamo Kamenyane serpentinite, Eastern Rhodopes, SE Bulgaria: a two-stage process. Contributions to Mineralogy and Petrology 164:1-15.

Ghosh D, Sarkar S N, Saha A K, Ray S L (1996) New insights on the early Archaean crustal evolution in eastern India: Re-evaluation of lead-lead, samarium-neodymium and rubidium strontium geochronology. Indian Minerals 50:175-188.

Ghosh G, Ghosh B, Mukhopadhyay J (2015) Paleoarchean-Mesoproterozoic sedimentation and tectonics along the west-northwestern margin of the Singhbhum Granite body, eastern India: a synthesis. In: Mazumder R, Eriksson P G (Eds.) Precambrian Basins of India Geological Society of London Memoir 43:121-138.

Ghosh S, De S, Mukhopadhyay J (2016) Provenance of >2.8 Ga Keonjhar Quartzite, Singhbhum Craton, Eastern India: implications for the Nature of Mesoarchean Upper Crust and Geodynamics. Journal of Geology 124:331-351.

Ghosh R, Vermeesch P, Gain D, Mondal R (2019) Genetic relationship among komatiites and associated basalts in the Badampahar greenstone belt (3.25-3.10 Ga), Singhbhum Craton, Eastern India. Precambrian Research 327:196-211.

Glikson A Y (1971) Primitive Archaean element distribution patterns: Chemical evidence and geotectonic significance: Earth and Planetary Science Letters 12:309-320.

Godel B, Barnes S J, Gürer D, Austin P, Fiorentini M L (2013) Chromite in komatiites: 3D morphologies with implications for crystallization mechanisms. Contributions to Mineralogy and Petrology 165:173-189.

Gole M J, Barnes S J (2020) The association between Ni-Cu-PGE sulfide and Ni-Co lateritic ores and volcanic facies within the komatiites of the 2.7 Ga East Yilgarn Craton Large Igneous Province, Western Australia. Ore Geology Reviews 116:103231.

González-Jiménez J M, Kerestedjian T, Proenza-Fernández J A, Gervilla-Linares F (2009) Metamorphism on chromite ores from the Dobromirtsi ultramafc massif, Rhodope Mountains (SE Bulgaria). Geologica Acta 7:413-429.

González-Jiménez J M, Grifn W L, Proenza J A, Gervilla F, O'Reilly S Y, Akbulut M, Pearson N J, Arai S (2014) Chromitites in ophiolites: How, where, when, why? Part II. The crystallisation of chromitites. Lithos 189:140-158.

González-Pérez I, Gervilla F, González-Jiménez J M, Kojonen K (2021) Genesis of an exotic platinum-group-mineral-rich and Mg-poor chromitite in the Kevitsa Ni-Cu-platinum-group-elements deposit. Mineralogy and Petrology 115(5):535-555.

Goswami J, Mishra S, Wiedenbeck M, Ray S, Saha A (1995) 3.55 Ga old zircon from Singhbhum-Orissa iron ore craton, eastern India. Current Science 69(12):1008-1012.

Groves D I, Hudson D R, Hack T B (1974) Modification of iron-nickel sulfides during serpentinization and talc-carbonate alteration at Black Swan, Western Australia. Economic Geology 69(8):1265-1281.

Grove T L, Parman S W, Dann J C (1999) Conditions of magma generation for Archean komatiites from the Barberton Mountainland, South Africa. In: Fei Y, Bertka C M, Mysen B O (Eds.) Mantle Petrology: Field Observations and High Pressure Experimentation, vol. 6. The Geochemical Society, Houston, pp. 155-167.

Grove T, Parman S (2004) Thermal evolution of the Earth as recorded by komatiites. Earth and Planetary Science Letters 219(3-4):173-187.

Gupta A (1985) Stratigraphy and petrochemistry of Dhanjori greenstone belt, eastern India. Quaternary Journal of Geological Mining and Metallurgical Society of India 57:248-263.

Habtoor A M, Ahmed A H, Akizawa N, Harbi H, Arai S (2017) Chemical homogeneity of high-Cr chromitites as indicator for widespread invasion of boninitic melt in mantle peridotite of Bir Tuluha ophiolite, Northern Arabian Shield, Saudi Arabia. Ore Geology Reviews 90:243-259.

Hamilton P, O'nions R, Bridgwater D, Nutman A (1983) Sm-Nd studies of Archaean metasediments and metavolcanics from West Greenland and their implications for the Earth's early history. Earth and Planetary Science Letters 62(2):263-272.

Hamilton P J, Evensen N M, O'nions R K, Smith H S, Erlank A J (1979) Sm-Nd dating of Onverwacht Group Volcanics, southern Africa. Nature 279(5711):298-300.

Hansen V L (2015) Impact origin of Archean cratons. Lithosphere 7(5):563-578.

Harrison T M, Schmitt A K, McCulloch M T, Lovera O M (2008) Early(≥4.5Ga) formation of terrestrial crust: Lu-Hf, $\delta^{18}O$, and Ti thermometry results for Hadean zircons. Earth and Planetary Science Letters 268:476-486.

Hasenstab E, Tusch J, Schnabel C, Marien C S, Van Kranendonk M J, Smithies H, Howard H, Maier W D, Münker C (2021) Evolution of the early to late Archean mantle from Hf-Nd-Ce isotope systematics in basalts and komatiites from the Pilbara Craton. Earth and Planetary Science Letters 553:116627.

Haugaard R, Waterton P, Ootes L, Pearson D G, Luo Y, Konhauser K (2021) Detrital chromites reveal Slave craton's missing komatiite. Geology 49(9):1079-1083.

Hegner E, Kröner A, Hofmann A W (1984) Age and isotope geochemistry of the Archaean Pongola and Usushwana suites in Swaziland, southern Africa: a case for crustal contamination of mantle-derived magma. Earth and Planetary Science Letters 70(2):267-279.

Hernández-González J S, Butjosa L, Pujol-Solà N, Aiglsperger T, Weber M, Escayola M, Ramírez-Cárdenas C, Blanco-Quintero I F, González-Jiménez J M, Proenza J A (2020) Petrology and geochemistry of high-Al chromitites from the Medellin Metaharzburgitic Unit (MMU), Colombia: Boletín de la Sociedad Geológica Mexicana 72(3):A120620.

Herzberg C (1992) Depth and degree of melting of komatiites. Journal of Geophysical Research: Solid Earth 97(B4):4521-4540.

Herzberg C (1995) Generation of plume magmas through time: An experimental perspective. Chemical Geology 126:1-16.

Herzberg C, O'hara M J (2002) Plume-associated ultramafic magmas of Phanerozoic age. Journal of Petrology 43(10):1857-1883.

Hey M H (1954) A new review of the chlorites. Mineralogical Magazine 30:217-292.

Hoffmann J E, Münker C, Polat A, König S, Mezger K, Rosing M T (2010) Highly depleted Hadean mantle reservoirs in the sources of early Archean arc-like rocks, Isua supracrustal belt, southern West Greenland. Geochimica et Cosmochimica Acta 74(24):7236-7260.

Hollings P, Wyman D (1999) Trace element and Sm–Nd systematics of volcanic and intrusive rocks from the 3 Ga Lumby Lake Greenstone belt, Superior Province: evidence for Archean plume-arc interaction. Lithos 46(2):189-213.

Horn I, Foley S F, Jackson S E, Jenner G A (1994) Experimentally determined partitioning of high field strength-and selected transition elements between spinel and basaltic melt. Chemical Geology 117(1-4):193-218.

Huang X, Ziwei B, DePaolo D J (1986) Sm-Nd isotope study of early Archean rocks, Qianan, Hebei province, China. Geochimica et Cosmochimica Acta 50(4):625-631.

Irvine T N (1967) Chromian spinel as a petrogenetic indicator: Part II. Petrological applications. Canadian Journal of Earth Sciences 4:71-103.

Irvine G J, Pearson D G, Kjarsgaard B A, Carlson R W, Kopylova M G, Dreibus G (2003) A Re-Os isotope and PGE study of kimberlite-derived peridotite xenoliths from Somerset Island and a comparison to the Slave and Kaapvaal cratons. Lithos 71(2-4):461-488.

Iyenger S V P, Chandy K C, Narayanswami, R (1981) Geochronology and Rb-Sr systematics of the igneous rocks of the Simlipal Complex, Orissa. Indian Journal of Earth Sciences 8:61-65.

Jacobsen S B, Wasserburg G J (1980) Sm-Nd isotopic evolution of chondrites, Earth Planetary Science Letters 50:139-155.

Jahn B -m, Gruau G, Glikson A Y (1982) Komatiites of the Onverwacht Group, S. Africa: REE geochemistry, Sm/Nd age and mantle evolution. Contributions to Mineralogy and Petrology 80:25-40.

Jahn B M, Condie K C (1995) Evolution of the Kaapvaal Craton as viewed from geochemical and Sm Nd isotopic analyses of intracratonic pelites. Geochimica et Cosmochimica Acta 59(11):2239-2258.

Jayananda M, Kano T, Peucat J J, Channabasappa S (2008) 3.35 Ga komatiite volcanism in the western Dharwar craton: constraints from Nd isotopes and whole rock geochemistry. Precambrian Research 162:160-179.

Jena B K, Behera U K (2000) The oldest supracrustal belt from Singhbhum craton and its possible correlation. Geological Survey of India Special Publication 57:106-121.

Jensen L S (1976) A new cation plot for classifying subalkalic volcanic rocks. Ontario's Ministry of Northern Development and Mines (MNDM). Paper number 66:22 pp.

Jodder J, Hofmann A, Ueckermann H (2021) 3.51 Ga old felsic volcanic rocks and carbonaceous cherts from the Gorumahisani Greenstone Belt–Insights into the Palaeoarchaean record of the Singhbhum Craton, India. Precambrian Research 357:106109.

Jodder J, Hofmann A, Xie H, Elburg M A, Wilson A (2023) Geochronology of the Daitari Greenstone Belt, Singhbhum Craton, India. Precambrian Research 388:106997.

Johnson T E, Brown M, Kaus B J P, VanTongeren J A (2014) Delamination and recycling of Archaean crust caused by gravitational instabilities. Nature Geoscience 7:47-52.

Johnson T E, Kirkland C L, Gardiner N J, Brown M, Smithies R H, Santosh M (2019) Secular change in TTG compositions: Implications for the evolution of Archaean geodynamics. Earth and Planetary Science Letters 505:65-75.

Kamber B S, Tomlinson E L (2019) Petrological, mineralogical and geochemical peculiarities of Archaean cratons. Chemical Geology 511:123-151.

Kamenetsky V S, Crawford A J, Mefre S (2001) Factors controlling chemistry of magmatic spinel: an empirical study of associated olivine, Cr-spinel and melt inclusions from primitive rocks. Journal of Petrology 42:655-671.

Kamenetsky V S, Park J -W, Mungall J E, Pushkarev E V, Ivanov A V, Kamenetsky M B, Yaxley G M (2015) Crystallization of platinum group minerals from silicate melts: Evidence from Cr spinel hosted inclusions in volcanic rocks. Geology 43:903-906.

Kang J, Chen L, Yu S, Zheng W, Dai Z, Zhou S, Ai Q (2022) Chromite geochemistry of the Jinchuan Ni-Cu sulfide-bearing ultramafic intrusion (NW China) and its petrogenetic implications. Ore Geology Reviews 141:104644.

Keller C, Schoene B (2012) Statistical geochemistry reveals disruption in secular lithospheric evolution about 2.5 Gyr ago. Nature 485:490-493.

Khatun S, Mondal S K, Zhou M F, Balaram V, Prichard H M (2014) Platinum-group element (PGE) geochemistry of Mesoarchean ultramafic-mafic cumulate rocks and chromitites from the Nuasahi Massif, Singhbhum Craton (India). Lithos 205:322-340.

Kimball K L (1990) Efects of hydrothermal alteration on the compositions of chromian spinels. Contributions to Mineralogy and Petrology 105:337-346.

Klemme S, Ivanic T J, Connolly J A, Harte B (2009) Thermodynamic modelling of Cr-bearing garnets with implications for diamond inclusions and peridotite xenoliths. Lithos 112:986-991.

Konnunaho J, Hanski E, Wing B, Bekker A, Lukkari S, Halkoaho T (2016) The Hietaharju PGE-enriched komatiite-hosted sulfide deposit in the Archean Suomussalmi greenstone belt, eastern Finland. Ore Geology Reviews 72:641-658.

Konnunaho J P, Hanski E J, Bekker A, Halkoaho T A, Hiebert R S, Wing B A (2013) The Archean komatiite-hosted, PGE-bearing Ni–Cu sulfide deposit at Vaara, eastern Finland: evidence for assimilation of external sulfur and post-depositional desulfurization. Mineralium Deposita 48:967-989.

Kröner A, Layer P W (1992) Crust Formation and Plate Motion in the Early Archean. Science 256:1405-1411.

Kröner A, Hoffmann J E, Xie H, Wu F, Münker C, Hegner E, Wong J, Wan Y, Liu D (2013) Generation of early Archaean felsic greenstone volcanic rocks through crustal melting in the Kaapvaal, craton, southern Africa. Earth and Planetary Science Letters 381:188-197.

Kullerud G, Yund R A, Moh G H (1969) Phase relations in the Cu-Fe-S, Cu-Ni-S and Fe-Ni-S systems. In: Wilson H D B (ed.) Magmatic ore Deposits. Economic Geology, Lancaster:323-343.

Kumar A, Rao Y B, Sivaraman T V, Gopalan K (1996) Sm-Nd ages of Archaean metavolcanics of the Dharwar craton, South India. Precambrian Research 80(3-4):205-216.

Kumar A, Parashuramulu V, Shankar R, Besse J (2017) Evidence for a Neoarchean LIP in the Singhbhum Craton, eastern India: implications to Vaalbara Super continent. Precambrian Research 292:163-174.

Kunugiza K, Takasu A, Banno S (1986) The origin and metamorphic history of the ultramafic and metagabbro bodies in the Sanbagawa metamorphic belt. Geological Society of America Memoir 164:375-386.

Lahaye Y, Arndt N, Byerly G, Chauvel C, Fourcade S, Gruau G (1995) The influence of alteration on the trace-element and Nd isotopic compositions of komatiites. Chemical Geology 126(1):43-64.

Lamadrid H M, Rimstidt J D, Schwarzenbach E M, Klein F, Ulrich S, Dolocan A, Bodnar R J (2017) Effect of water activity on rates of serpentinization of olivine. Nature Communications 8(1):16107.

Lambert R S (1980) The thermal history of the earth in the Archean. Precambrian Research 11(3-4):199-213.

Langmuir C H, Forsyth D W (2007) Mantle melting beneath mid-ocean ridges. Oceanography 20(1):78-89.

Leake B E, Woolley A R, Arps C E S, Birch W D, Gilbert M C, Grice J D, Hawthorne F C, Kato A, Kisch H J, Krivovichev V G, Linthout K, Laird J, Mandarino J A, Maresch W V, Nickel E H, Rock N M S, Schumacher J C, Smith D C, Stephenson N C N, Ungaretti L, Whittaker E J W, Youzhi G (1997) Nomenclature of amphiboles: Report of the Subcommittee on Amphiboles of the International

Mineralogical Association, Commission on New Minerals and Mineral Names. American Mineralogist 82:1019-1037.

Lenaz D, Maibam B, Adetunji J, Skogby H (2021) The Effects of High-Grade Metamorphism on Cr-Spinel from the Archean Sittampundi Complex, South India. Minerals 11(12):1370.

Lepage L D (2003) ILMAT: an excel worksheet for ilmenite-magnetite geothermometry and geobarometry. Computers & Geosciences 29:673-678.

Leroy S, Gente P, Fournier M, d'Acremont E, Patriat P, Beslier M O, Bellahsen N, Maia M, Blais A, Perrot J, Al-Kathiri A (2004) From rifting to spreading in the eastern Gulf of Aden: a geophysical survey of a young oceanic basin from margin to margin. Terra nova 16(4):185-192.

Lesher C M, Burnham O M, Keays R R, Barnes S J, Hulbert L (2001) Geochemical discrimination of barren and mineralized komatiites associated with magmatic Ni-Cu-(PGE) sulphide deposits. Canadian Mineralogist 39:673-696.

Lesher C M, Keays R R (2002) Komatiite-associated Ni-Cu-PGE deposits: Geology, mineralogy, geochemistry and genesis. In: Cabri L (ed) The geology, geochemistry, mineralogy and Mineral beneficiation of the platinum-group elements 54:579 - 618.

Lesher C M, Barnes S J (2009) Komatiite-associated Ni-Cu-(PGE) deposits. In: Li C, Ripley E M (Eds.) New Developments in Magmatic Ni-Cu and PGE Deposits. Geological Publishing House, Peijing, pp 27-120.

Lindsley D H (1981) The crystal chemistry and structure of oxide minerals as exemplified by the Fe-Ti oxides. In: Rumble D (ed) Oxide minerals, vol 3. Mineralogical Society of America, Washington, pp 1-52.

Liu Y, Gao S, Kelemen P B, Xu W (2008) Recycled crust controls contrasting source compositions of Mesozoic and Cenozoic basalts in the North China craton. Geochimica et Cosmochimica Acta 72:2349-2376.

Locmelis M, Pearson N J, Barnes S J, Fiorentini M L (2011) Ruthenium in komatiitic chromite. Geochimica et Cosmochimica Acta 75:3645-3661.

Locmelis M, Fiorentini M L, Barnes S J, Pearson N J (2013) Ruthenium variation in chromite from komatiites and komatiitic basalts—a potential mineralogical indicator for nickel sulfide mineralization. Economic Geology 108(2):355-364.

Locmelis M, Fiorentini M L, Barnes S J, Hanski E J, Kobussen A F (2018) Ruthenium in chromite as indicator for magmatic sulfide liquid equilibration in mafic-ultramafic systems. Ore Geology Reviews 97:152-170.

Loferski J P (1986) Petrology of metamorphosed chromite-bearing ultramafc rocks from the Red Lodge District. USGS Bulletin, Professional Paper 44.

López S, Fernández C, Castro A (2006) Evolution of the Archaean continental crust: Insights from the experimental study of Archaean granitoids. Current Science 91(5):607-621.

Lorand J P, Pattou L, Gros M (1999) Fractionation of platinum-group elements and gold in the upper mantle: a detailed study in Pyrenean orogenic lherzolites. Journal of Petrology 40(6):957-981.

Lorand J -P, Alard O (2001) Platinum-group element abundances in the upper mantle: new constraints from in situ and whole-rock analyses of Massif Central xenoliths (France). Geochimica et Cosmochimica Acta 65(16): 2789-2806.

Lorand J P, Luguet A, Alard O (2013) Platinum-group element systematics and petrogenetic processing of the continental upper mantle: A review. Lithos 164:2-21.

Ludwig K R (2008) Isoplot 3.7. Berkley Geochronology Center, Special Publication N◦4.

Luguet A, Shirey S B, Lorand J, Horan M F, Carlson R W (2007) Residual platinum-group minerals from highly depleted harzburgites of the Lherz massif (France) and their role in HSE fractionation of the mantle. Geochimica et Cosmochimica Acta 71(12):3082-3097.

Luguet A, Pearson D G (2019) Dating mantle peridotites using Re-Os isotopes: The complex message from whole rocks, base metal sulfides, and platinum group minerals. American Mineralogist 104(2):165-189.

Mahalik N K (1994) Geology of the contact between the Eastern Ghats Belt and North Orissa Carton, India. Journal of the Geological Society of India 44:41-51.

Maier W D, Barnes S J, Campbell I H, Fiorentini M L., Peltonen P, Barnes S J, Smithies R H (2009) Progressive mixing of meteoritic veneer into the early Earth's deep mantle. Nature 460(7255):620-623.

Maier W D, Mundl-Petermeier A (2023) Controls on Pt/Pd ratios in Bushveld magmas and cumulates: a review complemented by new W isotope data. Mineralium Deposita 58(3):553-568.

Majumder T, Chakraborty K (1977) Primary sedimentary structures in the banded iron formation of Orissa. Sedimentary Geology 19:287-300.

Maltese A, Caro G, Pandey O P, Upadhyay D, Mezger K (2022) Direct evidence for crust-mantle differentiation in the late Hadean. Communications Earth & Environment 3:12.

Martin H, Moyen J -F (2002) Secular changes in TTG composition as markers of the progressive cooling of the earth. Geology 30:319-322.

Matin A, Banerjee S, Gupta C D, Banerjee N (2012) Progressive deformation across a ductile shear zone: an example from the Singhbhum Shear Zone, eastern India. International Geology Review 54:290-301.

Mazumder R, Sarkar S (2004) Sedimentation history of the Palaeoproterozoic Dhanjori Formation, Singhbhum, eastern India. Precambrian Research 130:267-287.

Mazumder R (2005) Proterozoic sedimentation and volcanism in the Singhbhum crustal province, India and their implications. Sedimentary Geology 176:167-193.

Mazumder R, Arima M (2009) Implication of mafic magmatism in an intra-continental rift setting: a case study from the Palaeoproterozoic Dhanjori Formation, Singhbhum crustal province, India. Journal of Geology 117:455e466.

Mazumder R, Van Loon A J, Mallik L, Reddy S M, Arima M, Altermann W, Eriksson P G, De S (2012) Mesoarchaean-Palaeoproterozoic stratigraphic record of the Singhbhum crustal province, eastern India: A synthesis. In: Mazumder R, Saha D (Eds.) Palaeoproterozoic of India. Geological Society, London, Special Publication 365:31-49.

Mazumder R, Chaudhuri T (2019) Precambrian mafic dyke swarms in the Singhbhum craton (eastern India) and their links with dyke swarms of the eastern Dharwar craton (southern India) - Discussion. Precambrian Research 319:19-22.

Mazumder R, Chaudhuri T, Biswas S (2019) Palaeoarchaean sedimentation and magmatic processes in the eastern Iron Ore Group, eastern India: A commentary. Geological Journal 54:3078-3087.

Mazumder R, Chaudhuri T, De S, Bauer W, Al Hadi M, Sugitani K, van Zuilen M A, Senda R, Yamamoto M, Raju P S, Ohta T, Catuneanu O, Mazumder S, Saito S, Shimooka K (2022) Paleoarchean surface processes and volcanism: Insights from the eastern Iron Ore Group, Singhbhum craton, India. Earth-Science Reviews 232:104122.

McDonough W, Sun S (1995) The composition of the Earth. Chemical Geology 120(3-4):223-253.

McDonough W F, Rudnick R L (1998) Mineralogy and composition of the upper mantle. Reviews in mineralogy 37:139-164.

McKenzie D A, O'nions R K (1991) Partial melt distributions from inversion of rare earth element concentrations. Journal of Petrology 32(5):1021-1091.

McKenzie D (2020) Speculations on the generation and movement of komatiites. Journal of Petrology 61(7):egaa061.

Merlini A, Grieco G, Diella V (2009) Ferritchromite and chromian chlorite formation in mélange-hosted Kalkan chromitite (Southern Urals, Russia). American Mineralogist 94(10):1459-1467.

Miller G H, Stolper E M, Ahrens T J (1991) The equation of state of a molten komatiite: 1 shock wave compression to 36 GPa. Journal of Geophysical Research: Solid Earth 96(B7):11831-11848.

Miller S R, Mueller P A, Meert J G, Kamenov G D, Pivarunas A F, Sinha A K, Pandit M K (2018) Detrital Zircons Reveal evidence of Hadean Crust in the Singhbhum Craton. Journal of Geology 126:541-552.

Mishra S, Deomurari M P, Widenbeck M, Goswami J N, Ray S, Saha A K (1999) $^{207}Pb/^{206}Pb$ zircon ages and the evolution of the Singhbhum craton, eastern India: an ion microprobe study. Precambrian Research 93:139-151.

Misra S (1999) The Mayurbhanj Granite: Its nature, tectonic setting, mode of emplacement and pressure-temperature of magma generation. Indian Journal of Geology 71:33-52.

Misra S, Sarkar S S, Ghosh S (2002) Evolution of Mayurbhanj Granite Pluton, eastern Singhbhum, India: a case study of petrogenesis of an A-type granite in bimodal association. Journal of Asian Earth Sciences 20:965-989.

Misra S, Johnson P T (2005) Geochronological constraints on evolution of Singhbhum mobile belt and associated basic volcanics of eastern Indian shield. Gondwana Research 8:129-142.

Misra S (2006) Precambrian Chronostratigraphic Growth of Singhbhum-Orissa Craton, Eastern Indian Shield: An Alternative Model. Journal of The Geological Society of India 67:356-378.

Mondal S K, Baidya T K, Rao K N G, Glascock M D (2001) PGE and Ag mineralization in Breccia zone of the Precambrian Nuasahi ultramafic-mafic complex, Orissa India. Canadian Mineralogist 39:979-996.

Mondal S K, Ripley E M, Li C, Frei R (2006) The genesis of Archean chromitites from the Nuasahi and Sukinda massifs in the Singhbhum Craton, India. Precambrian Research 148:45-66.

Mondal S K, Frei R, Ripley E M (2007) Os isotope systematics of mesoarchean chromitite-PGE deposits in the Singhbhum Craton (India): Implications for the evolution of lithospheric mantle. Chemical Geology 244(3-4):391-408.

Mondal S K (2009) Chromite and PGE deposits of Mesoarchaean ultramafic-mafic suites within the greenstone belts of the Singhbhum Craton, India: Implications for mantle heterogeneity and tectonic setting. Journal of the Geological Society of India 73:36-51.

Mondal S K, Zhou M F (2010) Enrichment of PGE through interaction of evolved boninitic magmas with early formed cumulates in a gabbro-breccia zone of the Mesoarchean Nuasahi Massif (eastern India). Mineralium Deposita 45:69-91.

Mondal S K, Pramanik I, Mukherjee R, Bank S P (2015) PGE geochemistry of Precambrian mafic dykes from Singhbhum Craton (India).Goldschmidt Conference 2015, Prague.

Mondal S K, Khatun S, Prichard H M, Satyanarayanan M, Kumar G R (2019) Platinum-group element geochemistry of boninite-derived Mesoarchean chromitites and ultramafic-mafic cumulate rocks from the Sukinda Massif (Orissa, India). Ore Geology Reviews 104:722-744.

Mondal S K, Bhattacharjee C, Reisberg L (2021) 3.2-3.0 Ga Sm-Nd age of gabbro-anorthositic rocks from the Nuasahi and Mayurbhanj complexes (eastern India): major mafic magmatic event in the Singhbhum Craton and associated Ni-Cu-(PGE) sulphide mineralization. Goldschmidt Virtual, 4-9 July, Lyon, France, Abstract with program. Abstract 4656.

Moorbath S, Taylor P, Jones N (1986) Dating the oldest terrestrial rocks-fact and fiction. Chemical Geology 57:63-86.

Moorbath S, Taylor P N (1988) Early Precambrian crustal evolution in eastern India: the age of the Singhbhum Granite and included remnants of older gneiss. Journal of the Geological Society of India 31:82-84.

Morimoto N (1988) Nomenclature of pyroxenes. Mineralogy and Petrology 39:55-76.

Moyen J, Stevens G (2006) Experimental constraints on TTG petrogenesis: implications for Archean geodynamics. Geophysical Monograph-American Geophysical Union: 164:149.

Moyen J, Stevens G, Kisters A F, Belcher R W (2007) TTG Plutons of the Barberton Granitoid-Greenstone Terrain, South Africa. Developments in Precambrian Geology 15:607-667.

Moyen J F (2011) The composite Archaean grey gneisses: petrological significance, and evidence for a non-unique tectonic setting for Archaean crustal growth. Lithos 123(1-4):21-36.

Moyen J F, Martin H (2012) Forty years of TTG research. Lithos 148:312-336.

Mukherjee R, Mondal S K, Rosing M T, Frei R (2010) Compositional variations in the Mesoarchean chromites of the Nuggihalli schist belt, Western Dharwar Craton (India): potential parental melts and implication for tectonic setting. Contributions to Mineralogy and Petrology 160:865-885.

Mukherjee R, Mondal S K, Frei R, Rosing M T, Waight T E, Zhong H, Kumar G R (2012) The 3.1 Ga Nuggihalli chromite deposits, Western Dharwar craton (India): Geochemical and isotopic constraints on mantle sources, crustal evolution

and implications for supercontinent formation and ore mineralization. Lithos 155:392-409.

Mukherjee R, Mondal S K, Zhong H, Bai Z -J, Balaram V, Kumar G R R (2014) Platinum-group element geochemistry of komatiite-derived 3.1 Ga ultramafic-mafic rocks and chromitites from the Nuggihalli greenstone belt, western Dharwar craton (India). Chemical Geology 386:190-208.

Mukherjee R, Mondal S K, Gonzaléz-Jiménez J M, Griffin W L, Pearson N J, O'Reilly S Y (2015) Trace element fingerprints of chromite, magnetite and sulfide from the 3.1 Ga ultramafc-mafc rocks of the Nuggihalli greenstone belt, Western Dharwar Craton (India). Contributions to Mineralogy and Petrology 169:1-23.

Mukhopadhyay D (2001) The Archaean nucleus of Singhbhum: the present state of knowledge. Gondwana Research 4:307-318.

Mukhopadhyay J, Ghosh G, Nandi A K, Chaudhuri A K (2006) Depositional setting of the Kolhan Group: its implications for the development of a Meso to Neoproterozoic deep-water basin on the South Indian craton. South African Journal of Geology 109:183-192.

Mukhopadhyay J, Ghosh G, Beukes N, Gutzmer J (2007) Precambrian colluvial iron ores in the Singhbhum Craton: implications for origin, age of BIF-hosted high-grade iron ores and stratigraphy of the Iron Ore Group. Journal of the Geological Society of India 70:34.

Mukhopadhyay J, Beukes N, Armstrong R, Zimmermann U, Ghosh G, Medda R (2008) Dating the oldest greenstone in India: a 3.51-Ga precise U-Pb SHRIMP zircon age for dacitic lava of the southern Iron Ore Group, Singhbhum craton. The Journal of Geology 116:449-461.

Mukhopadhyay J, Ghosh G, Zimmermann U, Guha S, Mukherjee T (2012) A 3.51 Ga bimodal volcanics-BIF-ultramafic succession from Singhbhum Craton: implications for Palaeoarchaean geodynamic processes from the oldest greenstone succession of the Indian subcontinent. Geological Journal 47:284-311.

Mukhopadhyay J, Crowley Q G, Ghosh S, Ghosh G, Chakrabarti K, Misra B, Heron K, Bose S (2014) Oxygenation of the Archean atmosphere: New paleosol constraints from eastern India. Geology 42:923-926.

Mukhopadhyay D, Matin A (2020) The architecture and evolution of the Singhbhum Craton. Episodes 43(1):19-50.

Mungall J E, Brenan J M (2014) Partitioning of platinum-group elements and Au between sulfide liquid and basalt and the origins of mantle-crust fractionation of the chalcophile elements. Geochimica et Cosmochimica Acta 125:265-289.

Naldrett A J (2004) Magmatic Sulfide Deposits: Geology, Geochemistry and Exploration. Springer, Heidelberg.

Nebel O, Campbell I H, Sossi P A, Van Kranendonk M J (2014) Hafnium and iron isotopes in early Archean komatiites record a plume-driven convection cycle in the Hadean Earth. Earth and Planetary Science Letters 397:111-120.

Nebel O, Capitanio F A, Moyen J -F, Weinberg R F, Clos F, Nebel-Jacobsen Y J, Cawood P A (2018) When crust comes of age: on the chemical evolution of Archaean, felsic continental crust by crustal drip tectonics. Philosophical Transaction Royal Society A 376:20180103.

Nell J, O'Neill H S (1997) The Gibbs free energy of formation and heat capacity of β-Rh_2O_3 and $MgRh_2O_4$, the MgO-Rh-O phase diagram, and constraints on the stability of $Mg_2Rh^{4+}O_4$. Geochimica et cosmochimica acta 61(19):4159-4171.

Nelson B W, Roy R (1958) Synthesis of the chlorites and their structural and chemical constitution. American Mineralogist: Journal of Earth and Planetary Materials 43(7-8):707-725.

Nelson D R, Trendall A F, Altermann W (1999) Chronological correlations between the Pilbara and Kaapvaal cratons. Precambrian Research 97(3-4):165-189.

Nelson D R, Bhattacharya H N, Thern E R, Altermann W (2014) Geochemical and ion-microprobe U-Pb zircon constraints on the Archaean evolution of Singhbhum Craton, eastern India. Precambrian Research 255:412-432.

Nesbitt R W (1971) Skeletal crystal forms in the ultramafic rocks of the Yilgarn Block, Western Australia-evidence for an Archaean ultramafic liquid. In: Glover J D (ed.) Symposium on Archean Rocks. Geological Society of Australia Special Publication 3:331-347.

Nesbitt R W, Sun S -S (1976) Geochemistry of Archaean spinifex-textured peridotites and magnesian and low-magnesian tholeiites. Earth and Planetary Science Letters 31(3): 433-453.

Nesbitt R W, Sun S, Purvis A C (1979) Komatiites: geochemistry and genesis. Canadian Mineralogist 17:165-186.

Nesbitt R W, Jahn B -M, Purvis A C (1982) Komatiites: An early Precambrian phenomenon. Journal of Volcanology and Geothermal Research 14:31-45.

Netshidzivhe T, Tappe S, Wilson A H, Ishikawa A, Viljoen F (2023) The Paleoarchean Buffalo River komatiites: Progressive melting of a single large mantle plume beneath the growing Kaapvaal craton. Precambrian Research 393:107071.

Nicklas R W, Puchtel I S, Ash R D (2016) High-precision determination of the oxidation state of komatiite lavas using vanadium liquid mineral partitioning. Chemical Geology 433:36-45.

Nicklas R W, Puchtel I S, Ash R D, Piccoli P M, Hanski E, Nisbet E G, Waterton P M, Pearson D G, Anbar A D (2019) Secular mantle oxidation across the Archean Proterozoic boundary: evidence from V partitioning in komatiites and picrites. Geochimica et Cosmochimica Acta 250:49-75.

Nielsen R L, Beard J S (2000) Magnetite-melt HFSE partitioning. Chemical Geology 164(1-2):21-34.

Oberthür T, Davis D W, Blenkinsop T G, Höhndorf A (2002) Precise U-Pb mineral ages, Rb-Sr and Sm-Nd systematics for the Great Dyke, Zimbabwe-constraints on late Archean events in the Zimbabwe craton and Limpopo belt. Precambrian Research 113(3-4):293-305.

Ohtani E (1984) Generation of komatiite magma and gravitational differentiation in the deep upper mantle. Earth and planetary science letters 67(2):261-272.

Olierook H K H, Clark C, Reddy S M, Mazumder R, Jourdan F, Evans N J (2019) Evolution of the Singhbhum Craton and supracrustal provinces from age, isotopic and chemical constraints. Earth Science Reviews 193:237-259.

O'Neill C, Jellinek A M, Lenardic A (2007) Conditions for the onset of plate tectonics on terrestrial planets and moons. Earth and Planetary Science Letters 261(1-2) 20-32.

Pagé P, Barnes S -J (2009) Using trace elements in chromites to constrain the origin of podiform chromitites in the Thetford Mines ophiolite, Québec, Canada. Economic Geology 104:997-1018.

Pagé P, Barnes S -J, Bédard J H, Zientek M L (2012) In situ determination of Os, Ir, and Ru in chromites formed from komatiite, tholeiite and boninite magmas: implications for chromite control of Os, Ir and Ru during partial melting and crystal fractionation. Chemical Geology 302:3-15.

Pagé P, Barnes S -J (2016) The infuence of chromite on osmium, iridium, ruthenium and rhodium distribution during early magmatic processes. Chemical Geology 420:51-68.

Pal D C, Barton M D, Sarangi A K (2009) Deciphering a multistage history affecting U-Cu(-Fe) mineralization in the Singhbhum Shear Zone, eastern India, using pyrite textures and compositions in the Turamdih U-Cu(-Fe) deposit. Mineralium Deposita 44:61-80.

Pal D C, Trumbull R B, Wiedenbeck M (2010) Chemical and boron isotope compositions of tourmaline from the Jaduguda U (-Cu-Fe) deposit, Singhbhum shear zone, India: Implications for the sources and evolution of mineralizing fluids. Chemical Geology 277:245-260.

Pal D C, Sarkar S, Mishra B, Sarangi A K (2011) Chemical and sulfur isotope compositions of pyrite in the Jaduguda U (-Cu-Fe) deposit, Singhbhum shear zone, eastern India: Implications for sulfide mineralization. Journal of Earth System Science 120:475-488.

Pal D C, Rhede D (2013) Geochemistry and chemical dating of uraninite in the Jaduguda uranium deposit, Singhbhum shear zone, India implications for

uranium mineralization and geochemical evolution of uraninite. Economic Geology 108:1499-1515.

Pal D C, Banerjee A, Dutta A, Sarangi A K (2022) Hydrothermal alterations and U-REE mineralisation in the Narwapahar uranium deposit, Singhbhum shear zone, India. Journal of Earth System Science 131:31.

Pandey O P, Mezger K, Ranjan S, Upadhyay D, Villa I M, Nagler T F, Vollstaedt H (2019) Genesis of the Singhbhum Craton, eastern India; implications for Archean crust-mantle evolution of the Earth. Chemical Geology 512:85-106.

Parman S W, Dann J C, Grove T L, De Wit M J (1997) Emplacement conditions of komatiite magmas from the 3.49 Ga Komati Formation, Barberton greenstone belt, South Africa. Earth and Planetary Science Letters 150(3-4):303-323.

Parman S, Grove T L, Dann J (2001). The production of Barberton komatiites in an Archean subduction zone. Geophysical Research Letters 28:2513-2516.

Parman S W, Grove T L, Dann J C, de Wit M J (2004) A subduction origin for komatiites and cratonic lithospheric mantle. South African Journal of Geology 107:107-118.

Park J- W, Campbell I H, Eggins S M (2012) Enrichment of Rh, Ru, Ir and Os in Cr spinels from oxidized magmas: evidence from the Ambae volcano, Vanuatu. Geochimica et Cosmochimica Acta 78:28-50.

Park J- W, Kamenetsky V, Campbell I, Park G, Hanski E, Pushkarev E (2017) Empirical constraints on partitioning of platinum group elements between Cr-spinel and primitive terrestrial magmas. Geochimica et Cosmochimica Acta 216:393-416.

Paton C, Hellstrom J, Paul B, Woodhead J, Hergt J (2011) Iolite: Freeware for the visualisation and processing of mass spectrometric data. Journal of Analytical Atomic Spectrometry 26(12):2508-2518.

Paul D K, Mukhopadhayay D, Pyne T, Bishui P (1991) Rb-Sr age of granitoid in the Deo River section, Singhbhum and its relevance to the age of iron formation. Indian Minerals 45:51-56.

Peach C L, Mathez E A, Keays R R (1990) Sulfide melt-silicate melt distribution coefficients for noble metals and other chalcophile elements as deduced from MORB: Implications for partial melting. Geochimica et Cosmochimica Acta 54(12):3379-3389.

Peach C L, Mathez E A, Keays R R, Reeves S J (1994) Experimentally determined sulfide melt-silicate melt partition coefficients for iridium and palladium. Chemical Geology 117(1-4):361-377.

Peach C L, Mathez E A (1996) Constraints on the formation of platinum-group element deposits in igneous rocks. Economic Geology 91(2):439-450.

Pearson D, Brenker F, Nestola F, McNeill J, Nasdala L, Hutchison M T, Matveev S, Mather K, Silversmit G, Schmitz S, Vekemans B, Vincze L (2014) Hydrous mantle transition zone indicated by ringwoodite included within diamond. Nature 507:221-224.

Polat A, Kerrich R, Wyman D A (1999) Geochemical diversity in oceanic komatiites and basalts from the late Archean Wawa greenstone belts, Superior Province, Canada: trace element and Nd isotope evidence for a heterogeneous mantle. Precambrian Research 94(3-4):139-173.

Polat A, Hofmann A W, Rosing M T (2002) Boninite-like volcanic rocks in the 3.7-3.8 Ga Isua greenstone belt, West Greenland: geochemical evidence for intra-oceanic subduction zone processes in the early Earth. Chemical geology 184(3-4):231-254.

Polat A, Hofmann A W, Münker C, Regelous M, Appel P W (2003) Contrasting geochemical patterns in the 3.7-3.8 Ga pillow basalt cores and rims, Isua greenstone belt, Southwest Greenland: implications for postmagmatic alteration processes. Geochimica et Cosmochimica Acta 67(3):441-457.

Polat A, Frei R (2005) The origin of early Archean banded iron formations and of continental crust, Isua, southern West Greenland. Precambrian Research 138:151-175.

Pollack H N (1997) Thermal characteristics of the Archaean. Oxford monographs on geology and geophysics 35(1):223-232.

Prasek M K (2022) Fractionation Processes of Platinum-Group-Elements in Natural Systems and Experiments (Doctoral dissertation, McGill University (Canada)).

Prichard H M, Barnes S J, Fisher P C, Pagé P, Zientek M L (2017) Laurite and associated PGM in the Stillwater chromitites: Implications for processes of formation, and comparisons with laurite in the Bushveld and ophiolitic chromitites. The Canadian Mineralogist 55(1):121-144.

Prichard H M, Mondal S K, Mukherjee R, Fisher P C, Giles N (2018) Geochemistry and mineralogy of Pd in the magnetitite layer within the upper gabbro of the Mesoarchean Nuasahi Massif (Orissa, India). Mineralium Deposita 53:547-564.

Proenza J A, Ortega-Gutiérrez F, Camprubí A, Tritlla J, Elías-Herrera M, Reyes-Salas M (2004) Paleozoic serpentinite-enclosed chromitites from Tehuitzingo (Acatlán Complex, southern Mexico): a petrological and mineralogical study. Journal of South American Earth Science 16:649-666.

Proenza J A, Zaccarini F, Escayola M, Cábana C, Shalamuk A, Garuti G (2008) Composition and textures of chromite and platinum group minerals in chromitites of the western ophiolitic belt from Córdoba Pampeans Ranges, Argentine. Ore Geology Reviews 33:32-48.

Puchtel I S, Hofmann A W, Mezger K, Jochum K P, Shchipansky A A, Samsonov A V (1998) Oceanic plateau model for continental crustal growth in the Archaean: a case study from the Kostomuksha greenstone belt, NW Baltic Shield. Earth and Planetary Science Letters 155:57-74.

Puchtel I, Humayun M (2000) Platinum group elements in Kostomuksha komatiites and basalts: implications for oceanic crust recycling and core-mantle interaction. Geochimica et Cosmochimica Acta 64(24):4227-4242.

Puchtel I S, Humayun M, Campbell A J, Sproule R A, Lesher C M (2004) Platinum group element geochemistry of komatiites from the Alexo and Pyke Hill areas, Ontario, Canada. Geochimica et Cosmochimica Acta 68(6):1361-1383.

Puchtel I S, Humayun M (2005) Highly siderophile element geochemistry of ^{187}Os-enriched 2.8 Ga Kostomuksha komatiites, Baltic Shield. Geochimica et Cosmochimica Acta 69(6):1607-1618.

Puchtel I S, Walker R J, Anhaeusser C R, Gruau G (2009a) Re-Os isotope systematics and HSE abundances of the 3.5 Ga Schapenburg komatiites, South Africa:

Hydrous melting or prolonged survival of primordial heterogeneities in the mantle? Chemical Geology 262(3-4):355-369.

Puchtel I S, Walker R J, Brandon A D, Nisbet E G (2009b) Pt-Re-Os and Sm-Nd isotope and HSE and REE systematics of the 2.7 Ga Belingwe and Abitibi komatiites. Geochimica et Cosmochimica Acta 73(20):6367-6389.

Puchtel I S, Blichert-Toft J, Touboul M, Walker R J, Byerly G, Nisbet E G, Anhaeusser C R (2013) Insights into early Earth from Barberton komatiites: evidence from lithophile isotope and trace element systematics. Geochimica et Cosmochimica Acta 108:63-90.

Puchtel I S, Walker R J, Touboul M, Nisbet E G, Byerly G R (2014) Insights into Early Earth from the Pt-Re-Os isotope and Highly Siderophile Element abundance systematics of Barberton komatiites. Geochimica et Cosmochimica Acta 125:394-413.

Puchtel I S, Touboul M, Blichert-Toft J, Walker R J, Brandon A D, Nicklas R W, Kulikov V S, Samsonov A V (2016) Lithophile and siderophile element systematics of Earth's mantle at the Archean-Proterozoic boundary: Evidence from 2.4 Ga komatiites. Geochimica et Cosmochimica Acta 180:227-255.

Puchtel I S, Blichert-Toft J, Touboul M, Walker R J (2018) ^{182}W and HSE constraints from 2.7 Ga komatiites on the heterogeneous nature of the Archean mantle. Geochimica et Cosmochimica Acta 228:1-26.

Puchtel I S, Mundl-Petermeier A, Horan M, Hanski E J, Blichert-Toft J, Walker R J (2020) Ultra depleted 2.05 Ga komatiites of Finnish Lapland: Products of grainy late accretion or core-mantle interaction? Chemical Geology 554:119801.

Rapp R P, Watson E B (1995) Dehydration melting of metabasalt at 8-32 kbar: implications for continental growth and crust-mantle recycling. Journal of petrology 36(4):891-931.

Richter F M (1985) Models for the Archean thermal regime. Earth and Planetary Science Letters 73(2-4):350-360.

Rigden S M, Ahrens T J, Stolper E M (1984) Densities of liquid silicates at high pressures. Science 226(4678):1071-1074.

Righter K, Downs R T (2001) The crystal structures of synthetic Re- and PGE- bearing magnesioferrite Spinels: Implications for impacts, accretion and the mantle. Geophysical Research Letters 28(4):619-622.

Righter K, Campbell A J, Humayun M, Hervig R L (2004) Partitioning of Ru, Rh, Pd, Re, Ir, and Au between Cr-bearing spinel, olivine, pyroxene and silicate melts. Geochimica et Cosmochimica Acta 68(4):867-880.

Righter K, Sutton S R, Newville M, Le L, Schwandt C S, Uchida H, Lavina B, Downs R T (2006) An experimental study of the oxidation state of vanadium in spinel and basaltic melt with implications for the origin of planetary basalt. American Mineralogist 91(10):1643-1656.

Ringwood A E, Major A (1971) Synthesis of majorite and other high pressure garnets and perovskites. Earth and Planetary Science Letters 12:411-418.

Robin-Popieul C C M, Arndt N T, Chauvel C, Byerly G R, Sobolev A V, Wilson A (2012) A new model for Barberton komatiites: deep critical melting with high melt retention. Journal of Petrology 53:2191-2229.

Robinson J A, Wood B J (1998) The depth of the spinel to garnet transition at the peridotite solidus. Earth and Planetary Science Letters 164(1-2):277-284.

Rodgers J J, Santosh M (2003) Supercontinents in Earth's history. Gondwana Research 6:357-368.

Roeder P L, Campbell I H, Jamieson H E (1979) A re-evaluation of the olivine-spinel geothermometer. Contributions to Mineralogy and Petrology 68:325-334.

Roeder P L (1994) Chromite: from the fiery rain of chondrules to the Kilauea Iki lava lake. Canadian Mineralogist 32:729-746.

Rogers J J (1996) A history of continents in the past three billion years. The journal of geology 104(1):91-107.

Rollinson H (1995) Composition and tectonic settings of chromite deposits through time; discussion. Economic Geology 90(7):2091-2092.

Rosendahl B R (1987) Architecture of continental rifts with special reference to East Africa. Annual Review of Earth and Planetary Science 15(1):445-503.

Roy A, Sarkar A, Jayakumar S, Aggarwal S K, Ebihara M, Satoh H (2004) Late Archaean mantle metasomatism below eastern Indian craton: Evidence from trace elements, REE geochemistry and Sr-Nd-O isotope systematics of ultramafic dykes. Proceedings of the Indian Academy of Sciences-Earth and Planetary Science 113:649-665.

Roy S, Bandyopadhyay D, Morishita T, Dhar A, Koley M, Chattopadhaya S, Karmakar A, Ghosh B (2022) Microtextural evolution of chrome spinels in dunites from Mayodia ophiolite complex, Arunachal Pradesh, India: Implications for a missing link in the "two-stage" alteration mechanism. Lithos 420-421:106719.

Rozel A B, Golabek G J, Jain C, Tackley P J, Gerya T (2017) Continental crust formation on early Earth controlled by intrusive magmatism. Nature 545:332-335.

Rudnick R L, Gao S (2014) The Composition of the Continental Crust. Treatise on geochemistry (second edition):1-51.

Ruiz F V, Della Giustina M E, de Oliveira C G, Dantas E L, Hollanda M H (2019) The 3.5 Ga São Tomé layered mafic-ultramafic intrusion, NE Brazil: Insights into a Paleoarchean Fe-Ti-V oxide mineralization and its reworking during West Gondwana assembly. Precambrian Research 326:462-78.

Sack R O, Ghiorso M S (1991) Chromian spinels as petrogenetic indicators: Thermodynamics and petrological applications. American Mineralogist 76(5-6):827-847.

Saha A K (1972) Petrogenetic and structural evolution of the Singhbhum granite complex, eastern India. Proceedings of the 24th International Geological Congress, pp. 147-155.

Saha A K, Ray S L (1984) The structural and geochemical evolution of the Singhbhum granite batholithic complex, India. Tectonophysics 105(1-4):163-176.

Saha A K (1994) Crustal evolution of Singhbhum-North Orissa, eastern India. Journal of the Geological Society of India, Memoir 27:341.

Saha D, Bachhar P, Deb G K, Patranabis-Deb S, Banerjee A (2021) Tectonic evolution of the Paleoarchean to Mesoarchean Badampahar-Gorumahisani belt, Singhbhum craton, India-Implications for coexisting arc and plume signatures in a granite-greenstone terrain. Precambrian Research 357:106094.

Sahu N K, Mukherjee M M (2001) Spinifex textured komatiite from Badampahar-Gorumahisani schist belt, Mayurbhanj District, Orissa. Geological Society of India 57(6):529-534.

Sarkar S N, Saha A K, Boelrijk N A I M, Hebeda E H (1979) New data on the geochronology of the Older Metamorphic Group and the Singhbhum Granite of Singhbhum-Keonjhar-Mayurbhanj region, eastern India. Indian Journal of Earth Science 6:32-51.

Sarkar S N, Saha A K (1983) Structure and tectonics of the Singhbhum-Orissa Iron Ore Craton, eastern India. Recent Researches in Geology 10:1-25.

Sattari P, Brenan J M, Horn I, McDonough W F (2002) Experimental constraints on the sulfide-and chromite-silicate melt partitioning behavior of rhenium and platinum-group elements. Economic Geology 97(2):385-398.

Schneider K, Hoffmann J, Münker C, Patyniak M, Sprung P, Roerdink D, Garbe-Schönberg D, Kröner A (2019) Petrogenetic evolution of metabasalts and metakomatiites of the lower Onverwacht Group, Barberton Greenstone Belt (South Africa). Chemical Geology 511:152-177.

Schoene B, de Wit M J, Bowring S A (2008) Mesoarchean assembly and stabilization of the eastern Kaapvaal craton: A structural-thermochronological perspective. Tectonics 27(5).

Schoneveld L, Barnes S, Puchtel I S, Tessalina S, Locmelis M (2022) Distributions of Platinum Group Elements and Re-Os Isotope Systematics in Chromite from the Coobina Chromitite Deposit in Western Australia: Implications for Chromite as a Sulfide Mineralization Indicator. The Canadian Mineralogist 60(6):1045-1069.

Sengupta S (1990) Petrological studies on basic rocks of possible Archaean greenstone sequence and inference of paleo-tectonic setting. GSI Rep.

Sengupta S, Paul D K, De Laeter J, McNaughton N, Bandopadhyay P, De Smeth J (1991) Mid-Archaean evolution of the eastern Indian craton: geochemical and isotopic evidence from the Bonai pluton. Precambrian Research 49:23-37.

Sengupta S, Bandopadhyay P, De Smeth J B, Maitra M (1993) Petrogenesis of granitoid components from Bonai pluton and its implication on the formation of the eastern Indian Archaean sialic crust. Proceedings of the Indian Academy of Sciences India, section A, 63:189-189.

Sengupta S, Paul D K, Bishui P K, Gupta S N, Chakraborty R, Sen P (1994) A geochemical and Rb-Sr isotopic study of Kuilapal granite and Arkasoni granophyre from the eastern Indian craton. Indian Minerals 48:77-88.

Sengupta S, Acharyya S K, De Smith J B (1997) Geochemistry of Archaean volcanic rocks from Iron Ore Supergroup, Singhbhum, eastern India. Proceeding of Indian Academy of Science (Earth Planetary Science) 106:327-342.

Sengupta N, Mukhopadhyay D, Sengupta P, Hoffbauer R (2005) Tourmaline-bearing rocks in the Singhbhum shear zone, eastern India: Evidence of boron infiltration during regional metamorphism. American Mineralogist 90:1241-1255.

Sengupta P, Ray A, Pramanik S (2014) Mineralogical and chemical characteristics of newer dolerite dyke around Keonjhar, Orissa: implication for hydrothermal activity in subduction zone setting. Journal of Earth System Science 123:887-904.

Shankar R, Vijayagopal B, Kumar A (2014) Precise Pb-Pb baddeleyite ages of 1765 Ma for a Singhbhum ‘newer dolerite’ dyke swarm. Current Science 106:1306-1310.

Sharma M, Basu A R, Ray S L (1994) Sm-Nd isotopic and geochemical study of the Archaean tonalite amphibolite association from the eastern Indian Craton. Contributions to Mineralogy and Petrology 117:45-55.

Shaw D M (1970) Trace element fractionation during anatexis, Geochimica et Cosmochimica Acta 34:237-243.

Shimizu K, Komiya T, Hirose K, Shimizu N, Maruyama S (2001) Cr-spinel, an excellent micro-container for retaining primitive melts-implications for a hydrous plume origin for komatiites. Earth and Planetary Science Letters 189(3-4):177-188.

Shimizu K, Nakamura E, Maruyama S (2005) The Geochemistry of Ultramafic to Mafic Volcanics from the Belingwe Greenstone Belt, Zimbabwe: Magmatism in an Archean Continental Large Igneous Province. Journal of Petrology 46(11):2367-2394.

Sievwright R H, O'Neill H S C, Tolley J, Wilkinson J J, Berry A J (2020) Diffusion and partition coefficients of minor and trace elements in magnetite as a function of oxygen fugacity at 1150°C. Contributions to Mineralogy and Petrology 175(5):1-21.

Singh S P, Sinha P K, Sharan R R, Sesha Sai V V (2001) Petrology and geochemistry of the acid agglomerates, Dorea, Singhbhum, Jharkhand. PCEM, Patna Chapter Seminar Volume (Ed. S.P. Singh), pp.235-241.

Singh M R, Manikyamba C, Ray J, Ganguly S, Santosh M, Saha A, Rambabu S, Sawant S S (2016) Major, trace and platinum group element (PGE) geochemistry of Archean Iron Ore Group and Proterozoic Malangtoli metavolcanic rocks of

Singhbhum Craton, Eastern India: Inferences on mantle melting and Sulphur saturation history. Ore Geology Reviews 72:1263-1289.

Singh M R, Manikyamba C, Ganguly S, Ray J, Santosh M, Singh T D, Kumar B C (2017) Paleoproterozoic arc basalt boninite-high magnesian andesite-Nb enriched basalt association from the Malangtoli volcanic suite, Singhbhum Craton, eastern India: geochemical record for subduction initiation to arc maturation continuum. Journal of Asian Earth Sciences 134:191-206.

Singh P K, Verma S K, Moreno J A, Singh V K, Malviya V P, Oliveira E P, Mishra S, Arima M (2019) Geochemistry and SmNd isotope systematics of mafic-ultramafic rocks from the Babina and Mauranipur greenstone belts, Bundelkhand Craton, India: Implications for tectonic setting and Paleoarchean mantle evolution. Lithos 330:90-107.

Sinha D K, Gupta S, Nautiyal K, Akhila V R, Shrivastava V K, Padhi A K, Verma M B (2019) Serpentinized peridotite-hosted uranium mineralization (U-Cr-Ni-Mo-REE-Fe-Mg) in Kudada-Turamdih area: a new environment of metallogeny in Singhbhum shear zone, India. Current Science 117:830-838.

Smithies R H (2000) The Archaean tonalite-trondhjemite-granodiorite (TTG) series is not an analogue of Cenozoic adakite. Earth and Planetary Science Letters 182(1):115-125.

Smithies R H, Champion D C, Cassidy K F (2003) Formation of Earth's early Archaean continental crust. Precambrian Research 127(1-3):89-101.

Smithies R H, Champion D C, Van Kranendonk M J (2007) The oldest well-preserved Felsic volcanic rocks on earth: geochemical clues to the early evolution of the Pilbara Supergroup and implications for the growth of a Paleoarchean

Proto-continent. In: VanKranendonk M J, Smithies R H, Bennett V C (Eds.) Earth's Oldest Rocks. Developments in Precambrian Geology 15:339-368.

Sobolev A V, Asafov E V, Gurenko A A, Arndt N T, Batanova V G, Portnyagin M V, Garbe-Schönberg D, Krasheninnikov S P (2016) Komatiites reveal a hydrous Archaean deep-mantle reservoir. Nature 531(7596):628-632.

Sossi P A, Eggins S M, Nesbitt R W, Nebel O, Hergt J M, Campbell I H, O'Neill H S C, Van Kranendonk M, Rhodri Davies D (2016) Petrogenesis and geochemistry of Archean Komatiites. Journal of Petrology 57:147-184.

Srivastava D C, Pradhan A (1995) Late brittle tectonics in a Precambrian ductile belt: evidence from brittle structures in the Singhbhum Shear Zone, eastern India. Journal of Structural Geology 17:385-396.

Srivastava R, Söderlund U, Ernst R E, Mondal S K, Samal A K (2019) Precambrian mafic dyke swarms in the Singhbhum Craton (eastern India) and their links with dyke swarms of the eastern Dharwar Craton (southern India). Precambrian Research 329:5-17.

Staddon L G, Parkinson I J, Cavosie A J, Elliott T, Valley J W, Fournelle J, Shirey S B (2021) Detrital chromite from Jack Hills, Western Australia: signatures of metamorphism and constraints on provenance. Journal of Petrology 62(12):egab052.

Staude S, Oelze M, Markl G (2022) Multi-stage sulfide evolution of the Moran Ni sulfide ore, Kambalda, Western Australia: insights into the dynamics of ore forming processes of komatiite-hosted deposits. Miner Deposita 57:889-909.

Stevenson D J (1981) Models of the Earth's core. Science 214(4521):611-619.

Stowe C W (1997) Chromite deposits of the Shurugwi greenstone belt, Zimbabwe. In: Stowe C W (ed) Evolution of chromium ore fields. Hutchinson Ross Publication, New York, pp. 71-88.

Sun S S, Nesbitt R W (1978) Petrogenesis of Archean Ultrabasic and Basic Volcanics: Evidence from REE elements. Contrib Mineral Petrol 65:301-325.

Sunilkumar T, Parthasarathy R, Palrecha M, Shah V, Sinha K, Krishna Rao N (1996) Chemical age of detrital zircons from the basal quartz-pebble conglomerate of Dhanjori Group, Singbhum craton, Eastern India. Current Science 71:482-486.

Tait J, Zimmermann U, Miyazaki T, Presnyakov S, Chang Q, Mukhopadhyay J, Sergeev S (2011) Possible juvenile Palaeoarchaean TTG magmatism in eastern India and its constraints for the evolution of the Singhbhum craton. Geological Magazine 148:340-347.

Tanaka T, Togashi S, Kamioka H, Amakawa H, Kagami H, Hamamoto T, Yuhara M, Orihashi Y, Yoneda S, Shimizu H, Kunimaru T, Takahashi K, Yanagi T, Nakano T, Fujimaki H, Shinjo R, Asahara Y, Tanimizu M, Dragusanu C (2000) JNdi-1: A neodymium isotopic reference in consistency with LaJolla neodymium. Chemical Geology 168(3-4):279-281.

Taylor S R, McLennan S M 1985 The Continental Crust: its Composition and Evolution. Blackwell Scientific Publication, Oxford, p.312.

Tomlinson K Y, Stevenson R K, Hughes D J, Hall R P, Thurston P C, Henry P (1998) The Red Lake greenstone belt, Superior Province: evidence of plume-related magmatism at 3 Ga and evidence of an older enriched source. Precambrian Research 89(1-2):59-76.

Törmänen T, Konnunaho J P, Hanski E, Moilanen M, Heikura P (2016) The Paleoproterozoic komatiite-hosted PGE mineralization at Lomalampi, Central Lapland greenstone belt, northern Finland. Mineralium Deposita 51:411-430.

Tredoux M, Davies G, McDonald I, Lindsay N M (1995) The fractionation of platinum-group elements in magmatic systems, with the suggestion of a novel causal mechanism. South African Journal of Geology 98(2):157-167.

Tushipokla, Jayananda M (2013) Geochemical constraints on komatiite volcanism from Sargur Group Nagamangala greenstone belt, western Dharwar craton, southern India: implications for Mesoarchean mantle evolution and continental growth. Geoscience Frontiers 4:321-340.

Upadhyay D, Chattopadhyay S, Kooijman E, Mezger K, Berndt J (2014) Magmatic and metamorphic history of Paleoarchean tonalite-trondhjemite-granodiorite (TTG) suite from the Singhbhum craton, eastern India. Precambrian research 252:180-190.

Van Kranendonk M J, Smithies R H, Hickman A H, Wingate M T, Bodorkos S (2010) Evidence for Mesoarchean (˜3.2 Ga) rifting of the Pilbara Craton: The missing link in an early Precambrian Wilson cycle. Precambrian Research 177(1-2):145-161.

Van Kranendonk M J, Smithies R H, Griffin W L, Huston D L, Hickman A H, Champion D C, Anhaeusser C R, Pirajno F (2015) Making it thick: a volcanic plateau origin of Palaeoarchean continental lithosphere of the Pilbara and Kaapvaal cratons. Geological Society of London, Special Publication 389:83-111.

Viljoen M, Viljoen R (1969) Evidence for the existence of a mobile extrusive peridotitic magma from the Komati Formation of the Onverwacht Group.

Upper mantle project: Geological Society of South Africa Special Publication 2:87-112.

Vohra C P, Dasgupta S, Paul D K, Bishui P, Gupta S, Guha S (1991) Rb-Sr chronology and petrochemistry of granitoids from the south-eastern part of the Singhbhum craton, Orissa. Journal of the Geological Society of India 38:5-22.

Wainwright A N, El Atrassi F, Debaille V, Mattielli N (2019) Geochemistry and petrogenesis of Archean mafic rocks from the Amsaga area, West African craton, Mauritania. Precambrian Research 324:208-219.

Walter M J (1998) Melting of garnet peridotite and the origin of komatiite and depleted lithosphere. Journal of Petrology 39:29-60.

Wang D, Guo J, Huang G, Scheltens M (2015) The Neoarchean ultramafic–mafic complex in the Yinshan Block, North China Craton: Magmatic monitor of development of Archean lithospheric mantle. Precambrian Research 270:80-99.

Waterton P, Pearson D G, Kjarsgaard B, Hulbert L, Locock A, Parman S, Davis B (2017) Age, origin, and thermal evolution of the ultra-fresh ~ 1.9 Ga Winnipegosis Komatiites, Manitoba, Canada. Lithos 268-271:114-130.

Waterton P, Mungall J, Graham Pearson D (2021) The komatiite-mantle platinum-group element paradox. Geochimica et Cosmochimica Acta 313:214-242.

Whitney D L, Evans B W (2010) Abbreviations for names of rock-forming minerals. American Mineralogist 95:185-187.

Wilson A H, Shirey S B, Carlson R W (2003) Archaean ultra-depleted komatiites formed by hydrous melting of cratonic mantle. Nature 423(6942):858-861.

Wilson A H (2019) The late-Paleoarchean ultra-depleted Commondale komatiites: Earth's hottest lavas and consequences for eruption. Journal of Petrology 60(8):1575-1620.

Wittig N, Webb M, Pearson D G, Dale C W, Ottley C J, Hutchison M, Jensen S M, Luguet A (2010) Formation of the North Atlantic Craton: timing and mechanisms constrained from Re-Os isotope and PGE data of peridotite xenoliths from S.W. Greenland. Chemical Geology 276:166-187.

Wylie A G, Candela P A, Burke T M (1987) Compositional zoning in unusual Zn-rich chromite from Sykesville district of Maryland and its bearing on the origin of “ferrichromit”. American Mineralogist, 72, 413-422.

Xie Q, Kerrich R (1994) Silicate-perovskite and majorite signature komatiites from the Archean Abitibi Greenstone Belt: Implications for early mantle differentiation and stratification. Journal of Geophysical Research: Solid Earth 99(B8):15799-15812.

Xie H, Hofmann A, Hegner E, Wilson A, Wan Y, Liu D (2012) Zircon SHRIMP dating confirms a Palaeo- to Mesoarchaean supracrustal terrain in the Kaapvaal craton, southern Africa. Gondwana Research 21:818-828.

Yadav P K, Pradhan U K, Mukherjee A, Sar R N, Sahoo P, Das M (2015) Basic characterization of Kapili komatiite from Badampahar-Gorumahishani schist belt, Singhbhum Craton, Odisha, India. Indian Journal of Geoscience 69:1-12.

Yu H, Zhang H-F, Zou H-B, Yang Y-H (2019) Minor and trace element variations in chromite from the Songshugou dunites, North Qinling Orogen: evidence for amphibolite-facies metamorphism. Lithos 328-329:146-158.

Zaccarini F, Economou-Eliopoulos M, Kiseleva O, Garuti G, Tsikouras B, Pushkarev E, Idrus A (2022) Platinum Group Elements (PGE) Geochemistry and Mineralogy of Low Economic Potential (Rh-Pt-Pd)-Rich Chromitites from Ophiolite Complexes. Minerals 12(12):1565.

Zhang J, Herzberg C (1994) Melting experiments on anhydrous peridotite KLB-1 from 5.0 to 22.5 GPa. Journal of Geophysical Research 99:17729.

Zhou M -F, Kerrich R (1992) Morphology and composition of chromite in komatiites from the Belingwe Greenstone Belt, Zimbabwe. Canadian Mineralogist 30:303-317.

Zhou X, Banerjee R, Reisberg L C, Mondal S K (2023) Highly siderophile elements and Re-Os systematics of Archean komatiitic rocks in the Gorumahisani greenstone belt, Singhbhum craton, India. Goldschmidt conference, Lyon, France.

Zindler A, Hart S R, Frey F A, Jakobsson SP (1979) Nd and Sr isotope ratios and rare earth element abundances in Reykjanes Peninsula basalts evidence for mantle heterogeneity beneath Iceland. Earth and Planetary Science Letters 45(2):249-262.

Appendix 1 EPMA major and minor elements composition (wt.%) of komatiitic chromites, magnetites, and ilmenites from the Gorumahishani greenstone belt

Sample number	MIC/16/39	MIC/16/39	MIC/16/39	MIC/16/39	MIC/16/39	MIC/16/39	MIC/16/39	MIC/16/39	MIC/16/39	MIC/16/39	MIC/16/39	MIC/16/39	MIC/16/39
Location	Tua Dungri	Tua Dungri	Tua Dungri	Tua Dungri	Tua Dungri	Tua Dungri	Tua Dungri	Tua Dungri	Tua Dungri	Tua Dungri	Tua Dungri	Tua Dungri	Tua Dungri
EPMA point	35 / 4 .	35 / 5 .	35 / 6 .	35 / 12 .	35 / 13 .	35 / 14 .	35 / 15 .	35 / 16 .	35 / 17 .	35 / 18 .	43 / 1 .	45 / 5 .	45 / 6 .
Mineral Type	Chromite Type-I core	Chromite Type-I core	Chromite Type-I core	Chromite Type-I core	Chromite Type-I core	Chromite Type-I core	Chromite Type-I core	Chromite Type-I core	Chromite Type-I core	Chromite Type-I core	Chromite Type-I core	Chromite Type-I core	Chromite Type-I core
Al_2O_3	17.23	17.45	17.53	17.45	18.15	17.69	17.98	18.38	17.79	17.62	18.01	17.37	17.88
MnO	1.17	1.03	1.25	1.17	1.01	1.12	1.17	1.07	1.02	1.06	1.03	1.34	1.11
TiO_2	0.21	0.22	0.23	0.22	0.22	0.25	0.20	0.20	0.21	0.20	0.20	0.21	0.19
Cr_2O_3	44.46	44.73	44.45	44.54	44.82	45.08	44.95	44.89	45.05	44.77	45.27	44.56	45.03
MgO	2.61	2.50	2.33	2.50	2.96	3.06	3.18	3.01	3.04	2.60	3.30	2.00	2.73
SiO_2	0.26	0.25	0.27	0.30	0.26	0.24	0.24	0.26	0.25	0.29	0.29	0.26	0.21
Fe_2O_3	1.78	1.33	1.37	1.72	1.08	0.88	1.46	0.84	1.32	1.22	1.00	1.43	1.33
FeO	29.77	30.11	30.27	30.24	29.78	29.19	29.14	29.55	29.51	29.99	29.16	30.65	29.98
V_2O_3	0.27	0.26	0.29	0.28	0.26	0.26	0.23	0.24	0.27	0.24	0.24	0.27	0.28
NiO	0.11	0.14	0.15	0.13	0.14	0.14	0.19	0.18	0.20	0.15	0.19	0.12	0.15
ZnO													
CoO													
Na_2O													
K_2O													
CaO													
Total	97.87	98.01	98.14	98.55	98.67	97.91	98.74	98.62	98.66	98.13	98.68	98.21	98.89
Cation													
Al	5.587	5.648	5.671	5.621	5.801	5.700	5.740	5.867	5.692	5.687	5.744	5.632	5.720
Mn	0.272	0.239	0.290	0.270	0.231	0.259	0.267	0.247	0.235	0.245	0.235	0.311	0.256
Ti	0.043	0.045	0.047	0.045	0.044	0.052	0.041	0.040	0.042	0.041	0.040	0.043	0.040
Cr	9.668	9.710	9.646	9.623	9.608	9.742	9.623	9.614	9.670	9.693	9.685	9.695	9.663
Mg	1.069	1.025	0.954	1.019	1.195	1.249	1.284	1.216	1.229	1.062	1.330	0.820	1.104
Si	0.073	0.068	0.074	0.081	0.071	0.066	0.066	0.070	0.069	0.079	0.078	0.070	0.057
Fe^{3+}	0.369	0.274	0.284	0.353	0.220	0.181	0.297	0.172	0.270	0.251	0.203	0.297	0.271
Fe^{2+}	6.848	6.914	6.949	6.910	6.752	6.673	6.599	6.693	6.700	6.867	6.600	7.054	6.805
V	0.048	0.047	0.053	0.050	0.047	0.047	0.042	0.042	0.048	0.043	0.044	0.050	0.051
Ni	0.024	0.030	0.034	0.027	0.030	0.031	0.041	0.040	0.045	0.033	0.041	0.027	0.034

Zn													
Co													
Na													
K													
Ca													
Total	24.000	24.000	24.000	24.000	24.000	24.000	24.000	24.000	24.000	24.000	24.000	24.000	24.000
Mg#	0.14	0.13	0.12	0.13	0.15	0.16	0.16	0.15	0.16	0.13	0.17	0.10	0.14
Cr#	0.63	0.63	0.63	0.63	0.62	0.63	0.63	0.62	0.63	0.63	0.63	0.63	0.63
Fe^{3+}/R^{3+}	0.02	0.02	0.02	0.02	0.01	0.01	0.02	0.01	0.02	0.02	0.01	0.02	0.02

Sample number	MIC/16/39	MIC/16/39	MIC/16/39	MIC/16/39	MIC/16/39	MIC/16/39	MIC/16/39	MIC/16/39	MIC/16/39	MIC/16/39	MIC/16/39	MIC/16/39	MIC/16/39
Location	Tua Dungri	Tua Dungri	Tua Dungri	Tua Dungri	Tua Dungri	Tua Dungri	Tua Dungri	Tua Dungri	Tua Dungri	Tua Dungri	Tua Dungri	Tua Dungri	Tua Dungri
EPMA point	45 / 7 .	45 / 8 .	45 / 9 .	45 / 10 .	45 / 11 .	45 / 12 .	45 / 13 .	45 / 14 .	45 / 15 .	46 / 9 .	46 / 10 .	46 / 11 .	46 / 12 .
Mineral Type	Chromite Type-I core	Chromite Type-I core	Chromite Type-I core	Chromite Type-I core	Chromite Type-I core	Chromite Type-I core	Chromite Type-I core	Chromite Type-I core	Chromite Type-I core	Chromite Type-I core	Chromite Type-I core	Chromite Type-I core	Chromite Type-I core
Al_2O_3	17.61	17.94	17.86	17.83	17.70	17.84	17.62	17.33	17.36	17.29	17.68	17.53	17.68
MnO	1.08	0.98	1.05	1.02	1.12	0.94	1.08	1.15	1.21	1.17	1.00	1.06	1.01
TiO_2	0.18	0.20	0.22	0.21	0.21	0.22	0.19	0.21	0.22	0.21	0.20	0.19	0.21
Cr_2O_3	45.11	45.04	45.15	45.17	45.20	45.17	45.11	44.98	44.76	44.90	45.29	45.22	45.21
MgO	2.92	3.00	3.20	3.27	3.32	3.17	3.11	2.96	2.68	2.67	3.13	3.17	3.37
SiO_2	0.26	0.25	0.29	0.27	0.25	0.28	0.25	0.27	0.25	0.25	0.30	0.27	0.26
Fe_2O_3	1.59	1.04	1.25	1.27	1.44	1.58	1.57	1.37	1.92	1.63	1.57	1.12	1.16
FeO	29.61	29.64	29.42	29.19	28.85	29.66	29.32	29.21	29.93	29.64	29.48	29.13	28.88
V_2O_3	0.23	0.27	0.27	0.26	0.25	0.27	0.26	0.24	0.28	0.21	0.22	0.28	0.27
NiO	0.15	0.13	0.15	0.20	0.26	0.18	0.16	0.13	0.08	0.10	0.19	0.15	0.18
ZnO													
CoO													
Na_2O													
K_2O													
CaO													
Total	98.75	98.47	98.87	98.70	98.60	99.31	98.67	97.86	98.69	98.07	99.04	98.12	98.23
Cation													
Al	5.641	5.747	5.696	5.693	5.657	5.669	5.640	5.600	5.580	5.590	5.635	5.638	5.669
Mn	0.249	0.225	0.240	0.233	0.256	0.215	0.247	0.267	0.280	0.271	0.230	0.245	0.233

Ti	0.036	0.042	0.045	0.043	0.044	0.044	0.039	0.044	0.045	0.043	0.040	0.040	0.042
Cr	9.692	9.679	9.658	9.674	9.692	9.628	9.684	9.751	9.650	9.738	9.686	9.755	9.723
Mg	1.181	1.215	1.291	1.322	1.344	1.273	1.261	1.211	1.089	1.094	1.260	1.289	1.367
Si	0.072	0.068	0.077	0.073	0.067	0.075	0.069	0.075	0.069	0.067	0.080	0.074	0.070
Fe^{3+}	0.326	0.212	0.254	0.259	0.295	0.321	0.321	0.282	0.395	0.337	0.319	0.231	0.237
Fe^{2+}	6.728	6.737	6.657	6.613	6.544	6.688	6.658	6.698	6.826	6.800	6.669	6.646	6.569
V	0.042	0.048	0.049	0.047	0.045	0.049	0.046	0.043	0.050	0.038	0.040	0.050	0.048
Ni	0.033	0.028	0.032	0.042	0.056	0.040	0.034	0.029	0.018	0.022	0.041	0.033	0.040
Zn													
Co													
Na													
K													
Ca													
Total	24.000	24.000	24.000	24.000	24.000	24.000	24.000	24.000	24.000	24.000	24.000	24.000	24.000
Mg#	0.15	0.15	0.16	0.17	0.17	0.16	0.16	0.15	0.14	0.14	0.16	0.16	0.17
Cr#	0.63	0.63	0.63	0.63	0.63	0.63	0.63	0.64	0.63	0.64	0.63	0.63	0.63
Fe^{3+}/R^{3+}	0.02	0.01	0.02	0.02	0.02	0.02	0.02	0.02	0.03	0.02	0.02	0.01	0.02

Sample number	MIC/16/39	MIC/16/39	MIC/16/39	MIC/16/39	MIC/16/39	MIC/16/39	MIC/16/39	MIC/16/39	MIC/16/39	MIC/16/39	MIC/16/39	MIC/16/39	MIC/16/39
Location	Tua Dungri	Tua Dungri	Tua Dungri	Tua Dungri	Tua Dungri	Tua Dungri	Tua Dungri	Tua Dungri	Tua Dungri	Tua Dungri	Tua Dungri	Tua Dungri	Tua Dungri
EPMA point	46 / 13 .	46 / 14 .	46 / 15 .	46 / 16 .	46 / 17 .	53 / 1 .	6 / 1 .	7 / 1 .	8 / 1 .	9 / 1 .	10 / 1 .	11 / 1 .	24 / 1 .
Mineral Type	Chromite Type-I core	Chromite Type-I core	Chromite Type-I core	Chromite Type-I core	Chromite Type-I core	Chromite Type-I core	Chromite Type-I core	Chromite Type-I core	Chromite Type-I core	Chromite Type-I core	Chromite Type-I core	Chromite Type-I core	Chromite Type-I core
Al_2O_3	17.88	17.71	17.89	17.82	17.63	17.61	17.61	17.53	17.59	17.53	17.41	17.81	17.14
MnO	1.09	0.99	1.01	1.07	1.04	1.11	1.06	0.79	0.78	1.03	0.99	1.06	1.11
TiO_2	0.20	0.18	0.20	0.19	0.18	0.22	0.11	0.08	0.08	0.12	0.11	0.10	0.10
Cr_2O_3	45.26	45.40	45.28	45.16	45.25	44.55	44.61	45.05	46.84	45.39	45.51	44.76	45.77
MgO	3.28	3.35	3.29	3.25	3.14	2.50	3.04	3.27	3.60	3.71	3.75	3.00	3.47
SiO_2	0.23	0.24	0.24	0.26	0.25	0.23	0.09	0.11	0.10	0.13	0.13	0.11	0.12
Fe_2O_3	1.44	1.41	1.21	1.63	1.86	1.30	4.00	3.84	2.87	3.82	4.04	3.71	3.87
FeO	29.19	28.92	29.11	29.31	29.43	30.02	27.30	27.60	27.23	26.88	26.96	27.70	27.09
V_2O_3	0.28	0.24	0.24	0.26	0.24	0.27	0.15	0.15	0.15	0.17	0.12	0.14	0.15
NiO	0.19	0.23	0.14	0.15	0.15	0.13	0.28	0.00	0.20	0.15	0.20	0.13	0.10
ZnO							2.09	1.98	2.11	1.81	1.63	1.93	2.04

CoO							0.13	0.23	0.08	0.21	0.18	0.17	0.02
Na_2O							0.04	0.00	0.00	0.01	0.00	0.03	0.01
K_2O							0.00	0.00	0.00	0.00	0.00	0.00	0.00
CaO							0.00	0.00	0.03	0.00	0.00	0.01	0.01
Total	99.05	98.68	98.60	99.09	99.18	97.94	100.52	100.63	101.65	100.93	101.02	100.66	101.00
Cation													
Al	5.690	5.656	5.714	5.671	5.615	5.699	5.566	5.527	5.479	5.493	5.454	5.614	5.387
Mn	0.250	0.228	0.232	0.245	0.239	0.259	0.241	0.179	0.175	0.232	0.222	0.240	0.250
Ti	0.041	0.037	0.040	0.039	0.036	0.045	0.022	0.016	0.016	0.023	0.022	0.020	0.021
Cr	9.663	9.726	9.703	9.641	9.669	9.671	9.456	9.530	9.790	9.541	9.563	9.468	9.651
Mg	1.319	1.355	1.328	1.308	1.266	1.024	1.217	1.303	1.420	1.471	1.484	1.196	1.379
Si	0.062	0.064	0.065	0.071	0.068	0.064	0.025	0.030	0.026	0.034	0.034	0.029	0.033
Fe^{3+}	0.292	0.287	0.247	0.331	0.379	0.268	0.807	0.774	0.572	0.764	0.808	0.746	0.777
Fe^{2+}	6.591	6.553	6.599	6.617	6.653	6.893	6.122	6.175	6.020	5.978	5.992	6.197	6.041
V	0.050	0.043	0.042	0.046	0.043	0.048	0.026	0.026	0.025	0.030	0.021	0.024	0.026
Ni	0.042	0.051	0.031	0.032	0.032	0.028	0.061	0.000	0.042	0.031	0.042	0.028	0.021
Zn							0.414	0.390	0.411	0.354	0.320	0.381	0.402
Co							0.028	0.050	0.016	0.045	0.038	0.036	0.004
Na							0.015	0.001	0.000	0.004	0.000	0.014	0.006
K							0.000	0.000	0.000	0.000	0.000	0.000	0.000
Ca							0.000	0.000	0.008	0.000	0.000	0.004	0.004
Total	24.000	24.000	24.000	24.000	24.000	24.000	24.000	24.000	24.000	24.000	24.000	24.000	24.000
Mg#	0.17	0.17	0.17	0.17	0.16	0.13	0.17	0.17	0.19	0.20	0.20	0.16	0.19
Cr#	0.63	0.63	0.63	0.63	0.63	0.63	0.63	0.63	0.64	0.63	0.64	0.63	0.64
Fe^{3+}/R^{3+}	0.02	0.02	0.02	0.02	0.02	0.02	0.05	0.05	0.04	0.05	0.05	0.05	0.05

Sample number	MIC/16/39	MIC/16/39	MIC/16/39	MIC/16/39	MIC/16/39	SHB/18/24	SHB/18/24	SHB/18/24	SHB/18/24	SHB/18/24	SHB/18/24	SHB/18/24	SHB/18/24
Location	Tua Dungri	Tua Dungri	Tua Dungri	Tua Dungri	Tua Dungri	Kapili	Kapili	Kapili	Kapili	Kapili	Kapili	Kapili	Kapili
EPMA point	28 / 1 .	16 / 1 .	32 / 1 .	69 / 1 .	76 / 1 .	29 / 1 .	30 / 1 .	31 / 1 .	32 / 1 .	33 / 1 .	43 / 1 .	44 / 1 .	45 / 1 .
Mineral Type	Chromite Type-I core	Chromite Small type-I core	Chromite Small type-I core	Chromite Small type-I core	Chromite Small type-I core	Chromite Type-II core	Chromite Type-II core	Chromite Type-II core	Chromite Type-II core	Chromite Type-II core	Chromite Type-II core	Chromite Type-II core	Chromite Type-II core
Al_2O_3	17.32	0.23	0.96	0.37	0.37	4.03	5.05	5.16	5.01	3.62	2.80	4.40	4.44
MnO	1.02	1.42	1.74	1.41	1.43	0.83	0.94	0.54	0.77	0.94	3.85	0.93	0.82

TiO_2	0.08	0.26	0.79	0.65	0.67	0.37	0.37	0.34	0.37	0.32	1.51	0.35	0.38
Cr_2O_3	44.16	33.04	40.62	38.63	38.40	56.37	56.65	56.23	55.84	49.70	45.59	55.64	56.22
MgO	3.57	0.35	0.04	0.12	0.20	2.57	2.93	3.00	3.13	2.35	1.25	2.56	2.58
SiO_2	0.12	0.27	0.23	0.23	0.25	0.12	0.10	0.14	0.15	0.07	0.16	0.15	0.11
Fe_2O_3	3.94	32.24	22.96	25.73	26.18	7.62	5.97	5.54	6.63	13.67	14.94	6.62	6.27
FeO	26.42	29.80	30.94	30.62	30.70	27.28	26.71	26.66	26.37	26.95	25.51	26.67	27.33
V_2O_3	0.14	0.24	0.30	0.27	0.28	0.11	0.08	0.09	0.07	0.12	0.16	0.13	0.11
NiO	0.00	0.24	0.26	0.34	0.28								
ZnO	1.98					1.68	1.41	1.56	1.58	1.34	2.41	1.75	1.17
CoO	0.14												
Na_2O	0.00												
K_2O	0.00												
CaO	0.00												
Total	98.88	98.10	98.85	98.38	98.76	100.97	100.19	99.26	99.93	99.07	98.17	99.19	99.43
Cation													
Al	5.541	0.084	0.343	0.134	0.132	1.356	1.696	1.747	1.687	1.247	0.986	1.500	1.509
Mn	0.234	0.370	0.446	0.365	0.369	0.199	0.228	0.130	0.187	0.232	0.976	0.229	0.200
Ti	0.017	0.061	0.181	0.150	0.153	0.079	0.079	0.073	0.079	0.070	0.339	0.075	0.083
Cr	9.479	8.026	9.735	9.339	9.241	12.718	12.767	12.773	12.604	11.494	10.783	12.743	12.833
Mg	1.443	0.159	0.019	0.056	0.090	1.092	1.244	1.284	1.333	1.023	0.559	1.107	1.111
Si	0.033	0.084	0.071	0.071	0.077	0.034	0.028	0.041	0.043	0.019	0.049	0.044	0.033
Fe^{3+}	0.805	7.452	5.238	5.919	5.996	1.636	1.280	1.198	1.424	3.010	3.364	1.443	1.361
Fe^{2+}	5.997	7.655	7.843	7.828	7.815	6.510	6.369	6.405	6.296	6.592	6.382	6.460	6.599
V	0.025	0.049	0.060	0.055	0.057	0.021	0.015	0.018	0.014	0.023	0.031	0.025	0.021
Ni	0.000	0.059	0.063	0.083	0.070								
Zn	0.396					0.354	0.296	0.330	0.333	0.290	0.531	0.374	0.249
Co	0.030												
Na	0.000												
K	0.001												
Ca	0.000												
Total	24.000	24.000	24.000	24.000	24.000	24.000	24.000	24.000	24.000	24.000	24.000	24.000	24.000
Mg#	0.19	0.02	0.00	0.01	0.01	0.14	0.16	0.17	0.17	0.13	0.08	0.15	0.14
Cr#	0.63	0.99	0.97	0.99	0.99	0.90	0.88	0.88	0.88	0.90	0.92	0.89	0.89
Fe^{3+}/R^{3+}	0.05	0.48	0.34	0.38	0.39	0.10	0.08	0.08	0.09	0.19	0.22	0.09	0.09

Sample number	SHB/18/24	SHB/19-12/82	SHB/19-12/82	SHB/18/36	SHB/18/36	SHB/18/36	SHB/18/36	SHB/18/36	SHB/18/36	SHB/18/36	SHB/18/36	SHB/18/36	SHB/18/36

Location	Kapili	Kapili	Kapili	Kapili	Kapili	Kapili	Kapili	Kapili	Kapili	Kapili	Kapili	Kapili	Kapili
EPMA point	46 / 1 .	103 / 1 .	118 / 1 .	7 / 1 .	8 / 1 .	9 / 1 .	16 / 1 .	17 / 1 .	18 / 1 .	19 / 1 .	20 / 1 .	21 / 1 .	194 / 1 .
Mineral	Chromite	Chromite	Chromite	Chromite	Chromite	Chromite	Chromite	Chromite	Chromite	Chromite	Chromite	Chromite	Chromite
Type	Type-II	Type-II	Type-II	Type-II	Type-II	Type-II	Type-II	Type-II	Type-II	Type-II	Type-II	Type-II	Type-II
	core	core	core	core	core	core	core	core	core	core	core	core	core
Al_2O_3	3.13	3.69	4.68	4.26	4.60	4.92	5.20	4.63	4.91	3.55	9.14	4.91	4.54
MnO	0.89	0.61	0.71	2.10	0.47	3.00	3.84	0.55	4.19	4.38	4.40	3.75	0.59
TiO_2	0.40	0.44	0.37	0.60	0.51	0.52	0.55	0.50	0.56	0.50	2.50	0.47	0.53
Cr_2O_3	55.26	55.00	56.79	55.24	57.78	55.83	50.91	56.91	53.88	52.28	41.19	53.28	58.06
MgO	2.18	2.23	2.79	3.63	6.07	2.62	1.63	6.12	1.35	1.24	0.84	1.72	6.24
SiO_2	0.16	0.17	0.08	0.05	0.12	0.08	0.10	0.10	0.12	0.12	0.06	0.09	0.13
Fe_2O_3	8.30	7.27	5.92	7.55	7.02	6.56	10.82	6.95	6.95	10.17	9.19	8.37	7.09
FeO	27.62	26.69	26.54	25.01	23.47	26.18	26.42	23.17	25.57	26.23	27.91	26.29	22.91
V_2O_3	0.05	0.07	0.09	0.05	0.04	0.10	0.03	0.12	0.13	0.10	0.67	0.08	0.07
NiO		0.12	0.06										0.14
ZnO	1.00	1.96	1.61	0.30	0.28	0.37	0.79	0.13	1.66	0.44	3.03	0.64	0.37
CoO		0.00	0.19										0.23
Na_2O		0.08	0.01										0.00
K_2O		0.00	0.00										0.00
CaO		0.00	0.00										0.00
Total	98.99	98.33	99.83	98.79	100.36	100.19	100.28	99.18	99.31	99.01	98.91	99.59	100.87
Cation													
Al	1.082	1.278	1.581	1.449	1.510	1.657	1.763	1.536	1.686	1.231	3.108	1.675	1.480
Mn	0.220	0.153	0.173	0.512	0.110	0.726	0.937	0.131	1.033	1.092	1.074	0.919	0.137
Ti	0.088	0.098	0.080	0.129	0.107	0.111	0.119	0.106	0.122	0.111	0.541	0.102	0.111
Cr	12.793	12.777	12.882	12.593	12.718	12.606	11.581	12.661	12.407	12.164	9.396	12.196	12.711
Mg	0.953	0.978	1.195	1.558	2.521	1.117	0.698	2.567	0.586	0.543	0.360	0.741	2.575
Si	0.045	0.050	0.024	0.015	0.032	0.022	0.030	0.027	0.034	0.036	0.018	0.027	0.035
Fe^{3+}	1.828	1.607	1.277	1.638	1.470	1.410	2.343	1.472	1.523	2.251	1.996	1.824	1.477
Fe^{2+}	6.763	6.559	6.369	6.031	5.465	6.252	6.357	5.451	6.228	6.456	6.735	6.364	5.304
V	0.010	0.014	0.017	0.010	0.008	0.020	0.005	0.022	0.024	0.020	0.127	0.016	0.013
Ni		0.027	0.013										0.031
Zn	0.217	0.425	0.340	0.064	0.058	0.078	0.167	0.027	0.357	0.096	0.645	0.136	0.075
Co		0.000	0.043										0.050
Na		0.034	0.004										0.000
K		0.000	0.000										0.000
Ca		0.000	0.001										0.000

Total	24.000	24.000	24.000	24.000	24.000	24.000	24.000	24.000	24.000	24.000	24.000	24.000	24.000
Mg#	0.12	0.13	0.16	0.21	0.32	0.15	0.10	0.32	0.09	0.08	0.05	0.10	0.33
Cr#	0.92	0.91	0.89	0.90	0.89	0.88	0.87	0.89	0.88	0.91	0.75	0.88	0.90
Fe^{3+}/R^{3+}	0.12	0.10	0.08	0.10	0.09	0.09	0.15	0.09	0.10	0.14	0.14	0.12	0.09

Sample number	SHB/18/36	SHB/18/36	SHB/18/36	MIC/16/39	MIC/16/39	MIC/16/39	MIC/16/39	MIC/16/39	MIC/16/39	MIC/16/39	MIC/16/39	MIC/16/39	MIC/16/39
Location	Kapili	Kapili	Kapili	Tua Dungri	Tua Dungri	Tua Dungri	Tua Dungri	Tua Dungri	Tua Dungri	Tua Dungri	Tua Dungri	Tua Dungri	Tua Dungri
EPMA point	195 / 1 .	196 / 1 .	197 / 1 .	35 / 3 .	35 / 7 .	35 / 8 .	35 / 11 .	35 / 19 .	45 / 3 .	45 / 4 .	45 / 16 .	45 / 17 .	45 / 19 .
Mineral	Chromite	Chromite	Chromite	Ferrit-chromit	Ferrit-chromi	Ferrit-chromi	Ferrit-chromi	Ferrit-chromi	Ferrit-chromi	Ferrit-chromi	Ferrit-chromi	Ferrit-chromi	Ferrit-chromi
Type	Type-III core	Type-III core	Type-III core	Type-I inner rim	Type-I inner rim	Type-I inner rim	Type-I inner rim	Type-I inner rim	Type-I inner rim	Type-I inner rim	Type-I inner rim	Type-I inner rim	Type-I inner rim
Al_2O_3	4.12	4.28	5.77	1.35	3.24	0.69	0.85	1.37	0.44	1.27	9.95	0.95	0.15
MnO	3.62	3.97	3.66	1.52	1.50	1.37	1.57	1.48	1.41	1.68	1.56	1.52	1.20
TiO_2	0.68	0.56	0.78	0.92	0.69	0.89	0.86	0.85	0.64	0.79	0.38	0.64	0.23
Cr_2O_3	55.13	53.79	52.62	40.00	39.45	39.07	39.35	39.58	38.32	40.27	42.54	39.59	26.89
MgO	1.84	0.88	1.48	0.05	0.15	0.09	0.18	0.03	0.19	0.08	0.56	0.09	0.39
SiO_2	0.15	0.08	0.12	0.23	0.09	0.24	0.23	0.25	0.20	0.22	0.24	0.20	0.27
Fe_2O_3	8.02	9.19	6.20	22.96	20.37	24.46	24.54	23.53	26.36	22.82	10.82	24.29	39.68
FeO	26.76	26.23	26.31	31.29	30.09	31.10	30.88	31.27	30.65	30.78	31.14	30.80	30.16
V_2O_3	0.08	0.13	0.20	0.30	0.23	0.29	0.27	0.26	0.26	0.28	0.25	0.28	0.25
NiO	0.13	0.00	0.16	0.29	0.30	0.31	0.29	0.29	0.23	0.34	0.21	0.22	0.38
ZnO	0.39	2.44	1.27										
CoO	0.17	0.12	0.02										
Na_2O	0.01	0.00	0.01										
K_2O	0.00	0.00	0.00										
CaO	0.01	0.02	0.03										
Total	101.09	101.67	98.60	98.89	96.12	98.53	99.01	98.92	98.70	98.54	97.64	98.58	99.60
Cation													
Al	1.389	1.448	1.981	0.480	1.176	0.249	0.302	0.488	0.157	0.455	3.408	0.341	0.055
Mn	0.877	0.966	0.903	0.389	0.390	0.355	0.402	0.380	0.365	0.431	0.385	0.392	0.309
Ti	0.146	0.121	0.171	0.208	0.159	0.204	0.196	0.194	0.146	0.180	0.082	0.146	0.053
Cr	12.465	12.210	12.129	9.564	9.595	9.410	9.417	9.464	9.228	9.665	9.780	9.520	6.456
Mg	0.784	0.377	0.643	0.022	0.071	0.042	0.081	0.015	0.086	0.034	0.241	0.039	0.177
Si	0.042	0.022	0.036	0.069	0.028	0.073	0.069	0.076	0.062	0.068	0.068	0.060	0.083

Fe^{3+}	1.726	1.985	1.361	5.224	4.717	5.608	5.591	5.354	6.041	5.213	2.366	5.559	9.067
Fe^{2+}	6.399	6.298	6.414	7.914	7.743	7.923	7.818	7.907	7.806	7.813	7.573	7.833	7.658
V	0.015	0.024	0.039	0.059	0.046	0.059	0.053	0.052	0.053	0.057	0.048	0.056	0.050
Ni	0.030	0.000	0.037	0.071	0.075	0.075	0.071	0.072	0.056	0.084	0.049	0.055	0.092
Zn	0.083	0.516	0.273										
Co	0.039	0.027	0.004										
Na	0.005	0.000	0.003										
K	0.000	0.001	0.000										
Ca	0.002	0.006	0.008										
Total	24.000	24.000	24.000	24.000	24.000	24.000	24.000	24.000	24.000	24.000	24.000	24.000	24.000
Mg#	0.11	0.06	0.09	0.00	0.01	0.01	0.01	0.00	0.01	0.00	0.03	0.00	0.02
Cr#	0.90	0.89	0.86	0.95	0.89	0.97	0.97	0.95	0.98	0.96	0.74	0.97	0.99
Fe^{3+}/R^{3+}	0.11	0.13	0.09	0.34	0.30	0.37	0.37	0.35	0.39	0.34	0.15	0.36	0.58

Sample number	MIC/16/39	MIC/16/39	MIC/16/39	MIC/16/39	MIC/16/39	MIC/16/39	MIC/16/39	MIC/16/39	MIC/16/39	MIC/16/39	MIC/16/39	MIC/16/39	SHB/18/24
Location	Tua Dungri	Tua Dungri	Tua Dungri	Tua Dungri	Tua Dungri	Tua Dungri	Tua Dungri	Tua Dungri	Tua Dungri	Tua Dungri	Tua Dungri	Tua Dungri	Kapili
EPMA point	46 / 2 .	46 / 3 .	46 / 4 .	46 / 5 .	46 / 8 .	46 / 19 .	46 / 20 .	4 / 1 .	5 / 1 .	12 / 1 .	21 / 1 .	27 / 1 .	28 / 1 .
Mineral	Ferrit-chromit	Ferrit-chromit	Ferrit-chromit	Ferrit-chromit	Ferrit-chromit	Ferrit-chromit	Ferrit-chromit	Ferrit-chromit	Ferrit-chromit	Ferrit-chromit	Ferrit-chromit	Ferrit-chromit	Ferrit-chromit
Type	Type-I inner rim	Type-I inner rim	Type-I inner rim	Type-I inner rim	Type-I inner rim	Type-I inner rim	Type-I inner rim	Type-I inner rim	Type-I inner rim	Type-I inner rim	Type-I inner rim	Type-I inner rim	Type-II inner rim
Al_2O_3	0.39	0.49	0.23	0.23	2.23	1.40	0.21	1.21	3.45	0.67	1.03	0.68	1.72
MnO	1.44	1.54	1.24	1.35	1.57	1.51	1.36	1.36	1.34	1.31	1.48	1.10	1.55
TiO_2	0.59	0.72	0.31	0.31	0.61	0.71	0.25	0.59	0.53	0.53	0.61	0.56	2.79
Cr_2O_3	38.16	39.44	31.47	30.83	38.95	39.97	30.91	39.30	40.62	38.19	39.78	38.68	27.03
MgO	0.21	0.02	0.33	0.34	0.15	0.00	0.68	0.45	0.58	0.40	0.52	0.42	1.55
SiO_2	0.25	0.20	0.28	0.27	0.12	0.21	1.46	0.09	0.13	0.09	0.17	0.08	0.04
Fe_2O_3	26.62	24.79	34.25	35.39	23.54	23.03	31.62	25.36	21.81	26.79	25.39	27.16	32.26
FeO	30.62	30.88	30.29	30.31	30.57	30.94	30.81	29.42	29.89	29.26	29.25	29.74	30.19
V_2O_3	0.29	0.28	0.26	0.28	0.25	0.29	0.25	0.08	0.11	0.10	0.14	0.10	0.33
NiO	0.31	0.22	0.26	0.36	0.26	0.34	0.20	0.00	0.09	0.10	0.24	0.02	0.00
ZnO								0.67	0.57	0.52	0.88	0.70	
CoO								0.00	0.14	0.13	0.00	0.16	
Na_2O								0.06	0.00	0.03	0.09	0.03	
K_2O								0.01	0.00	0.00	0.00	0.01	

CaO								0.00	0.00	0.01	0.00	0.00	
Total	98.87	98.59	98.93	99.66	98.25	98.38	97.75	98.59	99.24	98.14	99.60	99.41	97.46
Cation													
Al	0.141	0.176	0.084	0.082	0.796	0.502	0.077	0.431	1.206	0.241	0.366	0.240	0.618
Mn	0.371	0.398	0.321	0.346	0.402	0.389	0.354	0.349	0.336	0.339	0.376	0.280	0.400
Ti	0.135	0.165	0.071	0.070	0.140	0.161	0.057	0.134	0.118	0.123	0.139	0.128	0.637
Cr	9.174	9.512	7.588	7.381	9.331	9.608	7.482	9.417	9.542	9.231	9.438	9.230	6.499
Mg	0.093	0.011	0.150	0.155	0.067	0.002	0.310	0.203	0.256	0.180	0.234	0.187	0.701
Si	0.075	0.061	0.086	0.082	0.038	0.063	0.447	0.027	0.038	0.028	0.051	0.024	0.013
Fe^{3+}	6.092	5.690	7.859	8.066	5.367	5.269	7.285	5.784	4.875	6.163	5.733	6.169	7.385
Fe^{2+}	7.786	7.877	7.725	7.676	7.746	7.867	7.890	7.456	7.425	7.482	7.341	7.507	7.680
V	0.058	0.057	0.052	0.056	0.051	0.057	0.050	0.015	0.021	0.021	0.028	0.019	0.066
Ni	0.075	0.053	0.064	0.087	0.063	0.082	0.050	0.000	0.022	0.025	0.057	0.004	0.000
Zn								0.150	0.125	0.116	0.196	0.155	
Co								0.000	0.033	0.031	0.000	0.038	
Na								0.030	0.002	0.015	0.042	0.015	
K								0.003	0.000	0.000	0.000	0.002	
Ca								0.000	0.000	0.005	0.000	0.000	
Total	24.000	24.000	24.000	24.000	24.000	24.000	24.000	24.000	24.000	24.000	24.000	24.000	24.000
Mg#	0.01	0.00	0.02	0.02	0.01	0.00	0.04	0.03	0.03	0.02	0.03	0.02	0.08
Cr#	0.98	0.98	0.99	0.99	0.92	0.95	0.99	0.96	0.89	0.97	0.96	0.97	0.91
Fe^{3+}/R^{3+}	0.40	0.37	0.51	0.52	0.35	0.34	0.49	0.37	0.31	0.39	0.37	0.39	0.51

Sample number	SHB/19-12/82	SHB/19-12/82	SHB/19-12/82	SHB/19-12/82	SHB/18/36	SHB/18/36	SHB/18/36	SHB/18/36	SHB/18/36	SHB/18/36	SHB/18/36	SHB/18/36	MIC/16/39
Location	Kapili	Kapili	Kapili	Kapili	Kapili	Kapili	Kapili	Kapili	Kapili	Kapili	Kapili	Kapili	Tua Dungri
EPMA point	102 / 1 .	104 / 1 .	117 / 1 .	119 / 1 .	4 / 1 .	6 / 1 .	10 / 1 .	15 / 1 .	22 / 1 .	187 / 1 .	191 / 1 .	192 / 1 .	13 / 1 .
Mineral	Ferrit-chromit	Ferrit-chromit	Ferrit-chromit	Ferrit-chromit	Al rich Cr-spinel	Al rich Cr-spinel	Al rich Cr-spinel	Al rich Cr-spinel	Al rich Cr-spinel	Al rich Cr-spinel	Al rich Cr-spinel	Al rich Cr-spinel	Chr mag-netite
Type	Type-II inner rim	Type-II inner rim	Type-II inner rim	Type-II inner rim	Type-III inner rims	Type-III inner rims	Type-III inner rims	Type-III inner rims	Type-III inner rims	Type-III inner rims	Type-III inner rims	Type-III inner rims	Type-I outer rim
Al_2O_3	0.88	0.97	1.34	1.32	21.15	17.23	14.98	12.65	16.99	14.40	19.28	15.14	0.05
MnO	1.41	1.72	2.50	1.22	3.64	3.48	3.13	2.90	3.30	3.94	3.10	3.99	0.32
TiO_2	1.83	1.47	2.33	2.62	6.42	6.72	5.92	5.41	5.67	6.68	4.50	7.46	0.18
Cr_2O_3	16.92	17.95	20.06	20.37	26.38	26.64	28.38	24.27	28.96	23.89	23.47	25.19	9.09
MgO	0.67	0.56	0.51	1.21	2.86	1.96	1.31	0.81	2.37	1.14	1.64	1.11	0.49

SiO_2	0.04	0.04	0.00	0.04	0.03	0.03	0.06	0.07	0.05	0.07	0.12	0.04	0.27
Fe_2O_3	44.71	43.65	39.93	40.25	2.10	4.22	5.58	14.88	4.96	10.62	8.99	5.84	57.08
FeO	29.95	28.63	28.33	30.33	34.15	34.26	32.76	31.93	33.01	32.15	29.80	32.72	29.86
V_2O_3	0.36	0.35	0.37	0.37	1.61	1.79	1.63	1.23	1.46	1.47	1.38	1.65	0.17
NiO	0.40	0.41	0.40	0.45						0.29	0.15	0.20	0.43
ZnO	0.00	0.56	1.45	0.17	1.64	2.77	3.97	4.61	1.91	4.42	5.48	4.48	
CoO	0.19	0.27	0.18	0.12						0.08	0.00	0.32	
Na_2O	0.00	0.00	0.00	0.04						0.00	0.02	0.04	
K_2O	0.00	0.00	0.00	0.00						0.00	0.00	0.00	
CaO	0.00	0.01	0.01	0.00						0.03	0.01	0.01	
Total	97.36	96.59	97.38	98.50	99.99	99.09	97.72	98.75	98.69	99.17	97.95	98.19	97.95
Cation													
Al	0.323	0.356	0.487	0.472	6.617	5.577	4.996	4.260	5.505	4.769	6.292	5.033	0.019
Mn	0.369	0.456	0.654	0.313	0.818	0.810	0.751	0.702	0.769	0.938	0.727	0.952	0.085
Ti	0.426	0.347	0.543	0.598	1.282	1.388	1.259	1.162	1.173	1.411	0.936	1.581	0.042
Cr	4.146	4.436	4.906	4.890	5.537	5.785	6.350	5.483	6.296	5.306	5.138	5.618	2.239
Mg	0.307	0.260	0.233	0.547	1.132	0.803	0.554	0.343	0.970	0.477	0.678	0.466	0.226
Si	0.012	0.012	0.000	0.012	0.009	0.008	0.018	0.020	0.015	0.019	0.033	0.012	0.085
Fe^{3+}	10.431	10.272	9.297	9.196	0.420	0.872	1.188	3.198	1.027	2.245	1.872	1.239	13.383
Fe^{2+}	7.763	7.485	7.329	7.702	7.582	7.870	7.752	7.628	7.592	7.554	6.901	7.718	7.779
V	0.074	0.073	0.075	0.074	0.282	0.324	0.304	0.232	0.266	0.273	0.253	0.308	0.035
Ni	0.100	0.102	0.099	0.110						0.066	0.034	0.045	0.107
Zn	0.000	0.130	0.330	0.039	0.322	0.561	0.829	0.973	0.388	0.916	1.121	0.933	
Co	0.047	0.067	0.045	0.028						0.017	0.000	0.072	
Na	0.000	0.000	0.000	0.017						0.000	0.009	0.019	
K	0.000	0.000	0.000	0.000						0.000	0.001	0.001	
Ca	0.000	0.004	0.002	0.001						0.009	0.004	0.004	
Total	24.000	24.000	24.000	24.000	24.000	24.000	24.000	24.000	24.000	24.000	24.000	24.000	24.000
Mg#	0.04	0.03	0.03	0.07	0.13	0.09	0.07	0.04	0.11	0.06	0.09	0.06	0.03
Cr#	0.93	0.93	0.91	0.91	0.46	0.51	0.56	0.56	0.53	0.53	0.45	0.53	0.99
Fe^{3+}/R^{3+}	0.70	0.68	0.63	0.63	0.03	0.07	0.09	0.25	0.08	0.18	0.14	0.10	0.86

Sample number	MIC/16/39	MIC/16/39	MIC/16/39	MIC/16/39	MIC/16/39	MIC/16/39	MIC/16/39	MIC/16/39	MIC/16/39	MIC/16/39	MIC/16/39	MIC/16/39	MIC/16/39
Location	Tua Dungri	Tua Dungri	Tua Dungri	Tua Dungri	Tua Dungri	Tua Dungri	Tua Dungri	Tua Dungri	Tua Dungri	Tua Dungri	Tua Dungri	Tua Dungri	Tua Dungri
EPMA point	14 / 1 .	15 / 1 .	17 / 1 .	21 / 1 .	35 / 2 .	35 / 9 .	35 / 10 .	35 / 20 .	37 / 1 .	44 / 1 .	45 / 2 .	45 / 20 .	46 / 1 .

Mineral	Chr mag-netite	Chr mag-netite	Chr mag-netite	Chr mag-netite	Chr mag-netite	Chr mag-netite	Chr mag-netite	Chr mag-netite	Chr mag-netite	Chr mag-netite	Chr mag-netite	Chr mag-netite	Chr mag-netite
Type	Type-I outer rim	Type-I outer rim	Type-I outer rim	Type-I outer rim	Type-I outer rim	Type-I outer rim	Type-I outer rim	Type-I outer rim	Type-I outer rim	Type-I outer rim	Type-I outer rim	Type-I outer rim	Type-I outer rim
Al_2O_3	0.10	0.07	0.08	0.06	0.17	0.19	0.18	0.18	0.10	0.13	0.08	0.05	0.05
MnO	0.70	0.47	0.65	0.48	0.93	1.01	0.98	0.87	0.65	0.95	0.69	0.41	0.31
TiO_2	0.18	0.15	0.17	0.16	0.25	0.27	0.31	0.23	0.23	0.21	0.21	0.18	0.14
Cr_2O_3	16.09	10.65	16.29	11.39	23.77	23.82	21.90	20.22	15.10	22.35	17.62	10.53	7.31
MgO	0.34	0.51	0.43	0.49	0.40	0.42	0.39	0.37	0.46	0.41	0.48	0.52	0.45
SiO_2	0.21	0.28	0.32	0.27	0.29	0.29	0.27	0.31	0.27	0.27	0.29	0.28	0.23
Fe_2O_3	49.54	55.27	49.95	55.02	41.80	42.34	43.94	45.24	51.12	44.29	49.68	57.01	59.03
FeO	29.75	29.59	30.16	29.98	30.12	30.17	29.99	29.89	30.01	30.19	30.41	30.55	29.75
V_2O_3	0.21	0.21	0.22	0.20	0.28	0.25	0.24	0.25	0.25	0.24	0.20	0.20	0.16
NiO	0.32	0.52	0.33	0.32	0.32	0.37	0.47	0.47	0.50	0.41	0.40	0.33	0.45
ZnO													
CoO													
Na_2O													
K_2O													
CaO													
Total	97.44	97.71	98.61	98.36	98.34	99.12	98.67	98.02	98.70	99.45	100.06	100.06	97.88
Cation													
Al	0.036	0.024	0.031	0.021	0.062	0.067	0.065	0.065	0.038	0.047	0.029	0.018	0.020
Mn	0.184	0.124	0.170	0.127	0.243	0.261	0.254	0.227	0.170	0.244	0.179	0.107	0.081
Ti	0.043	0.034	0.039	0.038	0.058	0.061	0.072	0.052	0.054	0.049	0.047	0.042	0.033
Cr	3.974	2.628	3.971	2.790	5.786	5.753	5.319	4.946	3.679	5.385	4.230	2.536	1.805
Mg	0.158	0.236	0.199	0.225	0.186	0.190	0.177	0.172	0.211	0.187	0.218	0.235	0.210
Si	0.066	0.088	0.097	0.083	0.091	0.087	0.083	0.097	0.083	0.083	0.088	0.086	0.071
Fe^{3+}	11.644	12.974	11.590	12.829	9.683	9.732	10.158	10.537	11.856	10.159	11.352	13.072	13.867
Fe^{2+}	7.770	7.719	7.777	7.769	7.754	7.706	7.705	7.736	7.735	7.697	7.721	7.785	7.768
V	0.043	0.043	0.046	0.040	0.057	0.050	0.049	0.051	0.051	0.049	0.039	0.039	0.033
Ni	0.081	0.130	0.082	0.079	0.080	0.092	0.117	0.117	0.123	0.101	0.097	0.080	0.112
Zn													
Co													
Na													
K													
Ca													
Total	24.000	24.000	24.000	24.000	24.000	24.000	24.000	24.000	24.000	24.000	24.000	24.000	24.000

Mg#	0.02	0.03	0.02	0.03	0.02	0.02	0.02	0.02	0.03	0.02	0.03	0.03	0.03
Cr#	0.99	0.99	0.99	0.99	0.99	0.99	0.99	0.99	0.99	0.99	0.99	0.99	0.99
Fe^{3+}/R^{3+}	0.74	0.83	0.74	0.82	0.62	0.63	0.65	0.68	0.76	0.65	0.73	0.84	0.88

Sample number	MIC/16/39	MIC/16/39	MIC/16/39	MIC/16/39	MIC/16/39	MIC/16/39	MIC/16/39	MIC/16/39	MIC/16/39	MIC/16/39	MIC/16/39	SHB/18/24	SHB/18/24
Location	Tua Dungri	Tua Dungri	Tua Dungri	Tua Dungri	Tua Dungri	Tua Dungri	Tua Dungri	Tua Dungri	Tua Dungri	Tua Dungri	Tua Dungri	Kapili	Kapili
EPMA point	46 / 6 .	46 / 7 .	70 / 1 .	77 / 1 .	1 / 1 .	2 / 1 .	3 / 1 .	13 / 1 .	22 / 1 .	26 / 1 .	29 / 1 .	26 / 1 .	27 / 1 .
Mineral	Chr mag-netite	Chr mag-netite	Chr mag-netite	Chr mag-netite	Chr mag-netite	Chr mag-netite	Chr mag-netite	Chr mag-netite	Chr mag-netite	Chr mag-netite	Chr mag-netite	Chr mag-netite	Chr mag-netite
Type	Type-I outer rim	Type-I outer rim	Type-I outer rim	Type-I outer rim	Type-I outer rim	Type-I outer rim	Type-I outer rim	Type-I outer rim	Type-I outer rim	Type-I outer rim	Type-I outer rim	Type-II outer rim	Type-II outer rim
Al_2O_3	0.18	0.19	0.06	0.09	0.00	0.02	0.06	0.05	0.02	0.00	0.06	0.04	0.53
MnO	1.02	1.01	0.56	0.62	0.13	0.14	0.66	0.15	0.40	0.20	0.52	0.27	0.81
TiO_2	0.26	0.24	0.18	0.19	0.00	0.00	0.07	0.01	0.03	0.03	0.05	0.38	0.99
Cr_2O_3	23.33	24.20	10.90	14.82	5.03	9.78	17.36	8.60	13.87	8.98	16.31	4.69	9.95
MgO	0.42	0.44	0.29	0.45	0.07	0.11	0.27	0.12	0.17	0.04	0.09	0.15	0.50
SiO_2	0.30	0.30	0.47	0.30	0.01	0.03	0.23	0.05	0.03	0.41	0.00	0.00	0.03
Fe_2O_3	42.90	42.67	54.71	51.85	62.28	57.70	48.82	58.52	53.15	57.33	50.11	62.12	54.49
FeO	30.16	30.43	30.37	30.18	29.76	29.76	29.17	29.69	29.58	30.50	29.32	30.82	30.09
V_2O_3	0.23	0.24	0.19	0.19	0.06	0.07	0.08	0.05	0.07	0.06	0.06	0.17	0.25
NiO	0.36	0.38	0.37	0.38	0.31	0.24	0.04	0.37	0.28	0.39	0.15		
ZnO					0.00	0.22	0.38	0.14	0.27	0.00	0.31	0.00	0.34
CoO					0.00	0.11	0.00	0.14	0.00	0.04	0.12		
Na_2O					0.06	0.07	0.00	0.00	0.00	0.00	0.00		
K_2O					0.00	0.00	0.01	0.00	0.01	0.00	0.00		
CaO					0.11	0.07	0.30	0.02	0.00	0.01	0.02		
Total	99.15	100.09	98.10	99.07	97.82	98.32	97.43	97.90	97.89	97.98	97.11	98.64	97.97
Cation													
Al	0.065	0.066	0.020	0.032	0.000	0.006	0.023	0.018	0.008	0.000	0.022	0.015	0.193
Mn	0.263	0.258	0.146	0.161	0.034	0.037	0.175	0.041	0.106	0.052	0.138	0.072	0.214
Ti	0.059	0.054	0.043	0.045	0.000	0.000	0.015	0.001	0.008	0.006	0.012	0.088	0.231
Cr	5.634	5.786	2.681	3.598	1.249	2.408	4.285	2.128	3.424	2.218	4.057	1.153	2.443
Mg	0.190	0.197	0.133	0.208	0.033	0.052	0.127	0.054	0.081	0.020	0.041	0.068	0.232
Si	0.093	0.091	0.148	0.091	0.002	0.009	0.071	0.016	0.010	0.127	0.000	0.000	0.009
Fe^{3+}	9.860	9.710	12.801	11.981	14.713	13.525	11.471	13.788	12.488	13.481	11.861	14.548	12.735

Fe^{2+}	7.704	7.696	7.896	7.752	7.813	7.753	7.616	7.775	7.725	7.970	7.712	8.020	7.815
V	0.046	0.049	0.039	0.039	0.011	0.014	0.016	0.010	0.015	0.012	0.012	0.036	0.050
Ni	0.087	0.092	0.093	0.093	0.078	0.060	0.011	0.094	0.071	0.099	0.037		
Zn					0.000	0.052	0.086	0.031	0.063	0.000	0.072	0.000	0.079
Co					0.000	0.027	0.000	0.034	0.000	0.010	0.029		
Na					0.029	0.034	0.000	0.001	0.000	0.002	0.000		
K					0.000	0.000	0.002	0.000	0.002	0.000	0.000		
Ca					0.038	0.025	0.101	0.008	0.000	0.003	0.007		
Total	24.000	24.000	24.000	24.000	24.000	24.000	24.000	24.000	24.000	24.000	24.000	24.000	24.000
Mg#	0.02	0.02	0.02	0.03	0.00	0.01	0.02	0.01	0.01	0.00	0.01	0.01	0.03
Cr#	0.99	0.99	0.99	0.99	1.00	1.00	0.99	0.99	1.00	1.00	0.99	0.99	0.93
Fe^{3+}/R^{3+}	0.63	0.62	0.83	0.77	0.92	0.85	0.73	0.87	0.78	0.86	0.74	0.93	0.83

Sample number	SHB/18/24	SHB/18/24	SHB/19-12/82	SHB/19-12/82	SHB/19-12/82	SHB/19-12/82	SHB/19-12/82	SHB/19-12/82	SHB/19-12/82	SHB/19-12/82	SHB/19-12/82	SHB/19-12/82	SHB/19-12/82
Location	Kapili	Kapili	Kapili	Kapili	Kapili	Kapili	Kapili	Kapili	Kapili	Kapili	Kapili	Kapili	Kapili
EPMA point	34 / 1 .	35 / 1 .	100 / 1 .	101 / 1 .	105 / 1 .	106 / 1 .	115 / 1 .	116 / 1 .	120 / 1 .	121 / 1 .	122 / 1 .	123 / 1 .	124 / 1 .
Mineral	Chr mag-netite	Chr mag-netite	Chr mag-netite	Chr mag-netite	Chr mag-netite	Chr mag-netite	Chr mag-netite	Chr mag-netite	Chr mag-netite	Chr mag-netite	Chr mag-netite	Chr mag-netite	Chr mag-netite
Type	Type-II outer rim	Type-II outer rim	Type-II outer rim	Type-II outer rim	Type-II outer rim	Type-II outer rim	Type-II outer rim	Type-II outer rim	Type-II outer rim	Type-II outer rim	Type-II outer rim	Type-II outer rim	Type-II outer rim
Al_2O_3	0.55	0.04	0.12	0.41	0.25	0.06	0.48	0.71	0.61	0.42	0.34	0.34	0.20
MnO	1.13	0.19	0.41	0.84	0.96	0.24	0.76	1.54	1.01	0.75	0.55	0.46	0.28
TiO_2	1.22	0.14	0.22	0.61	0.59	0.32	0.61	1.65	1.14	0.63	0.39	0.29	0.28
Cr_2O_3	10.55	4.75	5.02	8.55	10.84	5.11	9.04	13.26	11.21	8.69	6.82	6.84	5.98
MgO	0.47	0.15	1.05	0.27	0.46	0.18	0.34	0.66	0.57	0.31	0.26	0.29	0.28
SiO_2	0.00	0.00	0.77	0.03	0.29	0.00	0.01	0.00	0.02	0.04	0.00	0.03	0.02
Fe_2O_3	54.47	63.03	58.60	55.76	52.86	60.87	56.40	50.15	53.03	55.93	59.07	59.43	60.10
FeO	30.95	31.25	28.76	29.41	29.09	30.11	29.90	29.18	29.91	29.43	30.08	29.93	30.18
V_2O_3	0.31	0.30	0.27	0.31	0.27	0.27	0.33	0.32	0.33	0.32	0.33	0.29	0.31
NiO			0.54	0.52	0.38	0.45	0.57	0.68	0.53	0.27	0.47	0.62	0.36
ZnO	0.00	0.00	0.00	0.00	0.17	0.00	0.08	0.63	0.00	0.54	0.00	0.00	0.00
CoO			0.07	0.00	0.16	0.05	0.07	0.02	0.11	0.15	0.10	0.08	0.00
Na_2O			0.07	0.08	0.03	0.00	0.01	0.00	0.01	0.02	0.00	0.00	0.05
K_2O			0.00	0.00	0.00	0.00	0.00	0.00	0.01	0.00	0.00	0.00	0.00
CaO			0.03	0.03	0.01	0.01	0.03	0.02	0.00	0.00	0.00	0.00	0.00
Total	99.63	99.85	95.91	96.82	96.34	97.67	98.61	98.81	98.48	97.49	98.42	98.59	98.04

Cation													
Al	0.197	0.014	0.045	0.154	0.094	0.023	0.173	0.173	0.223	0.155	0.125	0.122	0.074
Mn	0.292	0.049	0.109	0.225	0.256	0.065	0.200	0.400	0.263	0.199	0.146	0.120	0.074
Ti	0.280	0.032	0.052	0.144	0.141	0.075	0.142	0.379	0.264	0.149	0.092	0.067	0.065
Cr	2.545	1.155	1.254	2.128	2.706	1.269	2.211	3.214	2.734	2.150	1.676	1.678	1.476
Mg	0.213	0.071	0.494	0.127	0.214	0.082	0.156	0.303	0.262	0.147	0.120	0.134	0.130
Si	0.000	0.000	0.242	0.009	0.093	0.000	0.002	0.000	0.006	0.012	0.000	0.009	0.006
Fe^{3+}	12.511	14.584	13.945	13.219	12.564	14.389	13.126	11.575	12.305	13.179	13.814	13.871	14.116
Fe^{2+}	7.900	8.034	7.605	7.749	7.683	7.911	7.733	7.486	7.712	7.706	7.817	7.764	7.879
V	0.062	0.061	0.056	0.064	0.056	0.056	0.067	0.065	0.066	0.065	0.067	0.059	0.064
Ni			0.138	0.131	0.097	0.113	0.143	0.169	0.132	0.067	0.118	0.155	0.090
Zn	0.000	0.000	0.000	0.000	0.040	0.000	0.018	0.142	0.000	0.124	0.000	0.000	0.000
Co			0.016	0.000	0.040	0.012	0.017	0.004	0.026	0.037	0.024	0.020	0.000
Na			0.034	0.040	0.012	0.000	0.003	0.000	0.005	0.011	0.000	0.000	0.025
K			0.000	0.000	0.000	0.000	0.000	0.000	0.003	0.000	0.001	0.000	0.000
Ca			0.011	0.009	0.004	0.005	0.009	0.006	0.000	0.000	0.000	0.000	0.000
Total	24.000	24.000	24.000	24.000	24.000	24.000	24.000	24.000	24.000	24.000	24.000	24.000	24.000
Mg#	0.03	0.01	0.06	0.02	0.03	0.01	0.02	0.04	0.03	0.02	0.02	0.02	0.02
Cr#	0.93	0.99	0.97	0.93	0.97	0.98	0.93	0.95	0.92	0.93	0.93	0.93	0.95
Fe^{3+}/R^{3+}	0.82	0.93	0.91	0.85	0.82	0.92	0.85	0.77	0.81	0.85	0.88	0.89	0.90

Sample number	SHB/19-12/82	SHB/18/36	SHB/18/36	SHB/18/36	SHB/18/36	SHB/19-12/39	SHB/19-12/39	SHB/19-12/39	MIC/16/33	MIC/16/33	MIC/16/33	MIC/16/33	MIC/16/33
Location	Kapili	Kapili	Kapili	Kapili	Kapili	Maha-rajgunj	Maha-rajgunj	Maha-rajgunj	Tua Dungri	Tua Dungri	Tua Dungri	Tua Dungri	Tua Dungri
EPMA point	125 / 1 .	23 / 1 .	186 / 1 .	189 / 1 .	193 / 1 .	241 / 1 .	243 / 1 .	244 / 1 .	8 / 1 .	9 / 1 .	13 / 1 .	14 / 1 .	15 / 1 .
Mineral	Chr mag-netite	Chr mag-netite	Chr mag-netite	Chr mag-netite	Chr mag-netite	Ferrit-chromit	Ferrit-chromit	Ferrit-chromit	Chr mag-netite	Chr mag-netite	Chr mag-netite	Chr mag-netite	Chr mag-netite
Type	Type-II outer rim	Type-III outer rim	Type-III outer rim	Type-III outer rim	Type-III outer rim	Type- IV	Type- IV	Type- IV	Type-V	Type-V	Type-V	Type-V	Type-V
Al_2O_3	0.03	1.09	0.25	0.02	0.01	2.56	2.40	1.74	0.03	0.00	0.03	0.02	0.00
MnO	0.25	2.35	1.00	0.54	0.31	3.48	2.84	3.13	0.05	0.00	0.02	0.10	0.28
TiO_2	0.13	0.22	0.11	0.50	1.34	1.20	1.75	0.63	0.08	0.08	0.00	0.75	0.10
Cr_2O_3	4.97	22.73	11.02	7.21	2.83	42.10	35.83	34.20	2.19	3.17	4.04	4.10	6.15
MgO	0.29	0.13	0.16	0.13	0.18	0.43	0.54	0.32	0.62	0.05	0.11	0.06	0.22
SiO_2	0.24	0.10	0.12	0.10	0.07	0.03	0.12	0.12	0.16	0.17	0.06	0.24	0.13
Fe_2O_3	61.94	41.63	56.18	58.89	62.62	17.61	22.03	28.47	63.30	61.93	61.97	59.63	59.41

FeO	30.26	27.90	29.08	29.62	31.57	28.57	29.02	27.68	28.93	29.84	29.58	30.65	29.77
V_2O_3	0.26	0.24	0.13	0.05	0.18	0.92	0.87	0.55	0.15	0.12	0.03	0.22	0.25
NiO	0.47		0.32	0.46	0.34	0.27	0.29	0.20	0.39	0.34	0.27	0.46	0.41
ZnO	0.19	1.16	0.75	0.28	0.00	1.45	1.29	1.61					
CoO	0.00		0.03	0.07	0.00	0.00	0.11	0.04					
Na_2O	0.04		0.06	0.02	0.03	0.00	0.00	0.00					
K_2O	0.01		0.00	0.00	0.00	0.00	0.00	0.00					
CaO	0.02		0.01	0.03	0.01	0.00	0.00	0.06					
Total	99.12	97.52	99.22	97.90	99.49	98.61	97.08	98.75	95.89	95.72	96.12	96.22	96.73
Cation													
Al	0.010	0.397	0.092	0.007	0.005	0.908	0.866	0.623	0.011	0.002	0.012	0.009	0.002
Mn	0.066	0.616	0.260	0.142	0.080	0.885	0.736	0.804	0.015	0.001	0.006	0.027	0.076
Ti	0.031	0.052	0.025	0.119	0.311	0.272	0.402	0.143	0.018	0.019	0.001	0.180	0.025
Cr	1.213	5.575	2.684	1.784	0.689	10.004	8.661	8.193	0.551	0.805	1.020	1.033	1.540
Mg	0.135	0.060	0.075	0.059	0.082	0.192	0.248	0.145	0.294	0.024	0.053	0.027	0.103
Si	0.075	0.030	0.036	0.030	0.022	0.008	0.038	0.037	0.051	0.055	0.018	0.075	0.043
Fe^{3+}	14.404	9.719	13.022	13.878	14.530	3.983	5.068	6.493	15.206	14.967	14.908	14.311	14.166
Fe^{2+}	7.821	7.238	7.491	7.756	8.142	7.181	7.420	7.014	7.723	8.013	7.907	8.173	7.888
V	0.053	0.049	0.027	0.011	0.037	0.182	0.175	0.111	0.031	0.026	0.007	0.046	0.053
Ni	0.117		0.080	0.115	0.084	0.065	0.071	0.048	0.100	0.088	0.068	0.119	0.105
Zn	0.043	0.265	0.171	0.064	0.000	0.322	0.290	0.360					
Co	0.000		0.007	0.018	0.000	0.000	0.026	0.010					
Na	0.020		0.028	0.009	0.016	0.000	0.000	0.000					
K	0.004		0.000	0.000	0.000	0.000	0.000	0.000					
Ca	0.007		0.003	0.008	0.004	0.000	0.000	0.021					
Total	24.000	24.000	24.000	24.000	24.000	24.000	24.000	24.000	24.000	24.000	24.000	24.000	24.000
Mg#	0.02	0.01	0.01	0.01	0.01	0.03	0.03	0.02	0.04	0.00	0.01	0.00	0.01
Cr#	0.99	0.93	0.97	1.00	0.99	0.92	0.91	0.93	0.98	1.00	0.99	0.99	1.00
Fe^{3+}/R^{3+}	0.92	0.62	0.82	0.89	0.95	0.27	0.35	0.42	0.96	0.95	0.94	0.93	0.90

Sample number	MIC/16/33	MIC/16/33	MIC/16/33	MIC/16/33	MIC/16/33	MIC/16/33	MIC/16/33	MIC/16/35	MIC/16/35	MIC/16/35	MIC/16/35	MIC/16/35	MIC/16/35
Location	Tua Dungri	Tua Dungri	Tua Dungri	Tua Dungri	Tua Dungri	Tua Dungri	Tua Dungri	Tua Dungri	Tua Dungri	Tua Dungri	Tua Dungri	Tua Dungri	Tua Dungri
EPMA point	20 / 1 .	27 / 1 .	28 / 1 .	29 / 1 .	30 / 1 .	31 / 1 .	35 / 1 .	38 / 1 .	39 / 1 .	40 / 1 .	41 / 1 .	46 / 1 .	49 / 1 .
Mineral	Chr mag-netite	Chr mag-netite	Chr mag-netite	Chr mag-netite	Chr mag-netite	Chr mag-netite	Chr mag-netite	Chr mag-netite	Chr mag-netite	Chr mag-netite	Chr mag-netite	Chr mag-netite	Chr mag-netite

Type	Type-V	Type-V	Type-V	Type-V	Type-V	Type-V	Type-V	Type-V	Type-V	Type-V	Type-V	Type-V	Type-V
Al_2O_3	0.02	0.02	0.02	0.03	0.01	0.03	0.01	0.35	0.35	0.34	0.38	0.36	0.38
MnO	0.36	0.38	0.03	0.57	0.01	0.06	0.10	0.78	0.80	0.85	0.19	0.94	0.11
TiO_2	0.13	0.12	0.19	0.22	0.11	0.08	0.08	0.32	0.12	0.39	1.07	0.11	0.11
Cr_2O_3	6.51	6.54	3.67	6.96	1.50	4.48	4.88	9.30	9.20	9.19	3.36	10.40	1.29
MgO	0.08	0.14	0.08	0.09	0.17	0.11	0.11	0.12	0.13	0.10	0.09	0.11	0.06
SiO_2	0.23	0.18	0.19	0.24	0.11	0.17	0.22	0.01	0.00	0.01	0.14	0.04	0.01
Fe_2O_3	58.67	58.24	60.94	58.40	63.79	61.57	61.02	57.01	56.77	56.71	60.80	54.53	65.71
FeO	30.35	29.40	29.80	30.36	29.60	30.20	30.09	29.66	29.08	29.50	30.84	28.67	30.20
V_2O_3	0.36	0.18	0.15	0.33	0.14	0.16	0.17	0.00	0.00	0.00	0.00	0.00	0.00
NiO	0.43	0.44	0.43	0.38	0.37	0.40	0.53	0.24	0.24	0.28	0.29	0.21	0.25
ZnO													
CoO													
Na_2O													
K_2O													
CaO													
Total	97.16	95.65	95.49	97.57	95.81	97.26	97.20	97.77	96.68	97.36	97.14	95.37	98.12
Cation													
Al	0.008	0.007	0.006	0.010	0.003	0.009	0.005	0.128	0.129	0.124	0.141	0.136	0.141
Mn	0.097	0.104	0.007	0.151	0.003	0.015	0.026	0.206	0.214	0.226	0.050	0.255	0.030
Ti	0.030	0.030	0.046	0.052	0.028	0.020	0.018	0.075	0.028	0.092	0.254	0.026	0.026
Cr	1.625	1.658	0.934	1.727	0.381	1.117	1.218	2.300	2.300	2.282	0.837	2.634	0.318
Mg	0.037	0.069	0.037	0.044	0.079	0.052	0.051	0.054	0.063	0.048	0.040	0.051	0.029
Si	0.073	0.059	0.061	0.076	0.034	0.055	0.068	0.003	0.001	0.002	0.043	0.014	0.004
Fe^{3+}	13.934	14.044	14.750	13.802	15.403	14.624	14.498	13.417	13.513	13.405	14.428	13.149	15.481
Fe^{2+}	8.010	7.879	8.016	7.973	7.944	7.971	7.945	7.757	7.692	7.750	8.133	7.682	7.908
V	0.075	0.038	0.032	0.068	0.030	0.033	0.035	0.000	0.000	0.000	0.000	0.000	0.000
Ni	0.110	0.113	0.110	0.096	0.096	0.103	0.134	0.061	0.060	0.072	0.074	0.053	0.063
Zn													
Co													
Na													
K													
Ca													
Total	24.000	24.000	24.000	24.000	24.000	24.000	24.000	24.000	24.000	24.000	24.000	24.000	24.000
Mg#	0.00	0.01	0.00	0.01	0.01	0.01	0.01	0.01	0.01	0.01	0.00	0.01	0.00
Cr#	1.00	1.00	0.99	0.99	0.99	0.99	1.00	0.95	0.95	0.95	0.86	0.95	0.69
Fe^{3+}/R^{3+}	0.90	0.89	0.94	0.89	0.98	0.93	0.92	0.85	0.85	0.85	0.94	0.83	0.97

Sample number	MIC/16/35	MIC/16/35	MIC/16/35	MIC/16/35	MIC/16/35	MIC/16/35	MIC/16/36	MIC/16/36	MIC/16/36	MIC/16/36	MIC/16/36	MIC/16/36	MIC/16/36
Location	Tua Dungri	Tua Dungri	Tua Dungri	Tua Dungri	Tua Dungri	Tua Dungri	Tua Dungri	Tua Dungri	Tua Dungri	Tua Dungri	Tua Dungri	Tua Dungri	Tua Dungri
EPMA point	50 / 1 .	54 / 1 .	56 / 1 .	57 / 1 .	66 / 1 .	67 / 1 .	68 / 1 .	69 / 1 .	70 / 1 .	71 / 1 .	72 / 1 .	73 / 1 .	74 / 1 .
Mineral	Chr mag-netite	Chr mag-netite	Chr mag-netite	Chr mag-netite	Chr mag-netite	Chr mag-netite	Chr mag-netite	Chr mag-netite	Chr mag-netite	Chr mag-netite	Chr mag-netite	Chr mag-netite	Chr mag-netite
Type	Type-V	Type-V	Type-V	Type-V	Type-V	Type-V	Type-V	Type-V	Type-V	Type-V	Type-V	Type-V	Type-V
Al_2O_3	0.33	0.34	0.35	0.35	0.37	0.38	0.37	0.37	0.37	0.36	0.36	0.36	0.35
MnO	0.80	1.07	0.85	0.91	0.04	0.07	0.16	0.54	0.22	2.80	0.29	0.17	2.03
TiO_2	0.09	0.09	0.07	0.10	0.13	0.13	0.02	0.77	0.05	7.67	0.12	0.04	6.98
Cr_2O_3	9.26	10.64	8.79	9.03	1.90	1.35	5.37	4.60	5.48	4.29	5.02	4.28	4.50
MgO	0.14	0.06	0.08	0.11	0.08	0.07	0.13	0.12	0.07	0.35	0.09	0.07	0.49
SiO_2	0.82	0.02	0.02	0.06	0.00	0.03	0.03	0.01	0.01	0.01	0.03	0.02	0.03
Fe_2O_3	54.68	55.07	56.93	56.37	64.74	65.62	61.91	61.30	61.64	46.74	62.28	62.80	49.36
FeO	29.96	28.77	28.95	28.90	30.07	30.34	30.10	30.34	30.10	33.39	30.19	30.07	34.03
V_2O_3	0.00	0.00	0.00	0.00	0.00	0.00	0.00	0.00	0.00	0.00	0.00	0.00	0.00
NiO	0.35	0.30	0.28	0.19	0.28	0.22	0.28	0.33	0.28	0.30	0.30	0.29	0.25
ZnO													
CoO													
Na_2O													
K_2O													
CaO													
Total	96.43	96.36	96.31	96.02	97.61	98.22	98.37	98.38	98.22	95.91	98.68	98.10	98.03
Cation													
Al	0.122	0.126	0.131	0.131	0.139	0.141	0.136	0.137	0.137	0.133	0.132	0.132	0.128
Mn	0.214	0.288	0.228	0.247	0.010	0.018	0.043	0.143	0.059	0.750	0.075	0.045	0.534
Ti	0.022	0.022	0.018	0.024	0.030	0.031	0.005	0.180	0.013	1.826	0.028	0.010	1.626
Cr	2.313	2.668	2.208	2.274	0.473	0.333	1.323	1.132	1.351	1.074	1.234	1.058	1.101
Mg	0.064	0.030	0.036	0.053	0.039	0.034	0.058	0.054	0.033	0.164	0.043	0.032	0.227
Si	0.260	0.006	0.008	0.019	0.000	0.010	0.008	0.002	0.004	0.003	0.008	0.005	0.009
Fe^{3+}	13.000	13.150	13.611	13.509	15.327	15.443	14.514	14.366	14.478	11.134	14.561	14.780	11.502
Fe^{2+}	7.916	7.634	7.691	7.696	7.912	7.935	7.841	7.903	7.856	8.840	7.843	7.864	8.812
V	0.000	0.000	0.000	0.000	0.000	0.000	0.000	0.000	0.000	0.000	0.000	0.000	0.000
Ni	0.088	0.076	0.070	0.047	0.070	0.055	0.071	0.084	0.069	0.076	0.075	0.074	0.063
Zn													

Co													
Na													
K													
Ca													
Total	24.000	24.000	24.000	24.000	24.000	24.000	24.000	24.000	24.000	24.000	24.000	24.000	24.000
Mg#	0.01	0.00	0.00	0.01	0.00	0.00	0.01	0.01	0.00	0.02	0.01	0.00	0.03
Cr#	0.95	0.96	0.94	0.95	0.77	0.70	0.91	0.89	0.91	0.89	0.90	0.89	0.90
Fe^{3+}/R^{3+}	0.84	0.82	0.85	0.85	0.96	0.97	0.91	0.92	0.91	0.90	0.91	0.93	0.90

Sample number	MIC/16/36	MIC/16/36	MIC/16/36	MIC/16/36	MIC/16/36	MIC/16/36	MIC/16/36	MIC/16/36	MIC/16/36	MIC/16/36	MIC/16/36	MIC/16/36	MIC/16/36
Location	Tua Dungri	Tua Dungri	Tua Dungri	Tua Dungri	Tua Dungri	Tua Dungri	Tua Dungri	Tua Dungri	Tua Dungri	Tua Dungri	Tua Dungri	Tua Dungri	Tua Dungri
EPMA point	75 / 1 .	76 / 1 .	77 / 1 .	78 / 1 .	79 / 1 .	80 / 1 .	81 / 1 .	82 / 1 .	83 / 1 .	84 / 1 .	87 / 1 .	88 / 1 .	89 / 1 .
Mineral	Chr mag-netite	Chr mag-netite	Chr mag-netite	Chr mag-netite	Chr mag-netite	Chr mag-netite	Chr mag-netite	Chr mag-netite	Chr mag-netite	Chr mag-netite	Chr mag-netite	Chr mag-netite	Chr mag-netite
Type	Type-V	Type-V	Type-V	Type-V	Type-V	Type-V	Type-V	Type-V	Type-V	Type-V	Type-V	Type-V	Type-V
Al_2O_3	0.38	0.38	0.36	0.38	0.34	0.34	0.38	0.38	0.36	0.38	0.39	0.37	0.36
MnO	0.25	0.19	0.27	0.12	0.34	0.20	0.21	0.12	0.18	0.14	0.07	0.46	0.15
TiO_2	0.08	0.20	0.24	0.04	0.12	0.02	0.06	0.09	0.15	0.09	0.09	0.09	0.10
Cr_2O_3	5.42	5.20	4.30	4.12	5.28	5.22	3.80	1.70	4.69	3.49	2.05	6.22	5.29
MgO	0.15	0.11	0.11	0.13	0.13	0.19	0.11	0.11	0.12	0.06	0.03	0.17	0.08
SiO_2	0.01	0.02	0.01	0.01	0.03	0.01	0.00	0.02	0.06	0.02	0.01	0.14	0.00
Fe_2O_3	62.50	61.98	62.87	63.98	62.25	62.67	63.70	66.14	62.42	64.31	65.29	60.26	62.26
FeO	30.38	30.27	30.28	30.45	30.09	30.07	30.24	30.37	30.25	30.47	30.43	29.84	30.45
V_2O_3	0.00	0.00	0.00	0.00	0.00	0.00	0.00	0.00	0.00	0.00	0.00	0.00	0.00
NiO	0.23	0.37	0.30	0.30	0.38	0.38	0.19	0.35	0.32	0.35	0.25	0.21	0.22
ZnO													
CoO													
Na_2O													
K_2O													
CaO													
Total	99.40	98.73	98.76	99.53	98.96	99.11	98.69	99.27	98.55	99.30	98.62	97.76	98.91
Cation													
Al	0.138	0.139	0.133	0.138	0.123	0.124	0.139	0.138	0.132	0.140	0.144	0.136	0.131
Mn	0.065	0.050	0.070	0.032	0.090	0.054	0.054	0.032	0.047	0.036	0.019	0.123	0.039
Ti	0.018	0.048	0.057	0.009	0.028	0.006	0.013	0.020	0.034	0.020	0.022	0.022	0.023

Cr	1.321	1.276	1.055	1.004	1.293	1.276	0.934	0.415	1.153	0.852	0.505	1.538	1.297
Mg	0.071	0.053	0.051	0.058	0.060	0.088	0.051	0.050	0.057	0.028	0.015	0.081	0.038
Si	0.004	0.006	0.004	0.002	0.010	0.004	0.001	0.005	0.018	0.006	0.003	0.043	0.001
Fe^{3+}	14.496	14.478	14.690	14.834	14.507	14.580	14.899	15.396	14.610	14.956	15.302	14.194	14.525
Fe^{2+}	7.831	7.858	7.863	7.846	7.794	7.773	7.861	7.856	7.868	7.875	7.927	7.810	7.893
V	0.000	0.000	0.000	0.000	0.000	0.000	0.000	0.000	0.000	0.000	0.000	0.000	0.000
Ni	0.056	0.093	0.076	0.075	0.094	0.095	0.047	0.087	0.081	0.086	0.063	0.052	0.054
Zn													
Co													
Na													
K													
Ca													
Total	24.000	24.000	24.000	24.000	24.000	24.000	24.000	24.000	24.000	24.000	24.000	24.000	24.000
Mg#	0.01	0.01	0.01	0.01	0.01	0.01	0.01	0.01	0.01	0.00	0.00	0.01	0.00
Cr#	0.91	0.90	0.89	0.88	0.91	0.91	0.87	0.75	0.90	0.86	0.78	0.92	0.91
Fe^{3+}/R^{3+}	0.91	0.91	0.93	0.93	0.91	0.91	0.93	0.97	0.92	0.94	0.96	0.89	0.91

Sample number	MIC/16/36	MIC/16/36	MIC/16/36	MIC/16/36	MIC/16/36	MIC/16/36	MIC/16/36	MIC/16/36	MIC/16/36	MIC/16/36	MIC/16/39	MIC/16/39	MIC/16/39
Location	Tua Dungri	Tua Dungri	Tua Dungri	Tua Dungri	Tua Dungri	Tua Dungri	Tua Dungri	Tua Dungri	Tua Dungri	Tua Dungri	Tua Dungri	Tua Dungri	Tua Dungri
EPMA point	90 / 1 .	91 / 1 .	92 / 1 .	93 / 1 .	94 / 1 .	95 / 1 .	96 / 1 .	98 / 1 .	99 / 1 .	100 / 1 .	6 / 1 .	7 / 1 .	8 / 1 .
Mineral	Chr mag-netite	Chr mag-netite	Chr mag-netite	Chr mag-netite	Chr mag-netite	Chr mag-netite	Chr mag-netite	Chr mag-netite	Chr mag-netite	Chr mag-netite	Chr mag-netite	Chr mag-netite	Chr mag-netite
Type	Type-V	Type-V	Type-V	Type-V	Type-V	Type-V	Type-V	Type-V	Type-V	Type-V	Type-V	Type-V	Type-V
Al_2O_3	0.37	0.37	0.39	0.36	0.38	0.34	0.39	0.38	0.39	0.38	0.03	0.06	0.04
MnO	0.34	0.08	0.42	0.18	0.29	0.17	0.18	0.17	0.06	0.19	0.39	0.45	0.29
TiO_2	0.12	0.11	0.52	0.41	0.44	0.03	0.04	0.10	0.13	0.14	0.15	0.16	0.13
Cr_2O_3	5.87	2.45	2.49	4.76	5.08	4.58	3.46	3.89	3.71	4.93	9.31	11.37	8.30
MgO	0.10	0.09	0.11	0.07	0.10	0.10	0.06	0.09	0.12	0.13	0.51	0.53	0.25
SiO_2	0.02	0.05	0.02	0.02	0.03	0.03	0.03	0.00	0.07	0.09	0.28	0.28	0.23
Fe_2O_3	61.03	65.27	64.09	62.55	61.95	63.05	63.59	63.28	63.11	62.03	55.88	54.34	56.34
FeO	30.00	30.57	30.38	30.84	30.60	30.26	30.07	30.12	30.22	30.17	29.35	29.63	29.39
V_2O_3	0.00	0.00	0.00	0.00	0.00	0.00	0.00	0.00	0.00	0.00	0.19	0.20	0.16
NiO	0.26	0.29	0.27	0.28	0.36	0.31	0.32	0.32	0.34	0.41	0.41	0.36	0.43
ZnO													
CoO													

Na_2O													
K_2O													
CaO													
Total	98.13	99.29	98.68	99.47	99.23	98.87	98.13	98.36	98.16	98.47	96.51	97.40	95.56
Cation													
Al	0.136	0.136	0.142	0.132	0.137	0.125	0.142	0.138	0.144	0.141	0.012	0.023	0.015
Mn	0.091	0.022	0.110	0.047	0.076	0.044	0.047	0.046	0.017	0.051	0.104	0.119	0.080
Ti	0.029	0.024	0.122	0.094	0.103	0.008	0.008	0.023	0.031	0.034	0.036	0.037	0.031
Cr	1.450	0.598	0.611	1.159	1.240	1.123	0.855	0.960	0.915	1.213	2.327	2.811	2.100
Mg	0.044	0.043	0.050	0.034	0.044	0.046	0.027	0.043	0.057	0.059	0.239	0.249	0.120
Si	0.007	0.017	0.005	0.007	0.009	0.010	0.010	0.001	0.022	0.028	0.087	0.088	0.075
Fe^{3+}	14.342	15.184	14.993	14.507	14.398	14.716	14.965	14.854	14.834	14.523	13.292	12.789	13.569
Fe^{2+}	7.835	7.904	7.899	7.950	7.902	7.849	7.864	7.856	7.892	7.850	7.757	7.750	7.866
V	0.000	0.000	0.000	0.000	0.000	0.000	0.000	0.000	0.000	0.000	0.041	0.042	0.035
Ni	0.066	0.072	0.068	0.070	0.090	0.078	0.080	0.080	0.086	0.102	0.104	0.092	0.110
Zn													
Co													
Na													
K													
Ca													
Total	24.000	24.000	24.000	24.000	24.000	24.000	24.000	24.000	24.000	24.000	24.000	24.000	24.000
Mg#	0.01	0.01	0.01	0.00	0.01	0.01	0.00	0.01	0.01	0.01	0.03	0.03	0.01
Cr#	0.91	0.81	0.81	0.90	0.90	0.90	0.86	0.87	0.86	0.90	0.99	0.99	0.99
Fe^{3+}/R^{3+}	0.90	0.95	0.95	0.92	0.91	0.92	0.94	0.93	0.93	0.91	0.85	0.82	0.87

Sample number	MIC/16/39	MIC/16/39	MIC/16/39	MIC/16/39	MIC/16/39	MIC/16/39	MIC/16/39	MIC/16/39	MIC/16/39	MIC/16/39	MIC/16/39	MIC/16/39	MIC/16/39
Location	Tua Dungri	Tua Dungri	Tua Dungri	Tua Dungri	Tua Dungri	Tua Dungri	Tua Dungri	Tua Dungri	Tua Dungri	Tua Dungri	Tua Dungri	Tua Dungri	Tua Dungri
EPMA point	11 / 1 .	22 / 1 .	23 / 1 .	24 / 1 .	25 / 1 .	28 / 1 .	29 / 1 .	30 / 1 .	31 / 1 .	32 / 1 .	33 / 1 .	34 / 1 .	38 / 1 .
Mineral	Chr mag-netite	Chr mag-netite	Chr mag-netite	Chr mag-netite	Chr mag-netite	Chr mag-netite	Chr mag-netite	Chr mag-netite	Chr mag-netite	Chr mag-netite	Chr mag-netite	Chr mag-netite	Chr mag-netite
Type	Type-V	Type-V	Type-V	Type-V	Type-V	Type-V	Type-V	Type-V	Type-V	Type-V	Type-V	Type-V	Type-V
Al_2O_3	0.03	0.05	0.04	0.09	0.23	0.08	0.07	0.06	0.05	0.08	0.04	0.04	0.11
MnO	0.51	0.36	0.40	0.56	0.82	0.66	0.47	0.38	0.45	0.51	0.40	0.42	0.70
TiO_2	0.16	0.13	0.15	0.16	0.19	0.14	0.16	0.15	0.16	0.15	0.17	0.13	0.20
Cr_2O_3	11.08	8.16	9.97	14.52	16.57	14.41	11.67	9.22	10.73	12.24	10.74	9.25	16.22

MgO	0.51	0.51	0.47	0.44	0.39	0.44	0.47	0.49	0.53	0.55	0.49	0.44	0.42
SiO_2	0.27	0.30	0.31	0.31	1.32	0.28	0.26	0.26	0.31	0.25	0.28	0.27	0.31
Fe_2O_3	55.18	58.01	56.73	51.53	46.37	51.77	53.89	56.52	55.99	54.46	55.99	56.32	49.62
FeO	29.75	29.77	30.09	30.01	31.26	29.78	29.58	29.65	30.02	29.87	30.19	29.53	30.03
V_2O_3	0.20	0.19	0.16	0.21	0.26	0.19	0.19	0.19	0.19	0.18	0.20	0.18	0.26
NiO	0.41	0.42	0.39	0.37	0.29	0.39	0.36	0.36	0.46	0.35	0.37	0.40	0.40
ZnO													
CoO													
Na_2O													
K_2O													
CaO													
Total	98.10	97.91	98.72	98.18	97.67	98.12	97.12	97.30	98.88	98.64	98.86	96.98	98.25
Cation													
Al	0.010	0.020	0.015	0.032	0.083	0.029	0.027	0.022	0.019	0.028	0.014	0.015	0.038
Mn	0.134	0.095	0.105	0.146	0.214	0.173	0.125	0.102	0.117	0.133	0.105	0.112	0.184
Ti	0.038	0.031	0.035	0.037	0.043	0.033	0.038	0.035	0.036	0.034	0.040	0.030	0.046
Cr	2.721	2.010	2.436	3.559	4.055	3.533	2.895	2.286	2.615	2.987	2.618	2.301	3.968
Mg	0.237	0.238	0.217	0.201	0.178	0.201	0.222	0.231	0.244	0.255	0.224	0.208	0.192
Si	0.084	0.093	0.095	0.095	0.409	0.086	0.082	0.082	0.097	0.077	0.087	0.086	0.095
Fe^{3+}	12.902	13.607	13.191	12.018	10.802	12.084	12.723	13.336	12.984	12.651	12.994	13.337	11.554
Fe^{2+}	7.731	7.761	7.777	7.777	8.092	7.724	7.761	7.775	7.736	7.711	7.786	7.771	7.770
V	0.041	0.038	0.033	0.042	0.052	0.039	0.039	0.040	0.039	0.038	0.040	0.038	0.052
Ni	0.102	0.106	0.097	0.092	0.072	0.098	0.090	0.091	0.113	0.086	0.092	0.101	0.100
Zn													
Co													
Na													
K													
Ca													
Total	24.000	24.000	24.000	24.000	24.000	24.000	24.000	24.000	24.000	24.000	24.000	24.000	24.000
Mg#	0.03	0.03	0.03	0.03	0.02	0.03	0.03	0.03	0.03	0.03	0.03	0.03	0.02
Cr#	1.00	0.99	0.99	0.99	0.98	0.99	0.99	0.99	0.99	0.99	0.99	0.99	0.99
Fe^{3+}/R^{3+}	0.83	0.87	0.84	0.77	0.72	0.77	0.81	0.85	0.83	0.81	0.83	0.85	0.74

Sample number	MIC/16/39	MIC/16/39	MIC/16/39	MIC/16/39	MIC/16/39	MIC/16/39	MIC/16/39	MIC/16/39	MIC/16/39	MIC/16/39	MIC/16/39	MIC/16/39	MIC/16/39
Location	Tua Dungri	Tua Dungri	Tua Dungri	Tua Dungri	Tua Dungri	Tua Dungri	Tua Dungri	Tua Dungri	Tua Dungri	Tua Dungri	Tua Dungri	Tua Dungri	Tua Dungri

EPMA point	40 / 1 .	41 / 1 .	42 / 1 .	47 / 1 .	48 / 1 .	59 / 1 .	60 / 1 .	61 / 1 .	62 / 1 .	63 / 1 .	64 / 1 .	65 / 1 .	66 / 1 .
Mineral	Chr mag-netite	Chr mag-netite	Chr mag-netite	Chr mag-netite	Chr mag-netite	Chr mag-netite	Chr mag-netite	Chr mag-netite	Chr mag-netite	Chr mag-netite	Chr mag-netite	Chr mag-netite	Chr mag-netite
Type	Type-V	Type-V	Type-V	Type-V	Type-V	Type-V	Type-V	Type-V	Type-V	Type-V	Type-V	Type-V	Type-V
Al_2O_3	0.06	0.09	0.10	0.04	0.02	0.06	0.03	0.03	0.02	0.03	0.12	0.05	0.04
MnO	0.45	0.49	0.72	0.47	0.21	0.40	0.26	0.32	0.09	0.23	0.42	0.44	0.23
TiO_2	0.15	0.29	0.23	0.15	0.15	0.13	0.16	0.13	0.15	0.14	0.15	0.16	0.16
Cr_2O_3	10.79	13.18	18.25	11.46	6.52	9.31	7.77	7.69	4.70	6.06	8.96	10.64	7.92
MgO	0.49	0.36	0.41	0.49	0.52	0.53	0.48	0.56	0.50	0.26	3.04	0.48	0.51
SiO_2	0.31	0.22	0.32	0.30	0.32	0.29	0.30	0.26	0.26	0.57	3.17	0.30	0.29
Fe_2O_3	56.02	51.90	48.06	54.74	60.70	57.59	59.47	59.72	61.45	59.76	54.46	56.78	58.62
FeO	30.19	29.73	30.34	29.85	30.31	30.14	30.35	30.32	29.86	30.85	30.94	30.47	30.09
V_2O_3	0.23	0.25	0.24	0.18	0.17	0.22	0.18	0.21	0.16	0.18	0.18	0.20	0.16
NiO	0.50	0.54	0.38	0.39	0.46	0.44	0.51	0.34	0.41	0.36	0.39	0.39	0.36
ZnO													
CoO													
Na_2O													
K_2O													
CaO													
Total	99.20	97.04	99.05	98.07	99.38	99.10	99.49	99.58	97.60	98.45	101.83	99.90	98.37
Cation													
Al	0.021	0.033	0.036	0.016	0.006	0.022	0.010	0.011	0.007	0.012	0.040	0.018	0.013
Mn	0.117	0.130	0.188	0.123	0.056	0.103	0.067	0.083	0.025	0.061	0.104	0.114	0.059
Ti	0.036	0.069	0.052	0.034	0.035	0.030	0.038	0.030	0.035	0.033	0.034	0.036	0.038
Cr	2.621	3.272	4.425	2.816	1.584	2.265	1.885	1.864	1.165	1.487	2.055	2.569	1.942
Mg	0.226	0.167	0.187	0.226	0.239	0.241	0.218	0.257	0.234	0.118	1.317	0.220	0.237
Si	0.096	0.069	0.098	0.094	0.097	0.091	0.091	0.080	0.083	0.178	0.920	0.090	0.091
Fe^{3+}	12.954	12.265	11.091	12.799	14.041	13.338	13.739	13.775	14.491	13.968	11.895	13.042	13.690
Fe^{2+}	7.758	7.808	7.780	7.757	7.793	7.757	7.791	7.772	7.824	8.014	7.509	7.777	7.808
V	0.046	0.051	0.050	0.038	0.035	0.044	0.036	0.043	0.034	0.037	0.034	0.040	0.033
Ni	0.124	0.136	0.094	0.097	0.115	0.109	0.125	0.084	0.102	0.091	0.091	0.095	0.090
Zn													
Co													
Na													
K													
Ca													
Total	24.000	24.000	24.000	24.000	24.000	24.000	24.000	24.000	24.000	24.000	24.000	24.000	24.000

Mg#	0.03	0.02	0.02	0.03	0.03	0.03	0.03	0.03	0.03	0.01	0.15	0.03	0.03
Cr#	0.99	0.99	0.99	0.99	1.00	0.99	0.99	0.99	0.99	0.99	0.98	0.99	0.99
Fe^{3+}/R^{3+}	0.83	0.79	0.71	0.82	0.90	0.85	0.88	0.88	0.93	0.90	0.85	0.83	0.88

Sample number	MIC/16/39	MIC/16/39	MIC/16/39	MIC/16/39	MIC/16/39	MIC/16/39	MIC/16/39	MIC/16/39	MIC/16/39	MIC/16/39	MIC/16/39	MIC/16/39	MIC/16/39
Location	Tua Dungri	Tua Dungri	Tua Dungri	Tua Dungri	Tua Dungri	Tua Dungri	Tua Dungri	Tua Dungri	Tua Dungri	Tua Dungri	Tua Dungri	Tua Dungri	Tua Dungri
EPMA point	67 / 1 .	68 / 1 .	71 / 1 .	74 / 1 .	75 / 1 .	78 / 1 .	79 / 1 .	80 / 1 .	81 / 1 .	82 / 1 .	83 / 1 .	84 / 1 .	85 / 1 .
Mineral	Chr mag-netite	Chr mag-netite	Chr mag-netite	Chr mag-netite	Chr mag-netite	Chr mag-netite	Chr mag-netite	Chr mag-netite	Chr mag-netite	Chr mag-netite	Chr mag-netite	Chr mag-netite	Chr mag-netite
Type	Type-V	Type-V	Type-V	Type-V	Type-V	Type-V	Type-V	Type-V	Type-V	Type-V	Type-V	Type-V	Type-V
Al_2O_3	0.04	0.01	0.06	0.06	0.04	0.06	0.04	0.06	0.05	0.03	0.04	0.04	0.04
MnO	0.16	0.09	0.49	0.49	0.33	0.41	0.38	0.56	0.48	0.40	0.32	0.41	0.28
TiO_2	0.12	0.13	0.17	0.15	0.12	0.18	0.16	0.15	0.16	0.14	0.15	0.15	0.16
Cr_2O_3	5.67	5.33	11.51	12.42	8.51	10.81	9.67	14.94	11.27	9.44	8.81	10.90	7.65
MgO	0.54	0.50	0.48	0.47	0.50	0.49	0.50	0.54	0.50	0.49	0.53	0.49	0.53
SiO_2	0.28	0.27	0.30	0.32	0.31	0.29	0.30	0.29	0.31	0.28	0.26	0.26	0.25
Fe_2O_3	60.88	61.77	55.59	54.91	59.37	56.32	57.86	52.34	56.43	58.39	58.70	56.66	59.14
FeO	29.85	30.21	30.39	30.54	30.64	30.26	30.34	30.22	30.58	30.49	30.28	30.52	30.03
V_2O_3	0.15	0.17	0.21	0.22	0.19	0.17	0.16	0.19	0.22	0.17	0.17	0.19	0.19
NiO	0.44	0.48	0.38	0.38	0.39	0.46	0.48	0.39	0.44	0.40	0.42	0.30	0.43
ZnO													
CoO													
Na_2O													
K_2O													
CaO													
Total	98.12	98.96	99.58	99.95	100.41	99.47	99.89	99.68	100.44	100.23	99.68	99.90	98.69
Cation													
Al	0.013	0.003	0.020	0.020	0.013	0.023	0.015	0.023	0.018	0.010	0.014	0.014	0.013
Mn	0.043	0.025	0.127	0.128	0.086	0.108	0.098	0.145	0.124	0.103	0.083	0.105	0.073
Ti	0.029	0.030	0.039	0.034	0.028	0.041	0.036	0.033	0.037	0.031	0.034	0.033	0.038
Cr	1.395	1.303	2.785	2.994	2.045	2.619	2.335	3.603	2.703	2.273	2.134	2.629	1.872
Mg	0.249	0.229	0.220	0.214	0.227	0.224	0.227	0.245	0.225	0.221	0.242	0.221	0.243
Si	0.087	0.085	0.093	0.096	0.096	0.090	0.092	0.088	0.093	0.086	0.078	0.080	0.076
Fe^{3+}	14.268	14.364	12.802	12.594	13.583	12.991	13.298	12.018	12.887	13.379	13.524	13.014	13.769
Fe^{2+}	7.774	7.808	7.779	7.784	7.789	7.757	7.749	7.710	7.760	7.763	7.753	7.791	7.768

V	0.030	0.034	0.043	0.044	0.037	0.035	0.032	0.038	0.044	0.034	0.035	0.038	0.039
Ni	0.111	0.120	0.093	0.092	0.096	0.113	0.119	0.096	0.109	0.099	0.104	0.074	0.107
Zn													
Co													
Na													
K													
Ca													
Total	24.000	24.000	24.000	24.000	24.000	24.000	24.000	24.000	24.000	24.000	24.000	24.000	24.000
Mg#	0.03	0.03	0.03	0.03	0.03	0.03	0.03	0.03	0.03	0.03	0.03	0.03	0.03
Cr#	0.99	1.00	0.99	0.99	0.99	0.99	0.99	0.99	0.99	1.00	0.99	0.99	0.99
Fe^{3+}/R^{3+}	0.91	0.92	0.82	0.81	0.87	0.83	0.85	0.77	0.83	0.85	0.86	0.83	0.88

Sample number	MIC/16/39	MIC/16/39	MIC/16/39	MIC/16/39	MIC/16/40	MIC/16/40	MIC/16/40	MIC/16/40	MIC/16/40	MIC/16/40	MIC/16/40	MIC/16/40	MIC/16/40
Location	Tua Dungri	Tua Dungri	Tua Dungri	Tua Dungri	Tua Dungri	Tua Dungri	Tua Dungri	Tua Dungri	Tua Dungri	Tua Dungri	Tua Dungri	Tua Dungri	Tua Dungri
EPMA point	86 / 1 .	87 / 1 .	14 / 1 .	16 / 1 .	101 / 1 .	102 / 1 .	104 / 1 .	105 / 1 .	107 / 1 .	108 / 1 .	109 / 1 .	110 / 1 .	111 / 1 .
Mineral	Chr mag-netite	Chr mag-netite	Chr mag-netite	Chr mag-netite	Chr mag-netite	Chr mag-netite	Chr mag-netite	Chr mag-netite	Chr mag-netite	Chr mag-netite	Chr mag-netite	Chr mag-netite	Chr mag-netite
Type	Type-V	Type-V	Type-V	Type-V	Type-V	Type-V	Type-V	Type-V	Type-V	Type-V	Type-V	Type-V	Type-V
Al_2O_3	0.04	0.04	0.05	0.02	0.01	0.02	0.01	0.01	0.00	0.02	0.03	0.02	0.00
MnO	0.35	0.49	0.55	0.08	0.04	0.01	0.29	0.01	0.01	0.03	0.04	0.06	0.03
TiO_2	0.19	0.20	0.01	0.03	0.06	0.05	0.99	0.28	0.03	0.13	0.13	0.12	0.05
Cr_2O_3	9.80	11.60	11.78	7.69	2.81	2.87	2.34	2.38	2.80	2.17	2.06	2.75	2.10
MgO	0.48	0.50	0.08	0.08	0.02	0.10	0.04	0.16	0.04	0.08	0.08	0.07	0.07
SiO_2	0.23	0.28	0.02	0.00	0.06	0.20	0.06	0.53	0.03	0.32	0.07	0.04	0.04
Fe_2O_3	57.44	55.42	54.15	59.61	64.37	62.56	62.62	62.61	63.72	62.63	64.48	63.42	64.23
FeO	30.31	30.35	28.97	30.12	30.54	29.90	31.17	30.80	29.96	30.12	30.20	29.96	29.89
V_2O_3	0.20	0.21	0.07	0.07	0.13	0.10	0.20	0.11	0.11	0.12	0.08	0.11	0.08
NiO	0.44	0.34	0.32	0.22	0.30	0.30	0.22	0.29	0.38	0.26	0.24	0.31	0.27
ZnO			0.07	0.17									
CoO			0.15	0.00									
Na_2O			0.02	0.00									
K_2O			0.00	0.01									
CaO			0.02	0.00									
Total	99.47	99.44	96.25	98.09	98.35	96.11	97.94	97.17	97.07	95.88	97.40	96.87	96.76
Cation													

Al	0.014	0.014	0.019	0.007	0.005	0.008	0.004	0.004	0.001	0.008	0.010	0.008	0.001
Mn	0.090	0.128	0.147	0.021	0.010	0.002	0.078	0.004	0.002	0.008	0.011	0.017	0.009
Ti	0.044	0.046	0.002	0.006	0.015	0.012	0.232	0.066	0.007	0.031	0.032	0.028	0.012
Cr	2.377	2.810	2.962	1.901	0.696	0.725	0.582	0.594	0.702	0.550	0.514	0.691	0.528
Mg	0.222	0.228	0.037	0.036	0.009	0.047	0.020	0.074	0.021	0.038	0.039	0.034	0.032
Si	0.071	0.087	0.007	0.001	0.019	0.065	0.018	0.166	0.008	0.103	0.021	0.012	0.014
Fe^{3+}	13.259	12.781	12.958	14.034	15.154	15.050	14.788	14.868	15.199	15.100	15.323	15.152	15.371
Fe^{2+}	7.775	7.778	7.705	7.882	7.991	7.994	8.181	8.128	7.941	8.070	7.974	7.956	7.949
V	0.040	0.043	0.014	0.014	0.026	0.021	0.042	0.024	0.022	0.025	0.016	0.023	0.016
Ni	0.109	0.085	0.083	0.056	0.075	0.077	0.056	0.074	0.097	0.067	0.061	0.079	0.069
Zn			0.015	0.039									
Co			0.037	0.000									
Na			0.007	0.000									
K			0.000	0.002									
Ca			0.005	0.000									
Total	24.000	24.000	24.000	24.000	24.000	24.000	24.000	24.000	24.000	24.000	24.000	24.000	24.000
Mg#	0.03	0.03	0.00	0.00	0.00	0.01	0.00	0.01	0.00	0.00	0.00	0.00	0.00
Cr#	0.99	1.00	0.99	1.00	0.99	0.99	0.99	0.99	1.00	0.99	0.98	0.99	1.00
Fe^{3+}/R^{3+}	0.85	0.82	0.81	0.88	0.96	0.95	0.96	0.96	0.96	0.96	0.97	0.96	0.97

Sample number	MIC/16/40	MIC/16/40	MIC/16/40	MIC/16/40	MIC/16/40	MIC/16/40	MIC/16/40	MIC/16/40	MIC/16/40	MIC/16/40	MIC/16/40	MIC/16/40	MIC/16/40
Location	Tua Dungri	Tua Dungri	Tua Dungri	Tua Dungri	Tua Dungri	Tua Dungri	Tua Dungri	Tua Dungri	Tua Dungri	Tua Dungri	Tua Dungri	Tua Dungri	Tua Dungri
EPMA point	112 / 1 .	113 / 1 .	114 / 1 .	115 / 1 .	118 / 1 .	121 / 1 .	124 / 1 .	126 / 1 .	127 / 1 .	128 / 1 .	129 / 1 .	130 / 1 .	131 / 1 .
Mineral	Chr mag-netite	Chr mag-netite	Chr mag-netite	Chr mag-netite	Chr mag-netite	Chr mag-netite	Chr mag-netite	Chr mag-netite	Chr mag-netite	Chr mag-netite	Chr mag-netite	Chr mag-netite	Chr mag-netite
Type	Type-V	Type-V	Type-V	Type-V	Type-V	Type-V	Type-V	Type-V	Type-V	Type-V	Type-V	Type-V	Type-V
Al_2O_3	0.01	0.01	0.00	0.02	0.04	0.01	0.01	0.04	0.03	0.02	0.02	0.01	0.02
MnO	0.01	0.02	0.07	0.03	0.05	0.04	0.01	0.03	0.04	0.05	0.02	0.03	0.04
TiO_2	0.04	0.25	0.10	0.08	0.28	0.05	0.04	0.07	0.11	0.06	0.07	0.09	0.09
Cr_2O_3	2.74	2.43	2.30	2.49	2.87	2.99	1.79	2.05	2.16	1.80	2.41	2.54	2.44
MgO	0.10	0.07	0.05	0.07	1.37	0.05	0.05	0.05	0.19	0.07	0.07	0.06	0.04
SiO_2	0.22	0.28	0.02	0.03	2.00	0.03	0.04	0.00	0.53	0.11	0.05	0.07	0.01
Fe_2O_3	62.05	62.61	64.08	64.74	58.67	63.39	64.00	64.88	61.99	64.53	64.87	64.15	64.23
FeO	29.68	30.35	30.11	30.37	30.73	30.10	29.78	30.14	30.07	30.14	30.61	30.37	30.20
V_2O_3	0.11	0.11	0.16	0.11	0.13	0.12	0.08	0.10	0.11	0.12	0.14	0.12	0.10

NiO	0.25	0.27	0.34	0.30	0.21	0.20	0.18	0.35	0.27	0.30	0.22	0.22	0.24
ZnO													
CoO													
Na_2O													
K_2O													
CaO													
Total	95.19	96.39	97.22	98.22	96.35	96.98	95.99	97.69	95.51	97.20	98.48	97.67	97.43
Cation													
Al	0.002	0.004	0.000	0.006	0.016	0.004	0.003	0.013	0.011	0.007	0.006	0.002	0.009
Mn	0.003	0.005	0.018	0.007	0.014	0.011	0.004	0.007	0.011	0.014	0.005	0.009	0.010
Ti	0.010	0.061	0.023	0.018	0.065	0.011	0.010	0.016	0.027	0.015	0.017	0.022	0.021
Cr	0.699	0.613	0.575	0.616	0.711	0.751	0.455	0.510	0.549	0.451	0.596	0.632	0.610
Mg	0.047	0.033	0.023	0.035	0.638	0.026	0.022	0.022	0.089	0.031	0.033	0.030	0.021
Si	0.070	0.089	0.005	0.009	0.624	0.010	0.014	0.001	0.171	0.035	0.015	0.022	0.005
Fe^{3+}	15.070	15.015	15.265	15.257	13.813	15.128	15.443	15.382	14.976	15.368	15.249	15.204	15.265
Fe^{2+}	8.010	8.089	7.971	7.953	8.039	7.984	7.985	7.941	8.074	7.978	7.995	7.998	7.976
V	0.022	0.022	0.034	0.022	0.027	0.025	0.017	0.020	0.023	0.024	0.028	0.025	0.022
Ni	0.065	0.069	0.086	0.077	0.053	0.050	0.047	0.088	0.070	0.077	0.056	0.057	0.062
Zn													
Co													
Na													
K													
Ca													
Total	24.000	24.000	24.000	24.000	24.000	24.000	24.000	24.000	24.000	24.000	24.000	24.000	24.000
Mg#	0.01	0.00	0.00	0.00	0.07	0.00	0.00	0.00	0.01	0.00	0.00	0.00	0.00
Cr#	1.00	0.99	1.00	0.99	0.98	1.00	0.99	0.98	0.98	0.98	0.99	1.00	0.99
Fe^{3+}/R^{3+}	0.96	0.96	0.96	0.96	0.95	0.95	0.97	0.97	0.96	0.97	0.96	0.96	0.96

Sample number	MIC/16/40	MIC/16/40	MIC/16/40	MIC/16/40	MIC/16/40	MIC/16/40	MIC/16/40	MIC/16/40	MIC/16/40	MIC/16/40	MIC/16/40	MIC/16/40	MIC/16/40
Location	Tua Dungri	Tua Dungri	Tua Dungri	Tua Dungri	Tua Dungri	Tua Dungri	Tua Dungri	Tua Dungri	Tua Dungri	Tua Dungri	Tua Dungri	Tua Dungri	Tua Dungri
EPMA point	132 / 1 .	133 / 1 .	134 / 1 .	135 / 1 .	136 / 1 .	137 / 1 .	138 / 1 .	139 / 1 .	140 / 1 .	141 / 1 .	142 / 1 .	143 / 1 .	144 / 1 .
Mineral	Chr mag-netite	Chr mag-netite	Chr mag-netite	Chr mag-netite	Chr mag-netite	Chr mag-netite	Chr mag-netite	Chr mag-netite	Chr mag-netite	Chr mag-netite	Chr mag-netite	Chr mag-netite	Chr mag-netite
Type	Type-V	Type-V	Type-V	Type-V	Type-V	Type-V	Type-V	Type-V	Type-V	Type-V	Type-V	Type-V	Type-V
Al_2O_3	0.02	0.01	0.01	0.02	0.00	0.02	0.02	0.02	0.02	0.00	0.03	0.03	0.01

MnO	0.01	0.01	0.02	0.02	0.02	0.02	0.01	0.04	0.00	0.08	0.02	0.04	0.06
TiO_2	0.08	0.06	0.11	0.04	0.07	0.21	0.31	0.10	0.09	0.28	0.13	0.30	0.03
Cr_2O_3	2.32	2.58	2.25	2.83	2.80	2.65	2.39	2.37	1.82	2.13	2.28	2.75	2.90
MgO	0.04	0.06	0.05	0.07	0.06	0.05	0.11	0.05	0.26	0.03	0.12	0.08	0.13
SiO_2	0.06	0.03	0.05	0.09	0.04	0.02	0.06	0.06	0.27	0.03	0.06	0.04	0.16
Fe_2O_3	64.22	64.17	64.43	63.95	64.56	64.40	64.27	64.29	64.87	64.22	64.13	63.92	63.20
FeO	30.31	30.33	30.21	30.44	30.62	30.70	30.75	30.27	30.52	30.44	30.25	30.68	29.91
V_2O_3	0.11	0.12	0.07	0.11	0.15	0.14	0.14	0.12	0.12	0.12	0.12	0.14	0.07
NiO	0.23	0.16	0.25	0.16	0.27	0.24	0.22	0.33	0.23	0.26	0.20	0.25	0.26
ZnO													
CoO													
Na_2O													
K_2O													
CaO													
Total	97.40	97.52	97.47	97.72	98.59	98.45	98.28	97.67	98.19	97.58	97.36	98.23	96.73
Cation													
Al	0.007	0.004	0.005	0.008	0.000	0.007	0.007	0.007	0.006	0.000	0.013	0.012	0.004
Mn	0.002	0.003	0.006	0.006	0.004	0.006	0.002	0.012	0.000	0.020	0.006	0.009	0.016
Ti	0.020	0.014	0.026	0.009	0.017	0.049	0.073	0.023	0.022	0.067	0.031	0.070	0.008
Cr	0.579	0.643	0.562	0.703	0.690	0.654	0.590	0.589	0.450	0.531	0.569	0.680	0.729
Mg	0.020	0.027	0.026	0.031	0.030	0.022	0.050	0.025	0.121	0.012	0.057	0.039	0.061
Si	0.020	0.009	0.016	0.029	0.012	0.006	0.019	0.020	0.085	0.009	0.020	0.013	0.051
Fe^{3+}	15.266	15.233	15.305	15.142	15.159	15.142	15.129	15.240	15.258	15.241	15.239	15.055	15.107
Fe^{2+}	8.005	8.001	7.975	8.009	7.989	8.023	8.043	7.974	7.977	8.029	7.988	8.029	7.944
V	0.023	0.024	0.015	0.023	0.031	0.029	0.030	0.026	0.024	0.025	0.026	0.029	0.014
Ni	0.058	0.042	0.064	0.040	0.068	0.061	0.056	0.084	0.057	0.065	0.050	0.064	0.066
Zn													
Co													
Na													
K													
Ca													
Total	24.000	24.000	24.000	24.000	24.000	24.000	24.000	24.000	24.000	24.000	24.000	24.000	24.000
Mg#	0.00	0.00	0.00	0.00	0.00	0.00	0.01	0.00	0.01	0.00	0.01	0.00	0.01
Cr#	0.99	0.99	0.99	0.99	1.00	0.99	0.99	0.99	0.99	1.00	0.98	0.98	0.99
Fe^{3+}/R^{3+}	0.96	0.96	0.96	0.96	0.96	0.96	0.96	0.96	0.97	0.97	0.96	0.96	0.95

Sample	MIC/16/	MIC/16/	MIC/16/	MIC/16/	MIC/16/	MIC/16/	MIC/16/	MIC/16/	MIC/16/	MIC/16/	MIC/16/	MIC/16/	MIC/16/

number	40	40	40	40	40	42	42	42	42	42	42	42	42
Location	Tua Dungri	Tua Dungri	Tua Dungri	Tua Dungri	Tua Dungri	Tua Dungri	Tua Dungri	Tua Dungri	Tua Dungri	Tua Dungri	Tua Dungri	Tua Dungri	Tua Dungri
EPMA point	145 / 1 .	146 / 1 .	149 / 1 .	150 / 1 .	151 / 1 .	88 / 1 .	89 / 1 .	91 / 1 .	92 / 1 .	101 / 1 .	102 / 1 .	104 / 1 .	106 / 1 .
Mineral	Chr mag-netite	Chr mag-netite	Chr mag-netite	Chr mag-netite	Chr mag-netite	Chr mag-netite	Chr mag-netite	Chr mag-netite	Chr mag-netite	Chr mag-netite	Chr mag-netite	Chr mag-netite	Chr mag-netite
Type	Type-V	Type-V	Type-V	Type-V	Type-V	Type-V	Type-V	Type-V	Type-V	Type-V	Type-V	Type-V	Type-V
Al_2O_3	0.02	0.01	0.35	0.34	0.36	0.03	0.02	0.05	0.02	0.02	0.03	0.02	0.03
MnO	0.03	0.04	0.11	0.08	0.11	0.05	0.01	0.05	0.02	0.03	0.01	0.01	0.01
TiO_2	0.04	0.06	0.00	0.13	0.11	0.06	0.09	0.17	0.03	0.04	0.04	0.11	0.03
Cr_2O_3	2.02	2.21	2.07	2.66	2.34	2.97	3.10	2.81	3.50	1.52	1.47	2.81	1.88
MgO	0.11	0.10	0.07	0.07	0.52	0.08	0.07	0.07	0.04	0.09	0.17	0.05	0.04
SiO_2	0.18	0.12	0.05	0.03	0.87	0.10	0.05	0.89	0.05	0.02	0.07	0.01	0.03
Fe_2O_3	62.99	63.80	64.46	64.74	61.52	63.01	62.92	60.34	62.32	65.09	65.01	62.44	64.53
FeO	29.68	29.82	29.85	30.41	29.87	29.82	29.78	30.65	29.68	29.93	29.73	29.39	29.86
V_2O_3	0.11	0.07	0.00	0.00	0.00	0.08	0.09	0.03	0.10	0.07	0.04	0.08	0.09
NiO	0.22	0.33	0.29	0.31	0.43	0.32	0.41	0.25	0.38	0.22	0.29	0.42	0.37
ZnO													
CoO													
Na_2O													
K_2O													
CaO													
Total	95.39	96.55	97.24	98.76	96.11	96.51	96.54	95.32	96.14	97.01	96.83	95.34	96.87
Cation													
Al	0.007	0.004	0.129	0.123	0.134	0.011	0.007	0.020	0.006	0.006	0.011	0.009	0.010
Mn	0.009	0.010	0.029	0.022	0.028	0.015	0.004	0.013	0.005	0.007	0.002	0.002	0.004
Ti	0.011	0.015	0.000	0.029	0.026	0.014	0.021	0.042	0.006	0.009	0.009	0.027	0.006
Cr	0.513	0.556	0.518	0.653	0.586	0.747	0.780	0.714	0.886	0.382	0.368	0.718	0.473
Mg	0.050	0.046	0.031	0.031	0.246	0.037	0.033	0.032	0.020	0.040	0.079	0.025	0.021
Si	0.058	0.037	0.016	0.009	0.276	0.030	0.015	0.287	0.015	0.007	0.022	0.004	0.009
Fe^{3+}	15.275	15.291	15.320	15.147	14.676	15.104	15.083	14.587	15.002	15.539	15.534	15.161	15.430
Fe^{2+}	7.997	7.941	7.883	7.906	7.919	7.943	7.933	8.233	7.941	7.940	7.894	7.929	7.933
V	0.023	0.015	0.000	0.000	0.000	0.016	0.020	0.007	0.021	0.014	0.008	0.017	0.019
Ni	0.057	0.084	0.074	0.078	0.109	0.082	0.105	0.064	0.098	0.055	0.073	0.108	0.095
Zn													
Co													
Na													

K													
Ca													
Total	24.000	24.000	24.000	24.000	24.000	24.000	24.000	24.000	24.000	24.000	24.000	24.000	24.000
Mg#	0.01	0.01	0.00	0.00	0.03	0.00	0.00	0.00	0.00	0.01	0.01	0.00	0.00
Cr#	0.99	0.99	0.80	0.84	0.81	0.99	0.99	0.97	0.99	0.98	0.97	0.99	0.98
Fe^{3+}/R^{3+}	0.97	0.96	0.96	0.95	0.95	0.95	0.95	0.95	0.94	0.98	0.98	0.95	0.97

Sample number	MIC/16/42	MIC/16/42	MIC/16/42	MIC/16/42	MIC/16/42	MIC/16/42	MIC/16/42	MIC/16/42	MIC/16/42	MIC/16/42	MIC/16/42	MIC/16/42	MIC/16/42
Location	Tua Dungri	Tua Dungri	Tua Dungri	Tua Dungri	Tua Dungri	Tua Dungri	Tua Dungri	Tua Dungri	Tua Dungri	Tua Dungri	Tua Dungri	Tua Dungri	Tua Dungri
EPMA point	107 / 1 .	120 / 1 .	122 / 1 .	123 / 1 .	124 / 1 .	125 / 1 .	126 / 1 .	127 / 1 .	128 / 1 .	129 / 1 .	130 / 1 .	131 / 1 .	132 / 1 .
Mineral	Chr mag-netite	Chr mag-netite	Chr mag-netite	Chr mag-netite	Chr mag-netite	Chr mag-netite	Chr mag-netite	Chr mag-netite	Chr mag-netite	Chr mag-netite	Chr mag-netite	Chr mag-netite	Chr mag-netite
Type	Type-V	Type-V	Type-V	Type-V	Type-V	Type-V	Type-V	Type-V	Type-V	Type-V	Type-V	Type-V	Type-V
Al_2O_3	0.02	0.03	0.02	0.03	0.01	0.03	0.07	0.03	0.03	0.05	0.03	0.02	0.08
MnO	0.01	0.07	0.12	0.08	0.11	0.08	0.14	0.04	0.19	0.03	0.06	0.09	0.03
TiO_2	0.03	0.02	0.06	0.02	0.05	0.08	0.51	0.06	0.38	0.01	0.02	0.06	0.22
Cr_2O_3	2.44	2.72	3.83	3.50	3.77	2.99	2.99	3.19	3.06	2.41	2.95	3.55	2.80
MgO	0.08	0.06	0.10	0.02	0.04	0.03	0.05	0.11	0.08	0.74	0.04	0.03	0.82
SiO_2	0.08	0.03	0.01	0.02	0.01	0.02	0.04	0.01	0.01	0.83	0.04	0.01	2.81
Fe_2O_3	62.88	63.35	63.01	62.88	63.01	64.17	61.93	63.04	61.98	62.26	64.00	62.62	55.27
FeO	29.37	29.60	29.93	29.77	29.96	30.18	30.30	29.63	29.67	29.66	30.07	29.75	31.69
V_2O_3	0.03	0.06	0.12	0.06	0.10	0.12	0.17	0.10	0.12	0.03	0.05	0.10	0.04
NiO	0.27	0.33	0.40	0.35	0.41	0.50	0.30	0.45	0.42	0.27	0.29	0.40	0.29
ZnO													
CoO													
Na_2O													
K_2O													
CaO													
Total	95.20	96.27	97.59	96.74	97.48	98.19	96.52	96.66	95.94	96.30	97.56	96.62	94.04
Cation													
Al	0.008	0.011	0.006	0.010	0.005	0.011	0.025	0.012	0.011	0.019	0.012	0.008	0.028
Mn	0.002	0.018	0.032	0.023	0.031	0.022	0.038	0.010	0.051	0.007	0.017	0.024	0.007
Ti	0.006	0.004	0.013	0.005	0.012	0.019	0.123	0.015	0.091	0.003	0.005	0.013	0.052
Cr	0.622	0.687	0.955	0.881	0.941	0.740	0.754	0.802	0.775	0.603	0.734	0.894	0.709
Mg	0.039	0.026	0.046	0.012	0.017	0.015	0.024	0.054	0.036	0.349	0.019	0.013	0.391

Si	0.026	0.011	0.003	0.007	0.004	0.005	0.014	0.003	0.003	0.263	0.013	0.003	0.900
Fe^{3+}	15.285	15.234	14.935	15.045	14.961	15.129	14.841	15.088	14.947	14.829	15.185	15.002	13.333
Fe^{2+}	7.935	7.911	7.884	7.916	7.905	7.909	8.070	7.880	7.951	7.851	7.929	7.920	8.495
V	0.006	0.013	0.024	0.013	0.020	0.024	0.036	0.021	0.026	0.006	0.010	0.021	0.008
Ni	0.069	0.085	0.101	0.088	0.104	0.125	0.076	0.115	0.108	0.070	0.074	0.102	0.076
Zn													
Co													
Na													
K													
Ca													
Total	24.000	24.000	24.000	24.000	24.000	24.000	24.000	24.000	24.000	24.000	24.000	24.000	24.000
Mg#	0.00	0.00	0.01	0.00	0.00	0.00	0.00	0.01	0.00	0.04	0.00	0.00	0.04
Cr#	0.99	0.98	0.99	0.99	0.99	0.98	0.97	0.99	0.99	0.97	0.98	0.99	0.96
Fe^{3+}/R^{3+}	0.96	0.96	0.94	0.94	0.94	0.95	0.95	0.95	0.95	0.96	0.95	0.94	0.95

Sample number	MIC/16/42	MIC/16/42	MIC/16/42	MIC/16/42	MIC/16/42	MIC/16/42	MIC/16/42	MIC/16/42	MIC/16/42	MIC/16/42	MIC/16/42	MIC/16/42	MIC/16/42
Location	Tua Dungri	Tua Dungri	Tua Dungri	Tua Dungri	Tua Dungri	Tua Dungri	Tua Dungri	Tua Dungri	Tua Dungri	Tua Dungri	Tua Dungri	Tua Dungri	Tua Dungri
EPMA point	133 / 1 .	135 / 1 .	136 / 1 .	182 / 1 .	183 / 1 .	184 / 1 .	185 / 1 .	186 / 1 .	187 / 1 .	188 / 1 .	189 / 1 .	190 / 1 .	192 / 1 .
Mineral	Chr mag-netite	Chr mag-netite	Chr mag-netite	Chr mag-netite	Chr mag-netite	Chr mag-netite	Chr mag-netite	Chr mag-netite	Chr mag-netite	Chr mag-netite	Chr mag-netite	Chr mag-netite	Chr mag-netite
Type	Type-V	Type-V	Type-V	Type-V	Type-V	Type-V	Type-V	Type-V	Type-V	Type-V	Type-V	Type-V	Type-V
Al_2O_3	0.02	0.01	0.01	0.01	0.03	0.01	0.02	0.03	0.02	0.03	0.02	0.03	0.04
MnO	0.08	0.08	0.00	0.05	0.06	0.04	0.02	0.05	0.00	0.00	0.02	0.01	0.02
TiO_2	0.02	0.54	0.07	0.08	0.06	0.02	0.04	0.10	0.11	0.01	0.03	0.03	0.25
Cr_2O_3	3.31	2.13	2.14	2.11	2.16	2.93	2.80	1.77	0.92	2.66	2.54	2.03	1.46
MgO	0.08	0.06	0.08	0.07	0.06	0.05	0.05	0.11	0.08	0.33	0.06	0.03	0.12
SiO_2	0.05	0.15	0.15	0.07	0.05	0.05	0.05	0.23	0.12	0.48	0.09	0.14	0.10
Fe_2O_3	63.06	62.30	63.91	64.33	64.12	63.18	62.81	63.35	65.52	63.06	63.59	64.48	64.48
FeO	29.74	30.07	29.96	29.94	29.93	29.70	29.56	29.75	30.04	29.92	29.91	30.08	30.03
V_2O_3	0.07	0.07	0.06	0.06	0.10	0.05	0.09	0.07	0.02	0.01	0.07	0.02	0.05
NiO	0.36	0.32	0.35	0.31	0.32	0.28	0.40	0.29	0.30	0.34	0.26	0.31	0.30
ZnO													
CoO													
Na_2O													
K_2O													

CaO													
Total	96.78	95.73	96.73	97.03	96.89	96.31	95.86	95.76	97.13	96.84	96.60	97.15	96.84
Cation													
Al	0.007	0.002	0.003	0.004	0.011	0.002	0.009	0.013	0.009	0.012	0.008	0.009	0.013
Mn	0.022	0.022	0.001	0.014	0.015	0.010	0.004	0.013	0.001	0.000	0.005	0.003	0.005
Ti	0.004	0.130	0.017	0.019	0.014	0.006	0.010	0.025	0.025	0.002	0.007	0.006	0.059
Cr	0.832	0.541	0.538	0.530	0.543	0.740	0.712	0.450	0.231	0.665	0.641	0.509	0.366
Mg	0.036	0.030	0.037	0.031	0.028	0.025	0.025	0.054	0.037	0.156	0.027	0.013	0.056
Si	0.015	0.049	0.048	0.021	0.016	0.015	0.017	0.073	0.039	0.151	0.027	0.046	0.033
Fe^{3+}	15.076	15.054	15.290	15.351	15.321	15.187	15.167	15.299	15.620	15.009	15.237	15.366	15.406
Fe^{2+}	7.901	8.074	7.965	7.939	7.948	7.933	7.933	7.983	7.959	7.915	7.965	7.966	7.974
V	0.016	0.014	0.013	0.012	0.022	0.010	0.020	0.014	0.004	0.003	0.015	0.004	0.010
Ni	0.091	0.082	0.089	0.080	0.082	0.072	0.104	0.076	0.075	0.087	0.068	0.078	0.077
Zn													
Co													
Na													
K													
Ca													
Total	24.000	24.000	24.000	24.000	24.000	24.000	24.000	24.000	24.000	24.000	24.000	24.000	24.000
Mg#	0.00	0.00	0.00	0.00	0.00	0.00	0.00	0.01	0.00	0.02	0.00	0.00	0.01
Cr#	0.99	1.00	0.99	0.99	0.98	1.00	0.99	0.97	0.96	0.98	0.99	0.98	0.97
Fe^{3+}/R^{3+}	0.95	0.97	0.97	0.97	0.97	0.95	0.95	0.97	0.98	0.96	0.96	0.97	0.98

Sample number	MIC/16/44	MIC/16/44	MIC/16/44	MIC/16/44	MIC/16/44	MIC/16/44	MIC/16/44	MIC/16/44	MIC/16/44	MIC/16/44	MIC/16/44	MIC/16/44	MIC/16/44
Location	Tua Dungri	Tua Dungri	Tua Dungri	Tua Dungri	Tua Dungri	Tua Dungri	Tua Dungri	Tua Dungri	Tua Dungri	Tua Dungri	Tua Dungri	Tua Dungri	Tua Dungri
EPMA point	145 / 1 .	148 / 1 .	149 / 1 .	150 / 1 .	151 / 1 .	157 / 1 .	159 / 1 .	160 / 1 .	162 / 1 .	166 / 1 .	168 / 1 .	169 / 1 .	170 / 1 .
Mineral	Chr mag-netite	Chr mag-netite	Chr mag-netite	Chr mag-netite	Chr mag-netite	Chr mag-netite	Chr mag-netite	Chr mag-netite	Chr mag-netite	Chr mag-netite	Chr mag-netite	Chr mag-netite	Chr mag-netite
Type	Type-V	Type-V	Type-V	Type-V	Type-V	Type-V	Type-V	Type-V	Type-V	Type-V	Type-V	Type-V	Type-V
Al_2O_3	0.03	0.02	0.17	0.04	0.02	0.03	0.14	0.02	0.10	0.01	0.02	0.02	0.09
MnO	0.02	0.11	0.01	0.14	0.09	0.11	0.06	0.04	0.03	0.06	0.19	0.14	0.07
TiO_2	0.02	0.05	0.00	0.04	0.01	0.05	0.01	0.02	0.05	0.02	0.02	0.01	0.06
Cr_2O_3	1.23	3.32	1.62	3.04	3.48	2.95	2.80	3.50	3.13	1.19	4.17	4.02	3.27
MgO	0.83	0.06	1.88	0.14	0.05	0.02	1.07	0.02	2.92	0.06	0.05	0.07	5.68
SiO_2	0.60	0.07	1.39	0.21	0.08	0.05	0.50	0.07	2.13	0.05	0.04	0.01	4.45

Fe_2O_3	63.69	63.83	60.48	62.95	63.23	63.54	62.70	63.08	61.52	64.97	62.08	62.76	56.01
FeO	28.94	30.02	27.79	29.57	29.95	29.88	28.65	29.76	28.80	29.52	29.49	29.83	27.06
V_2O_3	0.02	0.09	0.02	0.06	0.11	0.08	0.06	0.04	0.01	0.04	0.08	0.17	0.01
NiO	0.35	0.58	0.34	0.58	0.51	0.40	0.44	0.54	0.42	0.41	0.51	0.59	0.36
ZnO													
CoO													
Na_2O													
K_2O													
CaO													
Total	95.73	98.15	93.69	96.75	97.51	97.11	96.44	97.08	99.11	96.34	96.64	97.61	97.06
Cation													
Al	0.012	0.008	0.066	0.013	0.009	0.010	0.054	0.008	0.036	0.005	0.008	0.008	0.031
Mn	0.006	0.028	0.003	0.036	0.023	0.031	0.017	0.010	0.007	0.015	0.051	0.037	0.017
Ti	0.005	0.012	0.000	0.008	0.001	0.012	0.002	0.004	0.010	0.004	0.004	0.002	0.013
Cr	0.310	0.823	0.411	0.764	0.866	0.738	0.698	0.878	0.744	0.301	1.048	1.001	0.769
Mg	0.395	0.027	0.898	0.064	0.023	0.011	0.501	0.010	1.307	0.030	0.026	0.032	2.517
Si	0.191	0.020	0.445	0.065	0.024	0.015	0.159	0.021	0.640	0.017	0.012	0.003	1.323
Fe^{3+}	15.275	15.051	14.620	15.037	15.003	15.148	14.885	15.038	13.913	15.624	14.859	14.875	12.521
Fe^{2+}	7.712	7.866	7.464	7.851	7.897	7.916	7.557	7.886	7.238	7.888	7.845	7.857	6.722
V	0.003	0.018	0.004	0.013	0.024	0.017	0.013	0.008	0.002	0.009	0.018	0.035	0.003
Ni	0.089	0.147	0.088	0.148	0.130	0.103	0.112	0.137	0.102	0.106	0.129	0.149	0.085
Zn													
Co													
Na													
K													
Ca													
Total	24.000	24.000	24.000	24.000	24.000	24.000	24.000	24.000	24.000	24.000	24.000	24.000	24.000
Mg#	0.05	0.00	0.11	0.01	0.00	0.00	0.06	0.00	0.15	0.00	0.00	0.00	0.27
Cr#	0.96	0.99	0.86	0.98	0.99	0.99	0.93	0.99	0.95	0.98	0.99	0.99	0.96
Fe^{3+}/R^{3+}	0.98	0.95	0.97	0.95	0.94	0.95	0.95	0.94	0.95	0.98	0.93	0.94	0.94

Sample number	MIC/16/44	MIC/16/44	MIC/16/44	MIC/16/44	MIC/16/44	MIC/16/44	SHB/18/20	SHB/18/20	SHB/18/20	SHB/18/20	SHB/18/20	SHB/18/20	SHB/18/20
Location	Tua Dungri	Tua Dungri	Tua Dungri	Tua Dungri	Tua Dungri	Tua Dungri	Kapili	Kapili	Kapili	Kapili	Kapili	Kapili	Kapili
EPMA point	171 / 1 .	172 / 1 .	173 / 1 .	174 / 1 .	175 / 1 .	176 / 1 .	2 / 1 .	4 / 1 .	5 / 1 .	6 / 1 .	9 / 1 .	11 / 1 .	15 / 1 .
Mineral	Chr mag-	Chr mag-	Chr mag-	Chr mag-	Chr mag-	Chr mag-	Chr mag-	Chr mag-	Chr mag-	Chr mag-	Chr mag-	Chr mag-	Chr mag-

Type	netite Type-V	netite Type-V	netite Type-V	netite Type-V	netite Type-V	netite Type-V	netite Type-V	netite Type-V	netite Type-V	netite Type-V	netite Type-V	netite Type-V	netite Type-V
Al_2O_3	0.02	0.02	0.04	0.03	0.03	0.10	0.02	0.31	0.51	0.37	0.15	0.17	0.20
MnO	0.03	0.16	0.19	0.24	0.00	0.09	0.22	0.67	0.25	0.75	0.19	0.21	0.13
TiO_2	0.01	0.02	0.03	0.05	0.09	0.01	0.07	2.78	0.24	4.54	0.23	0.11	0.52
Cr_2O_3	2.40	3.97	4.76	4.65	2.23	2.86	5.13	5.56	6.01	6.15	4.96	5.19	4.36
MgO	0.21	0.07	0.06	0.10	0.09	3.77	0.05	0.11	0.06	0.08	0.02	0.07	0.07
SiO_2	0.21	0.00	0.05	0.04	0.07	2.80	0.00	0.08	0.04	0.00	0.00	0.01	0.04
Fe_2O_3	63.27	62.67	61.99	61.71	64.32	62.04	61.54	54.42	59.87	51.09	60.22	61.63	62.52
FeO	29.40	29.60	29.69	29.48	29.85	28.91	30.27	32.15	30.63	33.71	30.50	30.85	31.73
V_2O_3	0.01	0.10	0.01	0.07	0.02	0.02	0.12	0.24	0.24	0.21	0.31	0.25	0.22
NiO	0.36	0.55	0.40	0.49	0.40	0.39							
ZnO							0.00	0.18	0.35	0.34	0.08	0.03	0.00
CoO													
Na_2O													
K_2O													
CaO													
Total	95.91	97.16	97.23	96.85	97.10	100.98	97.42	96.51	98.19	97.23	96.65	98.51	99.79
Cation													
Al	0.009	0.007	0.016	0.010	0.013	0.034	0.009	0.116	0.186	0.135	0.054	0.062	0.074
Mn	0.007	0.042	0.051	0.064	0.000	0.021	0.057	0.180	0.066	0.199	0.051	0.055	0.034
Ti	0.001	0.005	0.008	0.013	0.022	0.002	0.015	0.662	0.056	1.071	0.054	0.026	0.121
Cr	0.607	0.994	1.190	1.166	0.558	0.660	1.280	1.392	1.483	1.526	1.245	1.278	1.060
Mg	0.100	0.031	0.027	0.046	0.040	1.645	0.024	0.051	0.027	0.036	0.009	0.031	0.032
Si	0.067	0.001	0.014	0.013	0.022	0.819	0.001	0.025	0.011	0.000	0.000	0.004	0.012
Fe^{3+}	15.244	14.925	14.742	14.730	15.331	13.653	14.607	12.967	14.052	12.064	14.399	14.451	14.465
Fe^{2+}	7.871	7.833	7.847	7.819	7.908	7.070	7.983	8.513	7.989	8.847	8.105	8.038	8.158
V	0.001	0.020	0.003	0.014	0.003	0.003	0.024	0.050	0.049	0.044	0.065	0.050	0.045
Ni	0.093	0.141	0.102	0.125	0.102	0.091							
Zn							0.000	0.043	0.082	0.078	0.019	0.007	0.000
Co													
Na													
K													
Ca													
Total	24.000	24.000	24.000	24.000	24.000	24.000	24.000	24.000	24.000	24.000	24.000	24.000	24.000
Mg#	0.01	0.00	0.00	0.01	0.01	0.19	0.00	0.01	0.00	0.00	0.00	0.00	0.00
Cr#	0.99	0.99	0.99	0.99	0.98	0.95	0.99	0.92	0.89	0.92	0.96	0.95	0.94

Fe^{3+}/R^{3+}	0.96	0.94	0.92	0.93	0.96	0.95	0.92	0.90	0.89	0.88	0.92	0.92	0.93
Sample number	SHB/18/20	SHB/18/20	SHB/18/20	SHB/18/20	SHB/18/20	SHB/18/20	SHB/18/20	SHB/18/20	SHB/18/20	SHB/18/25	SHB/18/25	SHB/18/25	SHB/18/25
Location	Kapili	Kapili	Kapili	Kapili	Kapili	Kapili	Kapili	Kapili	Kapili	Kapili	Kapili	Kapili	Kapili
EPMA point	17 / 1 .	18 / 1 .	20 / 1 .	21 / 1 .	22 / 1 .	23 / 1 .	24 / 1 .	25 / 1 .	27 / 1 .	31 / 1 .	32 / 1 .	34 / 1 .	35 / 1 .
Mineral	Chr mag-netite	Chr mag-netite	Chr mag-netite	Chr mag-netite	Chr mag-netite	Chr mag-netite	Chr mag-netite	Chr mag-netite	Chr mag-netite	Chr mag-netite	Chr mag-netite	Chr mag-netite	Chr mag-netite
Type	Type-V	Type-V	Type-V	Type-V	Type-V	Type-V	Type-V	Type-V	Type-V	Type-V	Type-V	Type-V	Type-V
Al_2O_3	0.21	0.23	0.57	0.03	0.10	0.07	0.28	0.47	0.02	1.24	1.35	0.47	0.37
MnO	0.15	0.26	0.68	0.12	0.08	0.08	0.00	0.63	0.16	1.60	1.11	0.87	0.57
TiO_2	0.24	0.16	0.54	0.07	0.22	0.11	0.12	3.11	0.13	2.94	2.95	0.35	0.35
Cr_2O_3	4.44	4.52	9.12	4.68	4.55	4.73	4.54	4.81	4.14	10.26	10.04	8.55	8.99
MgO	0.05	0.04	0.06	0.06	0.09	0.06	0.09	0.09	0.07	0.21	0.15	0.14	0.12
SiO_2	0.02	0.05	0.05	0.00	0.05	0.08	0.00	0.02	0.02	0.00	0.03	0.02	0.04
Fe_2O_3	61.49	62.62	54.75	62.37	61.47	62.30	62.53	54.80	61.83	48.80	47.03	54.15	55.23
FeO	30.88	31.16	30.22	30.37	30.86	30.71	30.51	32.84	30.23	31.55	31.84	29.22	30.12
V_2O_3	0.28	0.23	0.30	0.17	0.26	0.17	0.16	0.27	0.20	0.33	0.40	0.34	0.30
NiO													
ZnO	0.05	0.02	0.28	0.32	0.00	0.29	0.51	0.00	0.11	0.38	0.12	0.00	0.00
CoO													
Na_2O													
K_2O													
CaO													
Total	97.82	99.28	96.58	98.17	97.67	98.58	98.74	97.05	96.90	97.32	95.03	94.11	96.09
Cation													
Al	0.078	0.082	0.213	0.009	0.036	0.024	0.104	0.175	0.009	0.456	0.508	0.181	0.139
Mn	0.039	0.067	0.181	0.032	0.021	0.021	0.000	0.169	0.042	0.422	0.300	0.239	0.153
Ti	0.057	0.038	0.127	0.016	0.051	0.025	0.028	0.737	0.030	0.688	0.707	0.085	0.083
Cr	1.102	1.105	2.281	1.158	1.131	1.165	1.117	1.197	1.039	2.527	2.529	2.194	2.260
Mg	0.024	0.019	0.029	0.026	0.040	0.028	0.043	0.044	0.032	0.099	0.072	0.066	0.057
Si	0.007	0.014	0.016	0.000	0.015	0.024	0.000	0.005	0.006	0.000	0.009	0.008	0.013
Fe^{3+}	14.520	14.568	13.030	14.699	14.540	14.609	14.627	12.975	14.758	11.436	11.278	13.224	13.220
Fe^{2+}	8.104	8.056	7.993	7.953	8.112	8.003	7.931	8.642	8.018	8.217	8.484	7.931	8.012
V	0.057	0.047	0.063	0.034	0.054	0.035	0.032	0.057	0.041	0.069	0.085	0.072	0.063
Ni													
Zn	0.012	0.004	0.066	0.074	0.000	0.066	0.118	0.000	0.026	0.087	0.029	0.000	0.000

Co													
Na													
K													
Ca													
Total	24.000	24.000	24.000	24.000	24.000	24.000	24.000	24.000	24.000	24.000	24.000	24.000	24.000
Mg#	0.00	0.00	0.00	0.00	0.00	0.00	0.01	0.01	0.00	0.01	0.01	0.01	0.01
Cr#	0.93	0.93	0.91	0.99	0.97	0.98	0.91	0.87	0.99	0.85	0.83	0.92	0.94
Fe^{3+}/R^{3+}	0.92	0.92	0.84	0.93	0.93	0.92	0.92	0.90	0.93	0.79	0.79	0.85	0.85

Sample number	SHB/18/25	SHB/18/25	SHB/18/25	SHB/18/25	SHB/18/25	SHB/18/25	SHB/18/36	SHB/18/37	SHB/18/37	SHB/18/37	SHB/18/37	SHB/18/37	SHB/18/37
Location	Kapili	Kapili	Kapili	Kapili	Kapili	Kapili	Kapili	Kapili	Kapili	Kapili	Kapili	Kapili	Kapili
EPMA point	36 / 1 .	39 / 1 .	40 / 1 .	44 / 1 .	45 / 1 .	49 / 1 .	12 / 1 .	1 / 1 .	2 / 1 .	3 / 1 .	6 / 1 .	7 / 1 .	8 / 1 .
Mineral	Chr mag-netite	Chr mag-netite	Chr mag-netite	Chr mag-netite	Chr mag-netite	Chr mag-netite	Chr mag-netite	Chr mag-netite	Chr mag-netite	Chr mag-netite	Chr mag-netite	Chr mag-netite	Chr mag-netite
Type	Type-V	Type-V	Type-V	Type-V	Type-V	Type-V	Type-V	Type-V	Type-V	Type-V	Type-V	Type-V	Type-V
Al_2O_3	0.38	1.14	0.99	1.24	1.39	1.53	0.03	0.00	0.09	0.09	0.09	0.22	0.37
MnO	0.42	1.26	1.15	1.64	1.07	1.37	0.40	0.21	0.58	0.41	0.47	0.45	1.30
TiO_2	0.27	2.59	1.95	3.61	2.23	3.36	1.44	0.02	1.30	0.13	0.11	0.29	2.58
Cr_2O_3	8.86	10.67	10.41	10.09	9.77	10.27	3.36	8.24	8.91	8.72	9.01	9.55	12.11
MgO	0.07	0.20	0.15	0.16	0.17	0.25	0.10	0.10	0.14	0.13	0.08	0.08	0.19
SiO_2	0.04	0.01	0.08	0.00	0.02	0.00	0.01	0.07	0.00	0.03	0.00	0.09	0.00
Fe_2O_3	55.64	48.36	49.96	47.11	48.50	48.02	61.49	59.60	55.95	58.58	56.90	55.52	48.25
FeO	30.20	31.76	31.42	32.48	31.08	32.29	31.51	30.29	32.19	31.61	30.43	30.91	31.92
V_2O_3	0.33	0.40	0.39	0.41	0.36	0.37	0.08	0.04	0.45	0.52	0.36	0.49	0.54
NiO													
ZnO	0.26	0.00	0.02	0.02	0.00	0.55	0.00	0.41	0.00	0.06	0.07	0.28	0.28
CoO													
Na_2O													
K_2O													
CaO													
Total	96.46	96.40	96.52	96.75	94.59	98.01	98.43	98.97	99.60	100.27	97.51	97.90	97.55
Cation													
Al	0.142	0.421	0.368	0.456	0.525	0.556	0.011	0.000	0.032	0.031	0.032	0.082	0.137
Mn	0.113	0.337	0.305	0.434	0.290	0.357	0.107	0.054	0.150	0.105	0.125	0.120	0.344
Ti	0.065	0.613	0.461	0.849	0.536	0.779	0.338	0.004	0.299	0.030	0.027	0.069	0.604
Cr	2.221	2.652	2.589	2.496	2.472	2.506	0.829	2.019	2.162	2.105	2.238	2.361	2.988

Mg	0.031	0.094	0.072	0.076	0.082	0.116	0.048	0.044	0.064	0.058	0.037	0.035	0.090
Si	0.011	0.003	0.026	0.000	0.006	0.000	0.003	0.022	0.001	0.010	0.000	0.028	0.000
Fe^{3+}	13.278	11.444	11.828	11.097	11.688	11.152	14.430	13.902	12.932	13.467	13.456	13.058	11.331
Fe^{2+}	8.010	8.353	8.265	8.502	8.324	8.333	8.218	7.852	8.269	8.075	7.996	8.080	8.330
V	0.069	0.084	0.081	0.084	0.077	0.076	0.016	0.009	0.092	0.105	0.074	0.102	0.112
Ni													
Zn	0.060	0.000	0.005	0.005	0.000	0.124	0.000	0.093	0.000	0.013	0.016	0.066	0.064
Co													
Na													
K													
Ca													
Total	24.000	24.000	24.000	24.000	24.000	24.000	24.000	24.000	24.000	24.000	24.000	24.000	24.000
Mg#	0.00	0.01	0.01	0.01	0.01	0.01	0.01	0.01	0.01	0.01	0.00	0.00	0.01
Cr#	0.94	0.86	0.88	0.85	0.82	0.82	0.99	1.00	0.99	0.99	0.99	0.97	0.96
Fe^{3+}/R^{3+}	0.85	0.79	0.80	0.79	0.80	0.78	0.94	0.87	0.85	0.86	0.86	0.84	0.78

Sample number	SHB/18/37	SHB/18/37	SHB/18/37	SHB/18/37	SHB/18/39	SHB/18/39	SHB/18/39	SHB/18/39	SHB/18/39	SHB/18/39	SHB/18/39	SHB/18/39	SHB/18/39
Location	Kapili	Kapili	Kapili	Kapili	Kapili	Kapili	Kapili	Kapili	Kapili	Kapili	Kapili	Kapili	Kapili
EPMA point	9 / 1 .	12 / 1 .	13 / 1 .	14 / 1 .	17 / 1 .	18 / 1 .	19 / 1 .	20 / 1 .	21 / 1 .	27 / 1 .	28 / 1 .	29 / 1 .	30 / 1 .
Mineral	Chr mag-netite	Chr mag-netite	Chr mag-netite	Chr mag-netite	Chr mag-netite	Chr mag-netite	Chr mag-netite	Chr mag-netite	Chr mag-netite	Chr mag-netite	Chr mag-netite	Chr mag-netite	Chr mag-netite
Type	Type-V	Type-V	Type-V	Type-V	Type-V	Type-V	Type-V	Type-V	Type-V	Type-V	Type-V	Type-V	Type-V
Al_2O_3	0.04	0.05	0.16	0.16	1.41	0.68	1.25	1.61	1.12	1.42	0.30	1.54	0.22
MnO	0.46	0.40	0.66	0.37	0.40	0.59	0.46	0.47	0.30	0.42	0.49	0.39	0.20
TiO_2	0.05	0.05	0.85	0.33	1.12	2.76	0.82	0.81	0.42	0.61	4.65	0.78	0.61
Cr_2O_3	8.84	8.76	8.57	8.07	6.88	6.58	8.08	6.79	6.35	6.76	6.59	6.62	6.64
MgO	0.05	0.07	0.08	0.09	0.10	0.11	0.14	0.11	0.07	0.06	0.08	0.08	0.05
SiO_2	0.04	0.05	0.00	0.01	0.04	0.09	0.10	0.01	0.03	0.01	0.05	0.07	0.09
Fe_2O_3	57.61	57.23	56.05	57.40	55.14	50.90	53.38	55.94	55.53	55.53	48.29	55.35	56.74
FeO	30.37	30.09	31.38	30.91	31.87	31.80	30.39	31.42	30.17	30.99	33.51	30.88	30.62
V_2O_3	0.27	0.30	0.53	0.49	0.52	0.42	0.35	0.45	0.39	0.44	0.30	0.43	0.33
NiO													
ZnO	0.15	0.38	0.22	0.33	0.16	0.28	0.34	0.18	0.08	0.00	0.22	0.51	0.15
CoO													
Na_2O													
K_2O													

CaO													
Total	97.88	97.37	98.50	98.17	97.63	94.21	95.31	97.81	94.46	96.24	94.46	96.64	95.65
Cation													
Al	0.013	0.019	0.059	0.060	0.519	0.260	0.470	0.589	0.427	0.529	0.113	0.569	0.083
Mn	0.121	0.107	0.174	0.097	0.105	0.162	0.123	0.124	0.082	0.112	0.134	0.105	0.055
Ti	0.012	0.013	0.200	0.078	0.261	0.672	0.196	0.190	0.102	0.145	1.127	0.183	0.146
Cr	2.190	2.181	2.105	1.992	1.694	1.681	2.036	1.667	1.619	1.688	1.681	1.646	1.681
Mg	0.022	0.033	0.037	0.044	0.046	0.052	0.066	0.052	0.033	0.029	0.039	0.036	0.022
Si	0.014	0.014	0.000	0.003	0.014	0.029	0.033	0.004	0.009	0.004	0.015	0.022	0.029
Fe^{3+}	13.581	13.560	13.110	13.481	12.920	12.387	12.814	13.077	13.485	13.208	11.729	13.104	13.675
Fe^{2+}	7.957	7.922	8.155	8.067	8.299	8.600	8.108	8.162	8.143	8.193	9.045	8.125	8.202
V	0.055	0.062	0.109	0.102	0.106	0.090	0.074	0.093	0.083	0.093	0.064	0.090	0.070
Ni													
Zn	0.035	0.089	0.051	0.077	0.036	0.067	0.080	0.042	0.018	0.000	0.052	0.119	0.036
Co													
Na													
K													
Ca													
Total	24.000	24.000	24.000	24.000	24.000	24.000	24.000	24.000	24.000	24.000	24.000	24.000	24.000
Mg#	0.00	0.00	0.00	0.01	0.01	0.01	0.01	0.01	0.00	0.00	0.00	0.00	0.00
Cr#	0.99	0.99	0.97	0.97	0.77	0.87	0.81	0.74	0.79	0.76	0.94	0.74	0.95
Fe^{3+}/R^{3+}	0.86	0.86	0.86	0.87	0.85	0.86	0.84	0.85	0.87	0.86	0.87	0.86	0.89

Sample number	SHB/18/39	SHB/18/39	SHB/19-12/78	SHB/19-12/78	SHB/19-12/78	SHB/19-12/78	SHB/19-12/78	SHB/19-12/78	SHB/19-12/78	SHB/19-12/78	SHB/19-12/78	SHB/19-12/78	SHB/19-12/78
Location	Kapili	Kapili	Kapili	Kapili	Kapili	Kapili	Kapili	Kapili	Kapili	Kapili	Kapili	Kapili	Kapili
EPMA point	31 / 1 .	32 / 1 .	155 / 1 .	156 / 1 .	157 / 1 .	158 / 1 .	159 / 1 .	162 / 1 .	163 / 1 .	164 / 1 .	165 / 1 .	166 / 1 .	167 / 1 .
Mineral	Chr mag-netite	Chr mag-netite	Chr mag-netite	Chr mag-netite	Chr mag-netite	Chr mag-netite	Chr mag-netite	Chr mag-netite	Chr mag-netite	Chr mag-netite	Chr mag-netite	Chr mag-netite	Chr mag-netite
Type	Type-V	Type-V	Type-V	Type-V	Type-V	Type-V	Type-V	Type-V	Type-V	Type-V	Type-V	Type-V	Type-V
Al_2O_3	1.34	0.41	0.17	0.23	0.23	0.18	0.08	0.06	0.42	0.55	0.50	0.14	0.24
MnO	0.31	0.34	0.49	1.37	0.67	0.54	0.52	0.56	1.01	0.77	0.68	0.74	0.48
TiO_2	0.39	0.64	0.64	5.27	0.91	0.95	0.58	0.34	1.45	1.53	1.45	0.53	0.83
Cr_2O_3	6.47	6.03	6.86	7.33	7.63	7.33	6.23	6.72	10.15	10.87	9.57	6.98	6.63
MgO	0.08	0.06	0.26	0.41	0.40	0.40	0.40	1.47	0.49	0.67	0.60	0.26	0.23
SiO_2	0.04	0.09	0.05	0.00	0.08	0.03	0.07	1.76	0.01	0.06	0.07	0.10	0.03
Fe_2O_3	56.35	57.37	58.22	49.10	57.57	56.87	57.83	54.58	52.59	51.20	53.37	58.06	56.68

FeO	30.73	30.94	30.12	33.07	30.51	29.98	28.03	29.53	29.76	29.79	30.39	29.61	29.92
V_2O_3	0.46	0.42	0.35	0.31	0.37	0.34	0.31	0.26	0.37	0.37	0.35	0.31	0.36
NiO			0.47	0.58	0.42	0.59	0.15	0.39	0.65	0.57	0.38	0.57	0.55
ZnO	0.27	0.10	0.15	0.23	0.13	0.00	0.00	0.18	0.06	0.07	0.00	0.05	0.00
CoO			0.05	0.06	0.06	0.00	0.10	0.02	0.00	0.00	0.14	0.16	0.01
Na_2O			0.02	0.02	0.00	0.05	0.02	0.00	0.01	0.05	0.00	0.00	0.01
K_2O			0.00	0.00	0.00	0.00	0.00	0.00	0.00	0.00	0.00	0.00	0.00
CaO			0.02	0.01	0.02	0.00	1.21	0.03	0.02	0.01	0.00	0.02	0.00
Total	96.44	96.39	97.87	97.99	99.00	97.25	95.53	95.89	96.97	96.51	97.48	97.52	95.98
Cation													
Al	0.499	0.152	0.061	0.085	0.085	0.066	0.028	0.020	0.155	0.203	0.184	0.053	0.091
Mn	0.082	0.093	0.131	0.359	0.174	0.142	0.141	0.149	0.269	0.204	0.178	0.197	0.131
Ti	0.093	0.152	0.150	1.229	0.211	0.225	0.140	0.080	0.341	0.362	0.340	0.126	0.199
Cr	1.615	1.514	1.696	1.799	1.859	1.818	1.572	1.666	2.516	2.699	2.357	1.732	1.670
Mg	0.037	0.027	0.121	0.189	0.186	0.187	0.189	0.687	0.227	0.315	0.277	0.119	0.107
Si	0.012	0.030	0.015	0.000	0.025	0.010	0.021	0.551	0.002	0.019	0.021	0.032	0.011
Fe^{3+}	13.388	13.709	13.697	11.466	13.359	13.435	13.879	12.888	12.415	12.105	12.517	13.709	13.591
Fe^{2+}	8.115	8.215	7.875	8.582	7.868	7.871	7.477	7.748	7.808	7.828	7.921	7.769	7.973
V	0.096	0.087	0.072	0.064	0.074	0.070	0.066	0.055	0.076	0.076	0.073	0.064	0.076
Ni			0.119	0.146	0.104	0.150	0.039	0.099	0.164	0.144	0.096	0.144	0.142
Zn	0.063	0.023	0.033	0.052	0.029	0.000	0.000	0.042	0.013	0.017	0.000	0.012	0.000
Co			0.013	0.015	0.015	0.000	0.025	0.005	0.000	0.001	0.034	0.039	0.003
Na			0.011	0.010	0.002	0.026	0.009	0.000	0.006	0.022	0.000	0.000	0.006
K			0.000	0.000	0.000	0.000	0.000	0.000	0.001	0.000	0.000	0.000	0.000
Ca			0.007	0.005	0.008	0.000	0.414	0.010	0.008	0.003	0.000	0.005	0.000
Total	24.000	24.000	24.000	24.000	24.000	24.000	24.000	24.000	24.000	24.000	24.000	24.000	24.000
Mg#	0.00	0.00	0.02	0.02	0.02	0.02	0.02	0.08	0.03	0.04	0.03	0.02	0.01
Cr#	0.76	0.91	0.97	0.95	0.96	0.96	0.98	0.99	0.94	0.93	0.93	0.97	0.95
Fe^{3+}/R^{3+}	0.86	0.89	0.89	0.86	0.87	0.88	0.90	0.88	0.82	0.81	0.83	0.88	0.89

Sample number	SHB/19-12/78	SHB/19-12/78	SHB/19-12/78	SHB/19-12/78	SHB/19-12/78	SHB/19-12/78	SHB/19-12/78	SHB/19-12/78	SHB/19-12/78	SHB/19-12/78	SHB/19-12/78	SHB/19-12/79	SHB/19-12/79
Location	Kapili	Kapili	Kapili	Kapili	Kapili	Kapili	Kapili	Kapili	Kapili	Kapili	Kapili	Kapili	Kapili
EPMA point	168 / 1 .	169 / 1 .	170 / 1 .	171 / 1 .	172 / 1 .	177 / 1 .	178 / 1 .	179 / 1 .	180 / 1 .	181 / 1 .	182 / 1 .	30 / 1 .	33 / 1 .
Mineral	Chr mag-netite	Chr mag-netite	Chr mag-netite	Chr mag-netite	Chr mag-netite	Chr mag-netite	Chr mag-netite	Chr mag-netite	Chr mag-netite	Chr mag-netite	Chr mag-netite	Chr mag-netite	Chr mag-netite
Type	Type-V	Type-V	Type-V	Type-V	Type-V	Type-V	Type-V	Type-V	Type-V	Type-V	Type-V	Type-V	Type-V

Al_2O_3	0.28	0.28	0.31	0.18	0.00	0.08	0.04	0.26	0.27	0.12	0.16	0.36	0.14
MnO	0.77	0.43	0.74	0.59	0.28	0.60	0.83	0.86	0.56	0.45	0.55	0.93	0.54
TiO_2	0.86	1.11	1.18	0.72	0.17	0.55	2.59	1.05	1.19	0.59	0.61	1.39	0.59
Cr_2O_3	7.19	7.20	7.27	6.61	5.42	6.77	6.41	7.36	7.68	6.67	6.60	8.78	5.10
MgO	0.33	0.47	0.40	0.16	0.15	0.16	0.30	0.37	0.50	0.15	0.20	0.51	0.32
SiO_2	0.04	0.02	0.06	0.05	0.04	0.07	0.23	0.07	0.04	0.01	0.03	0.03	0.00
Fe_2O_3	56.76	55.00	56.42	56.97	59.71	58.61	54.81	56.08	56.87	58.04	58.98	55.18	60.47
FeO	29.84	29.57	30.23	29.90	29.56	30.15	31.67	29.63	30.71	29.82	30.20	29.74	29.72
V_2O_3	0.35	0.37	0.34	0.36	0.32	0.38	0.30	0.36	0.37	0.32	0.34	0.26	0.25
NiO	0.38	0.50	0.58	0.36	0.48	0.45	0.49	0.63	0.30	0.55	0.48	0.61	0.46
ZnO	0.13	0.04	0.00	0.16	0.01	0.22	0.21	0.00	0.00	0.18	0.34	0.20	0.00
CoO	0.00	0.03	0.00	0.00	0.09	0.15	0.00	0.18	0.23	0.00	0.00	0.08	0.11
Na_2O	0.04	0.00	0.00	0.00	0.00	0.00	0.02	0.00	0.00	0.03	0.00	0.04	0.04
K_2O	0.00	0.00	0.00	0.00	0.00	0.00	0.00	0.01	0.00	0.01	0.00	0.01	0.00
CaO	0.00	0.01	0.00	0.01	0.02	0.01	0.02	0.03	0.00	0.02	0.01	0.00	0.01
Total	96.98	95.01	97.51	96.06	96.24	98.18	97.90	96.87	98.72	96.95	98.49	98.12	97.75
Cation													
Al	0.105	0.107	0.113	0.068	0.000	0.029	0.016	0.095	0.099	0.044	0.058	0.130	0.053
Mn	0.206	0.116	0.196	0.160	0.075	0.158	0.219	0.229	0.146	0.119	0.144	0.245	0.142
Ti	0.205	0.267	0.277	0.172	0.040	0.128	0.607	0.250	0.277	0.141	0.143	0.325	0.138
Cr	1.790	1.828	1.798	1.666	1.368	1.671	1.580	1.833	1.876	1.666	1.624	2.155	1.263
Mg	0.153	0.223	0.185	0.075	0.071	0.075	0.137	0.171	0.229	0.068	0.090	0.237	0.151
Si	0.014	0.005	0.018	0.014	0.011	0.021	0.072	0.023	0.011	0.004	0.009	0.009	0.000
Fe^{3+}	13.449	13.287	13.286	13.666	14.329	13.767	12.862	13.300	13.220	13.802	13.805	12.888	14.252
Fe^{2+}	7.858	7.939	7.910	7.971	7.884	7.869	8.258	7.809	7.935	7.881	7.855	7.720	7.784
V	0.073	0.078	0.071	0.076	0.067	0.078	0.061	0.076	0.076	0.066	0.069	0.053	0.052
Ni	0.095	0.128	0.145	0.091	0.123	0.112	0.123	0.159	0.074	0.140	0.119	0.151	0.116
Zn	0.031	0.010	0.000	0.037	0.003	0.050	0.048	0.000	0.000	0.041	0.078	0.045	0.000
Co	0.000	0.007	0.000	0.000	0.022	0.037	0.000	0.045	0.056	0.000	0.000	0.021	0.028
Na	0.020	0.000	0.000	0.000	0.000	0.000	0.012	0.000	0.000	0.016	0.000	0.018	0.019
K	0.001	0.000	0.000	0.000	0.001	0.000	0.000	0.002	0.000	0.003	0.000	0.002	0.000
Ca	0.000	0.005	0.000	0.003	0.008	0.004	0.005	0.008	0.000	0.008	0.005	0.001	0.002
Total	24.000	24.000	24.000	24.000	24.000	24.000	24.000	24.000	24.000	24.000	24.000	24.000	24.000
Mg#	0.02	0.03	0.02	0.01	0.01	0.01	0.02	0.02	0.03	0.01	0.01	0.03	0.02
Cr#	0.94	0.94	0.94	0.96	1.00	0.98	0.99	0.95	0.95	0.97	0.97	0.94	0.96
Fe^{3+}/R^{3+}	0.88	0.87	0.87	0.89	0.91	0.89	0.89	0.87	0.87	0.89	0.89	0.85	0.92

Sample number	SHB/19-12/79	SHB/19-12/79	SHB/19-12/79	SHB/19-12/79	SHB/19-12/79	SHB/19-12/79	SHB/19-12/79	SHB/19-12/79	SHB/19-12/79	SHB/19-12/79	SHB/19-12/79	SHB/19-12/79	SHB/19-12/79
Location	Kapili	Kapili	Kapili	Kapili	Kapili	Kapili	Kapili	Kapili	Kapili	Kapili	Kapili	Kapili	Kapili
EPMA point	34 / 1 .	35 / 1 .	36 / 1 .	37 / 1 .	38 / 1 .	39 / 1 .	40 / 1 .	41 / 1 .	42 / 1 .	43 / 1 .	44 / 1 .	45 / 1 .	46 / 1 .
Mineral	Chr mag-netite	Chr mag-netite	Chr mag-netite	Chr mag-netite	Chr mag-netite	Chr mag-netite	Chr mag-netite	Chr mag-netite	Chr mag-netite	Chr mag-netite	Chr mag-netite	Chr mag-netite	Chr mag-netite
Type	Type-V	Type-V	Type-V	Type-V	Type-V	Type-V	Type-V	Type-V	Type-V	Type-V	Type-V	Type-V	Type-V
Al_2O_3	0.20	0.33	0.35	0.27	0.11	0.04	0.28	0.16	0.20	0.31	0.10	0.21	0.79
MnO	0.43	0.77	0.84	0.51	0.42	0.31	0.60	0.20	0.43	0.75	0.54	0.44	1.07
TiO_2	0.84	1.07	1.35	0.77	0.39	0.21	0.93	0.37	0.49	0.97	0.95	0.54	2.63
Cr_2O_3	6.53	8.10	9.19	7.16	5.58	4.24	7.96	5.72	5.78	8.22	5.52	6.87	18.64
MgO	0.40	0.51	0.69	0.43	0.26	0.29	0.54	0.36	0.30	0.48	0.33	0.33	1.10
SiO_2	0.00	0.00	0.04	0.10	0.06	0.04	0.00	0.00	0.00	0.02	0.03	0.04	0.05
Fe_2O_3	59.07	56.37	54.93	57.00	60.51	62.36	56.17	60.04	59.96	57.46	59.79	58.67	42.79
FeO	30.39	30.04	29.91	29.37	30.01	29.89	29.57	29.72	29.75	30.38	30.20	29.91	30.11
V_2O_3	0.26	0.28	0.30	0.28	0.25	0.24	0.24	0.25	0.22	0.28	0.25	0.25	0.33
NiO	0.37	0.22	0.30	0.53	0.51	0.44	0.34	0.45	0.50	0.30	0.33	0.41	0.59
ZnO	0.00	0.19	0.24	0.00	0.00	0.00	0.10	0.01	0.02	0.00	0.27	0.00	0.62
CoO	0.00	0.00	0.09	0.31	0.00	0.00	0.00	0.11	0.10	0.23	0.05	0.20	0.09
Na_2O	0.07	0.00	0.03	0.03	0.05	0.00	0.00	0.02	0.00	0.00	0.02	0.00	0.01
K_2O	0.00	0.00	0.01	0.00	0.00	0.01	0.00	0.00	0.00	0.00	0.00	0.00	0.00
CaO	0.01	0.00	0.01	0.06	0.00	0.05	0.00	0.04	0.03	0.02	0.05	0.02	0.01
Total	98.56	97.86	98.28	96.83	98.13	98.11	96.75	97.44	97.79	99.39	98.42	97.89	98.80
Cation													
Al	0.073	0.120	0.127	0.102	0.040	0.013	0.104	0.061	0.074	0.112	0.037	0.075	0.282
Mn	0.113	0.203	0.219	0.137	0.110	0.082	0.160	0.052	0.115	0.194	0.141	0.117	0.275
Ti	0.196	0.250	0.315	0.182	0.092	0.050	0.221	0.088	0.116	0.224	0.221	0.127	0.601
Cr	1.601	1.994	2.248	1.785	1.376	1.048	1.983	1.419	1.430	1.993	1.357	1.697	4.485
Mg	0.184	0.236	0.320	0.204	0.120	0.136	0.256	0.169	0.142	0.217	0.154	0.156	0.498
Si	0.000	0.000	0.013	0.031	0.017	0.013	0.000	0.000	0.000	0.005	0.008	0.013	0.014
Fe^{3+}	13.778	13.215	12.788	13.515	14.210	14.669	13.320	14.190	14.125	13.268	13.993	13.792	9.803
Fe^{2+}	7.877	7.825	7.737	7.739	7.831	7.812	7.793	7.806	7.788	7.796	7.856	7.813	7.665
V	0.052	0.057	0.060	0.058	0.052	0.049	0.050	0.051	0.046	0.057	0.051	0.052	0.067
Ni	0.092	0.056	0.075	0.133	0.129	0.110	0.087	0.113	0.125	0.075	0.083	0.103	0.145
Zn	0.000	0.043	0.055	0.000	0.000	0.000	0.024	0.001	0.004	0.000	0.062	0.000	0.140
Co	0.000	0.000	0.021	0.079	0.000	0.000	0.000	0.028	0.024	0.055	0.012	0.050	0.021
Na	0.032	0.000	0.015	0.015	0.022	0.000	0.000	0.010	0.000	0.000	0.009	0.000	0.003

K	0.000	0.000	0.002	0.000	0.000	0.002	0.001	0.000	0.000	0.000	0.000	0.000	0.000
Ca	0.002	0.001	0.005	0.022	0.000	0.018	0.001	0.012	0.011	0.005	0.016	0.005	0.002
Total	24.000	24.000	24.000	24.000	24.000	24.000	24.000	24.000	24.000	24.000	24.000	24.000	24.000
Mg#	0.02	0.03	0.04	0.03	0.02	0.02	0.03	0.02	0.02	0.03	0.02	0.02	0.06
Cr#	0.96	0.94	0.95	0.95	0.97	0.99	0.95	0.96	0.95	0.95	0.97	0.96	0.94
Fe^{3+}/R^{3+}	0.89	0.86	0.84	0.88	0.91	0.93	0.86	0.91	0.90	0.86	0.91	0.89	0.67

Sample number	SHB/19-12/79	SHB/19-12/82	SHB/19-12/82	SHB/19-12/82	SHB/19-12/82	SHB/19-12/82	SHB/19-12/82	SHB/19-12/82	SHB/19-12/82	SHB/19-12/82	SHB/19-12/82	SHB/19-12/82	SHB/19-12/82
Location	Kapili	Kapili	Kapili	Kapili	Kapili	Kapili	Kapili	Kapili	Kapili	Kapili	Kapili	Kapili	Kapili
EPMA point	51 / 1 .	87 / 1 .	88 / 1 .	89 / 1 .	91 / 1 .	92 / 1 .	93 / 1 .	94 / 1 .	95 / 1 .	107 / 1 .	108 / 1 .	109 / 1 .	110 / 1 .
Mineral	Chr mag-netite	Chr mag-netite	Chr mag-netite	Chr mag-netite	Chr mag-netite	Chr mag-netite	Chr mag-netite	Chr mag-netite	Chr mag-netite	Chr mag-netite	Chr mag-netite	Chr mag-netite	Chr mag-netite
Type	Type-V	Type-V	Type-V	Type-V	Type-V	Type-V	Type-V	Type-V	Type-V	Type-V	Type-V	Type-V	Type-V
Al_2O_3	0.23	0.37	0.31	0.37	0.08	0.22	0.10	0.21	0.09	0.31	0.40	0.44	0.35
MnO	0.41	0.66	0.55	0.72	0.30	0.27	0.35	0.40	0.12	0.70	1.35	0.81	0.51
TiO_2	0.57	0.45	0.40	0.58	0.16	0.20	0.17	0.32	0.12	0.35	2.08	0.74	0.45
Cr_2O_3	6.92	7.81	7.20	6.74	4.77	5.68	6.07	5.34	4.98	7.13	8.92	8.84	7.47
MgO	0.31	0.39	0.35	0.36	0.14	0.36	0.19	0.27	0.23	0.29	0.34	0.31	0.28
SiO_2	0.00	0.00	0.02	0.06	0.00	0.03	0.00	0.01	0.00	0.06	0.00	0.05	0.00
Fe_2O_3	58.49	57.19	58.41	58.19	61.45	60.31	60.41	59.97	61.51	57.39	52.50	54.82	57.48
FeO	29.63	29.54	29.68	29.66	29.77	29.45	30.17	29.58	29.93	28.96	29.84	29.68	29.61
V_2O_3	0.27	0.34	0.29	0.27	0.25	0.32	0.32	0.28	0.28	0.30	0.31	0.32	0.31
NiO	0.68	0.52	0.48	0.54	0.50	0.60	0.25	0.55	0.46	0.55	0.71	0.34	0.50
ZnO	0.02	0.00	0.00	0.00	0.00	0.17	0.00	0.00	0.00	0.15	0.09	0.00	0.04
CoO	0.15	0.00	0.15	0.00	0.09	0.00	0.13	0.00	0.15	0.13	0.00	0.09	0.14
Na_2O	0.04	0.01	0.00	0.00	0.00	0.08	0.04	0.00	0.00	0.00	0.06	0.00	0.01
K_2O	0.00	0.00	0.00	0.00	0.00	0.01	0.00	0.00	0.00	0.00	0.00	0.00	0.00
CaO	0.02	0.01	0.00	0.00	0.03	0.00	0.02	0.03	0.02	0.04	0.00	0.02	0.00
Total	97.74	97.30	97.82	97.49	97.55	97.71	98.22	96.96	97.88	96.35	96.58	96.45	97.13
Cation													
Al	0.086	0.138	0.114	0.137	0.029	0.081	0.035	0.079	0.031	0.116	0.116	0.165	0.130
Mn	0.109	0.176	0.147	0.191	0.081	0.071	0.094	0.108	0.032	0.187	0.361	0.217	0.135
Ti	0.134	0.105	0.093	0.137	0.038	0.047	0.041	0.077	0.029	0.084	0.492	0.176	0.106
Cr	1.712	1.937	1.779	1.669	1.188	1.406	1.497	1.333	1.233	1.789	2.222	2.209	1.859
Mg	0.143	0.184	0.161	0.168	0.063	0.169	0.089	0.129	0.106	0.135	0.160	0.145	0.133
Si	0.000	0.001	0.005	0.017	0.000	0.008	0.000	0.002	0.000	0.017	0.000	0.016	0.000

Fe^{3+}	13.770	13.501	13.731	13.718	14.554	14.206	14.186	14.253	14.506	13.702	12.456	13.043	13.609
Fe^{2+}	7.753	7.750	7.753	7.771	7.835	7.710	7.873	7.813	7.844	7.684	7.869	7.848	7.791
V	0.055	0.070	0.060	0.056	0.051	0.065	0.067	0.059	0.058	0.063	0.064	0.066	0.063
Ni	0.171	0.130	0.120	0.136	0.128	0.152	0.062	0.139	0.117	0.141	0.180	0.085	0.126
Zn	0.006	0.000	0.000	0.000	0.000	0.040	0.000	0.000	0.000	0.036	0.022	0.000	0.009
Co	0.037	0.000	0.037	0.000	0.023	0.000	0.032	0.000	0.038	0.033	0.000	0.023	0.035
Na	0.018	0.003	0.000	0.000	0.000	0.039	0.019	0.000	0.000	0.001	0.028	0.000	0.005
K	0.000	0.000	0.000	0.000	0.000	0.003	0.000	0.000	0.000	0.000	0.000	0.000	0.000
Ca	0.007	0.003	0.000	0.000	0.009	0.001	0.007	0.009	0.007	0.012	0.000	0.006	0.000
Total	24.000	24.000	24.000	24.000	24.000	24.000	24.000	24.000	24.000	24.000	24.000	24.000	24.000
Mg#	0.02	0.02	0.02	0.02	0.01	0.02	0.01	0.02	0.01	0.02	0.02	0.02	0.02
Cr#	0.95	0.93	0.94	0.92	0.98	0.95	0.98	0.94	0.98	0.94	0.95	0.93	0.93
Fe^{3+}/R^{3+}	0.88	0.87	0.88	0.88	0.92	0.91	0.90	0.91	0.92	0.88	0.84	0.85	0.87

Sample number	SHB/19-12/82	SHB/19-12/82	SHB/19-12/82	SHB/19-12/24	SHB/19-12/24	SHB/19-12/24	SHB/19-12/24	SHB/19-12/24	SHB/19-12/24	SHB/19-12/24	SHB/19-12/24	SHB/19-12/24	SHB/19-12/24
Location	Kapili	Kapili	Kapili	Chuka Pahar	Chuka Pahar	Chuka Pahar	Chuka Pahar	Chuka Pahar	Chuka Pahar	Chuka Pahar	Chuka Pahar	Chuka Pahar	Chuka Pahar
EPMA point	111 / 1 .	112 / 1 .	127 / 1 .	57 / 1 .	58 / 1 .	59 / 1 .	60 / 1 .	61 / 1 .	62 / 1 .	63 / 1 .	64 / 1 .	65 / 1 .	66 / 1 .
Mineral	Chr mag-netite	Chr mag-netite	Chr mag-netite	Chr mag-netite	Chr mag-netite	Chr mag-netite	Chr mag-netite	Chr mag-netite	Chr mag-netite	Chr mag-netite	Chr mag-netite	Chr mag-netite	Chr mag-netite
Type	Type-V	Type-V	Type-V	Type-V	Type-V	Type-V	Type-V	Type-V	Type-V	Type-V	Type-V	Type-V	Type-V
Al_2O_3	0.16	0.03	0.02	0.03	0.17	0.15	0.15	0.12	0.13	0.11	0.12	0.02	0.02
MnO	0.79	0.00	0.31	1.71	1.64	1.45	1.26	1.13	1.41	1.52	1.39	1.07	1.19
TiO_2	1.65	0.15	0.33	0.03	0.14	0.17	0.18	0.21	0.12	0.07	0.08	0.03	0.00
Cr_2O_3	4.85	4.04	3.65	16.74	16.55	15.04	14.42	14.96	15.17	15.66	14.93	10.39	11.02
MgO	0.42	0.24	0.19	0.17	0.18	0.16	0.24	0.28	0.28	0.22	0.17	0.11	0.09
SiO_2	0.03	0.04	0.00	0.00	0.02	0.06	0.05	0.00	0.04	0.00	0.02	0.00	0.00
Fe_2O_3	57.69	61.00	64.16	49.77	48.75	49.85	51.66	50.33	50.50	50.63	50.98	57.19	55.36
FeO	30.00	29.77	30.65	28.53	28.91	29.10	29.42	29.34	28.98	29.20	29.25	28.83	27.87
V_2O_3	0.28	0.25	0.27	0.26	0.36	0.37	0.38	0.37	0.35	0.36	0.32	0.09	0.06
NiO	0.35	0.19	0.60	0.30	0.26	0.00	0.30	0.02	0.12	0.15	0.18	0.53	0.32
ZnO	0.19	0.00	0.00	0.12	0.00	0.21	0.00	0.13	0.18	0.00	0.00	0.28	0.54
CoO	0.06	0.00	0.07	0.09	0.00	0.00	0.18	0.08	0.08	0.09	0.02	0.00	0.02
Na_2O	0.00	0.00	0.00	0.01	0.00	0.03	0.02	0.00	0.01	0.00	0.00	0.01	0.07
K_2O	0.01	0.01	0.00	0.00	0.01	0.00	0.00	0.00	0.00	0.01	0.00	0.00	0.00
CaO	0.02	0.02	0.00	0.02	0.01	0.01	0.02	0.01	0.00	0.00	0.00	0.05	0.09

Total	96.50	95.72	100.23	97.77	96.97	96.59	98.29	96.97	97.38	98.01	97.47	98.58	96.66
Cation													
Al	0.060	0.012	0.007	0.010	0.061	0.055	0.054	0.044	0.048	0.039	0.045	0.006	0.009
Mn	0.213	0.000	0.079	0.451	0.435	0.387	0.332	0.301	0.373	0.400	0.370	0.281	0.320
Ti	0.392	0.035	0.076	0.007	0.032	0.040	0.041	0.050	0.028	0.017	0.020	0.006	0.000
Cr	1.215	1.023	0.883	4.131	4.110	3.755	3.538	3.719	3.754	3.851	3.696	2.552	2.760
Mg	0.199	0.116	0.085	0.078	0.086	0.076	0.111	0.130	0.128	0.102	0.079	0.051	0.043
Si	0.008	0.014	0.000	0.000	0.007	0.019	0.016	0.000	0.012	0.001	0.006	0.000	0.000
Fe^{3+}	13.749	14.711	14.797	11.688	11.528	11.843	12.062	11.908	11.898	11.856	12.009	13.376	13.196
Fe^{2+}	7.946	7.978	7.855	7.445	7.596	7.682	7.634	7.714	7.587	7.600	7.658	7.492	7.382
V	0.058	0.052	0.054	0.053	0.074	0.077	0.077	0.077	0.073	0.073	0.066	0.018	0.012
Ni	0.090	0.048	0.147	0.076	0.065	0.000	0.076	0.004	0.031	0.037	0.045	0.133	0.083
Zn	0.045	0.000	0.000	0.027	0.000	0.048	0.000	0.031	0.042	0.000	0.000	0.065	0.126
Co	0.015	0.000	0.016	0.023	0.000	0.000	0.045	0.019	0.021	0.021	0.005	0.000	0.005
Na	0.002	0.000	0.001	0.006	0.000	0.014	0.007	0.000	0.002	0.000	0.000	0.003	0.034
K	0.002	0.003	0.000	0.000	0.002	0.001	0.000	0.000	0.001	0.004	0.001	0.000	0.000
Ca	0.005	0.007	0.000	0.007	0.003	0.003	0.007	0.004	0.000	0.000	0.001	0.017	0.031
Total	24.000	24.000	24.000	24.000	24.000	24.000	24.000	24.000	24.000	24.000	24.000	24.000	24.000
Mg#	0.02	0.01	0.01	0.01	0.01	0.01	0.01	0.02	0.02	0.01	0.01	0.01	0.01
Cr#	0.95	0.99	0.99	1.00	0.99	0.99	0.98	0.99	0.99	0.99	0.99	1.00	1.00
Fe^{3+}/R^{3+}	0.92	0.93	0.94	0.74	0.73	0.76	0.77	0.76	0.76	0.75	0.76	0.84	0.83

Sample number	SHB/19-12/24	SHB/19-12/24	SHB/19-12/24	SHB/19-12/24	SHB/19-12/24	SHB/19-12/24	SHB/19-12/24	SHB/19-12/24	SHB/19-12/24	SHB/19-12/24	SHB/19-12/24	SHB/19-12/35	SHB/19-12/35
Location	Chuka Pahar	Chuka Pahar	Chuka Pahar	Chuka Pahar	Chuka Pahar	Chuka Pahar	Chuka Pahar	Chuka Pahar	Chuka Pahar	Chuka Pahar	Chuka Pahar	Maharajgunj	Maharaj-gunj
EPMA point	67 / 1 .	68 / 1 .	69 / 1 .	70 / 1 .	74 / 1 .	75 / 1 .	76 / 1 .	77 / 1 .	78 / 1 .	79 / 1 .	80 / 1 .	131 / 1 .	132 / 1 .
Mineral	Chr mag-netite	Chr mag-netite	Chr mag-netite	Chr mag-netite	Chr mag-netite	Chr mag-netite	Chr mag-netite	Chr mag-netite	Chr mag-netite	Chr mag-netite	Chr mag-netite	Chr mag-netite	Chr mag-netite
Type	Type-V	Type-V	Type-V	Type-V	Type-V	Type-V	Type-V	Type-V	Type-V	Type-V	Type-V	Type-V	Type-V
Al_2O_3	0.17	0.16	0.23	0.16	0.11	0.13	0.13	0.14	0.11	0.01	0.11	0.25	0.42
MnO	1.62	1.62	1.72	2.00	1.57	1.90	1.57	1.57	1.49	1.21	2.19	0.82	1.12
TiO_2	0.06	0.23	0.13	0.05	0.04	0.05	0.04	0.10	0.07	0.02	0.04	0.07	0.06
Cr_2O_3	16.07	15.08	15.92	17.35	14.28	16.91	14.23	14.70	15.59	12.11	19.57	12.79	13.66
MgO	0.18	0.15	0.19	0.13	0.17	0.15	0.17	0.18	0.20	0.13	0.19	0.11	0.09
SiO_2	0.01	0.05	0.00	0.01	0.01	0.00	0.00	0.02	0.02	0.02	0.00	0.00	0.02
Fe_2O_3	48.75	49.99	49.37	48.78	50.70	48.94	51.31	50.90	50.11	53.31	46.81	52.94	53.34

FeO	28.30	28.85	28.67	28.13	28.70	28.27	28.79	28.86	28.87	27.85	27.46	29.10	29.46
V_2O_3	0.35	0.39	0.40	0.34	0.42	0.38	0.39	0.41	0.35	0.06	0.19	0.17	0.19
NiO	0.28	0.12	0.32	0.35	0.16	0.34	0.31	0.52	0.35	0.31	0.32	0.18	0.13
ZnO	0.23	0.31	0.17	0.62	0.16	0.35	0.00	0.00	0.00	0.26	0.42	0.27	0.30
CoO	0.03	0.08	0.00	0.00	0.00	0.06	0.05	0.00	0.00	0.00	0.23	0.07	0.13
Na_2O	0.00	0.05	0.00	0.02	0.01	0.05	0.00	0.00	0.01	0.04	0.01	0.01	0.06
K_2O	0.00	0.00	0.02	0.00	0.00	0.00	0.00	0.00	0.00	0.00	0.00	0.01	0.01
CaO	0.00	0.00	0.00	0.00	0.00	0.00	0.01	0.03	0.03	0.06	0.03	0.02	0.02
Total	96.05	97.06	97.14	97.95	96.35	97.53	96.98	97.42	97.19	95.40	97.57	96.80	98.99
Cation													
Al	0.064	0.057	0.084	0.058	0.043	0.046	0.047	0.052	0.040	0.005	0.042	0.093	0.153
Mn	0.435	0.431	0.457	0.529	0.422	0.503	0.418	0.415	0.397	0.329	0.578	0.220	0.293
Ti	0.014	0.054	0.030	0.013	0.010	0.011	0.009	0.024	0.016	0.004	0.009	0.017	0.013
Cr	4.033	3.746	3.950	4.271	3.576	4.178	3.542	3.639	3.868	3.069	4.829	3.192	3.329
Mg	0.084	0.071	0.087	0.060	0.080	0.069	0.078	0.085	0.092	0.062	0.089	0.049	0.040
Si	0.002	0.015	0.000	0.002	0.004	0.000	0.000	0.005	0.005	0.007	0.000	0.000	0.005
Fe^{3+}	11.647	11.818	11.657	11.430	12.086	11.515	12.154	11.996	11.831	12.863	10.996	12.574	12.369
Fe^{2+}	7.514	7.580	7.524	7.327	7.605	7.392	7.578	7.558	7.575	7.466	7.167	7.681	7.593
V	0.074	0.080	0.083	0.070	0.089	0.079	0.080	0.085	0.073	0.013	0.039	0.036	0.038
Ni	0.072	0.030	0.082	0.089	0.041	0.085	0.078	0.130	0.087	0.080	0.081	0.044	0.032
Zn	0.053	0.071	0.039	0.143	0.036	0.082	0.000	0.000	0.000	0.062	0.096	0.062	0.067
Co	0.007	0.020	0.000	0.000	0.000	0.015	0.013	0.000	0.000	0.000	0.059	0.019	0.031
Na	0.000	0.025	0.001	0.008	0.006	0.025	0.000	0.000	0.005	0.019	0.007	0.005	0.027
K	0.000	0.001	0.006	0.000	0.000	0.000	0.000	0.000	0.000	0.000	0.000	0.002	0.002
Ca	0.000	0.000	0.000	0.000	0.001	0.000	0.003	0.010	0.010	0.020	0.010	0.006	0.008
Total	24.000	24.000	24.000	24.000	24.000	24.000	24.000	24.000	24.000	24.000	24.000	24.000	24.000
Mg#	0.01	0.01	0.01	0.01	0.01	0.01	0.01	0.01	0.01	0.01	0.01	0.01	0.01
Cr#	0.98	0.98	0.98	0.99	0.99	0.99	0.99	0.99	0.99	1.00	0.99	0.97	0.96
Fe^{3+}/R^{3+}	0.74	0.76	0.74	0.73	0.77	0.73	0.77	0.76	0.75	0.81	0.69	0.79	0.78

Sample number	SHB/19-12/35	SHB/19-12/35	SHB/19-12/35	SHB/19-12/35	SHB/19-12/35	SHB/19-12/35	SHB/19-12/35	SHB/19-12/35	SHB/19-12/35	SHB/19-12/35	SHB/19-12/35	SHB/19-12/35	SHB/19-12/35
Location	Maharaj-gunj	Maharaj-gunj	Maharaj-gunj	Maharaj-gunj	Maharaj-gunj	Maharaj-gunj	Maharaj-gunj	Maharaj-gunj	Maharaj-gunj	Maharaj-gunj	Maharaj-gunj	Maharaj-gunj	Maharaj-gunj
EPMA point	133 / 1 .	134 / 1 .	135 / 1 .	136 / 1 .	137 / 1 .	138 / 1 .	139 / 1 .	142 / 1 .	143 / 1 .	144 / 1 .	145 / 1 .	146 / 1 .	147 / 1 .
Mineral	Chr mag-netite	Chr mag-netite	Chr mag-netite	Chr mag-netite	Chr mag-netite	Chr mag-netite	Chr mag-netite	Chr mag-netite	Chr mag-netite	Chr mag-netite	Chr mag-netite	Chr mag-netite	Chr mag-netite

Type	Type-V	Type-V	Type-V	Type-V	Type-V	Type-V	Type-V	Type-V	Type-V	Type-V	Type-V	Type-V	Type-V
Al_2O_3	0.38	0.19	0.69	0.40	0.79	0.89	0.89	0.55	0.92	0.49	0.93	0.61	0.83
MnO	1.00	1.05	0.88	0.98	0.78	0.98	0.92	1.13	1.13	0.96	0.92	0.92	0.84
TiO_2	0.08	0.03	0.04	0.08	0.12	0.11	0.12	0.07	1.13	0.04	0.23	0.10	0.08
Cr_2O_3	12.84	13.02	13.00	13.39	12.90	13.20	13.81	13.65	12.20	13.61	12.35	13.71	13.55
MgO	0.07	0.12	0.05	0.09	0.13	0.12	0.15	0.11	0.09	0.13	0.16	0.14	0.13
SiO_2	0.02	0.00	0.03	0.04	0.00	0.00	0.03	0.00	0.04	0.00	0.00	0.00	0.00
Fe_2O_3	54.03	53.31	52.54	53.17	52.48	53.12	51.64	52.46	50.72	53.21	53.25	52.47	53.09
FeO	29.57	28.62	29.91	29.12	29.49	29.54	29.38	28.98	29.72	29.47	29.69	29.67	30.24
V_2O_3	0.16	0.16	0.21	0.16	0.18	0.19	0.17	0.17	0.19	0.19	0.21	0.19	0.22
NiO	0.16	0.15	0.06	0.26	0.18	0.26	0.35	0.41	0.36	0.27	0.25	0.16	0.08
ZnO	0.47	0.53	0.04	0.50	0.29	0.35	0.07	0.16	0.44	0.33	0.29	0.02	0.00
CoO	0.00	0.25	0.00	0.09	0.00	0.10	0.11	0.17	0.10	0.00	0.00	0.21	0.11
Na_2O	0.00	0.02	0.00	0.08	0.02	0.05	0.04	0.01	0.00	0.04	0.00	0.00	0.04
K_2O	0.00	0.00	0.02	0.00	0.00	0.00	0.00	0.00	0.00	0.01	0.01	0.01	0.00
CaO	0.00	0.00	0.00	0.02	0.00	0.00	0.00	0.00	0.02	0.01	0.03	0.00	0.01
Total	98.78	97.45	97.45	98.39	97.36	98.90	97.70	97.85	97.05	98.76	98.34	98.20	99.22
Cation													
Al	0.138	0.069	0.254	0.147	0.290	0.321	0.325	0.200	0.341	0.178	0.340	0.222	0.298
Mn	0.262	0.280	0.232	0.257	0.206	0.256	0.243	0.297	0.299	0.252	0.241	0.242	0.219
Ti	0.019	0.006	0.009	0.019	0.029	0.025	0.029	0.016	0.267	0.010	0.054	0.023	0.017
Cr	3.141	3.230	3.215	3.283	3.190	3.211	3.398	3.363	3.023	3.322	3.022	3.362	3.285
Mg	0.030	0.054	0.021	0.041	0.060	0.056	0.071	0.052	0.040	0.058	0.072	0.064	0.061
Si	0.006	0.001	0.011	0.011	0.000	0.000	0.011	0.000	0.012	0.000	0.000	0.000	0.000
Fe^{3+}	12.574	12.587	12.365	12.408	12.353	12.300	12.091	12.300	11.964	12.363	12.401	12.251	12.250
Fe^{2+}	7.649	7.508	7.823	7.552	7.714	7.601	7.644	7.550	7.791	7.610	7.684	7.699	7.756
V	0.032	0.033	0.042	0.034	0.037	0.039	0.036	0.035	0.039	0.039	0.043	0.040	0.044
Ni	0.040	0.037	0.015	0.064	0.045	0.064	0.088	0.102	0.091	0.068	0.063	0.039	0.020
Zn	0.107	0.123	0.009	0.115	0.066	0.079	0.016	0.037	0.102	0.074	0.066	0.004	0.000
Co	0.000	0.063	0.000	0.022	0.000	0.025	0.028	0.041	0.025	0.000	0.000	0.051	0.028
Na	0.000	0.009	0.000	0.040	0.010	0.022	0.018	0.006	0.000	0.020	0.000	0.000	0.017
K	0.000	0.000	0.005	0.000	0.000	0.000	0.001	0.000	0.000	0.004	0.004	0.002	0.000
Ca	0.001	0.001	0.000	0.006	0.001	0.000	0.001	0.000	0.007	0.002	0.010	0.000	0.004
Total	24.000	24.000	24.000	24.000	24.000	24.000	24.000	24.000	24.000	24.000	24.000	24.000	24.000
Mg#	0.00	0.01	0.00	0.01	0.01	0.01	0.01	0.01	0.01	0.01	0.01	0.01	0.01
Cr#	0.96	0.98	0.93	0.96	0.92	0.91	0.91	0.94	0.90	0.95	0.90	0.94	0.92
Fe^{3+}/R^{3+}	0.79	0.79	0.78	0.78	0.78	0.78	0.76	0.78	0.78	0.78	0.79	0.77	0.77

Sample number	SHB/19-12/35	SHB/19-12/35	SHB/19-12/37	SHB/19-12/37	SHB/19-12/37	SHB/19-12/37	SHB/19-12/37	SHB/19-12/37	SHB/19-12/37	SHB/19-12/37	SHB/19-12/37	SHB/19-12/37	SHB/19-12/37
Location	Maharaj-gunj	Maharaj-gunj	Maharaj-gunj	Maharaj-gunj	Maharaj-gunj	Maharaj-gunj	Maharaj-gunj	Maharaj-gunj	Maharaj-gunj	Maharaj-gunj	Maharaj-gunj	Maharaj-gunj	Maharaj-gunj
EPMA point	148 / 1 .	149 / 1 .	208 / 1 .	209 / 1 .	210 / 1 .	211 / 1 .	212 / 1 .	216 / 1 .	217 / 1 .	218 / 1 .	219 / 1 .	220 / 1 .	221 / 1 .
Mineral	Chr mag-netite	Chr mag-netite	Chr mag-netite	Chr mag-netite	Chr mag-netite	Chr mag-netite	Chr mag-netite	Chr mag-netite	Chr mag-netite	Chr mag-netite	Chr mag-netite	Chr mag-netite	Chr mag-netite
Type	Type-V	Type-V	Type-V	Type-V	Type-V	Type-V	Type-V	Type-V	Type-V	Type-V	Type-V	Type-V	Type-V
Al_2O_3	0.74	0.43	0.15	0.09	0.08	0.32	0.11	0.36	0.36	0.12	0.18	0.05	0.00
MnO	0.75	0.86	1.02	1.08	0.99	1.33	0.86	1.48	1.19	1.36	1.53	1.28	0.12
TiO_2	0.17	0.06	0.05	0.38	0.02	1.29	0.10	0.06	0.07	0.06	0.03	0.05	0.00
Cr_2O_3	11.22	12.51	12.97	13.64	13.31	13.11	12.91	17.57	17.53	17.42	16.93	14.34	5.23
MgO	0.16	0.11	0.05	0.07	0.19	0.16	0.15	0.18	0.12	0.13	0.10	0.12	0.09
SiO_2	0.03	0.04	0.02	0.00	0.00	0.00	0.04	0.05	0.05	0.05	0.04	0.02	0.00
Fe_2O_3	55.10	53.80	54.67	53.48	54.00	51.35	54.20	48.56	47.97	48.21	48.35	51.60	61.76
FeO	29.85	29.82	29.66	29.45	29.12	30.32	29.20	28.68	29.41	28.57	28.47	28.22	29.51
V_2O_3	0.22	0.21	0.11	0.07	0.13	0.20	0.06	0.25	0.28	0.09	0.17	0.04	0.00
NiO	0.53	0.18	0.43	0.49	0.17	0.37	0.39	0.48	0.19	0.00	0.10	0.17	0.44
ZnO	0.00	0.11	0.00	0.33	0.09	0.00	0.23	0.33	0.00	0.30	0.25	0.20	0.00
CoO	0.11	0.00	0.08	0.00	0.20	0.00	0.00	0.09	0.12	0.00	0.00	0.21	0.00
Na_2O	0.05	0.02	0.00	0.00	0.06	0.04	0.06	0.00	0.00	0.00	0.00	0.00	0.03
K_2O	0.00	0.00	0.00	0.00	0.00	0.01	0.00	0.00	0.00	0.00	0.00	0.00	0.00
CaO	0.00	0.02	0.01	0.00	0.02	0.01	0.02	0.00	0.00	0.00	0.00	0.01	0.00
Total	98.92	98.17	99.23	99.08	98.38	98.50	98.33	98.09	97.27	96.30	96.15	96.32	97.18
Cation													
Al	0.270	0.157	0.054	0.032	0.030	0.118	0.041	0.132	0.134	0.045	0.067	0.018	0.000
Mn	0.196	0.225	0.266	0.282	0.260	0.349	0.227	0.389	0.316	0.366	0.411	0.345	0.031
Ti	0.038	0.013	0.013	0.087	0.004	0.301	0.024	0.014	0.016	0.014	0.007	0.012	0.000
Cr	2.731	3.075	3.161	3.329	3.268	3.206	3.172	4.310	4.337	4.360	4.245	3.597	1.307
Mg	0.072	0.052	0.021	0.032	0.088	0.074	0.067	0.084	0.054	0.062	0.048	0.057	0.043
Si	0.009	0.013	0.007	0.000	0.000	0.000	0.014	0.016	0.014	0.015	0.013	0.008	0.000
Fe^{3+}	12.770	12.585	12.680	12.423	12.616	11.955	12.673	11.342	11.298	11.486	11.538	12.320	14.691
Fe^{2+}	7.688	7.751	7.645	7.602	7.562	7.845	7.586	7.444	7.698	7.566	7.550	7.488	7.800
V	0.045	0.044	0.022	0.014	0.026	0.040	0.013	0.052	0.057	0.018	0.036	0.009	0.001
Ni	0.131	0.045	0.106	0.122	0.043	0.091	0.097	0.119	0.047	0.000	0.025	0.043	0.113
Zn	0.000	0.026	0.000	0.076	0.021	0.000	0.052	0.076	0.000	0.070	0.058	0.047	0.000

Co	0.026	0.000	0.020	0.000	0.049	0.000	0.000	0.021	0.030	0.000	0.000	0.054	0.000
Na	0.024	0.008	0.001	0.000	0.027	0.017	0.027	0.000	0.000	0.000	0.000	0.000	0.015
K	0.000	0.000	0.000	0.000	0.000	0.002	0.000	0.000	0.000	0.000	0.000	0.000	0.000
Ca	0.000	0.007	0.005	0.000	0.007	0.003	0.007	0.000	0.001	0.001	0.000	0.003	0.000
Total	24.000	24.000	24.000	24.000	24.000	24.000	24.000	24.000	24.000	24.000	24.000	24.000	24.000
Mg#	0.01	0.01	0.00	0.00	0.01	0.01	0.01	0.01	0.01	0.01	0.01	0.01	0.01
Cr#	0.91	0.95	0.98	0.99	0.99	0.96	0.99	0.97	0.97	0.99	0.98	1.00	1.00
Fe^{3+}/R^{3+}	0.81	0.80	0.80	0.79	0.79	0.78	0.80	0.72	0.72	0.72	0.73	0.77	0.92

Sample number	MIC/16/33	MIC/16/33	MIC/16/33	MIC/16/33	MIC/16/33	MIC/16/33	MIC/16/33	MIC/16/33	MIC/16/33	MIC/16/33	MIC/16/33	MIC/16/35	MIC/16/35
Location	Tua Dungri	Tua Dungri	Tua Dungri	Tua Dungri	Tua Dungri	Tua Dungri	Tua Dungri	Tua Dungri	Tua Dungri	Tua Dungri	Tua Dungri	Tua Dungri	Tua Dungri
EPMA point	7 / 1 .	11 / 1 .	12 / 1 .	17 / 1 .	21 / 1 .	22 / 1 .	23 / 1 .	25 / 1 .	26 / 1 .	33 / 1 .	34 / 1 .	37 / 1 .	58 / 1 .
Mineral	Magne-tite	Magne-tite	Magne-tite	Magne-tite	Magne-tite	Magne-tite	Magne-tite	Magne-tite	Magne-tite	Magne-tite	Magne-tite	Magne-tite	Magne-tite
Type	Type-V	Type-V	Type-V	Type-V	Type-V	Type-V	Type-V	Type-V	Type-V	Type-V	Type-V	Type-V	Type-V
Al_2O_3	0.01	0.01	0.02	0.00	0.19	0.06	0.12	0.01	0.01	0.02	0.02	0.39	0.33
MnO	0.02	0.04	0.06	0.05	0.05	0.08	0.05	0.07	0.10	0.09	0.04	0.04	0.02
TiO_2	0.08	0.08	0.06	0.09	0.08	0.05	0.05	0.30	0.07	0.09	0.09	0.14	0.12
Cr_2O_3	0.10	0.10	0.10	0.09	0.10	0.08	0.09	0.50	0.11	0.09	0.10	0.91	0.11
MgO	0.05	0.07	0.14	0.06	1.26	0.24	0.16	0.11	0.10	0.03	0.07	0.82	0.93
SiO_2	0.20	0.22	0.09	0.21	0.51	0.07	0.09	0.04	0.14	0.23	0.22	0.70	0.59
Fe_2O_3	64.92	66.28	65.75	65.12	65.91	66.30	65.40	64.69	64.86	65.26	65.04	64.47	64.52
FeO	29.69	30.14	29.51	29.83	28.95	29.74	29.55	29.74	29.46	29.98	29.96	29.94	29.05
V_2O_3	0.16	0.10	0.12	0.15	0.14	0.14	0.13	0.13	0.13	0.13	0.13	0.00	0.00
NiO	0.56	0.51	0.52	0.44	0.37	0.29	0.36	0.35	0.34	0.40	0.27	0.21	0.22
ZnO													
CoO													
Na_2O													
K_2O													
CaO													
Total	95.80	97.55	96.37	96.03	97.57	97.05	96.00	95.94	95.32	96.33	95.95	97.62	95.89
Cation													
Al	0.004	0.003	0.006	0.002	0.070	0.024	0.047	0.005	0.005	0.007	0.008	0.143	0.124
Mn	0.005	0.011	0.015	0.013	0.014	0.023	0.014	0.019	0.027	0.025	0.010	0.010	0.004
Ti	0.020	0.018	0.016	0.021	0.019	0.011	0.013	0.071	0.018	0.023	0.022	0.033	0.028

Cr	0.027	0.026	0.025	0.022	0.025	0.020	0.022	0.128	0.028	0.024	0.026	0.225	0.027
Mg	0.023	0.033	0.066	0.031	0.584	0.115	0.074	0.054	0.048	0.014	0.033	0.382	0.441
Si	0.065	0.068	0.028	0.068	0.159	0.021	0.028	0.012	0.044	0.074	0.071	0.219	0.189
Fe^{3+}	15.699	15.736	15.803	15.706	15.459	15.805	15.766	15.616	15.760	15.690	15.696	15.128	15.416
Fe^{2+}	7.980	7.954	7.881	7.994	7.546	7.878	7.916	7.977	7.954	8.010	8.036	7.809	7.714
V	0.034	0.021	0.026	0.031	0.030	0.029	0.028	0.028	0.027	0.028	0.028	0.000	0.000
Ni	0.144	0.130	0.135	0.112	0.093	0.074	0.092	0.090	0.087	0.104	0.070	0.052	0.057
Zn													
Co													
Na													
K													
Ca													
Total	24.000	24.000	24.000	24.000	24.000	24.000	24.000	24.000	24.000	24.000	24.000	24.000	24.000
Mg#	0.00	0.00	0.01	0.00	0.07	0.01	0.01	0.01	0.01	0.00	0.00	0.05	0.05
Cr#	0.87	0.89	0.80	0.93	0.26	0.46	0.32	0.96	0.85	0.77	0.77	0.61	0.18
Fe^{3+}/R^{3+}	1.00	1.00	1.00	1.00	0.99	1.00	1.00	0.99	1.00	1.00	1.00	0.98	0.99

Sample number	MIC/16/35	MIC/16/35	MIC/16/35	MIC/16/35	MIC/16/35	MIC/16/36	MIC/16/36	MIC/16/38	MIC/16/38	MIC/16/38	MIC/16/38	MIC/16/38	MIC/16/38
Location	Tua Dungri	Tua Dungri	Tua Dungri	Tua Dungri	Tua Dungri	Tua Dungri	Tua Dungri	Tua Dungri	Tua Dungri	Tua Dungri	Tua Dungri	Tua Dungri	Tua Dungri
EPMA point	60 / 1 .	61 / 1 .	62 / 1 .	64 / 1 .	65 / 1 .	86 / 1 .	97 / 1 .	5 / 1 .	6 / 1 .	7 / 1 .	9 / 1 .	10 / 1 .	11 / 1 .
Mineral	Magne-tite	Magne-tite	Magne-tite	Magne-tite	Magne-tite	Magne-tite	Magne-tite	Magne-tite	Magne-tite	Magne-tite	Magne-tite	Magne-tite	Magne-tite
Type	Type-V	Type-V	Type-V	Type-V	Type-V	Type-V	Type-V	Type-V	Type-V	Type-V	Type-V	Type-V	Type-V
Al_2O_3	0.15	0.38	0.26	0.38	0.40	0.38	0.38	0.02	0.02	0.01	0.01	0.04	0.11
MnO	0.01	0.03	0.02	0.03	0.01	0.02	0.06	0.08	0.12	0.14	0.14	0.11	0.07
TiO_2	0.15	0.12	0.11	0.15	0.15	0.15	0.11	0.16	0.16	0.14	0.22	0.17	0.12
Cr_2O_3	0.14	0.07	0.11	0.07	0.07	0.10	0.51	0.18	0.18	0.15	0.22	0.12	0.26
MgO	0.38	0.11	0.54	0.09	0.06	0.14	0.11	0.37	0.42	0.42	0.45	0.13	0.09
SiO_2	0.41	0.16	0.65	0.04	0.05	0.18	0.06	0.22	0.20	0.13	0.20	0.02	0.16
Fe_2O_3	64.50	66.29	65.18	66.55	67.10	66.12	66.74	66.06	67.34	66.78	66.72	66.42	66.23
FeO	29.62	30.24	30.02	30.01	30.39	30.31	30.34	29.36	29.75	29.73	29.85	29.92	30.30
V_2O_3	0.00	0.00	0.00	0.00	0.00	0.00	0.00	0.13	0.13	0.13	0.13	0.14	0.13
NiO	0.14	0.27	0.33	0.41	0.41	0.21	0.27	0.92	0.94	0.45	0.57	0.44	0.43
ZnO													
CoO													

Na_2O													
K_2O													
CaO													
Total	95.51	97.68	97.22	97.73	98.64	97.60	98.58	97.50	99.25	98.08	98.51	97.51	97.90
Cation													
Al	0.057	0.141	0.096	0.140	0.146	0.141	0.140	0.007	0.008	0.004	0.004	0.016	0.039
Mn	0.004	0.009	0.006	0.009	0.002	0.005	0.016	0.022	0.031	0.038	0.038	0.030	0.018
Ti	0.037	0.030	0.027	0.035	0.035	0.035	0.025	0.037	0.036	0.034	0.051	0.040	0.029
Cr	0.036	0.017	0.028	0.017	0.017	0.026	0.126	0.045	0.045	0.037	0.055	0.030	0.064
Mg	0.183	0.051	0.251	0.044	0.028	0.064	0.051	0.176	0.192	0.194	0.208	0.062	0.043
Si	0.132	0.050	0.203	0.012	0.016	0.058	0.017	0.070	0.061	0.041	0.061	0.007	0.050
Fe^{3+}	15.570	15.682	15.416	15.748	15.733	15.648	15.649	15.653	15.673	15.729	15.639	15.777	15.660
Fe^{2+}	7.945	7.951	7.891	7.891	7.920	7.972	7.907	7.731	7.694	7.783	7.775	7.899	7.960
V	0.000	0.000	0.000	0.000	0.000	0.000	0.000	0.027	0.027	0.027	0.026	0.028	0.026
Ni	0.036	0.070	0.083	0.104	0.102	0.053	0.069	0.232	0.234	0.113	0.143	0.112	0.110
Zn													
Co													
Na													
K													
Ca													
Total	24.000	24.000	24.000	24.000	24.000	24.000	24.000	24.000	24.000	24.000	24.000	24.000	24.000
Mg#	0.02	0.01	0.03	0.01	0.00	0.01	0.01	0.02	0.02	0.02	0.03	0.01	0.01
Cr#	0.39	0.11	0.22	0.11	0.11	0.15	0.47	0.86	0.86	0.89	0.94	0.66	0.62
Fe^{3+}/R^{3+}	0.99	0.99	0.99	0.99	0.99	0.99	0.98	1.00	1.00	1.00	1.00	1.00	0.99

Sample number	MIC/16/38	MIC/16/38	MIC/16/38	MIC/16/38	MIC/16/38	MIC/16/38	MIC/16/42	MIC/16/44	MIC/16/44	MIC/16/44	MIC/16/44	MIC/16/44	MIC/16/44
Location	Tua Dungri	Tua Dungri	Tua Dungri	Tua Dungri	Tua Dungri	Tua Dungri	Tua Dungri	Tua Dungri	Tua Dungri	Tua Dungri	Tua Dungri	Tua Dungri	Tua Dungri
EPMA point	14 / 1 .	15 / 1 .	16 / 1 .	17 / 1 .	18 / 1 .	20 / 1 .	94 / 1 .	139 / 1 .	140 / 1 .	141 / 1 .	142 / 1 .	143 / 1 .	144 / 1 .
Mineral	Magne-tite	Magne-tite	Magne-tite	Magne-tite	Magne-tite	Magne-tite	Magne-tite	Magne-tite	Magne-tite	Magne-tite	Magne-tite	Magne-tite	Magne-tite
Type	Type-V	Type-V	Type-V	Type-V	Type-V	Type-V	Type-V	Type-V	Type-V	Type-V	Type-V	Type-V	Type-V
Al_2O_3	0.02	0.01	0.01	0.01	0.01	0.02	0.07	0.01	0.01	0.05	0.02	0.02	0.03
MnO	0.06	0.12	0.12	0.11	0.14	0.11	0.02	0.00	0.02	0.00	0.08	0.04	0.02
TiO_2	0.15	0.14	0.13	0.14	0.18	0.15	0.10	0.02	0.02	0.02	0.01	0.01	0.00
Cr_2O_3	0.13	0.12	0.16	0.11	0.12	0.13	0.45	0.00	0.01	0.01	0.02	0.00	0.00

MgO	0.46	0.40	0.44	0.46	0.44	0.46	0.54	0.08	0.10	0.11	0.05	0.06	0.07
SiO_2	0.26	0.23	0.18	0.24	0.25	0.28	0.67	0.14	0.10	0.14	0.15	0.05	0.13
Fe_2O_3	66.02	66.57	66.97	66.42	67.11	66.66	63.55	66.20	66.82	66.16	66.42	67.09	67.28
FeO	29.74	29.91	29.88	29.72	30.01	29.68	29.45	29.75	29.90	29.75	29.91	29.88	30.22
V_2O_3	0.14	0.13	0.12	0.15	0.13	0.12	0.02	0.02	0.00	0.02	0.01	0.01	0.03
NiO	0.45	0.45	0.46	0.54	0.62	0.76	0.28	0.34	0.24	0.29	0.26	0.37	0.32
ZnO													
CoO													
Na_2O													
K_2O													
CaO													
Total	97.45	98.08	98.48	97.90	99.00	98.38	95.15	96.57	97.22	96.55	96.94	97.52	98.10
Cation													
Al	0.007	0.004	0.003	0.004	0.002	0.008	0.025	0.004	0.005	0.018	0.009	0.007	0.010
Mn	0.017	0.032	0.033	0.030	0.038	0.029	0.007	0.000	0.005	0.000	0.020	0.011	0.006
Ti	0.036	0.033	0.031	0.032	0.041	0.035	0.025	0.004	0.004	0.006	0.003	0.003	0.001
Cr	0.033	0.029	0.040	0.028	0.029	0.033	0.114	0.001	0.002	0.003	0.004	0.000	0.000
Mg	0.217	0.188	0.205	0.216	0.203	0.212	0.258	0.037	0.049	0.054	0.026	0.028	0.030
Si	0.083	0.073	0.058	0.074	0.077	0.086	0.215	0.043	0.030	0.045	0.047	0.016	0.039
Fe^{3+}	15.636	15.673	15.703	15.661	15.650	15.641	15.366	15.884	15.924	15.869	15.877	15.947	15.892
Fe^{2+}	7.828	7.826	7.786	7.787	7.778	7.740	7.913	7.932	7.919	7.929	7.945	7.893	7.934
V	0.028	0.027	0.025	0.031	0.028	0.025	0.005	0.005	0.001	0.003	0.003	0.003	0.005
Ni	0.114	0.114	0.116	0.137	0.154	0.191	0.073	0.087	0.062	0.074	0.066	0.094	0.082
Zn													
Co													
Na													
K													
Ca													
Total	24.000	24.000	24.000	24.000	24.000	24.000	24.000	24.000	24.000	24.000	24.000	24.000	24.000
Mg#	0.03	0.02	0.03	0.03	0.03	0.03	0.03	0.00	0.01	0.01	0.00	0.00	0.00
Cr#	0.82	0.89	0.93	0.89	0.94	0.81	0.82	0.14	0.24	0.13	0.33	0.02	0.04
Fe^{3+}/R^{3+}	1.00	1.00	1.00	1.00	1.00	1.00	0.99	1.00	1.00	1.00	1.00	1.00	1.00

Sample number	MIC/16/44	MIC/16/44	MIC/16/44	MIC/16/44	MIC/16/44	MIC/16/44	MIC/16/44	MIC/16/44	MIC/16/44	MIC/16/44	SHB/18/20	SHB/18/25	SHB/18/25
Location	Tua Dungri	Tua Dungri	Tua Dungri	Tua Dungri	Tua Dungri	Tua Dungri	Tua Dungri	Tua Dungri	Tua Dungri	Tua Dungri	Kapili	Kapili	Kapili

EPMA point	146 / 1 .	147 / 1 .	161 / 1 .	163 / 1 .	164 / 1 .	167 / 1 .	177 / 1 .	179 / 1 .	180 / 1 .	181 / 1 .	7 / 1 .	37 / 1 .	38 / 1 .
Mineral	Magne-tite	Magne-tite	Magne-tite	Magne-tite	Magne-tite	Magne-tite	Magne-tite	Magne-tite	Magne-tite	Magne-tite	Magne-tite	Magne-tite	Magne-tite
Type	Type-V	Type-V	Type-V	Type-V	Type-V	Type-V	Type-V	Type-V	Type-V	Type-V	Type-V	Type-V	Type-V
Al_2O_3	0.75	0.03	0.02	0.03	0.05	0.02	0.04	0.03	0.03	0.04	0.02	0.00	0.00
MnO	0.02	0.03	0.04	0.01	0.02	0.03	0.04	0.04	0.04	0.02	0.02	0.00	0.00
TiO_2	0.01	0.06	0.03	0.01	0.02	0.01	0.03	0.00	0.01	0.02	0.03	0.00	0.01
Cr_2O_3	0.01	0.14	0.98	0.92	0.00	0.01	0.01	0.02	0.01	0.02	0.04	0.12	0.00
MgO	2.21	0.05	0.06	0.26	3.78	0.06	0.09	0.19	0.01	0.06	0.03	0.06	0.05
SiO_2	1.90	0.09	0.05	0.32	3.61	0.10	0.08	0.64	0.09	0.17	0.01	0.00	0.05
Fe_2O_3	63.04	66.57	65.88	64.09	59.65	67.07	66.50	64.36	66.67	65.05	66.42	65.43	65.78
FeO	29.29	29.97	29.93	29.33	28.50	29.98	29.81	29.81	29.84	29.39	30.12	29.38	29.64
V_2O_3	0.01	0.01	0.06	0.02	0.02	0.00	0.05	0.02	0.01	0.03	0.08	0.00	0.00
NiO	0.25	0.31	0.43	0.33	0.34	0.34	0.33	0.38	0.41	0.34	0.00	0.00	0.00
ZnO													
CoO													
Na_2O													
K_2O													
CaO													
Total	97.48	97.24	97.49	95.32	96.00	97.62	96.97	95.49	97.12	95.13	96.75	94.99	95.52
Cation													
Al	0.271	0.010	0.009	0.010	0.019	0.006	0.016	0.011	0.010	0.014	0.007	0.000	0.000
Mn	0.006	0.007	0.010	0.002	0.006	0.009	0.011	0.012	0.011	0.005	0.005	0.000	0.000
Ti	0.002	0.014	0.008	0.002	0.004	0.002	0.006	0.000	0.002	0.005	0.006	0.000	0.002
Cr	0.003	0.036	0.245	0.234	0.000	0.002	0.001	0.004	0.004	0.004	0.009	0.031	0.000
Mg	1.009	0.021	0.028	0.126	1.727	0.028	0.045	0.093	0.003	0.028	0.014	0.030	0.024
Si	0.583	0.028	0.017	0.103	1.105	0.031	0.026	0.205	0.030	0.056	0.003	0.000	0.016
Fe^{3+}	14.551	15.866	15.656	15.533	13.749	15.924	15.889	15.563	15.917	15.840	15.918	15.969	15.965
Fe^{2+}	7.512	7.938	7.904	7.901	7.301	7.911	7.914	8.009	7.916	7.952	8.022	7.970	7.994
V	0.002	0.001	0.013	0.004	0.004	0.001	0.010	0.004	0.002	0.007	0.016	0.000	0.000
Ni	0.061	0.078	0.110	0.084	0.084	0.086	0.083	0.099	0.105	0.090	0.000	0.000	0.000
Zn													
Co													
Na													
K													
Ca													
Total	24.000	24.000	24.000	24.000	24.000	24.000	24.000	24.000	24.000	24.000	24.000	24.000	24.000

Mg#	0.12	0.00	0.00	0.02	0.19	0.00	0.01	0.01	0.00	0.00	0.00	0.00	0.00
Cr#	0.01	0.79	0.96	0.96	0.02	0.27	0.08	0.28	0.27	0.22	0.56	1.00	
Fe^{3+}/R^{3+}	0.98	1.00	0.98	0.98	1.00	1.00	1.00	1.00	1.00	1.00	1.00	1.00	1.00

Sample number	SHB/18/36	SHB/18/36	SHB/18/36	SHB/18/37	SHB/18/37	SHB/18/37	SHB/18/37	SHB/19-12/82	SHB/19-12/82	SHB/19-12/78	SHB/19-12/39	SHB/19-12/39	SHB/19-12/39
Location	Kapili	Kapili	Kapili	Kapili	Kapili	Kapili	Kapili	Kapili	Kapili	Kapili	Maharaj-gunj	Maharaj-gunj	Maharaj-gunj
EPMA point	1 / 1 .	2 / 1 .	24 / 1 .	4 / 1 .	5 / 1 .	10 / 1 .	16 / 1 .	90 / 1 .	126 / 1 .	173 / 1 .	232 / 1 .	237 / 1 .	238 / 1 .
Mineral	Magne-tite	Magne-tite	Magne-tite	Magne-tite	Magne-tite	Magne-tite	Magne-tite	Ilmenite	Ilmenite	Ilmenite	Ilmenite	Ilmenite	Ilmenite
Type	Type-V	Type-V	Type-V	Type-V	Type-V	Type-V	Type-V						
Al_2O_3	0.00	0.03	0.00	0.00	0.00	0.01	0.01	0.18	0.17	0.14	0.15	0.14	0.13
MnO	0.08	0.01	0.00	0.05	0.00	0.00	0.02	10.92	11.68	8.99	8.42	8.94	8.36
TiO_2	0.00	0.00	0.00	0.03	0.03	0.00	0.04	49.63	50.84	50.22	52.72	52.66	52.45
Cr_2O_3	0.00	0.05	0.64	0.06	0.24	0.08	0.01						
MgO	0.09	0.05	0.15	0.08	0.17	0.20	0.05	1.26	1.21	0.58	0.22	0.26	0.27
SiO_2	0.06	0.07	0.16	0.10	0.24	0.21	0.05	0.01	0.09	0.06	0.06	0.00	0.06
Fe_2O_3	68.94	68.54	66.70	68.04	68.37	68.28	68.18	2.16	2.54	1.91	0.00	0.07	0.00
FeO	31.00	30.93	30.45	30.86	31.41	30.88	30.71	31.29	31.68	34.86	36.88	37.84	37.70
V_2O_3	0.04	0.02	0.01	0.04	0.08	0.02	0.01	0.00	0.00	0.12	0.11	0.03	0.01
NiO	0.00	0.07	0.02	0.00	0.00	0.08	0.08	0.01	0.13	0.15	0.01	0.00	0.00
ZnO								0.00	0.00	0.00	0.05	0.00	0.23
CoO								0.10	0.10	0.00	0.16	0.00	0.11
Na_2O								0.03	0.03	0.00	0.01	0.03	0.00
K_2O								0.00	0.01	0.00	0.00	0.00	0.00
CaO								0.03	0.03	0.06	0.01	0.01	0.02
Total	100.20	99.77	98.13	99.25	100.54	99.76	99.16	95.48	98.37	97.10	98.58	99.94	99.00
Cation													
Al	0.000	0.011	0.000	0.000	0.000	0.004	0.002	0.011	0.010	0.009	0.009	0.008	0.008
Mn	0.021	0.003	0.000	0.012	0.000	0.000	0.006	0.483	0.502	0.394	0.364	0.381	0.360
Ti	0.000	0.000	0.000	0.008	0.007	0.000	0.009	1.952	1.942	1.953	2.026	1.994	2.005
Cr	0.000	0.011	0.159	0.014	0.058	0.019	0.003						
Mg	0.041	0.024	0.068	0.035	0.078	0.094	0.025	0.098	0.092	0.045	0.017	0.019	0.020
Si	0.017	0.021	0.051	0.031	0.072	0.064	0.016	0.000	0.004	0.003	0.003	0.000	0.003
Fe^{3+}	15.944	15.923	15.734	15.885	15.735	15.838	15.940	0.085	0.097	0.074	0.000	0.003	0.000
Fe^{2+}	7.969	7.986	7.982	8.007	8.034	7.961	7.979	1.368	1.345	1.507	1.576	1.593	1.602

V	0.007	0.004	0.002	0.008	0.016	0.004	0.001	0.000	0.000	0.005	0.005	0.001	0.001
Ni	0.000	0.017	0.004	0.000	0.000	0.017	0.018	0.000	0.005	0.006	0.000	0.000	0.000
Zn								0.000	0.000	0.000	0.002	0.000	0.009
Co								0.004	0.004	0.000	0.007	0.000	0.004
Na								0.003	0.003	0.000	0.001	0.003	0.000
K								0.000	0.000	0.000	0.000	0.000	0.000
Ca								0.002	0.001	0.003	0.000	0.000	0.001
Total	24.000	24.000	24.000	24.000	24.000	24.000	24.000	4.000	4.000	4.000	4.000	4.000	4.000
Mg#	0.01	0.00	0.01	0.00	0.01	0.01	0.00						
Cr#	0.00	0.52	1.00	1.00	1.00	0.84	0.59						
Fe^{3+}/R^{3+}	1.00	1.00	0.99	1.00	1.00	1.00	1.00						

Chr magnetite: Chrome magnetite, Mg#: $Mg/(Mg+Fe^{2+})$, Cr#: $Cr/(Cr+Al)$, R^{3+}: $Al+Fe^{3+}+Cr$

List of publications

(I) Peer-Reviewed Articles

*__Banerjee R__, Biswas B K, Mondal S K (**2023**) Origin of alteration patterns in accessory chromites from the Kudada ultramafic rocks, East Singhbhum district (Jharkhand, India). ***Journal of the Geological Society of India*** 99:345-356 **Corresponding author*.

Banerjee R, *Mondal S K, Reisberg L and Park J -W (**2022**) Fractionation of trace and platinum-group elements during metamorphism of komatiitic chromites from the early Archean Gorumahishani greenstone belt, Singhbhum Craton (eastern India). ***Contribution to Mineralogy and Petrology*** 177, 75. **Corresponding author.*

Banerjee R, *Mondal S K (**2021**) Petrology and geochemistry of the Deccan basalts from the KBH-7 borehole, Koyna Seismic Zone (Western Ghats, India): Implications for nature of crustal contamination and sulfide saturation of magma. ***Lithos*** 380-381, 105864. **Corresponding author.*

(II) Conference abstracts

*Zhou X, **Banerjee R**, Reisberg L, Mondal S K (**2023**) Highly siderophile elements and Re-Os systematics of Archean komatiitic rocks in Gorumahisani greenstone belt, Singhbhum craton, India. Abstract with program. **Goldschmidt 2023**, Lyon, France. **Presenting author.*

Banerjee R, Zhou X, Mondal S K, Reisberg L, Park J -W. (**2022**) PGE geochemistry of early Archean komatiitic chromites from the Singhbhum Craton (India). Abstract only. **IMA 2022**.

***Banerjee R**, Mondal S K, Reisberg L, Zhou X (**2021**) Origin of Ni-Cu-sulfide minerals in the komatiitic rock suite of the Archean Gorumahisani Greenstone belt, Singhbhum Craton (eastern India). Abstract with the program. **Virtual Goldschmidt 2021**. **Presenting author*.

Banerjee R, Mondal S K (**2020**) Compositional variation and patterns of alteration in chromites of Archean komatiites from Kapili area, Gorumahisani greenstone belt, Singhbhum Craton (eastern India). International Geological Congress 2020 (virtual).

***Banerjee R**, Mondal S K (**2019**) Geochemistry of the Deccan Basalts from Borehole KBH-7 of the Koyna Seismic Zone (India): nature of crustal contamination and sulfide saturation of magma. **Goldschmidt 2019**, Barcelona, Spain. **Presenting author.*

*Mondal S K, Das E, **Banerjee R**, Reisberg L (**2019**): Trace element in chromites of komatiites from the Archean Gorumahisani greenstone belt, Singhbhum Craton (India). **Goldschmidt 2019**, Barcelona, Spain. **presenting author.*

Ghosh D**, *Banerjee R**, Bera P, Mondal S K (**2016**): Petrographic Character of the Deccan Basalt in the Koyna Bore Hole, India**.** In 'Development in Geosciences in the Past Decade - Emerging Trends for the Future and Impact on Society', Annual General Meeting of Geological Society of India, 203-207. **Presenting author.*

Bhattacharjee S, ***Banerjee R**, Pal D C (2014): Micro-domain analysis of pyrite and magnetite, the tale they can tell: an example from Singhbhum Shear Zone, eastern India. PRITHVI-2014 hosted by IIT-KGP. (poster). *Presenting author.